Multiwavelength variability of black hole x-ray binaries in the low/hard state

Thesis

How to cite:

Brocksopp, Catherine (2000). Multiwavelength variability of black hole x-ray binaries in the low/hard state. PhD thesis The Open University.

The Open University

Multiwavelength Variability Of Black Hole X-ray Binaries In The Low/Hard State

Catherine Brocksopp B.Sc. M.Sc.

Submitted for the degree of Doctor of Philosophy

September 2000

AUTHOR NO : T1139004
DATE OF SUBMISSION : 3 OCTOBER 2000
DATE OF AWARD : 20 DECEMBER 2000

CONTENTS

LIST OF FIGURES

LIST OF TABLES

Multiwavelength Variability Of Black Hole X-ray Binaries In The Low/Hard State

Catherine Brocksopp B.Sc. M.Sc.
September 2000

The Open University
Submitted for the degree of Doctor of Philosophy

The behaviour of black hole X-ray binaries can be classified into five spectral states which are defined in terms of the X-ray spectral and timing properties of the source. These states show distinct and observable characteristics and transitions from one state to another often take place.

Perhaps the most interesting of the five is the low/hard state; in this state the X-ray emission appears to be confined to a Comptonising corona surrounding the black hole, the optical and infrared emission comes from a cold accretion disc with a large inner disc radius and a weak continuous jet is emitted from the central regions of the disc.

In this thesis I study three black hole candidates which show low/hard state behaviour either most of the time (Cygnus X-1), quasi-periodically (LMC X-3) or intermittently (GS 1354−64). Observations were taken at X-ray, radio and optical wavelengths in order to study the properties of the low/hard state and the relationship between the accretion disc and the jet.

I have been grateful to many people during the past few years but particularly Rob Fender – he had no idea that taking me on as an MSc. student would result in being stuck with me for an extra three years. As my 'official' supervisors, Paul Roche and Carole Haswell have also been extremely supportive (even if they did leave.....!).

This thesis contains large amounts of data and I cannot name everyone who has contributed – but particular thanks to Guy Pooley, Tolya Tarasov, Victor Lyuty, Valeri Larionov and the Amsterdam astronomy department. Consequently I have had a large number of collaborators who are mentioned in the relevent chapters and are very much appreciated.

I am also extremely grateful to the astronomy departments of Sussex University, where I began my PhD and made use of the facilities even after transferring, and of the Open University where I transferred to and subsequently took advantage of their travel budget.

Final thanks to those people who have helped proof-read my thesis, particularly Rob Fender but also Paul Roche, Jörn Wilms, Simon Clark and Carole Haswell.

Chapter 1

INTRODUCTION

The black hole X-ray binaries Cygnus X-1, LMC X-3 and GS 1354−64 are three very different and yet very similar systems (see Table 1.1). Cyg X-1 is a high mass X-ray binary, luminous at both optical and X-ray wavelengths and is a weak, but persistent, radio source. LMC X-3 is also a high mass X-ray binary, although in this case it is thought that the black hole is more massive than the stellar companion and it is a much fainter source; the X-ray spectrum is considerably softer than that of Cyg X-1 and no radio counterpart has ever been discovered. However, as both are persistently emitting sources with comparable orbital and long term modulations, one might expect the two systems to be similar. Of particular relevance to this work is the recent discovery of quasi-periodic hard state behaviour in LMC X-3 which is indeed more akin to Cyg X-1. Initially GS 1354−64 appears to be a very different object – it is a faint, low mass, recurrent X-ray transient but may have had extremely luminous and soft X-ray outbursts previously. However, the most recent outburst showed surprisingly hard X-ray emission and can therefore be compared with Cyg X-1.

The three objects are considered individually in Chapters 2–8 with final comparisons and conclusions summarised in Chapter 9. The remainder of this chapter outlines the features of typical black hole X-ray binaries, although many of these are not exclusively relevant to the black hole candidates. Black hole diagnostics are considered first, followed by a description of the canonical X-ray spectral states. Finally the various other components of these systems are considered – the accretion disc and its corona surrounding the black hole, the radio jets which are emitted from the centre of the disc and the stellar winds

Table 1.1: A comparison between the three black hole candidates studied in this thesis.

	Cyg X-1	LMC X-3	GS 1354–64
X-ray source	persistent	persistent	transient
Black Hole Diagnostic	Mass estimate	Mass estimate	X-ray energy/power spectra
Mass of star ($M_\odot$)	~ 17.8	> 4	?
Mass of black hole ($M_\odot$)	~ 10.1	> 7	?
Orbital period (days)	5.6	1.7	?
Super-orbital period (days)	150 (294 ?)	200 ?	?
Distance (kpc)	2.5	40–50	10

which, in the case of a high mass companion star, can lead to important observational peculiarities. These various components are illustrated in Fig. 1.1.

1.1 Black Hole Candidate Diagnostics

The most convincing method of determining whether or not a black hole is present in an X-ray binary system is to calculate its mass – if higher than the Oppenheimer–Volkov (1939) limit, the theoretical maximum mass of a neutron star (i.e. 1.5–3.2 M$_\odot$), then it can be assumed that the compact object is a black hole.

As long as the stellar companion is bright enough for a radial velocity curve to be constructed then this is relatively straightforward:

$$\text{Kepler's 3rd law :} \qquad \frac{G(M_s + M_x)}{a^3} = \left(\frac{2\pi}{P}\right)^2 \tag{1.1}$$

where M_s and M_x are the masses of the star and the X-ray source respectively, a is the binary separation and P is the orbital period. If the distance from the two objects to the system centre of mass are a_s and a_x then $a = a_s + a_x$ and $M_s a_s = M_x a_x$. Then:

$$\frac{GM_x^3}{(M_s + M_x)^2} = \left(\frac{2\pi}{P}\right)^2 a_s^3 \tag{1.2}$$

The projected orbital velocity observed, i.e. the semi-amplitude of the radial velocity curve, is $K_s = V_s \sin i = \frac{2\pi a_s}{P} \sin i$. Therefore, as P and K_s can be determined from

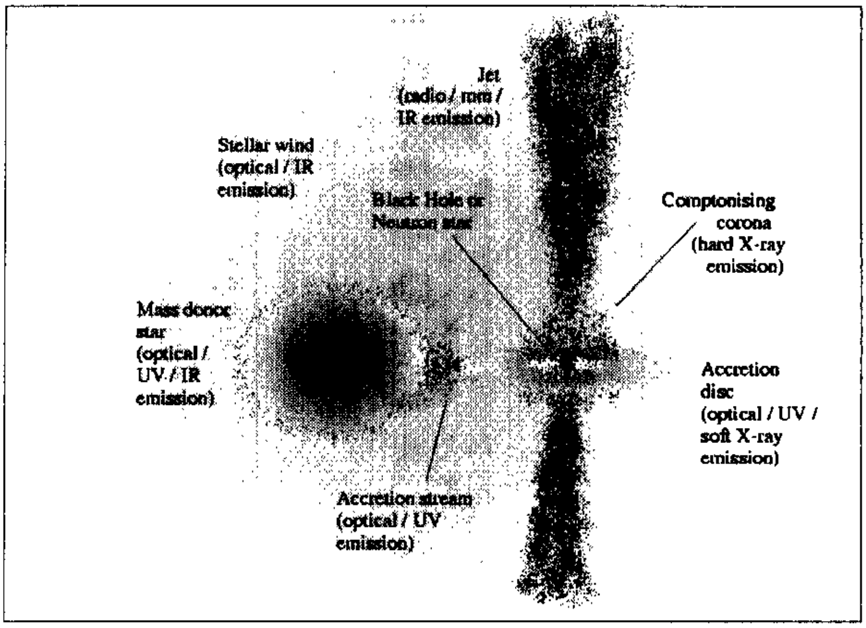

Figure 1.1: Schematic showing the components of a jet-emitting X-ray binary. It is likely that all three systems studied here are of this form, although the stellar component to GS 1354−64 would not be as massive as the star shown in the figure and would not emit a stellar wind (courtesy R.P. Fender).

spectroscopic observations, the mass function can be calculated:

$$f(M) = \frac{(M_x \sin i)^3}{(M_s + M_x)^2} = \frac{PK_s^3}{2\pi G} \tag{1.3}$$

The inclination angle can be constrained depending on the presence or otherwise of eclipses (upper limit) and by assuming that the rotation of the star is synchronous with the orbit (lower limit). Additionally, a lower limit to M_x can be obtained by assuming $M_s = 0$ and $\sin i = 1$. A range of possible masses for the stellar companion can be estimated depending on spectral type and luminosity and so therefore the mass of the compact object can also be estimated. This has been achieved for an increasing number of black hole X-ray binaries – see e.g. Charles (1998 and references within) for a list, currently containing ~8 X-ray transients as well as 3 persistent sources.

Unfortunately, however, it is not always possible to determine the mass of the two objects. Many of the stellar companions are too faint in quiescence for the orbital period to be determined – indeed, a number of transient sources may only be detected during

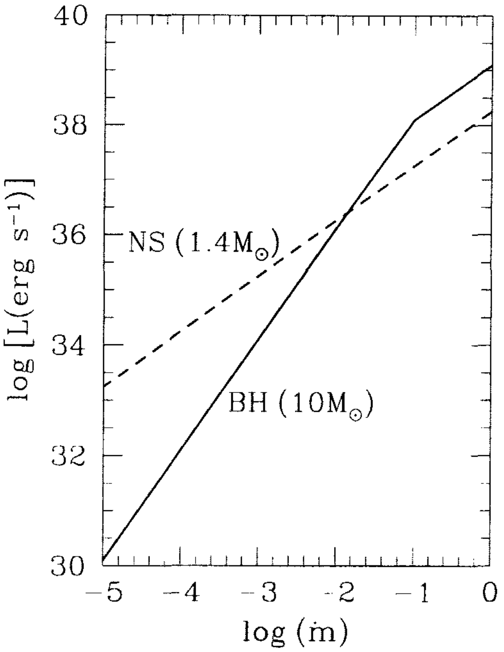

Figure 1.2: The predicted change in luminosity for an increase in the (Eddington scaled) mass accretion rate. The luminosity of a neutron star system increases proportionally to the mass accretion rate (as for a thin disc) as the advected energy is later radiated from the neutron star surface. The luminosity of a black hole system is surprisingly low when advection is important, rising significantly during outburst when advection is less significant (Narayan, Garcia & McClintock, 1997).

outburst. Therefore other characteristics have been used to distinguish between black hole and neutron star systems; these supposed signatures of a black hole have since been found to be unreliable – despite various systems (apparently) classified successfully using these methods.

From an observer's point of view, the main difference between a neutron star and a black hole is the presence or otherwise of a solid surface – one would expect an observable difference between matter accreting onto a neutron star and matter passing through the event horizon of a black hole. This is indeed the case – in a number of neutron star systems X-ray bursts are detected, when a flux increase of up to an order of magnitude takes place within about a second, decaying over 10–60 seconds and repeating on timescales of hours or days. It is thought that bursts arise when a critical amount of material has accreted onto the neutron star, causing a thermonuclear flash and hence X-ray emission. Unfortunately, while bursting behaviour is an extremely reliable neutron star diagnostic, an absence of bursts does not rule them out. Bursts are not observed in all neutron star systems, particularly for X-ray sources in which the X-ray luminosity is approximately one third of the Eddington luminosity or more (Van Paradijs 1998). Similarly, the presence of X-ray pulsations is a recognised neutron star signature but, again, pulsations are not present in all systems.

Expected signatures of accretion onto a black hole are less well understood. One would need to show that, as material flows inwards towards the compact object, there is a point at which the flow becomes radiatively inefficient, its energy passing through the event horizon. A number of theories have been put forward, most notably the Advection Dominated Accretion Flow (ADAF) models of e.g. Narayan, Mahadevan & Quartaert (1998 and references within. See also Section 1.3). However, again the same problem occurs – advective flows need not only take place in black hole systems; e.g. Shahbaz et al. (1998) suggest that one may be present in the X-ray burst source Aql X-1. Observational consequences of advective flows in the two types of system are discussed by Narayan, Garcia & McClintock (1997) – they show that, assuming energy advected onto the neutron star will then be radiated away, there should be distinct differences between the luminosity–mass accretion rate relationship of the two types of system (Fig. 1.2). This is supported by their observations showing that the (non-ADAF) outbursts of black hole systems are much more luminous relative to their (ADAF-dominated) quiescent state.

It is not only the X-ray lightcurves which can help distinguish between neutron star and black hole systems – indeed, the majority of current black hole candidates were initially classified on their X-ray spectral and timing similarities with Cyg X-1, the classical black hole candidate. As shown in subsequent chapters, Cyg X-1 was originally observed in two different 'states': a 'high' state in which the X-ray spectrum was dominated by an ultrasoft component but also showed a high energy power law tail, and a 'low' state in which only the power law was present (at all energies) and the lightcurve was dominated by aperiodic 'flickering'. More recently it has been shown that rapid X-ray variability, the ultrasoft component and the hard power law tails are not exclusively found in the black hole candidates – however it is possible that black hole candidates are the only systems in which the power law can still dominate at high luminosities. Further details of the spectral and temporal properties of X-ray binaries in the various spectral states can be found in

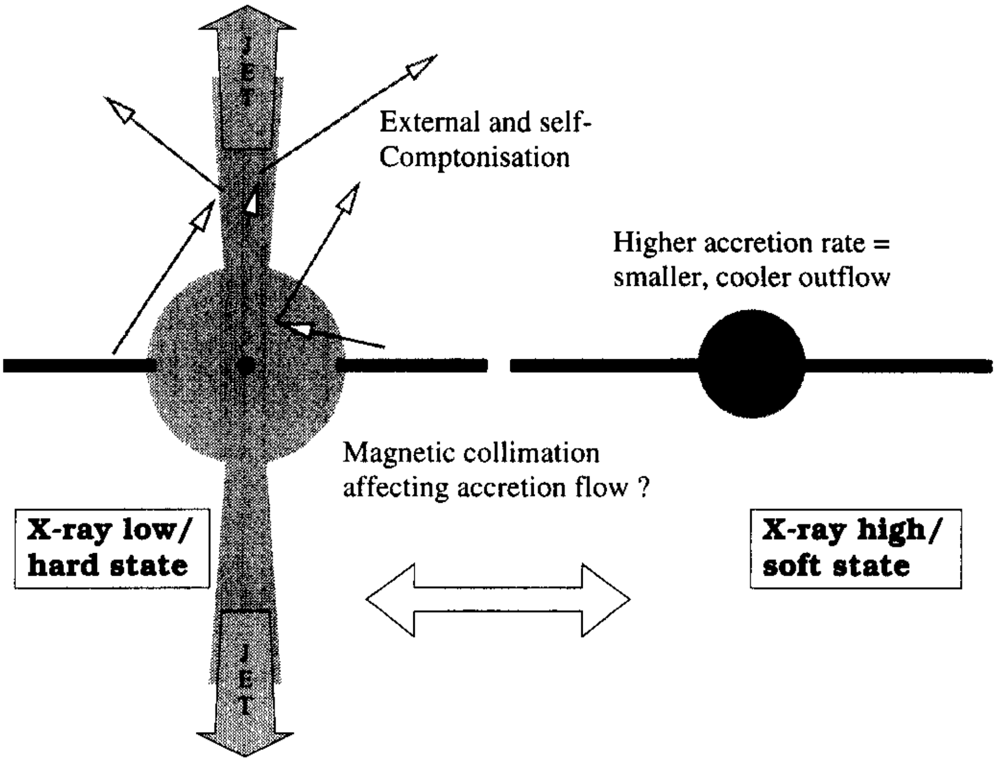

Figure 1.3: A comparison between the apparent geometries of the low/hard and the high/soft states of black hole candidates – during the soft state the jet becomes quenched and the accretion disc is supposed to extend to the last stable orbit around the black hole (courtesy: R.P. Fender).

the next section.

1.2 X-ray States

The different X-ray spectral states of black hole candidates were originally noticed in the 1970's when Cyg X-1 was found at either a 'high' or 'low' soft X-ray luminosity, accompanied by different spectral behaviour. An 'off' and a 'very high' state were added later in order to describe the behaviour of newly discovered black hole candidates (GX 339−4 and GS 1124−68, Tanaka & Lewin (1995) and references within). This rather vague classification was in use for about twenty years before a unified system of spectral and temporal properties, based loosely on the mass accretion rate, was devised (Van der Klis 1994, 1995). There are now five spectral states, with the 'intermediate' state apparently some hybrid between the low and the high states. A schematic showing the geometry of the low/hard and high/soft states, predicted from X-ray spectral properties, can be seen

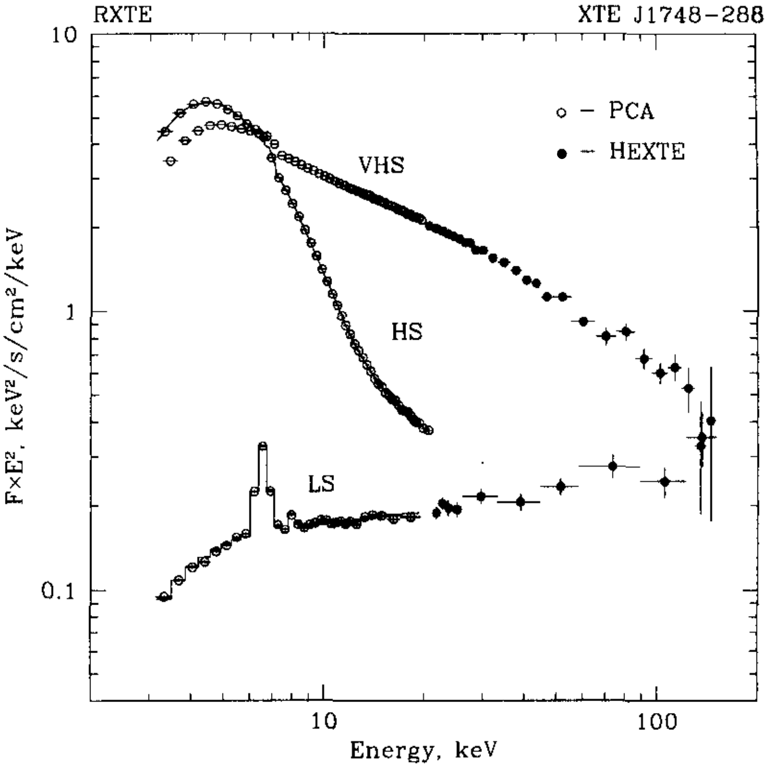

Figure 1.4: Energy spectra of the black hole candidate XTE J1748−288 – clearly the soft disc contribution is present during the high and very high states but not during the low state (Revnivtsev, Trudolyubov & Borozdin 2000).

in Fig. 1.3 – the radio behaviour is also shown (see below for description). Lightcurves and typical energy and power spectra for the various states can be seen in Figs. 1.4, 1.5 and 1.6 and explained below.

The low/hard state is perhaps the most well-studied, mainly on account of it being the state in which Cyg X-1 is usually found. The X-ray energy spectrum shows a power law, with no obvious soft blackbody contribution from the accretion disc. Therefore it is thought that the disc is truncated at a large inner radius at which point the gas flow becomes *advection-dominated* (e.g. Esin et al. 1998). The power law emission is thought to be produced by the Compton upscattering of low energy (ultraviolet, optical) seed photons (originating in the disc or ADAF?) by a corona surrounding the compact object (e.g. Shapiro, Lightman & Eardley 1976). Power spectra of black hole candidates in the low/hard state typically show a flat power law ($P \propto \nu^{-\gamma}$, $\gamma \sim$ 0–0.3) below the break frequency ($\sim$ 0.04–0.4 Hz); above the break frequency the power law steepens to $\gamma = 1 - 1.7$, gradually steepening further to $\gamma = 1.5 - 2$ around $\geq$ 10 Hz with 'bumps' or 'shoulders' on the way. The overall shape is approximately that of a Lorentzian centred on $\nu = 0$, although a QPO may also be present (Van der Klis 1995). The off state may well be a faint low/hard state as the X-ray properties are similar.

When a source enters the high/soft state, possibly via the intermediate state during the transition, the disc contribution increases significantly until the power law tail steepens and is only apparent at high energies. It is thought that on entering the soft state, the inner radius of the disc decreases to the last stable orbit around the black hole and that the ADAF is restricted to the much smaller and cooler Comptonising corona - hence the dramatic hard and soft X-ray anti-correlation during the soft state (e.g. GX 339–4 - see Fig. 1.6). The power spectrum during the soft state simply shows a power law ($\gamma \sim 1$) and a lower noise amplitude than that of the low state. It should be noted, however, that the observed lags between soft and hard X-rays are comparable when in the low and high states but increase significantly during the transition - as the lag time is thought to

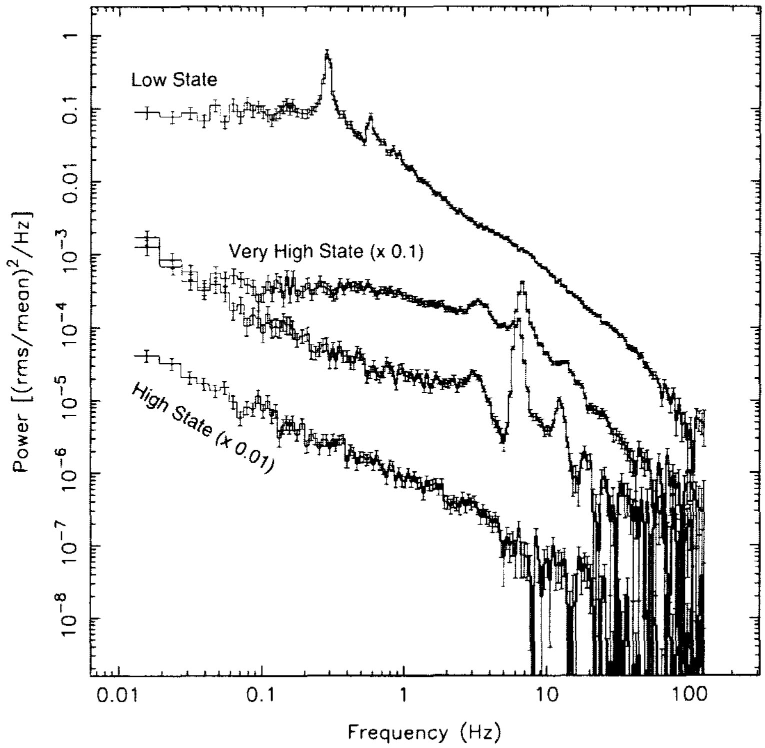

Figure 1.5: Power spectra of the black hole candidate XTE J1550–564 in the low, the high and the very high states (Wijnands 2000).

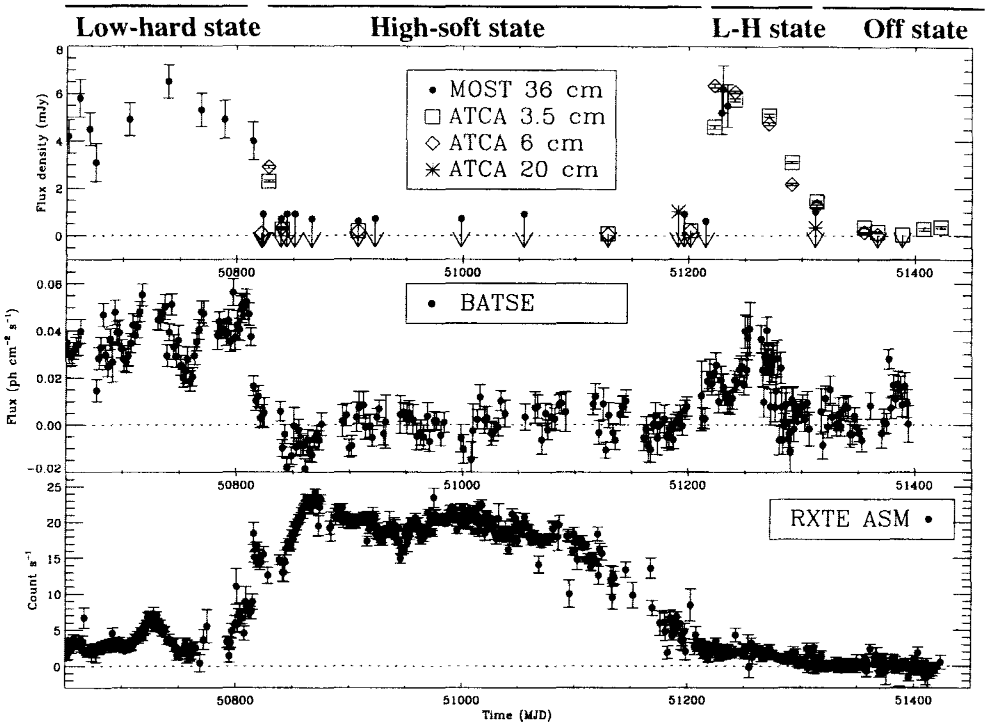

Figure 1.6: Lightcurves of GX 339−4 in the low/hard, high/soft and off states at hard and soft X-ray and radio wavelengths (Corbel et al. 1999)

represent the crossing time of the corona, it appears that some part of the theory may be incorrect (Pottschmidt et al. 2000).

While the X-ray energy spectrum of the very high state is comparable with that of the high state, but with considerably higher luminosity, the power spectrum differs greatly. Only five systems (GX 339−4 and four SXTs) have been observed in this state, but the very high state power spectra appear to be characterised by a noise amplitude part way between that of the low and high states and a QPO at significantly higher frequencies than those of the low/hard state.

Until recently, these spectral states were only considered to be properties of the X-ray emission – however, it appears that the radio behaviour of black hole X-ray binaries can be classified into the same five states. If we assume that the radio emission from X-ray binaries is from a synchrotron-emitting jet originating at the centre of the accretion disc (see Section 1.4), then it can be shown that a weak jet is present during the low and off states but that it is quenched during the high state. The jet's behaviour during the intermediate state is currently undetermined – there are suggestions that it may be quenched (e.g. Corbel et al. 2000) but also that plasmon ejections take place during hard/soft state transitions and so this may occur as the system passes through the intermediate state (note that radio emission may still be observed during the high state due to plasmons ejected during the transitions). Relativistic plasmon ejections may also take place during the very high state, although distinguishing between the very high and intermediate states is non-straightforward (Homan et al. 2000). Radio jets are summarised further in Section 1.4 and observations presented in subsequent chapters.

1.3 Accretion Discs

All three X-ray binaries studied here show evidence for an accretion disc surrounding the compact object (see Chapters 2, 5 and 8). While this is generally expected in a low mass system in which accretion takes place via Roche lobe overflow, it may be surprising in the case of a high mass wind-emitting system such as Cyg X-1 (although the wind has sufficient angular momentum that we may expect a small disc to form). As mentioned further in Chapters 2, 3 and 4, it is thought that the gravitational field of the black hole attracts the wind and focusses it towards the L1 point, resulting in quasi-Roche lobe overflow.

Accretion onto Black Holes

Simple considerations of fluid dynamics and conservation of mass, energy and angular momentum can lead to a set of equations from which we can determine (or at least parametrise) properties of the disc – these include surface density, viscosity and the vertical thickness of the disc at different radii from the compact object (see e.g. Frank, King & Raine (1992) for further details).

Chen et al. (1995) and Narayan, Mahadevan & Quataert (1998) show that four different solutions can be obtained from these equations when considering accretion onto a black hole:

- Thin disc model of Shakura & Sunyaev (1973) – the accreting gas forms an optically thick, geometrically thin disc around the compact object and an approximately blackbody spectrum should be observed locally. This is the classic disc solution and has been used to describe the discs of cataclysmic variables, including during outbursts (see below); in the case of neutron stars and black holes it is less appropriate due to the additional irradiation 'puffing up' the disc.

- Two-temperature disc model of Shapiro, Lightman & Eardley (1976) (and subsequently Mitsuda et al. 1984, Makishima et al. 1986) – in this optically thick gas flow the ions have a much greater temperature than the electrons. The solution has a much hotter inner disc, as a result of which a central corona is thought to be present. This corona is thus able to produce the observed power law spectrum of the hard X-rays and γ-rays by inverse Compton scattering soft disc photons – a two-temperature disc plus spherical corona model has been successful recently in describing observations of the black hole candidates Cyg X-1 and GX 339−4 (Nowak et al. 1999, Wilms et al. 1999, and references within).
- Optically thick ADAF – if the accretion rate is super-Eddington then the large optical depth of the flow is able to trap most of the radiation, advecting it into the black hole (e.g. Abramowicz et al. 1988).
- Optically thin ADAF – in the case of a low, sub-Eddington mass accretion rate the inflowing gas has a very low density and cannot radiate and cool efficiently. This stored thermal energy is therefore again advected into the black hole. This model also requires a two-temperature plasma (e.g. Narayan & Yi 1994).

Various combinations of these ADAF solutions have been suggested for the spectral states outlined above, depending on the value of $\dot{M}$, relative to the Eddington limit. Esin et al. (1998) find that the critical value is $\dot{M} \sim 0.08$; therefore it would seem that the low and quiescent states are the result of an optically thin ADAF, the other three states an optically thick ADAF.

It should be noted, that ADAF solutions for accretion onto black holes are very much a theory, and a controversial one at that. The recent time lag observations of Pottschmidt et al. (2000) contradict current models for the corona and show that while the postulated ADAF+corona fits the spectral observations, we may not yet have the system geometry determined. However, it is certainly the case that material flows through the accretion disc, radiating at various wavelengths until it reaches the inner regions around the black hole. There it becomes a very inefficient radiator of light, but the mechanisms by which it switches from efficient to inefficient are not well understood.

Disc Instability Model

It is well-known that accretion does not always continue in a smooth steady state and that outbursts are observed in many (all?) X-ray binaries; in many cases we owe the discovery of the systems to the occurence of outbursts. These can take place on a timescale of weeks for dwarf novae and decades for the case of soft X-ray transients. The outbursts are thought to be due, not to a variable mass accretion rate, but to a build up of material in the disc – when a critical value of surface density is reached the disc is emptied rapidly.

Using the thin disc approximation (see Frank, King & Raine (1992), and references within) and assuming a slowly rotating non-magnetic star in a steady state, the solution for an accretion disc surrounding it is:

$$\nu\Sigma = \frac{\dot{M}}{3\pi}\left(1 - \left(\frac{R_*}{R}\right)^{1/2}\right) \qquad (1.4)$$

where ν = viscosity, Σ = surface density, R_* is the stellar radius and R is the radius from the star.

There seem to be two timescales which are important to the stability of an accretion disc: viscous - the slow build up of material in the disc, prior to its reaching the critical values of viscosity necessary for an outburst, and thermal – if the disc becomes unstable to temperature perturbations then a rapid thermal runaway takes place. Whether or not the disc is stable depends on the value of $\frac{\delta\mu}{\delta\Sigma}$, where $\mu = \nu\Sigma$ for the disc to be stable to temperature perturbations the gradient of a $\log\mu$ vs. $\log\Sigma$ graph must be positive (Fig. 1.7 shows the characteristic 'S' curve shape of this graph). If the disc is optically thick then $\mu \propto \Sigma^{7/5}$, if optically thin then $\mu \propto \Sigma$. Thus in both cases the disc is viscously stable because $\frac{\delta\mu}{\delta\Sigma} > 0$. However, at the transition between optically thick and thin, $\mu \propto \Sigma^{-2/5}$ and so the disc becomes unstable.

At very large radii $\mu = \frac{\dot{M}}{3\pi} = \mu_s$. If μ_s is on a stable branch of the 'S' curve and $\mu \neq \mu_s$, then the disc will evolve $\mu \rightarrow \mu_s$ on a viscous timescale and approach stability. If μ_s is on an unstable branch and $\mu \neq \mu_s$ then the disc will evolve away from μ_s on a thermal timescale and enter an outburst. Thus the disc undergoes limit cycle behaviour – see Fig. 1.7.

While this model was developed initially for the outbursts of dwarf novae it is thought that it is also applicable to the outbursts of soft X-ray transients and also transients such as GS 1354–64 which remained in the hard state throughout its most recent outburst (see Chapter 8).

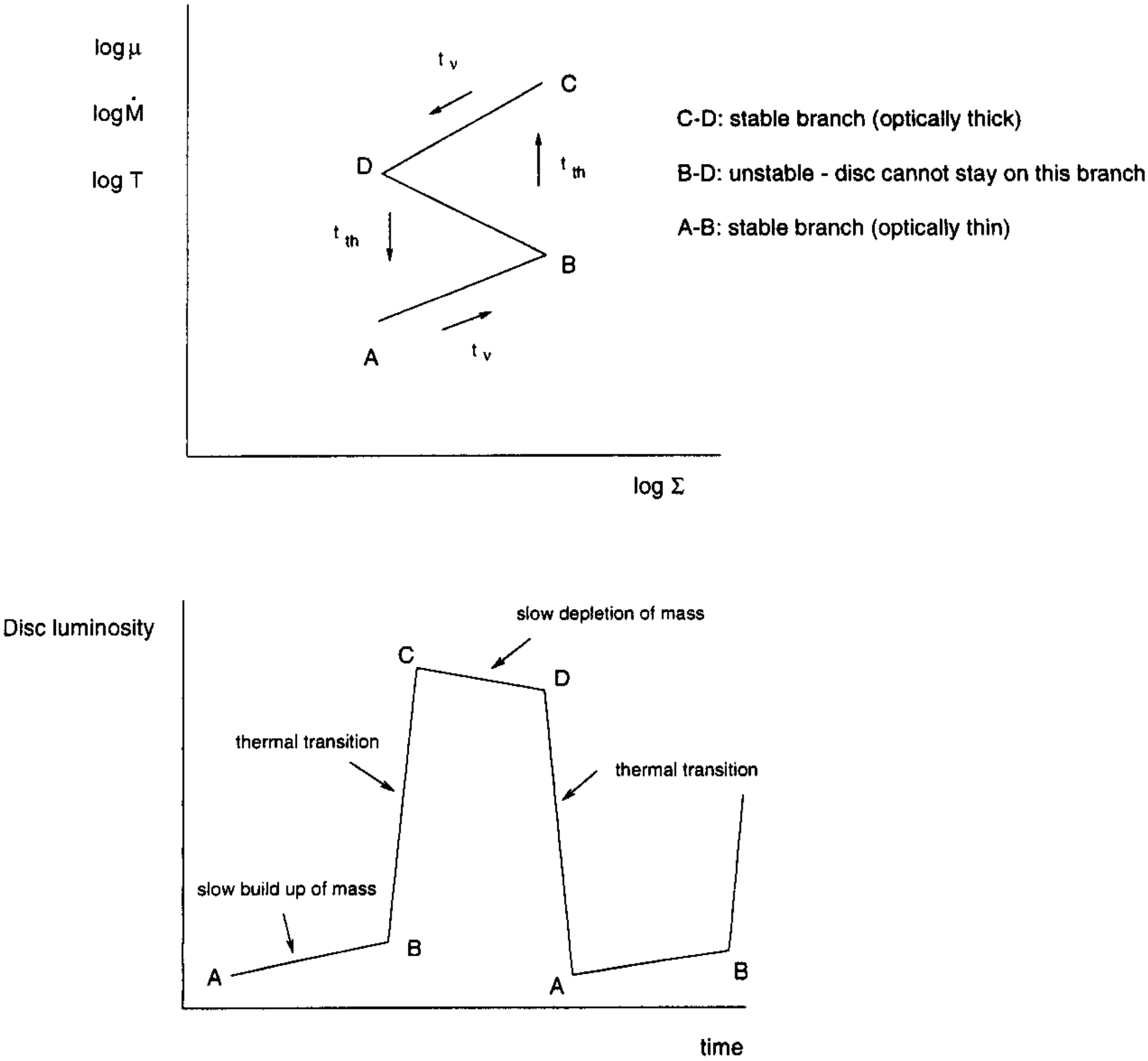

A-B: Slow build up of mass in the disc on a viscous timescale

B-C: Critical disc mass reached. Disc makes transition to hot state on a thermal timescale = outburst

C-D: Mass drains onto central object on a slow viscous timescale

D-A: Transition back to cool, low viscosity state on a thermal timescale = return to quiescence

Figure 1.7: Schematic illustrating the disc instability model (see Frank, King & Raine (1992), and references within). As the mass held by the disc increases the viscosity also changes. At a critical value of viscosity the disc becomes unstable to further temperature perturbations – an outburst takes place on a thermal timescale as the disc jumps to a new stable branch of the 'S' curve. A second thermal transition takes place as the disc material is depleted and limit cycle behaviour continues.

Disc Precession

Long-term variations have now been discovered in various X-ray binaries such as SS 433 (e.g. Abell & Margon 1979), Her X-1 (Tananbaum et al. 1972) and LMC X-4 (Heemskerk & Van Paradijs 1989) and interpreted as the precession period of the accretion disc in each system. It is still not understood exactly how this takes place, although there are a number of suggestions assuming very different mechanisms.

Models of rigid disc precession induced by the gravitational pull of the companion star were suggested by e.g. Gerend & Boynton (1976) for Her X-1 and Leibowitz (1984) for SS 433. They all show that a tilted disc will precess about its central star – however, while these models could reproduce the observations, they were not able to indicate how the disc could become tilted. This was resolved by Papaloizou & Terquem (1995) who showed that tidal forces exerted by the companion star could also tilt the disc, as long as the sound-crossing time of the disc was small compared with the precession period. Their work is confirmed by Larwood (1998) who shows that the ratio of precessional to orbital periods of Her X-1, SS 433, SMC X-1 and LMC X-4 are consistent (i.e. ≥ 10) with such a model, but that of Cyg X-2 is not.

Alternatively, Pringle (1996) showed that the central X-ray source will illuminate the disc in such a way that a radiative force will be exerted, creating a warp which causes the disc to precess. Wijers & Pringle (1998) further argue that the tilted disc models do not explain how the disc can precess as a whole, when the precession rate is a strong function of radius, or how the disc avoids sinking back into the plane of the orbit on a viscous timescale. They show in addition that, unlike a tidally precessing disc, the radiative warp mechanism allows for prograde precession – as seems to be the case in e.g. Cyg X-2, if a precessing disc is indeed the origin of its long period.

A third possible mechanism by which a disc can precess is the torque exerted by a wind-emitting disc (e.g. Schandl & Meyer 1994). As the coronal wind leaves the disc it exerts repulsive forces, sufficient to twist and/or tilt the disc. Thus irradiation by the X-ray source and the subsequent driving of the wind is asymmetric around the disc leading to a self-perpetuating periodicity.

Further theoretical investigation by Ogilvie & Dubus (2000) suggests that the long periods of X-ray binaries are not necessarily all produced by the same mechanism. Indeed, they show that radiative warps can only produce a steadily precessing disc for a narrow range of parameters – it appears that Her X-1, SS 433 and LMC X-4 are close to the stability limit; SMC X-1, Cyg X-2 and Cen X-3 are far from the stability limit and so any precession is likely to be chaotic or quasi-periodic. They further suggest that Cyg X-1, LMC X-3 and Sco X-1 are unlikely to show periodic precession – indeed the long periods seen in these systems may be due to precession only partially, if at all. This is investigated further in Chapters 4 and 6.

1.4 Radio jets

As mentioned above, the low/hard (and quiescent?) state of X-ray binaries is associated with the ejection of a radio-emitting jet from the central regions of the accretion disc surrounding the compact object. During the high/soft (and intermediate?) state the jet becomes quenched, although it is possible that radio emission is still observed from previously ejected material. Finally, the characteristics of the radio emission during the very high state are currently undetermined – ejections of radio-bright plasmons have been suggested but these may be the result of the state *transition* rather than the state itself.

Regardless of the type of ejection (i.e. a weak continuous jet, as in GX 339−4; very luminous plasmons, as in Cyg X-3; quasi-periodic smaller plasmons, as in GRS 1915+105; see Fig. 1.8) the subsequent radio emission is non-thermal and shows a synchrotron spectrum:

For a Maxwellian distribution of electrons with energy E:

$$N(E)dE = N_0 E^{-p} dE \tag{1.5}$$

Then the source flux density, S is a power law function of frequency:

$$S_\nu \propto \nu^\alpha \tag{1.6}$$

where $p = 1 - 2\alpha$ and α is known as the spectral index.

For an optically thin synchrotron source a spectral index of typically -1 is expected, assuming that the source is simple and homogeneous (note that this is not the case for collimated jets in which an optical depth gradient is present). A steepening of the spectrum, due to energy losses from the spiraling electrons and from the inverse Compton effect, will be observed at high frequencies. A sharper turnover will also take place at the lower end of the frequency range, typically producing a steeper, optically thick spectrum due to synchrotron self-absorption by the jet itself; this self-absorbed part of the spectrum will have a spectral index of $+2.5$, steeper than a black body as the electrons radiate

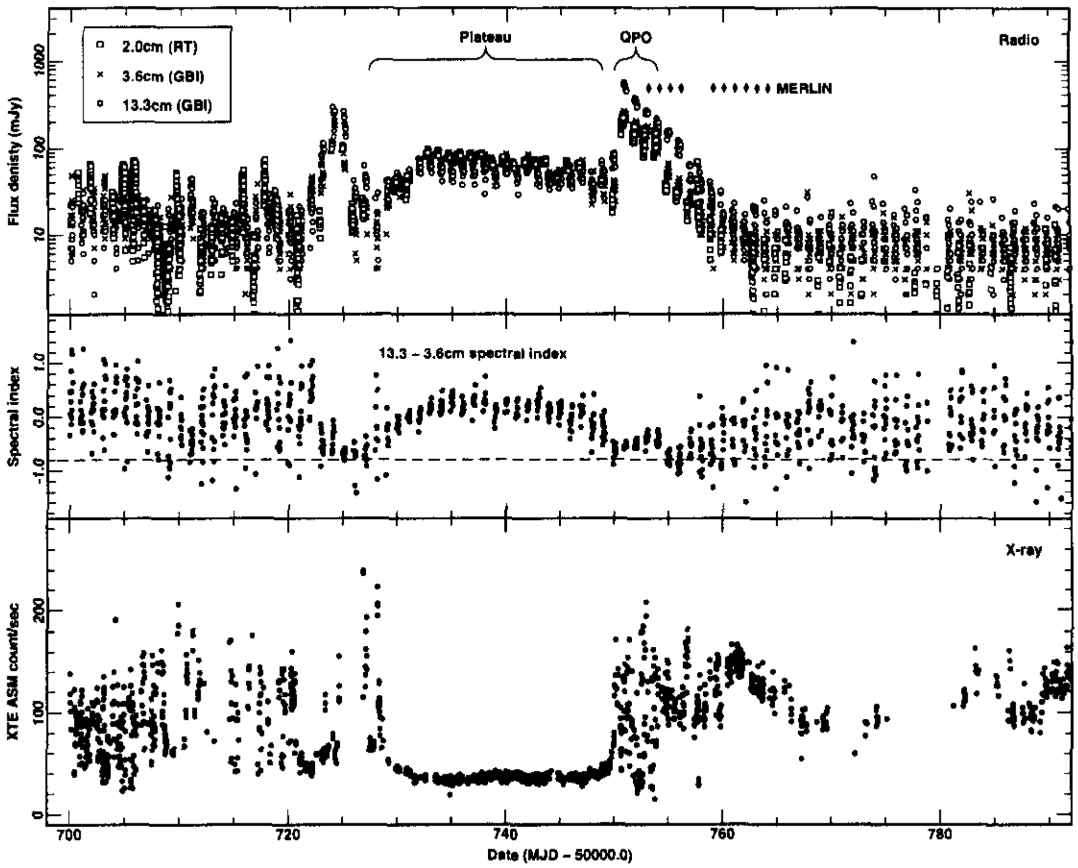

Figure 1.8: Radio lightcurves at 2.0, 3.6 and 13.3 GHz of GRS 1915+105 illustrating the different types of radio jet – continuous jet (plateau), QPO ejections and luminous one-off ejections. The evolution of the spectral index (3.6 – 13.3 GHz) and the XTE lightcurve are also shown (Fender et al. 1999).

at different frequencies and hence have different effective temperatures. Possible further reduction of emission at low frequencies may take place due to absorption by an intervening thermal plasma and/or the Tzsytovich–Razin effect, in which below a certain cut-off frequency the refractive index of an intervening thermal plasma is <1 and the emission is suppressed.

The plasmon ejections seen during e.g. state transitions and outbursts tend to be optically thick, becoming optically thin to progressively longer wavelengths as the plasmon expands – in this type of ejection the Van der Laan (1966) model works reasonably well. In the case of a continuous jet the Van der Laan 'bubble' model breaks down; the continuous jets of X-ray binaries in the hard state are optically thick and partially self-absorbed,

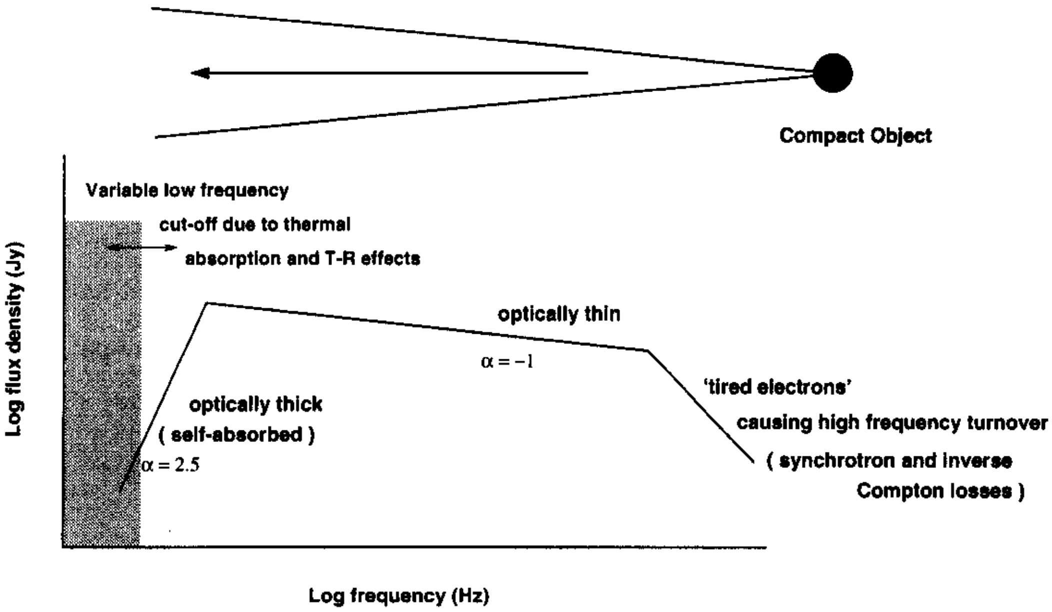

Figure 1.9: Schematic showing the spectrum of a typical, simple and homogeneous synchrotron source – N.B. this is not to scale and the cut-offs to the optically thin spectrum are more gradual than shown here, although take place within a decade in frequency. The source becomes optically thin to lower frequencies as distance from the compact object increases (see Fig. 1.11).

showing a characteristic 'flat' spectrum ($\alpha \sim 0$).

The Flat Spectrum

The flat spectrum continuous jet is increasingly becoming a reliable characteristic of black hole candidates in the low/hard state; it is also seen in Z-sources (horizontal branch; see Van der Klis (1995) for definition of Z-source spectral states) with sufficiently similar properties for there to be no distinct way of distinguishing between black hole candidate and Z-source on the basis of their radio emission. However it appears that the Z-sources are much more variable in their radio emission than the black hole candidates (Fender, private communication). Conversely, atoll sources are sometimes detected in the radio but generally only during transient outbursts (e.g. Aql. X-1) and during times of very high mass accretion rate (e.g. GX 13+1); X-ray pulsars have never been detected at radio wavelengths, perhaps due to the inferred high magnetic fields and/or very large (1000 km) inner disc radius.

While the origin of the flat spectrum is not well-understood it is thought to be the effect of partial self-absorption in the core. This was modelled by Blandford & Königl (1979) who predicted that for a 'simple isothermal' conical jet the optical depth to synchrotron self-absorption will depend on the frequency and the distance from the compact object – i.e. the distance from the compact object of an emission site will be $r \propto \nu^{-1}$. Therefore the observed flux density $S_{obs} \propto \nu^2 r^2 T$ is independent of frequency and so a flat spectrum is expected for a continuous jet.

The implications of this flat spectrum are extremely significant – for a jet with a flat spectrum out to ν_{high} the luminosity is $L_{jet} \propto \nu_{high} S_\nu$. Thus the power of the jet is:

$$P_{jet} \sim \nu_{high} S_\nu \eta^{-1} F(\Gamma, i) \tag{1.7}$$

where η is the radiative efficiency and $F(\Gamma, i)$ is a correction factor for relativistic bulk motion (e.g. Fender 2000). Thus assuming that (i) the flat spectrum extends to the near-infrared (as seen in e.g. GRS 1915+105, Cyg X-1), (ii) the radiative efficiency of the jet is $\leq 5\%$ (based on observations and theory) and (iii) relativistic beaming of the radio emission is negligible, then the power required by the jets of X-ray binaries in the low/hard state is $\geq 5\%$ of the total accretion luminosity of the X-ray source (e.g. for Cyg X-1 $P_{jet} \sim 10^{36}$ erg/s, compared with an observed X-ray luminosity of $\sim 3 \times 10^{37}$ erg/s. This is not accounted for in current X-ray models. Furthermore, Fender (2000) also shows that considerations of the bulk relativistic motions indicate that this is fairly likely to be an underestimate.

The Disc / Jet / Corona Coupling

Various theories of producing, accelerating and collimating the jets have been suggested, the most well-known being the 'bead-on-a-wire' magnetohydrodynamical model of Blandford & Payne (1982); this invokes plasma passing along magnetic field lines, which are frozen in to the accretion disc. If the angle between the field line and the disc is less than 60° then the plasma will be accelerated away by centrifugal forces. Collimation can then be achieved by the poloidal component of the magnetic field (Koide et al. 1998).

There are many other theories and all require the presence of an accretion disc – whatever the jet origin, from both theory and observations, it appears that the accretion disc is essential for jet production (see e.g. Falcke & Biermann, 1996 and references within). However, simultaneous X-ray and radio observations have shown that there is no simple connection between the two – clearly some complex coupling between the disc, the Comp-

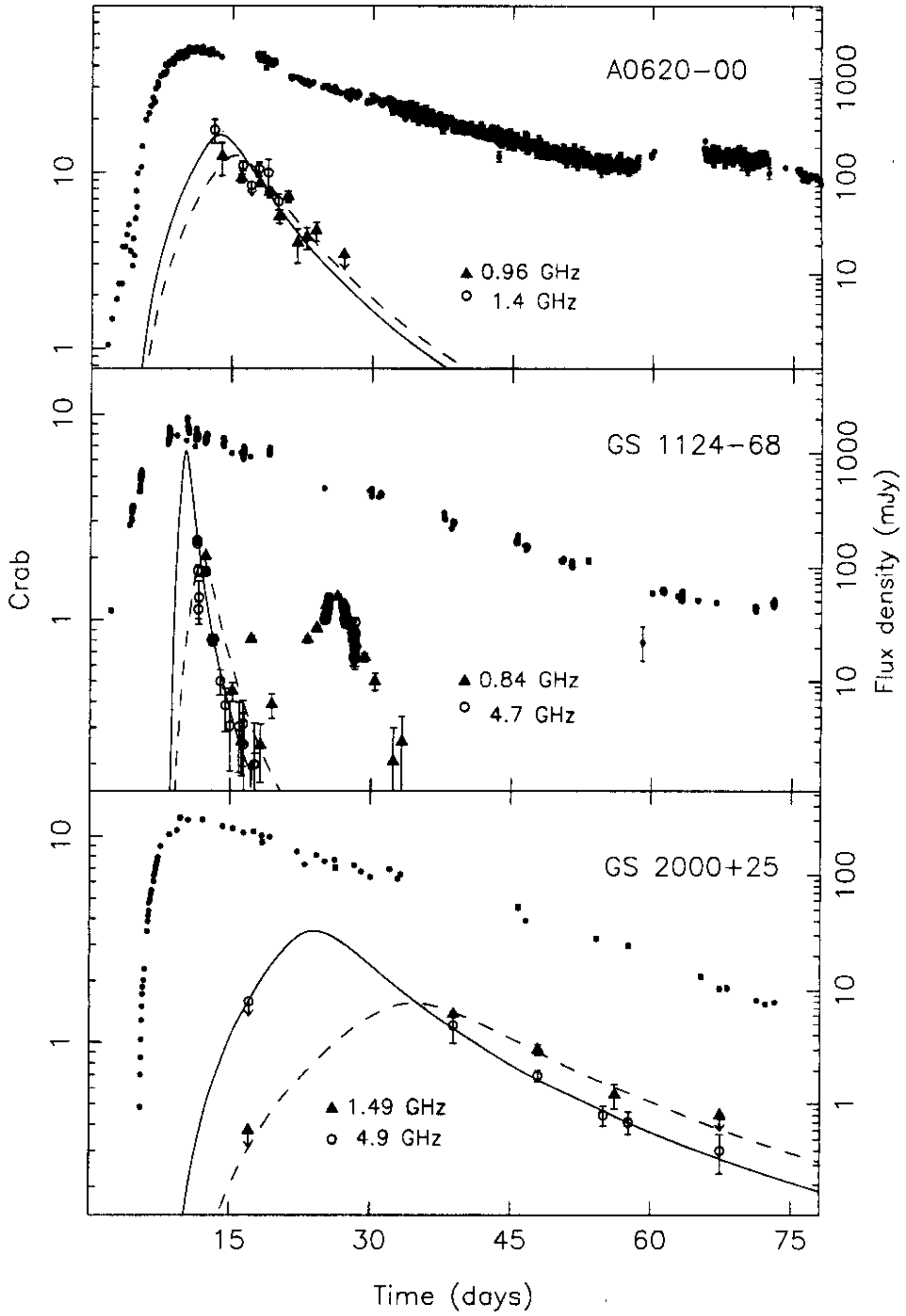

Figure 1.10: Radio and X-ray lightcurves for the soft X-ray transients A0620−00, GS 1124−68 and GS 2000+25 – clearly some degree of correlation is present but it is not clear exactly how the disc and jet behaviours are related (Kuulkers et al. 1999).

tonising corona and the jet is a common feature of X-ray binaries in the low/hard state. It would need to explain the observed, apparently self-contradictory, behaviour such as (loosely) correlated soft X-ray transient outbursts (Fig. 1.10), the proposed disappearance

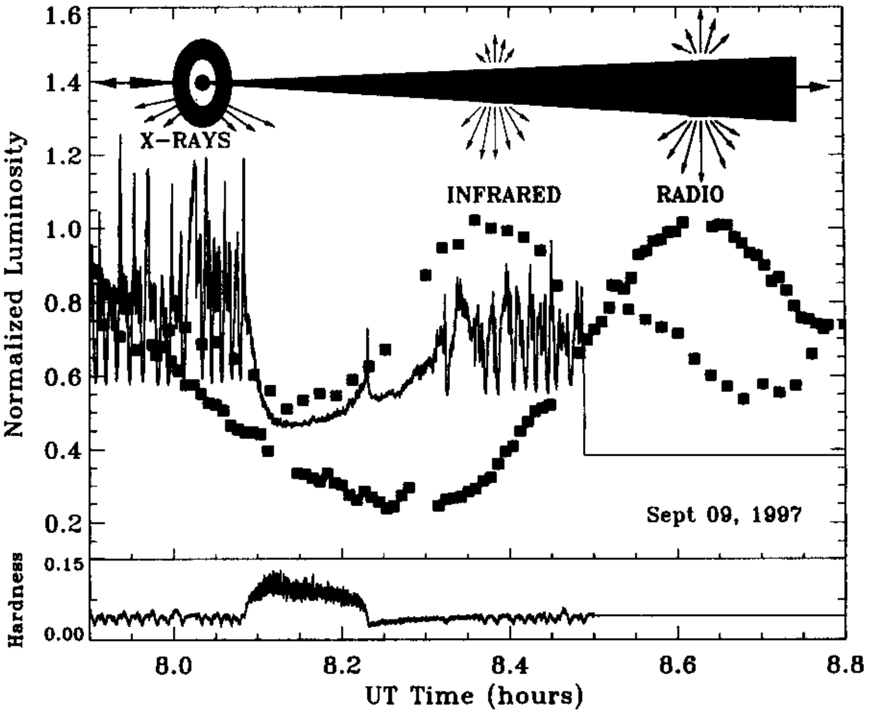

Figure 1.11: High time resolution plot of one of the quasi-periodic X-ray dips of GRS 1915+105; it is followed immediately by the infrared and subsequent radio synchrotron events as the ejected plasmons become optically thin to progressively longer wavelengths (Mirabel & Rodríguez 1999).

of part of the inner disc into the black hole prior to ejections in the case of GRS 1915+105 (Fig. 1.11) and the anti-correlated soft state behaviour (Fig. 1.6).

Correlated events between various wavelength regimes have occurred in many X-ray binaries, including GRO J1655-40 (Tavani et al. 1996), Cyg X-3 (McCollough et al. 1998) and V404 Cyg (Han & Hjellming 1992). The anti-correlated soft state behaviour has already been emphasised above. However, perhaps the most dramatic example of correlated X-ray/radio emission can be found in GRS 1915+105 during the periods of quasi-periodic oscillations shown in Fig. 1.8. One of these oscillations is shown in greater detail in Fig. 1.11 and it is clear to see that a synchrotron ejection takes place simultaneously with X-ray dips, emitting first at infrared wavelengths and then in the radio. It was proposed that some of the inner parts of the accretion disc fall into the black hole, causing the X-ray dips, followed by the immediate ejection of material in the jet (e.g. Mirabel et al. 1998). As seen above, the power required for the flat synchrotron spectrum in the infrared is highly significant. GRS 1915+105 is also well-known for its radio plateau states which coincide with hard X-ray outbursts (Fender et al. 1999).

Polarisation

Although the polarisation of X-ray binaries tends to be weak and therefore poorly studied and/or understood, important information can be obtained from the presence or otherwise of polarised radio emission.

In a synchrotron source electrons are accelerated in a spiral around magnetic field lines by the Lorentz $\underline{V} \times \underline{B}$ force, emitting beamed radiation. This radiation is therefore linearly polarised at a position angle orthogonal to the magnetic field. Thus detection of linear polarisation from an X-ray binary can determine the orientation of the jet.

Circular polarisation can also be observed in jet sources, either produced (i) intrinsically by the synchrotron mechanism or (ii) by the passage of linearly polarised radiation through plasma with elliptical propagation modes (Kennett & Melrose 1998). Recent work by Fender et al. (2000a), in which circular polarisation was discovered in SS 433, showed that theoretically it should be possible to distinguish between these two origins from their spectra. The circular polarisation spectrum should be $m_c \propto \nu^{-1/2}$ in the first case and $m_c \propto \nu^{-1}$ (or $\propto \nu^{-3}$ if highly relativistic plasma) in the second; m_c is the fractional circular polarisation ($=$ Stokes $|V|/I$).

Determination of the composition (i.e. e^-e^+ or e^-p^+) of the jet should also be possible, given an estimate of the Lorentz factor, γ $(= (1-(\frac{v}{c})^2)^{-1/2})$ – this can be determined from the circular polarisation spectrum. Wardle et al. (1998) concluded that for the low value of γ for the source 3C 279, if each electron were accompanied by a proton then considerably more kinetic energy would be required to power the jet than that observed to be dissipated at the head of the jet – therefore e^-e^+ pairs were deemed more likely. While a similar method could potentially be used to determine the composition of jets in X-ray binaries, it should be noted that in most Galactic jet sources there is no observed hotspot and hence no way of estimating the amount of power dissipated in the ISM.

1.5 Stellar Winds

Low mass stars, such as the Sun, are thought to contain a convection zone whose motions heat a surrounding corona. Gas pressure within the corona is sufficient to overcome the gravitational forces of the star and to drive a cool wind (e.g. the solar wind has a velocity of ~ 400 km/s and a mass loss rate of $\sim 10^{-13} M_{\odot}$/yr.). High mass stars also emit winds (typically with velocity of $\sim 10^4$ km/s and mass loss rate of $\sim 10^{-5} M_{\odot}$/yr.) but in this case it is via a very different mechanism. With surface temperatures of 10^4–10^5 K, they are thought to lack the outer convection zone and, hence, the coronal heating and subsequent high gas pressure required to overcome their gravitational forces. Instead these hot stars have sufficiently high surface temperatures (and therefore radiative fluxes) for radiation pressure to drive the wind.

While hot stars with strong stellar winds can have their luminosity–mass ratio very close to the Eddington limit, only the outer atmosphere contributes to the outflow from the stable and gravitationally bound star. Due to the small forces produced, it is perhaps surprising that the mechanism by which this takes place is 'line-scattering', so called because a bound electron will scatter photons of just the right energy to oscillate between two discrete energy levels, resulting in narrow lines in the star's energy spectrum.

However, line scattering has a resonant nature as a result of the oscillations between the two energy levels and hence amplification is important. The amplification can theoretically be sufficient to drive material outwards with an acceleration 10^3 times the gravitational acceleration. This does not happen in practice as significant self-absorption takes place, saturating the lines. This keeps the line-force smaller than the gravitational force, allowing the inner atmosphere to remain bound. To counter-balance this, in the outward-moving part of the upper atmosphere the Doppler effect red-shifts local line resonances and this has the effect of desaturating the lines, thus covering a broader range of the spectrum. Hence, a feedback system is established with the line-force becoming great enough to overcome gravity and accelerate the outflow which had been required in order to create the force in the first place. A more detailed, quantitative account of mechanisms behind radiatively driven stellar winds is beyond the scope of this thesis but can be found in the definitive paper Castor, Abbott & Klein (1975) or the more recent book by Lamers & Cassinelli (1999).

The presence of a radiatively driven stellar wind will be shown in optical and UV spectra in the form of a P Cygni profile, named after the first star in which it was observed. As the optically thick wind column advances towards the observer it absorbs/scatters light emitted by the star and is blue-shifted. The velocity of the blue wing of the resulting absorption line gives the final wind velocity (v_{∞}).

At the same time, wind material from the edge of the absorption column can scatter

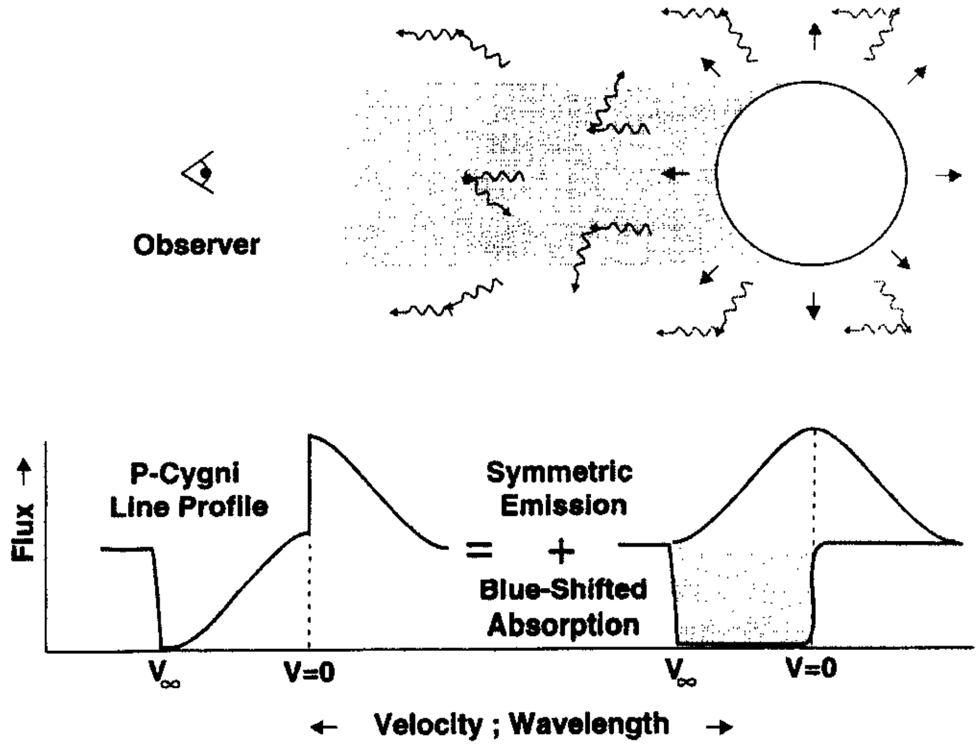

Figure 1.12: Schematic showing the formation of a P Cygni profile.

radiation towards the observer, resulting in an emission line. Because one hemisphere is approaching and one receding, this emission can be blue- or red-shifted resulting in a symmetric profile about $v = 0$. This superimposition of emission line and blue-shifted absorption trough is known as a P Cygni profile and can been seen in a schematic in Fig. 1.12.

If the wind emitting star is part of a binary system, however, different characteristics may be expected. Most of the wind passing within a radius r_{acc} will be accreted, where

$$r_{acc} = \frac{GM}{v_{rel}^2} \quad , \qquad v_{rel}^2 = v_w^2 + v^2 \tag{1.8}$$

and the mass accretion rate $\dot{M}$ is

$$\dot{M} \sim \frac{\pi r_{acc}^2 \dot{M}_w}{\Omega a^2} \tag{1.9}$$

where $\dot{M}_w$ is the mass loss due to the wind, Ω is the solid angle of the wind emission and a is the binary separation.

This simplified approach still does not take into account any effect that the secondary has on the wind. If the secondary is an X-ray source, as obviously the case for X-ray binaries, then X-ray heating of the wind should take place, changing the ionisation and hence the accelerative properties of the wind. This 'Hatchett–McCray' (Hatchett & McCray 1977) effect is mentioned in more detail in Chapter 3.

If the secondary is a black hole then its gravitational field should also be considered – indeed in the case of Cyg X-1 it appears that the wind is focussed towards the L1 point of the binary system, thus the black hole accretes wind material via a quasi-Roche lobe overflow mechanism. This has been modelled by Friend & Castor (1982) who adopt the wind momentum equation of Castor, Abbott & Klein (1975); the wind velocity is considered to obey a simple power law:

$$v_w = v_\infty \left[1 - \frac{R^*}{R}\right]^a \tag{1.10}$$

where v_∞ is the terminal velocity of the wind, R^* is the radius of the optical star, R is the distance from the centre of the star and a is a (constant) power law index. The original model was adapted to include the effects of gravity and continuum radiation pressure of the compact object and the centrifugal force due to orbital motion. By applying this new model to five different high mass X-ray binary systems (including Cyg X-1), Friend & Castor (1982) found that in a binary system non-sphericity of the wind is extremely important, resulting in enhanced emission produced between the two stars – this is indeed observed in e.g. Cyg X-1, and investigated in Chapters 3 and 4. It also appears that in systems for which the star has a greater Roche lobe fill-out factor, this focussing effect is more acute.

Chapter 2

INTRODUCTION TO CYGNUS X-1

2.1 Historical Background

Cygnus X-1 is probably the best known of the black hole X-ray binaries on account of its providing the first observational evidence for black holes. It was discovered by Bowyer et al. (1965) during two Aerobee rocket surveys in which eight new X-ray sources were detected, including Cyg X-2.

Webster & Murdin (1972) and Bolton (1972) independently identified the X-ray source Cyg X-1 with the 9th magnitude supergiant HDE 226868 (spectral type O9.7 Iab) subsequent radial velocity measurements resulted in a mass function of 0.12–0.16, suggestive of a compact object more massive than 3 $M_\odot$, the generally accepted maximum mass of a *neutron star* (see Fig. 2.1). *The values of the masses of the two components have been* refined a number of times, most recently by Herrero et al. (1995) giving 17.8 $M_\odot$ for the supergiant companion star and 10.1 $M_\odot$ for the black hole.

The radio counterpart to the system was also discovered in April and October 1971. Braes & Miley (1971) and Wade & Hjellming (1972) found a source with flux density $\sim$ 15–20 mJy in the X-ray error box – interestingly there had been no radio source above 5 mJy in February 1971 (Braes & Miley 1971). It was later shown by Tananbaum et al. (1972a) and Hjellming (1973) that an anti-correlated X-ray/radio state change (soft → hard) had taken place in March/April 1971. Tananbaum et al. (1972a) also noticed that a significant hardening of the X-ray spectrum (1–100 keV) had taken place at the time of transition.

No further changes were reported until May 1975 when a new X-ray outburst was

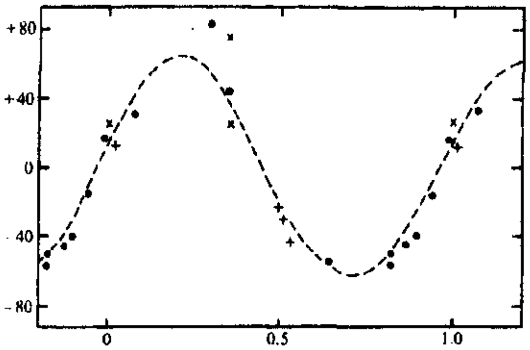

Figure 2.1: The radial velocity curve of Webster & Murdin (1972) which suggested the black hole nature of Cyg X-1. Orbital phase is on the horizontal axis, radial velocity (km/s) on the vertical axis.

observed by the All Sky Monitor on-board *Ariel – V*, the flux rising by 260% (Holt et al. 1975) – at the time it was attributed to another transition to the 'soft state' although current definitions of 'soft state' would not include this 1975 event. Optical photometry showed that while there was no overall change to the shape of the lightcurve (Lyuty 1985), rapid flares of up to ~ 0.1 magnitudes took place on a timescale of minutes (Natali, Fabrianesi & Messi 1978); an increase in colour $B - V$ was also seen. The flickering behaviour was dampened when the X-ray source returned to the low state. A radio outburst also took place, the flux reaching a maximum of 45 mJy at 8 GHz which has never been achieved since (Hjellming, Gibson & Owen 1975). This seemed a different type of outburst from previously, despite the X-ray softening – this time the soft X-rays and the radio were correlated. Observations of the downwards transition showed that the whole outburst had lasted only ~ 30 days (Eyles et al. 1975) and was more like a soft X-ray transient event than true state change, probably similar to the event seen in 1998 and described in Chapter 4.

Another increase in the soft X-rays, accompanied by spectral softening was observed in 1975 by *Copernicus*; simultaneous optical monitoring showed that the normally sinusoidal B band lightcurve changed shape at the time of the outburst (Walker et al. 1976). No radio observations were reported. However there *were* radio observations taken in February 1976, when another anti-correlated soft X-ray/radio transition from soft to hard state was observed (Braes & Miley 1976).

The next twenty years were relatively quiet with no reports of major outburst or state

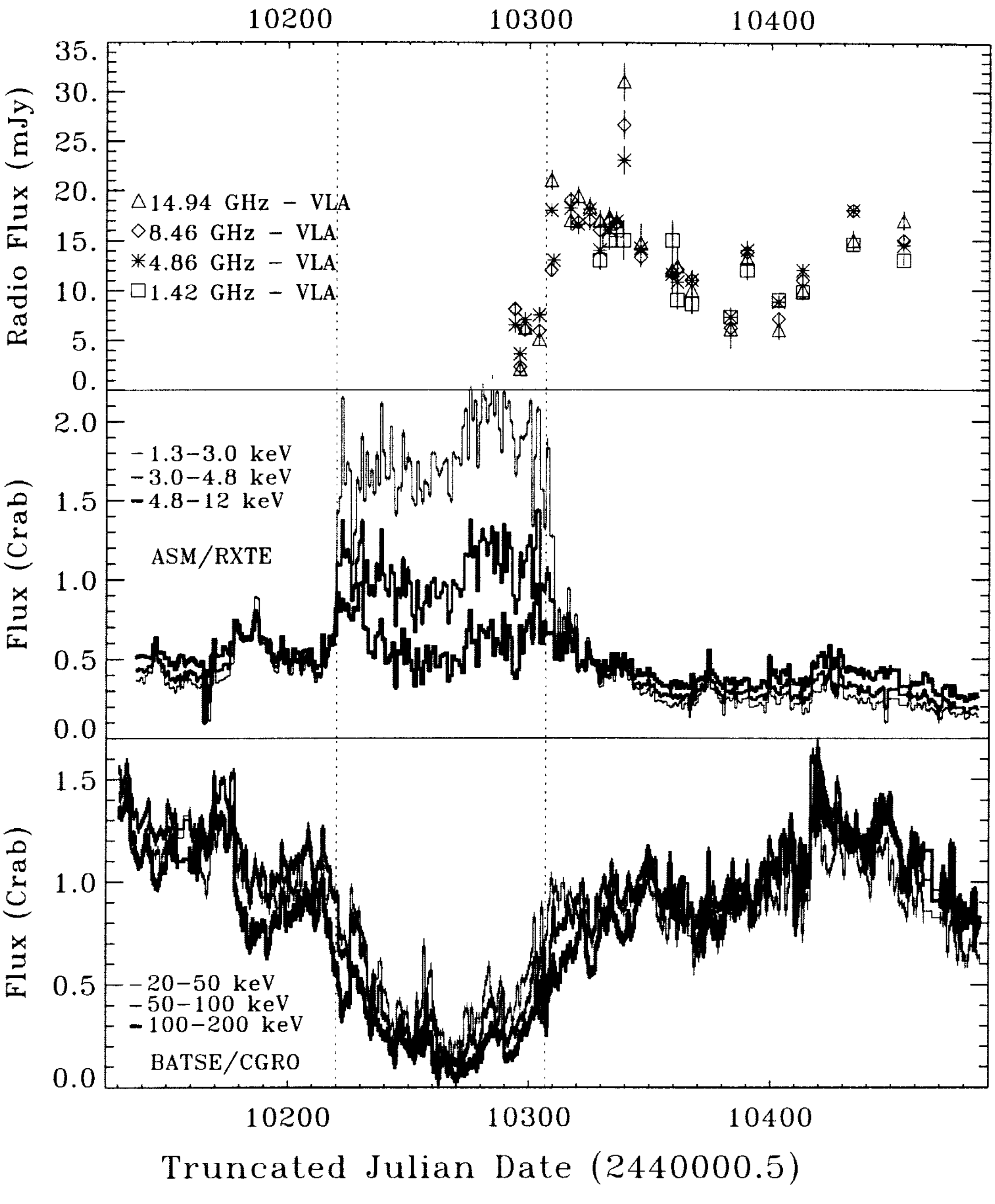

Figure 2.2: *RXTE*/ASM, *CGRO*/BATSE and VLA data from the 1996 state change of Cyg X-1 - the hard and soft X-rays are clearly anti-correlated with each other and the radio data appears to follow the behaviour of the hard X-rays, with a flare just after the transition (from Zhang et al. 1997).

transitions, although it is probable that some small correlated flares took place - e.g. the 1980 'high state' reported by Ogawura et al. (1982) which was probably a pair of small outbursts accompanied by spectral softening. It should be noted that all 'transitions' up to this point were observed prior to the state classification of Van der Klis (1995) and so the 'hard' and 'soft' definitions may be slightly different.

Finally in March 1996 a transition to the soft state took place; this was the first state change for which full X-ray monitoring at low and high energies was available throughout both upwards and downwards transitions. VLA radio data was obtained during the downwards transition (Zhang et al. 1997, see Fig. 2.2) and showed the expected anti-correlation with the soft X-rays; a small flare following the return to the hard state was also observed. Optical photometry during this period showed that the *V* band flux remained constant throughout, although small increases in magnitude for the *B* and to a greater extent the *U* band were observed (Voloshina et al. 1997). Additional correlated flaring events have been observed since then and are discussed in Chapter 4.

During the past twenty five years Cyg X-1 has been responsible for a huge contribution to the literature, both in its own right and as a comparison for other potential black hole candidates. Most of this research has investigated its X-ray properties, its various periodicities (including many revisions of the orbital ephemeris) and the peculiar nature of the two optical emission lines. These are discussed further in the next few sections.

2.2 Ultra-violet, Optical and Infrared Properties

Photometry

The optical counterpart to Cyg X-1 has been observed regularly since the early 1970's. Walker & Quintanilla (1974, 1978) and Lyuty, Sunyaev & Cherepashchuk (1973, 1974) reported the ellipsoidal orbital variability due to tidal distortion of the star by the gravitational field of the compact object. They further determined system parameters which are consistent with those obtained from spectroscopic observations (see below).

However, the mean orbital lightcurve is not simply a double-peaked sine wave. Lester et al. (1976 and references within) found that there is a significant amount of scatter, suggesting that intrinsic variability of the sugergiant or variable obscuration by a gas stream is present. In addition to this, the minimum at phase 0.5 (inferior conjunction of the X-ray source) is deeper than that at phase 0.0 and both minima are too bright to be accounted for purely by the luminosity difference between the star and accretion disc.

Phase dependent colour variations and luminosity differences between the two maxima were also reported. Lyuty (1985) and Voloshina & Lyuty (1995) further investigate the additional radiation seen at phase zero for some, but not all, orbits. They suggest that this was caused by the interaction of a wind from the accretion disc and the magnetosphere of HDE 226868. Relativistic electrons in the wind then lose energy to synchrotron radiation which can be seen as a narrow peak at phase zero.

The most detailed theoretical model of the Cyg X-1 ellipsoidal variability has been presented by Balog, Goncharskii & Cherepashchuk (1981) and takes ellipsoidality, irradiation by the X-ray source and Roche lobe filling factor into account. Parameters obtained with this model were generally in agreement with previous attempts but to a higher accuracy. The data deviated from the theoretical curves slightly at phase 0.5, prompting the suggestion of partial eclipses by the accretion disc. This is not in agreement with the spectroscopy and would appear unlikely – given the wind accretion mechanism of the system, Cyg X-1 would be expected to have too small a disc to partially eclipse the star. However, as the hard state requires the disc to have a large inner disc radius to explain the strong disc:jet connection (see Chapter 4) further investigation is important. Note that in a larger sample of data there is evidence for a slight excess, rather than an eclipse, possibly due to the stellar wind or accretion stream (Brocksopp et al. 1998 and Chapter 3). The model also finds that a Roche lobe filling factor of 0.9 makes a better fit to the data than 1.0 – they note that the observed accretion phenomena are still consistent with such a filling factor.

Infrared observations of the orbital modulation are less common but Leahy & Ananth (1992) found that a double-peaked ellipsoidal variability was also present, with an amplitude significantly greater than that in the optical – however, the two datasets were not simultaneous and Nadzhip et al. (1996) later obtained infrared data showing amplitudes only marginally greater than those in the optical. The infrared amplitudes are sufficiently high to suggest a Roche lobe filling factor of 1.0 – this effect was assumed to be due to the greater opacity of the stellar wind in the infrared than the optical.

Perhaps surprisingly, give the high luminosity of the supergiant, photometry of Cyg X-1 has also revealed the presence of an accretion disc. A disc is required to be a component of the binary system in order to fit the X-ray properties, the possible disc precession period and the reported 'flickering' of the optical lightcurve (e.g. Khaliullin 1975). Bruevich et al. (1978) create a geometric model which incorporates reflection of the stellar emission from

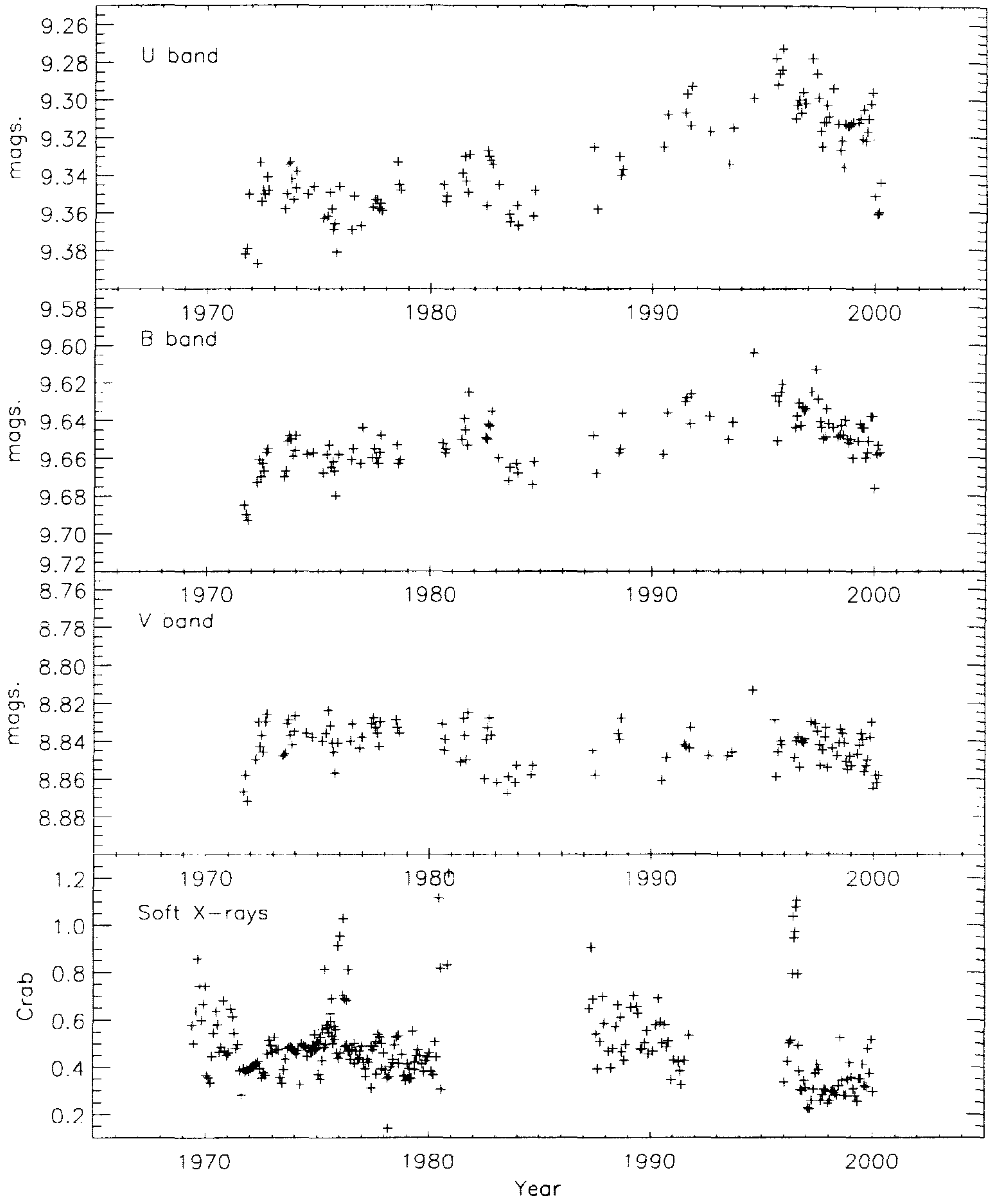

Figure 2.3: Thirty years' worth of U, B and V band photometry and X-ray data. The two 'states' spanning the years 1970–1985 and 1985–2000 can be seen clearly in the U band but not in the V band or the X-rays (Lyuty et al. 2000, in prep.).

the disc. This shows that the disc can actually contribute ~ 2% (a more recent estimate is ~ 4%, Lyuty, private communication) to the total optical luminosity. A further 4% of the X-ray luminosity can be reprocessed as optical light from the disc and this can be estimated to contribute ~ 0.4% of the total optical luminosity (after Balog, Goncharskii & Cherepashchuk 1981). Study of the infrared photometry by Beall et al. (1984) does not reveal the presence of an accretion disc, suggesting that all infrared emisison is from the supergiant.

A recent study by Lyuty et al. (2000, in prep.) looks at the long term lightcurve of the optical photometry. The U band clearly shows two distinct 'states' – data from 1970 to 1985 are ~ 0.1 magnitudes fainter than between 1985 and 2000. The B band data shows similar behaviour to a lesser extent and the V band does not appear to show it at all. The three photometric bands are plotted with X-ray data in Fig. 2.3.

Spectroscopy

The spectrum of Cyg X-1 is that of a typical O9 supergiant with emission components at Hα and He II λ4686, both of which are superimposed onto absorption lines (see Fig. 2.4). Whilst there are many papers in the literature investigating the optical spectroscopy of Cyg X-1, the majority tend to focus on either the orbital ephemeris and hence the mass of the two components or the nature of the peculiar emission lines.

The ephemeris has been revised many times since the original radial velocity curves of Webster & Murdin (1972) and Bolton (1972). Its accuracy improved considerably over the next decade and the ephemeris of Gies & Bolton (1982) – $P_{orb} = 5.59974 \pm 0.00008$ days – has been quoted as the definitive value until 1998 when it was revised independently by LaSala et al. (1998), Sowers et al. (1998) and Brocksopp et al. (1998). The results of all these were consistent with those of Gies & Bolton (1982) although the accuracy of the Brocksopp et al. (1998) result was superior to the other two, particularly with the comparison with 27 years' worth of photometry ($P_{orb} = 5.599829 \pm 0.000016$ days).

The masses of the two components of the binary system have been estimated by a number of authors; Aab et al. (1981, 1984) determine the mass of the stellar companion to be 19.5 $M_\odot$, later revising this to 37.6 $M_\odot$ with the inclusion of additional data. Lower limits to the mass of the black hole were calculated to be 5.5 $M_\odot$ (Brucato & Kristian 1973, Bolton 1975) and 10 $M_\odot$ (Aab 1983). Gies & Bolton (1986) found that the lower limits to the masses were 20 and 7 $M_\odot$ for the star and black hole respectively but suggested that

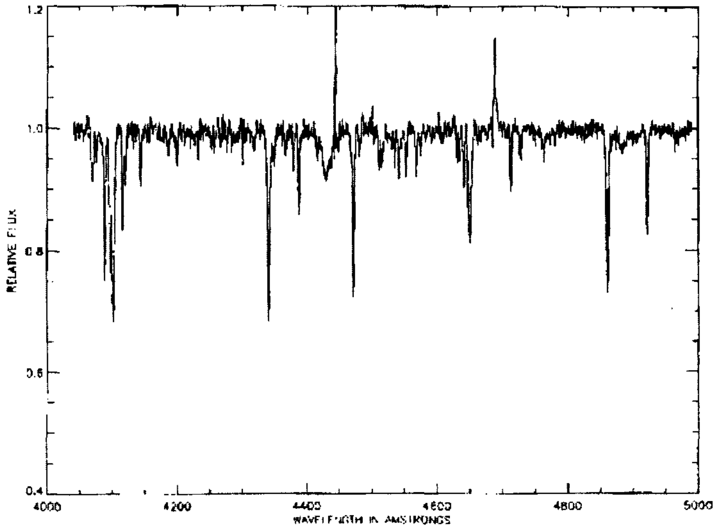

Figure 2.4: The spectrum of HDE 226868 from 4000 to 5000 Å. The emission at 4443 Å is a cosmic ray (from Herrero et al. 1995)

33 and 16 $M_\odot$ were more likely. More conservative masses (supergiant: 17.8 $M_\odot$, compact object: 10 $M_\odot$) were determined by Herrero et al. (1995) using an alternative method which was independent of the distance and the mass-luminosity relation of the source.

Some authors (e.g. Avni & Bahcall 1975) attempted to excuse the apparent black hole nature of the secondary by invoking an early type companion or triple system – no evidence for a third star was found (e.g. Abt, Hintzen & Levy 1977) and Shafter et al. (1980) deduced that, for a component other than a black hole to be present, the secondary could only be four magnitudes fainter than HDE 226868 – this was clearly not the case.

Following the determination of the orbital ephemeris and parameters, few authors have studied the absorption lines of Cyg X-1. Orbital variability in the equivalent width data of a number of absorption lines has been claimed by Aab et al. (1983) and Canalizo et al. (1995); the latter also discovered variations in $H\beta$ and a number of He I line profiles which they assumed were due to contamination by emission components from the stellar wind – they were unable to confirm whether or not the variability was orbit dependent. The most extensive study of the absorption spectrum was by Gies & Bolton (1986) – they find that there is no significant variability in the spectral type and the line strength of the absorption lines is consistent with the spectral type. Hence any additional contribution (e.g. an accretion disc) can only contribute up to 7% of the total optical emission. There was no significant orbital variability in equivalent width data, contrary to the results of

Aab et al. (1983) who claimed that the equivalent widths peak at phase 0.0 and 0.5, with minima at 0.25 and 0.75 – note that the amplitudes of these 'modulations' did not always reach $> 3\sigma$ from the mean.

More commonly, however, it has been the emission lines of Cyg X-1 that have invoked further study. It is clear that the Hα and He II λ4686Ålines are a superposition of an absorption and an emission component; hence a number of authors have attempted to subtract the absorption spectrum to leave 'pure' emission. This has also revealed the presence of weak Hβ emission (e.g. Aab et al. 1983). In most cases this was achieved by subtracting the spectrum of a 'normal supergiant' (e.g. Gies & Bolton 1986), despite the assumptions implicit in such a procedure – these include an optically thin emission component, identical line strengths of the two stars, no orbital variability in line strength, although supposedly it is only the second of these which can alter the results significantly (Gies & Bolton 1986). Aab et al. (1983) have attempted to construct the absorption line profile from other line profiles of Cyg X-1 rather than relying on a reference star. Gies & Bolton (1986a) have also computed theoretical emission line profiles based on the focussed stellar wind model of Friend & Castor (1982) and using the Sobolev theory (Mihalas 1978). Their results compared reasonably well with the observed profiles and the errors were within those expected on account of assumptions required for the Sobolev theory failing near the stellar surface.

Despite the errors in the method of separating emission and absorption components, similar results have been achieved. The radial velocity curve of the He II emission component is 115–120° out of phase with that of the absorption (e.g. Aab 1983a), suggesting that the emission originates in the accretion stream near the L1 point. The Hα emission was slightly more difficult to isolate and appeared to consist of two profiles, one of which moved similarly to the He II emission (Ninkov, Walker & Yang 1987a). More recently the Hα has instead been treated as the superposition of a P Cygni profile, as is typical for wind-emitting systems, and an emission component (Sowers et al. 1998).

Evidence for variability in the stellar wind is found at ultra-violet wavelengths. In determining the orbital inclination and mass of the compact object from *IUE* spectra, Davis & Hartmann (1983) calculate the wind velocity and find that the wind is slowed at phase 0.5 in accordance with the Hatchett-McCray effect. Treves et al. (1980) also find orbital variability in the equivalent width data of some prominent ultra-violet absorption lines and, again, this is apparently due to the Hatchett-McCray effect causing the disappearance of wind P Cygni profiles at orbital phase zero.

2.3 X-ray Properties

The majority of research into Cyg X-1 has been in the X-ray regime, in terms of both spectral and temporal properties. While early observations tended to take place at the time of transitions from one spectral state to another, more recent lines of research have included fitting models to the energy and power density spectra, finding correlations between these spectral/temporal properties and using analysis of time lags to determine the system's geometry – both hard and soft states have been investigated although as the soft state occurs so rarely this is less understood. Energy spectra for Cyg X-1 in the low, intermediate and high states are shown in Fig. 2.5.

It should be noted that further classification into 'states' was observed in the 50–10000 keV data from *HEAO* 3 (Ling et al. 1983, 1987) – however, γ-ray observations are not included here.

The low/hard state

The short time-scale variability (flickering) of Cyg X-1 in the hard state has been modelled in terms of random 'shot noise' pulses, following the failure to find any periodicity (e.g. Terrell 1972); however, a mHz QPO was detected in a number of energy ranges (e.g. Vikhlinin et al. 1994 and references within). The shots are thought to be the result of magnetic flares in the accretion disc (e.g. Lochner et al. 1991 and references within). The power spectrum of Cyg X-1 is flat below a break frequency ($\sim$ 0.04–0.4 Hz) and follows a power law with slope -1, steepening to -2 at $\sim$ 1 Hz – as observed in *EXOSAT* data by Belloni & Hasinger (1990). They interpret the power spectrum in terms of a shot noise model in which the break frequency is determined by the relaxation time of the shots. Cross-correlation techniques have been used between X-ray lightcurves of different energy ranges and a hard X-ray lag found, in keeping with the model of Compton upscattering of soft photons by a corona (e.g. Miyamoto & Kitamoto 1989). The time lags have been thought to represent the diffusion times through the corona – i.e. a small lag suggests a small corona. However, as the smallest lag times therefore suggest a very small corona ($R < 30GM/c^2$), it appears that current accretion models are insufficient to explain the observations (Pottschmidt et al. 1998).

The energy spectrum of Cyg X-1 in the hard state can be described by a power law (with

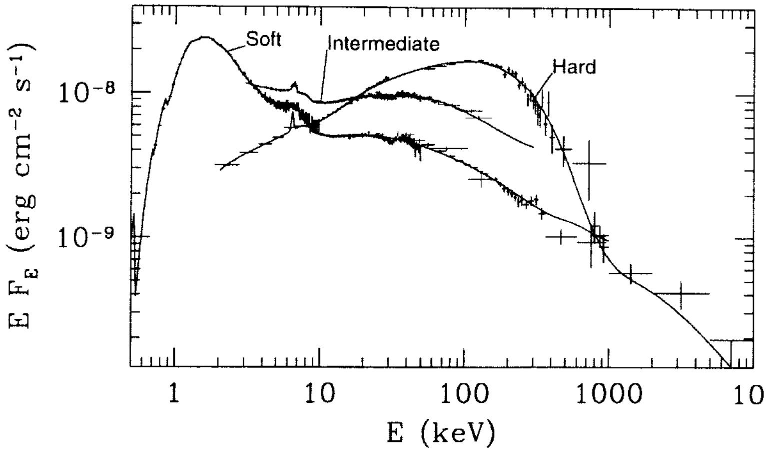

Figure 2.5: X-ray energy spectra of the three states in which Cyg X-1 has been observed (from Gierliński et al. 1999).

spectral index ~ 0.6–0.7) at energies above ~ 3 keV, with a Compton reflection continuum component above ~ 10 keV. There is also an iron K line and an iron Kα fluorescent line included in this reflection spectrum (e.g. Done et al. 1992). Dove et al. (1997) further investigated the energy spectrum and found that the accretion disc corona (ADC) model of e.g. Titarchuk (1994) with a slab geometry did not reproduce the observed broad X-ray spectrum of Cyg X-1 – the resultant theoretical spectra were much softer. However, they found that an ADC model with a *spherical* corona could result in a self-consistent solution of temperature and opacity which fit the observations. The model was later extended by Nowak et al. (1999, and references within) so as to include the observed timing properties of the system – they suggested that the time delays originate in the corona, rather than in the disc and being reprocessed. They further concluded that, since the corona is small, if the time delays are due to linear disturbances propagating through the corona then the propagation speeds are very slow – this is inconsistent with ADAF models.

The hard state of Cyg X-1 is surprisingly variable in terms of spectral and temporal properties, although the state does not actually change. Gilfanov, Churazov & Revnivtsev (1999) studied *RXTE*/PCA data and found that steepening of the hard state spectrum is accompanied by simultaneous increases in break frequency and the amount of reflection; they suggested that this is due to a decrease in the inner radius of the disc. Pottschmidt et al. (1999) also found that spectral hardening is correlated with a decrease in time lags and increase in the relaxation time of the 'shots' – this might suggest that a corona with large optical depth and/or temperature is physically smaller. As more scattering events result in a longer relaxation time, this is also consistent with the observed shot noise variability.

Crary et al. (1996) looked at 1100 days' worth of *CGRO*/BATSE data and found that the slope of the energy spectrum is correlated with the intensity and variability of the hard X-ray flux; a model by Chakrabarti & Titarchuk (1995) suggested that the mass accretion rate is indeed correlated with spectral index and predicts a shock in the accretion disc surrounding a black hole. In the context of this shock model, Molteni, Sponholtz & Chakrabarti (1996) proposed that the location of the shock and the X-ray luminosity vary quasi-periodically with the frequency of oscillations depending on the mass accretion rate.

The soft (intermediate?) state

The energy spectrum during the soft state has been modelled by a number of authors but with similar results. Most recently, Gierliński et al. (1999) described the spectrum as having a dominant soft component up to ~ 2keV with a power law tail up to ~ 800 keV. The soft component is fit by a multi-temperature blackbody disc spectrum (optically thick) and they suggest that for the disc to extend down to the last stable orbit would require a black hole mass of ~ 10 $M_\odot$. The high energy tail is produced by the Compton scattering of disc photons from an optically thin corona - whereas most authors (e.g. Cui et al. 1998) have used a thermal spectrum for the corona, Gierliński et al. (1999) claimed a better fit with the use of a hybrid thermal/non-thermal electron distribution. Additional features included in the model are a reflection component from the cold disc and a broad iron Kα line.

Belloni et al. (1996) have suggested that the 1996 state change did not fully reach the soft state and may only have achieved an intermediate state. By comparing the power density spectra of the states before and after the upwards transition they found that there is low frequency noise, band-limited noise and an energy-dependent QPO in the softer state, similar to those seen in the very high state, but not consistent with the soft state. While the luminosity was insufficient for it to have reached the very high state it may have achieved some intermediate state – as was perhaps the case in the 1970's. However, Gierliński et al. (1999) showed that the source was in the intermediate state in May 1996, and softened further by June 1996, indeed reaching the soft state (Fig. 2.5).

State transitions

The transition periods have also been studied by a number of authors. Zhang et al. (1997) found that while the luminosities of 1.3–3 keV and the 100–200 keV ranges changed dramatically, the overall 1.3–200 keV luminosity remained approximately constant to within ~ 15 %, thus suggesting that the increased soft X-ray emission comes from only a small increase in $\dot{M}$ accompanied by a decrease in inner disc radius. Cui et al. 1998 noted that the temporal and spectral properties of both the upwards and the downwards transitions are similar. The power density spectrum shows a low frequency power law, a flat component in the $\sim$ 1–3 Hz range and a steeper power law at higher frequencies – again this is noted to be similar to the very high state. They also found a QPO varying from 4 to 12 Hz and becoming more prominent at higher energies.

Another interesting result seen during the transition periods is a large increase in the hard X-ray lags, whereas the lags in the hard and soft states are comparable (Pottschmidt et al. 2000). As the magnitude of the hard X-ray lags is thought to determine the geometry of the Comptonising corona, then either this clearly has implications for models in which there is no corona in the soft state or the 1996 state change was indeed only to the intermediate state. It certainly appears that it is not possible to determine the geometry of the corona from studies of X-ray lags alone.

2.4 Radio Properties

Compared with the other wavebands there has been relatively little work on Cyg X-1 at radio wavelengths. The two 3 mJy modulations (see Sec. 2.5 and Chapter 4) have only been discovered recently and radio observations have generally been restricted to times of X-ray variability. Futhermore, unlike some radio emitting X-ray binaries for which jets had been detected there seemed to be little evidence for a jet in the case of Cyg X-1 (Martí et al. 1996).

The most notable property of the radio emission of Cyg X-1 is the flat spectrum and this was noticed at the time of the initial radio observations of the source (Hjellming 1973). More recently Fender et al. (2000) have studied the flat spectrum at radio and milimetre wavelengths – the spectrum is indeed flat across the spectrum up to the infrared, at which point the emission is dominated by the sugergiant (Fig. 2.6). High resolution observations of the system have been attempted (UKIRT+adaptive optics – Brocksopp, unpublished; IRAS – Fuchs 2000, private communication) but have been insufficient to resolve the jet (predicted $K \sim 13$) from the star ($K \sim 6.5$). This would perhaps be an interesting project for the proposed Large Optical Array.

The flat synchrotron spectrum, (anti-)correlated X-ray/radio behaviour and the very constant radio emission with little variability other than two regular modulations strongly suggest that a jet is responsible for the emission – some cloud of radio emission could not produce the observed properties of the system. However, it is only recently that a jet has been imaged – VLBA observations of Cyg X-1 at 8 and 15 GHz have finally revealed a ~ milliarcsecond jet (Fig. 2.7, Stirling et al. 2000 in prep.).

2.5 Periodicities

Since the initial discovery of the 5.6 day orbital period in the radial velocity measurements (Fig. 2.1), there have been numerous other detections. A double-peaked modulation was found in the optical (Walker 1972, Lyuty 1972) and the infrared (Leahy & Ananth 1992; Nadzhip et al. 1996) photomery, the minima of which are seen at the two conjunctions and the maxima produced as the tidally distorted star is viewed from the side.

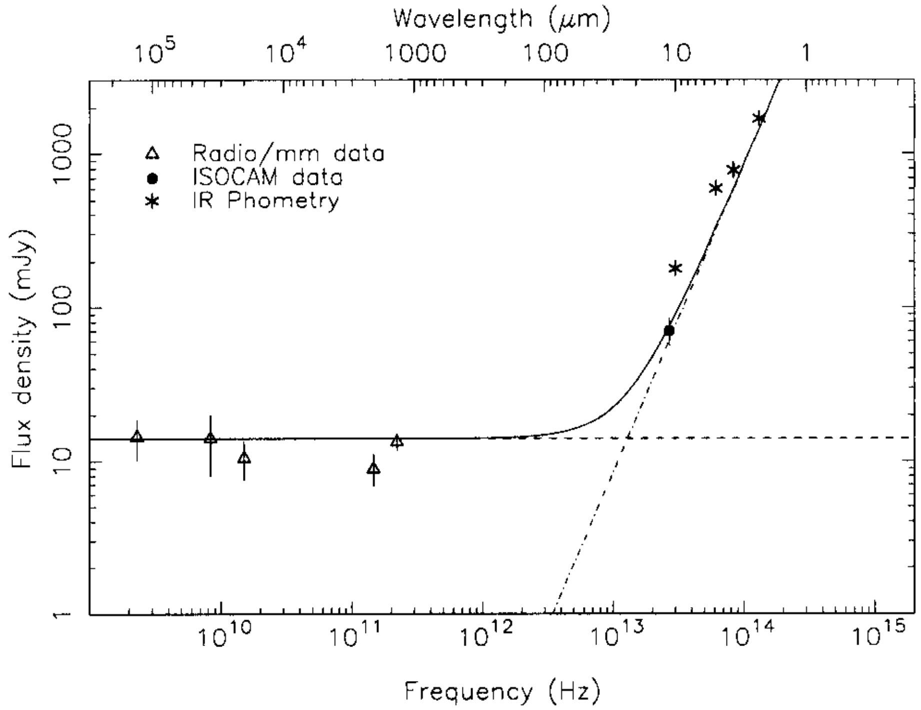

Figure 2.6: The flat spectrum of Cyg X-1 extends through the millimetre wavelengths and into the infrared, where it becomes dominated by emission from the supergiant (Fender et al. 2000).

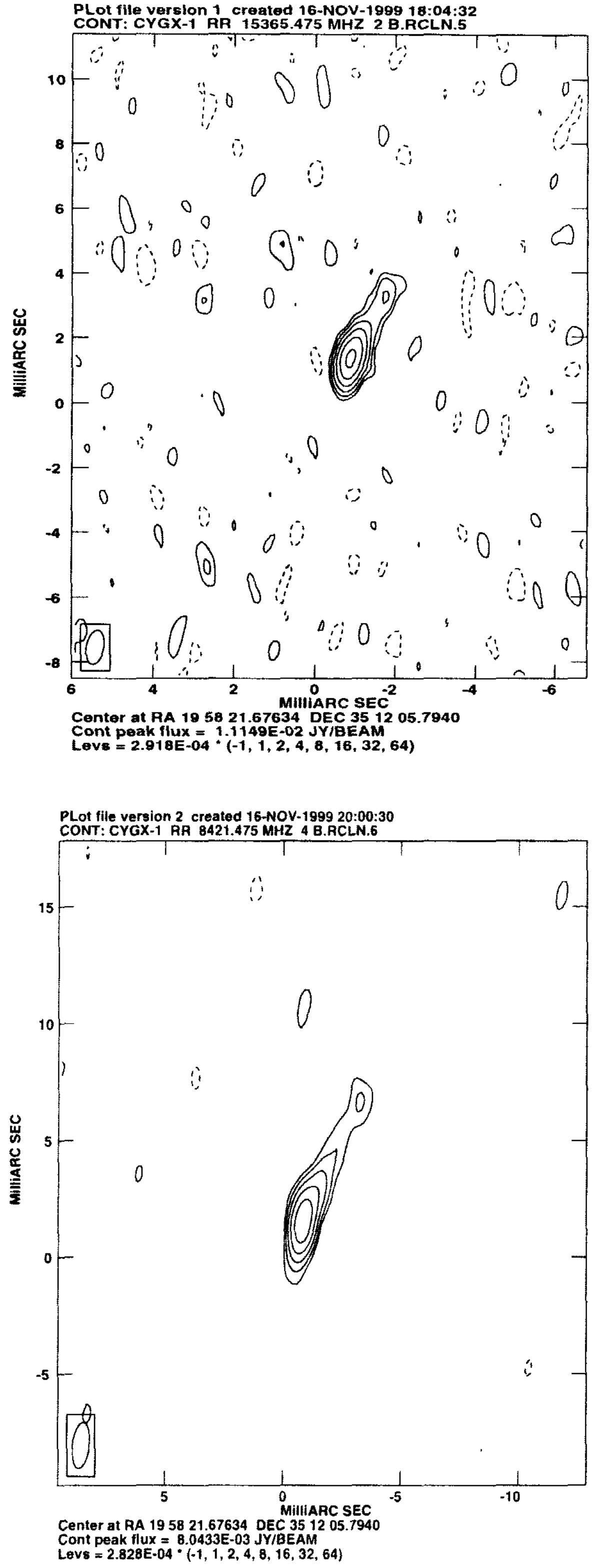

Figure 2.7: The jet of Cyg X-1 has finally been imaged at 15 GHz (top) and 8 GHz (bottom) with milliarcsecond resolution by the VLBA (Stirling et al. 2000, in prep.). The jet was observed at various orbital phases but the resolution and sensitivity of the resultant images were insufficient to determine whether any orbital variability was present.

The orbital period has also been detected in the hard X-rays by Paciesas et al. (1997) and the soft X-rays by Wen et al. (2000) – there was also a mention of it earlier in Bolton (1972) and Holt et al. (1976); additionally there are a number of papers in the literature investigating the 'absorption dips' just prior to orbital phase 0 (e.g. Balucińska-Church et al. 2000). This is perhaps surprising for what is considered to be a non-eclipsing system. Brocksopp et al. (1999, see also Chapter 4) concluded that phase dependent absorption by the stellar wind of the supergiant is most likely to be responsible. Wen et al. (2000) modelled the soft X-ray modulation in terms of wind absorption. The model worked well for the hard state data, assuming an inclination angle of $\sim 30°$, although they found additionally that partial obscuration of the X-ray source by the accretion stream is an alternative mechanism that fits the data. Finally, the orbital period has also been detected in the radio (Pooley, Fender & Brocksopp 1999) – this is unlikely to be the result of partial obscuration by the accretion stream as the emission sites are a considerable distance from the orbital plane. The radio modulation is investigated in terms of stellar wind absorption for three different frequencies in Chapter 4.

It is interesting to note that the nature of the modulation is very different when the source is in the soft state – Cui, Chen & Zhang (1998) reported that the orbital period was not present in the *RXTE* data during the soft state, as did Wen et al. (2000). The latter suggested that during the soft state either the wind is suppressed in the region of the X-ray source or the X-ray emitting region shrinks so that obscuration by the accretion stream no longer occurs, depending on the mechanism for the observed modulation. Voloshina et al. (1997) suggested that the optical modulation could still be observed during the soft state but that it had become single-peaked. This was probably due to components other than those producing the orbital modulation dominating the emission during the soft state and this is addressed further in Chapter 4.

There have been numerous other 'periods' mentioned in the literature, usually attributed to possible third bodies, disc precession or mass transfer rate variability. A 39 (or 78) day modulation was found in three years' (1974–1977) worth of combined U and V band polarisation data (Kemp, Herman & Barbour 1978). They also found a corresponding 78 day modulation in the 3–6 keV X-ray data from the *Ariel* – V/ASM. The 39 day period was also reported in the intensity ratios of certain spectral lines and in the half-width of the He I λ4471 line (Kopylov & Sokolov 1984) and was assumed to be due to precession of the rotation axis of HDE 226868. At the other end of the scale, a 4.5 year

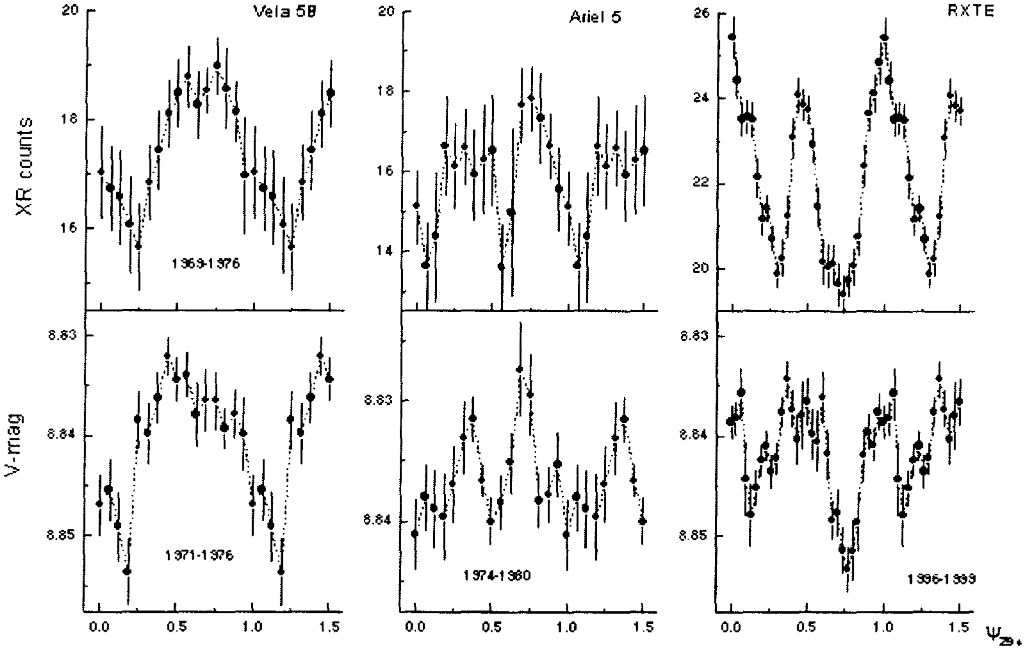

Figure 2.8: V band and soft X-ray data folded on the 294 day period for different time intervals. A single-peaked curve can be seen in the earlier data but it becomes double-peaked in later data (Lyuty et al. 2000, in prep.). N.B. The 'ephemeris' used for all six plots is that of Priedhorsky, Terril & Holt (1983) - P=294 days, T_0 is the year 1974.05.

period was reported by Wilson & Fox (1981), thought to be due to variability in periastron longitude for an elliptical orbit. This has never been confirmed and the orbit is believed to be circular.

Walker & Quintanilla (1978) reported a ~ 150 day period in four years' worth of B band photometry. Presumably double this, a 294 day period was found in X-ray data by Priedhorsky, Terrell & Holt (1983) and later by Kemp et al. (1983) in optical photometry. More recently Pooley, Fender & Brocksopp (1999) and Brocksopp et al. (1999) have investigated a ~ 140 day period but found little evidence for the 294 day modulation; interestingly, *CGRO*/BATSE data prior to the 1996 state change showed a more significant 294 day modulation than after the state change. They concluded that the two periods are related, the shorter one being approximately half of the longer. No evidence for the 294 day period was found in the depths of spectral lines (Gies & Bolton 1984), however Ninkov, Walker & Yang (1987) found that the equivalent width of the $H\gamma$ and $H\beta$ lines was significantly greater at phase zero of the 294 day period.

It is interesting to note that in the two 'U band states' discovered by Lyuty et al. (2000, in prep.) there is no significant difference in the orbital lightcurves. However, the 294 day mean lightcurves for the two 'states' are very different – in the first state a single-peaked 294 day modulation is clearly present in both optical *and* X-ray data, but in the second the modulation becomes double-peaked, suggesting that the 140 day modulation is more appropriate.

Chapter 3

OPTICAL OBSERVATIONS OF CYGNUS X-1

3.1 A New Ephemeris for Cyg X-1

In collaboration with A.E. Tarasov, V.M. Lyuty & P. Roche[1]

The spectroscopic ephemeris has been revised many times since 1972 using a variety of spectral lines. The results of Gies & Bolton (1982) have been quoted ($P_{orb} = 5.59974 \pm 0.0008$ days) as the definitive values for over a decade and there has been little disagreement; while a variable orbital period was tentatively suggested (Ninkov, Walker & Yang 1987) this has never been confirmed and appears unlikely. Likewise there is very little evidence to suggest that the orbit may be non-circular. It is only recently that a new ephemeris has been calculated ($P_{orb} = 5.5998 \pm 0.0001$ days) and this is within the errors of the Gies & Bolton (1982) result (LaSala et al. 1998). A more accurate result is given as $P_{orb} = 5.59977 \pm 0.00002$ days (Sowers et al. 1998) which is subsequently fit successfully to Hipparcos photometrical data.

The spectrum is that of a typical O9 supergiant with moderate Hα emission, presumably coming from the supergiant (e.g. Brucato & Zappala 1974), and also He II λ4686 emission. Both of these emission lines are superimposed on absorption components and, by distinguishing the two components, it has been shown by a number of authors (e.g. Aab 1983) that the He II emission component is $\sim 115 - 120°$ out of phase with the He II absorption component and the supergiant. As a result of this it is thought that the He II emission originates in the accretion stream.

---

[1] Published in A&A, 343, 86 (1999)

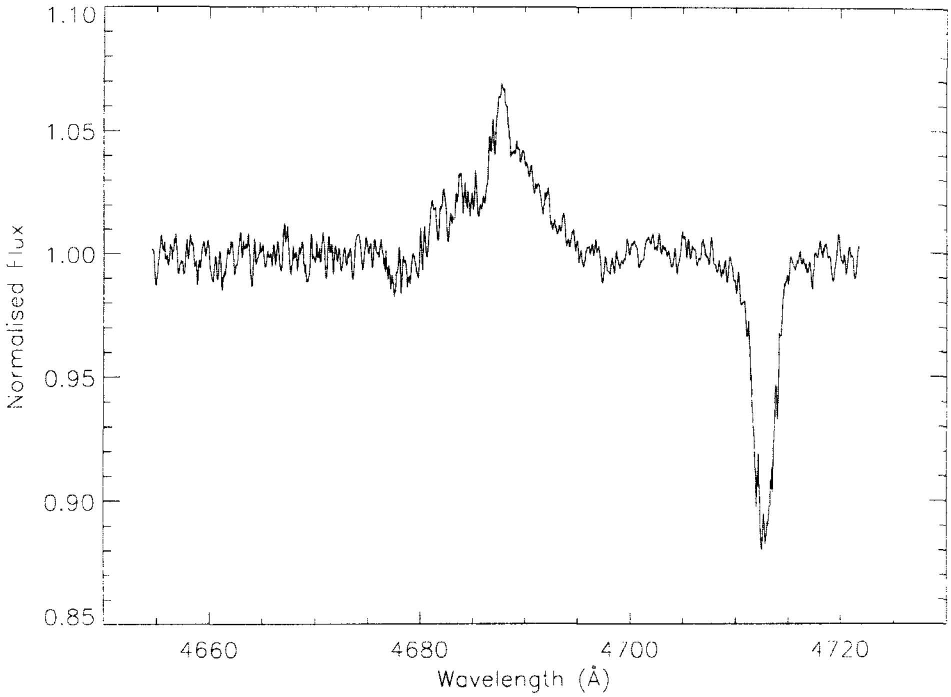

Figure 3.1: Typical spectrum from the CrAO 2.6 metre telescope, showing the He II λ4686 and He I λ4713 lines.

Neither of these absorption components are suitable for measuring radial velocity due to the inaccuracies involved in the removal of the superimposed emission. Instead, as was the case for previous authors, we turn to the He I absorption lines which are uncontaminated by emission.

3.1.1 Spectroscopy

Our spectra were obtained in 1997 June/July using the Coudé spectrograph of the Crimean Astrophysical Observatory's 2.6 metre telescope. The detector was a CDS9000 (1024×256 pixels) CCD array. All observations were made in the second order of a diffraction grating with reciprocal dispersion of 3Å/mm and resolution of 25000. The typical exposure time for each spectrum totalled 1.5 hours resulting in a S/N of ~100.

With a spectral width of 60Å, our 20 spectra centred on He II λ4686 also included the He I λ4713 line (see Fig. 3.1). This is the line we have used for our radial velocity studies, although a variety of other lines have been used by other authors (see below). Our choice of He I λ4713 was influenced by its probable lack of wind contamination and by

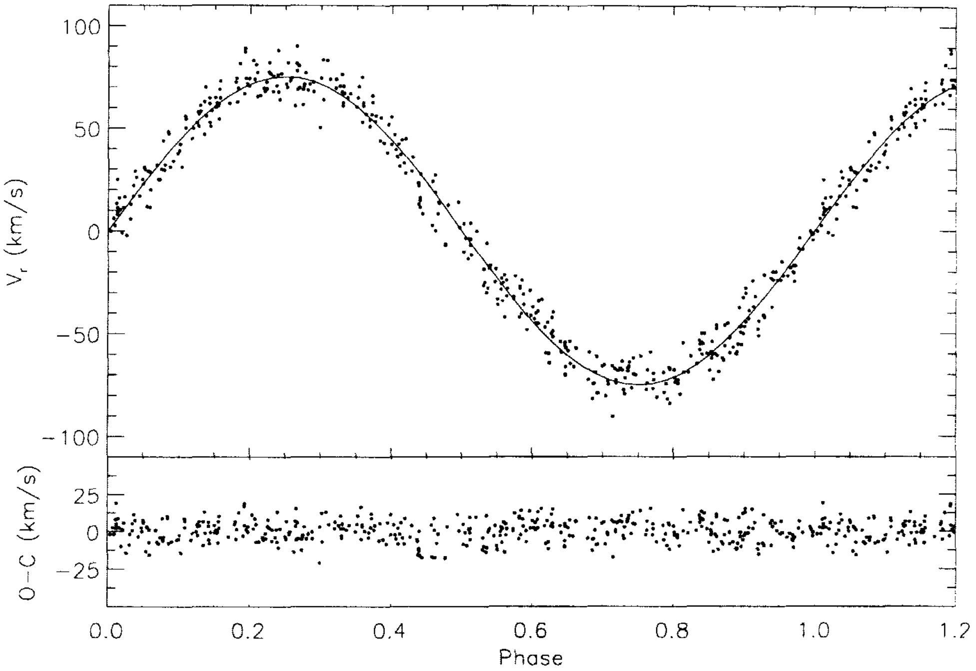

Figure 3.2: Top: Radial velocity curve using accumulated data compared with theoretical curve from Balog et al. (1981). Bottom: Residuals

its proximity to the very interesting He II λ4686 emission line – with such high resolution and the necessarily long exposure times it was a great advantage to obtain both lines on the same spectrum.

The spectra were reduced using standard flat–field normalisation and sky subtraction techniques. Wavelength calibration was achieved using ThAr comparison spectra and to an accuracy of less than 0.5 km/s. The radial velocities were calculated by fitting a Gaussian to the core of each line and subsequent values of V_r can be found in Table 3.1.

The radial velocities of a total of 48 different lines were obtained from the literature and used in the calculation of our ephemeris – the majority of these can be found in Table 2 of Gies & Bolton (1982); we also use additional He I lines (λ4921, λ5015, λ5047, λ5875, λ6678), oxygen lines (O II λ4349, O II λ4366, O III λ4650), Mg II λ4481 and N II λ4630. As with previous authors all lines were treated equally, although we note that inhomogeneities in the atmosphere of the supergiant (due to the variety of velocities in the stellar wind) cause greater shifting in the red He I lines than the blue – unfortunately it is not possible to correct for this without knowing exactly which authors used which lines for each radial

Table 3.1: Radial velocities for Crimean observations of 1997

JDh (2400000+)	V_r (km/s)	r.m.s. error
50615.4956	-48.5	1.0
50623.4675	66.4	1.4
50624.4585	-14.3	1.2
50625.4553	-63.3	2.3
50626.4792	-72.7	1.3
50648.4623	-78.5	1.3
50649.5196	-7.5	1.8
50650.5054	56.8	1.3
50651.5033	62.9	1.4
50653.5095	-65.4	1.1
50658.4643	-26.1	1.0
50660.3914	-52.1	1.6
50661.3882	33.5	1.7
50663.4452	4.2	1.0
50667.4747	77.3	1.6
50668.4164	66.2	1.7
50669.4382	10.0	2.5
50675.3550	-44.7	1.2
50676.4727	-86.0	1.4
50677.4751	-28.8	1.4

velocity measurement.

The FOTEL3 software (Hadrava 1998) was used to calculate the ephemeris. Initially the fourteen datasets (Table 3.2) were considered separately and the individual 'best solutions' (for P, T_0, K and $f(M)$) determined. Zero eccentricity was assumed. This enabled us to weight each point by the inverse of the r.m.s. error and also to subtract centre of mass velocities (γ-velocities) for each source; this accounts for differences between the datasets due to systematic errors of the observers, the various telescopes and instruments, choice of lines, methods of radial velocity determination used and physical effects such as

Table 3.2: Sources of RV velocities for Cygnus X-1

JD (2400000+)	Source	No. of spectra	γ-vel. (km/s)	O–C (km/s)
41159–41588	Smith et al., 1973	9	0.1±2.2	6.3
41163–41255	Webster & Murdin, 1972	16	0.1±2.7	10.5
41213–44795	Gies & Bolton, 1982	78	-1.8±0.8	6.6
41214–41477	Brucato & Kristian, 1973	12	1.1±1.7	5.8
41269–41012	Mason et al., 1974	14	2.5±2.3	8.7
41515–42670	Walker et al., 1978	13	-0.6±1.0	3.7
41844–41290	Brucato & Zappala, 1974	17	-3.9±1.8	7.6
42205–42910	Abt et al., 1977	79	-7.9±1.1	7.9
43090–44768	Aab, 1983	24	-6.3±1.3	5.9
44513–45895	Ninkov et al., 1987	84	-5.6±0.7	6.6
46332–46635	Sowers et al., 1998	14	-9.8±1.4	5.1
49217–49538	Canalizo et al., 1995	6	10.6±1.9	3.6
50228–50255	LaSala et al., 1998	33	-0.9±1.8	10.2
50615–50677	Crimea 1997 (this work)	20	-4.1±1.9	8.4

Table 3.3: The Orbital Elements of Cygnus X-1

Element	Spectroscopic	Photometric
Period (days)	5.599829±0.000016	5.599836±0.000037
T_0 (JDh)	2441874.707±0.009	2441163.529±0.009
K_1 (km/s)	74.93±0.56	–
$f(M)(M_\odot)$	0.244	–

hidden emission in the red wings of lines (this can be caused by the stellar wind, resulting in a bluewards shift in γ-velocity).

To obtain the orbital solution the software was then run on the dataset as a whole over ~ 6 iterations. Prior to the second iteration we rejected those spectra for which O$-$C > 20 km/s – with so many radial velocities from fourteen different sources we still had a total of 421 points from which to determine the orbital parameters (N.B. in retrospect I acknowledge that this was not a good rejection criterion). We have also omitted the results of Seyfert & Popper (1941) due to their considerable uncertainties and the inclusion of hydrogen lines in determining the radial velocities. The resultant radial velocity curve for the whole of our compiled dataset is shown in Fig. 3.2; residuals are also plotted and show a definite lack of structure. The orbital parameters were obtained and can be found in Table 3.1.1, along with the elements calculated using the photometric data (see next section). We calculate the orbital period to be $P_{orb,sp} = 5.599829 \pm 0.000016$ days and define T_0 as the time of superior conjunction of the black hole.

Our new, high quality spectra have enabled us to extend the baseline for the ephemeris by over 400 days. As well as improving the accuracy of the radial velocity curve it also emphasizes the stability of the orbit of Cygnus X-1 over long time intervals. In order to check this stability a model dataset has been computed, with similar sampling to the original. Random noise and a sinusoidal period have been added and the Lomb-Scargle periodogram calculated. This was compared with that of the real data and it was found that the FWHM of the peaks match to within the errors of the ephemeris – had any variability in P taken place over the course of the observations then the FWHM would be significantly different.

3.1.2 Photometry

The photometric UBV data were obtained at the 60cm telescope at the Crimean Laboratory (Nauchny, Crimea) of the Sternberg Astronomical Institute during 1971–1997 by V.M. Lyuty. The pulse-counting photometer was used except for eight nights in July–August 1997 when it was changed to a CCD photometer with ST6V Camera (SBIG). All observations were made with reference to the standard BD +35°3816, $V = 9^m.976$, $B - V = 0^m.590$, $U - B = 0^m.064$ (Lyuty 1972). We therefore have a homogeneous photometric dataset spanning 26 years and containing more than 800 observtions. For this reason we did not use the photometric data of other authors except those of Khaliullin & Khaliullina

(1981) which were obtained with the same telescope, photometer and local standard.

A Discrete Fourier Transform was used to obtain the photometric period in each of the U, B and V filters. The mean for the three filters, $P_{orb,phot} = 5.599836 \pm 0.000024$ days, is in remarkable agreement with the spectroscopic period. We do not present the power spectrum here as the peak corresponding to the photometric period (and its aliases) is the only significant peak in the frequency range from zero up to the Nyquist frequency.

Previously Kemp et al. (1987) gave the most accurate value for the photometric period and the epoch of primary minimum (superior conjunction of X-ray source) as:

$$\text{Min I} = \text{JD}2441163.631(\pm 0.005) + 5.59985(\pm 0.00012)E\text{days}$$

The low accuracy of the period value may be due to combining different datasets. However, using the same data Lloyd & Walker (1989) obtained $P_{orb} = 5.59982 \pm 0.00005$, which coincides with the more accurate value of 5.59982($\pm$.00004) (Voloshina et al. 1997). Nadzhip et al. (1996) also improved the epoch of primary minimum to JD 2441163.547$\pm$0.005.

Our new epoch of superior conjunction (Table 3.1.1) corresponds to primary minimum at JD2441163.529 $\pm$ 0.009, so, we can give the most accurate ephemeris as:

$$\text{Min I} = \text{JD}2441163.529(\pm 0.009) + 5.599829(\pm 0.000016)E$$

Using this ephemeris we have constructed the mean UBV curves for our 27 years' worth of photometric data (Fig. 3.3). To increase the homogeneity of the dataset we have not used all available measurements, but only 1–5 per night, totalling 827 UBV measurements (while only $\sim$ 3 points were taken during most nights, on some occasions $\sim$ 50 points were made in order to study the fast variability – it was in these instances that $\sim$ 4–5 points were selected from the beginning, middle and end of the night in order to be consistent with the rest of the dataset). The observed mean curves are compared with the theoretical ellipsoidal curves of Balog, Goncharskij & Cherepashchuk (1981), for which $i = 50°, q = 0.33, \mu = 0.9, T_* = 30000K$.

The discrepancy between the observed mean lightcurves and the theoretical curve could be explained in terms of the stellar wind – at phase 0.5 the star is furthest from us and so we observe the part of the wind which is accelerated by the gravitational field of the black hole. Were the accretion disk responsible then we would require a hot disc, radiating significantly at the blue end of the spectrum in order to produce the greater discrepancy in the U band (see Fig. 3.3). Further analysis of the photometry is in preparation.

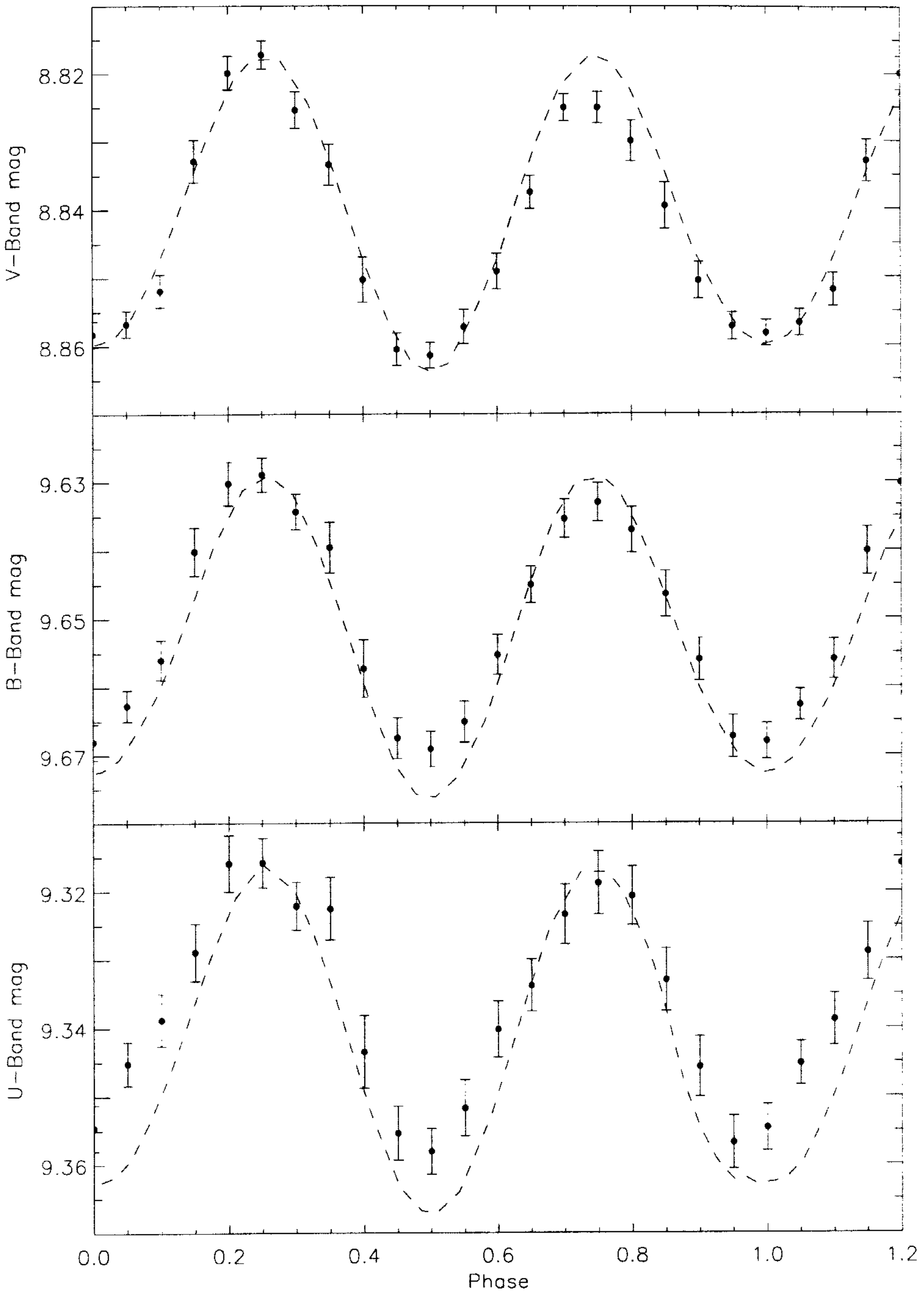

Figure 3.3: Observed mean lightcurves for 1971-1997 compared with theoretical ellipsoidal curve of Balog, Goncharskij & Cherepashchuk (1981).

3.2 Evidence for a Photo-ionisation Wake?

In collaboration with P. Roche & L. Kaper

The stellar wind of an OB star, such as the optical counterpart to Cyg X-1, is emitted by radiation pressure in the star's outer atmosphere which scatters and absorbs photons in various spectral lines formed in the wind. The acceleration of the wind is influenced by the degree of X-ray heating and ionisation from a compact object situated in the path of the wind (Hatchett & McCray 1977). While an increase in X-ray luminosity increases the line-driving force and hence the wind velocity, once the X-ray luminosity is of the order 10^{34} ergs/s the line force and wind velocity begin to decrease again. This is due to the increasing proportion of highly ionised species and an increase in optical depth of the lines. By the time the X-ray luminosity reaches 5×10^{34} ergs/s the high ionisation in the region around the compact object is sufficient to overcome the line-driving force, thus quenching the radiative acceleration (Macgregor & Vitello 1982).

This region of high ionisation around the compact object is known as the Strömgren zone. On colliding with the Strömgren zone the stellar wind is attenuated, resulting in the formation of strong shocks and dense sheets of gas trailing the X-ray source (Fransson & Fabian 1980). Predicted theoretically (Hatchett & McCray 1977, Fransson & Fabian 1980), observational evidence for this 'photo-ionisation' wake at certain phases of the binary orbit has now been discovered in the HMXB systems Vela X-1 and 4U 1700−37 (Kaper et al. 1994).

In a HMXB, such as Vela X-1, one would not expect to see any orbital variability in the absorption lines – other than the radial velocity of the binary system. However, distinct orbital variability is seen in some of the lines from the wind of Vela X-1. The Hβ and He I λ4471 profiles of Kaper et al. (1994) are shown in Fig. 3.4 – the spectrum at phase 0.37 is single, the rest are composites of two or three. The dashed line represents the average of all spectra and clearly indicates the presence of an additional blue-shifted absorption component at phases 0.6–0.9. A red-shifted emission component is also present at phases 0.6 and 0.9.

These features can be explained in terms of a photo-ionisation wake forming at the interface between the Strömgren zone and the stellar wind and trailing out almost halfway round the orbit. At the orbital phases for which the photo-ionisation wake passes in front of the supergiant a blue-shifted absorption component can be seen in the spectra; the

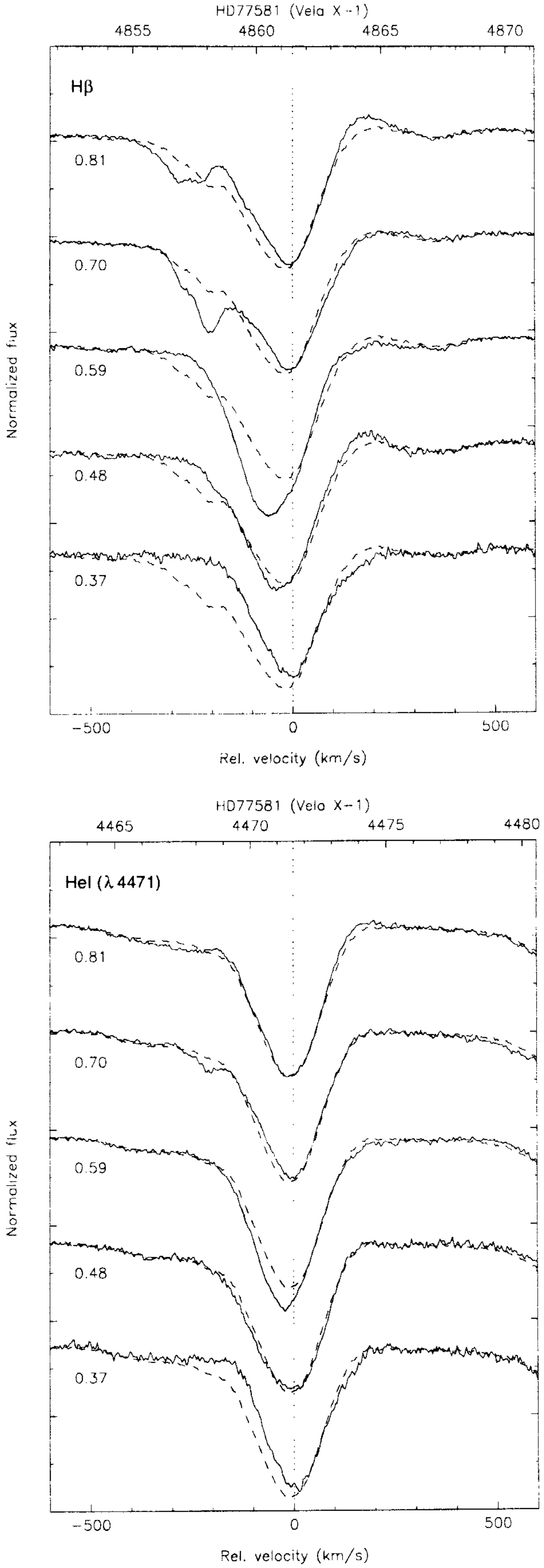

Figure 3.4: Hβ and He II λ4471 profiles of Vela X-1 clearly showing a blue-shifted absorption component at phases 0.6 – 0.9 and additional emission at phases 0.6 and 0.9 (from Kaper et al. 1994). The dotted line is the mean of all spectra.

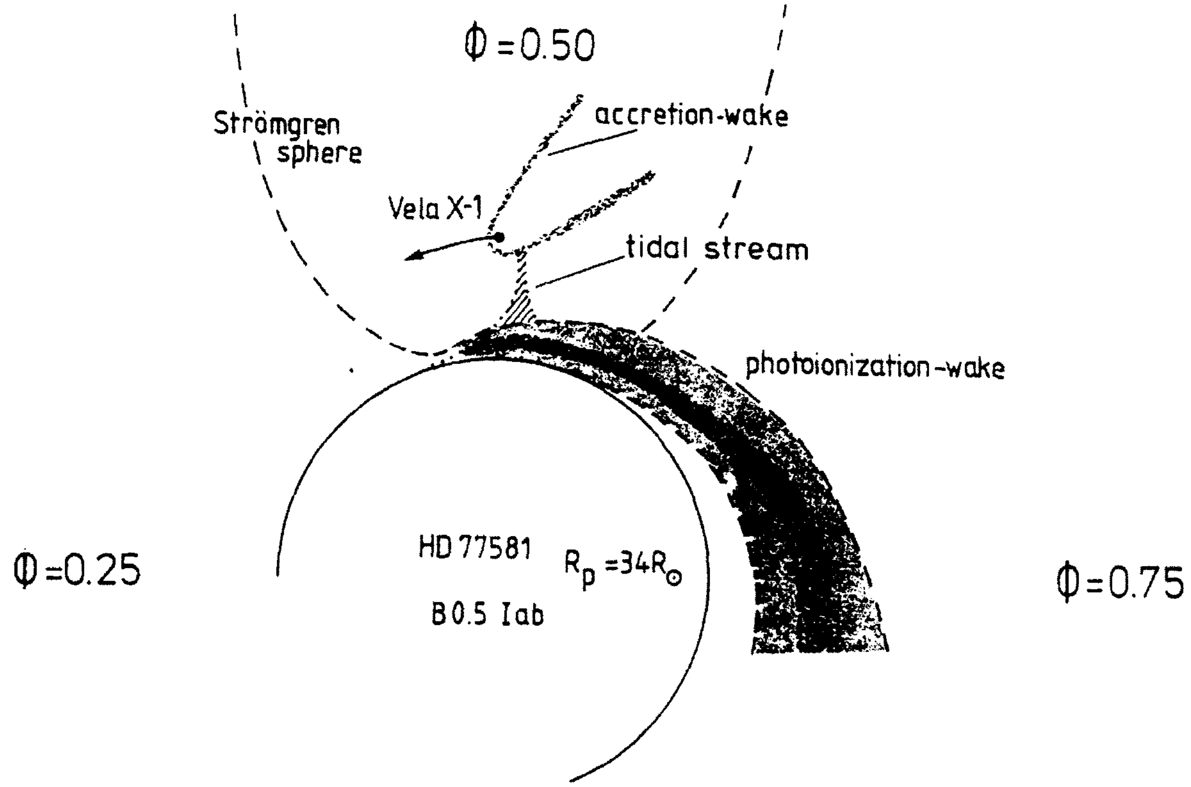

Figure 3.5: A schematic showing the components of the Vela X-1 system. The line of sight to the OB star passes through additional absorption at phases 0.5–0.8, due to the presence of a photo-ionisation wake trailing after the neutron star. (From Kaper et al. 1994)

amount of red-shifted emission that can be observed is determined by the position of the Strömgren zone relative to the line of sight. A schematic showing this taking place in Vela X-1 can be seen in Fig. 3.5. Also shown are a tidal stream from the OB star to the neutron star and an accretion wake which forms as the neutron star passes through the stellar wind.

While the orbital variability has been tentatively explained in terms of obscuration by the tidal stream and/or accretion wake, these components are too small to produce the significant amounts of absorption seen (Kaper et al. 1994 and references within). It therefore seems that the photo-ionisation model fits the data much more satisfactorily.

Given the similar 'OB supergiant + compact object' natures of Cyg X-1 and Vela X-1, it was suggested that Cyg X-1 may also be a suitable candidate for investigating a photo-ionisation wake. Notable differences between the two systems are that Cyg X-1 has a black hole compact object to Vela X-1's neutron star and that whereas Vela X-1 is an eclipsing binary (as is 4U 1700−37), the inclination of Cyg X-1 is thought to be ~ 30° (e.g. Gies & Bolton 1986).

3.2.1 Observations and Data Reduction

The spectra were obtained by E.J. Zuiderwijk over seven nights at the 2.5m Isaac Newton Telescope, La Palma in July 1994; the Intermediate Dispersion Spectrograph and Tek3 chip were used. Various wavelength regions were observed, notably the peculiar emission lines of Hα and He II λ4686 as well as a number of absorption lines; the spectra were centred on $\lambda\lambda$4113, 4405, 4627, 4938, 6560 Å with a reciprocal dispersion of 6–9 Å/mm. The unreduced data were subsequently obtained from the INT archive.

IRAF was used for the reduction of the spectra which consisted of standard bias subtraction, flat field division, optimal extraction, wavelength calibration and continuum normalisation. Further details of the reduction are outlined below.

The bias frames from each night were checked individually and then combined using IMCOMBINE, producing an average of approximately ten frames with which any structure in the bias across the CCD could be removed. A very simple rejection algorithm was used (minmax) in which the highest pixel in each frame was rejected. Frames were weighted according to their median value. IMARITH was then used to subtract this average bias from the flat field, arc and object frames. The median of approximately forty columns of the overscan region for each frame was determined; the columns were then fitted with a first order Chebyshev polynomial, rejecting points 3σ from the fit. The fitting and subsequent subtraction of the fit from each column of the data were achieved using COLBIAS.

As only a total of five flat field frames (tungsten lamp) at each wavelength had been taken over the seven nights I have averaged them all together, again with IMCOMBINE but this time using a more sophisticated rejection method (crreject) – the spread of data points was determined, taking the gain and read-noise into account, and points 3σ above this fit were rejected. The combined flat fields were normalised to unity using RESPONSE. The arc and object frames were then divided (IMARITH) by the resultant in order to remove any pixel-to-pixel variations in response.

Extracting the spectra involved a number of steps, all using the IRAF package APALL. The extraction window was defined so as to include all the light from the star – given the high luminosity of the optical counterpart to Cyg X-1 it was possible to allow some light from the wings of the spatial profile to escape in order to maximise the signal-to-noise ratio. It was also possible to refrain from removing the relatively insignificant sky background – a process which can introduce noise to the spectrum. While the shape of the spatial profile should not vary along the dispersion axis this is not necssarily true of the intensity; the position of the peak may also vary with wavelength due to the optical properties of the telescope and spectrograph. It is therefore necessary to trace the peak of the spatial profile across the CCD prior to extraction. For the extraction itself the counts within the extraction window were summed – any changes in the shape of the spatial profile were assumed smooth and pixels at the centre of the profile were weighted more heavily than those in the wings, in accordance with the optimal extraction algorithm of Horne (1986).

The arc frames (copper-argon and copper-neon lamps) were extracted similarly to their corresponding object frames. Each was then examined and their emission lines identified. IDENTIFY was used to fit a Gaussian to each identified line in order to determine its pixel value and hence assign a wavelength. The dispersion solution was obtained by fitting a low order cubic spline through these points - in the majority of cases a minimum of 10–15 lines were fit with an RMS less than 10% of a pixel. Finally, the object spectra were calibrated by applying the dispersion solutions of their corresponding arc frames (DISPCOR).

As there were no observations of a spectrophotometric standard taken it was not possible to flux calibrate the spectra. Instead CONTINUUM was used to fit the continuum with a cubic spline and normalise its flux to unity. Finally ASTHEDIT and SETJD were used to determine airmass and the heliocentric Julian dates.

In order to determine radial velocities using the cross-correlation technique it was necessary to re-do the last few steps. The dispersion solutions were reapplied, this time using a log-linearised scale with identical wavelength ranges for all spectra. Following normalisation SARITH was used to subtract one from each of the spectra. Further details for the reasoning behind this can be found in the next section.

3.2.2 Results - absorption lines

From the large selection of lines available in the spectra at these five wavelength ranges I have chosen the strongest hydrogen and helium lines for investigation. While the signal-to-noise ratio of the spectra is relatively good, the resolution is not as high as that of the spectra shown in Fig. 3.4 (Kaper et al. 1994) and so some of the detail in the weaker lines cannot be seen clearly.

Spectral profiles

Fig. 3.6 shows the phase resolved spectra of the regions of the Hβ, Hγ and Hδ absorption lines. Fig. 3.7 and 3.8 show similar plots of He I λ4026, λ4121, λ4144, λ4388, λ4471 and λ4923. In all cases it can be seen that, while there is clearly some orbital variability of the line, it is the velocity rather than the profile that is changing. Therefore the lines appear to be purely photospheric with no significant additional variable contribution from the wind.

This is supported by Canalizo et al. (1995) who found that while the amount of absorption in the blue wing of He I λ5876 and Hβ (and, to a lesser extent, some other He I lines) does vary with orbital phase, the *minimum* absorption occurs at phase 0.6 – there is no additional blue-shifted absorption. This would be expected as the reduction in both wind speed and line-driving force caused by the Strömgren zone surrounding the X-ray source can be observed at this orbital phase (e.g. Davis & Hartmann 1983, Treves et al. 1980).

Alternatively, this variation in absorption has also been considered as a hidden emission component. To investigate these hidden emission components a number of previous authors have attempted to subtract the absorption spectra of various standard OB stars from that of Cyg X-1 (e.g. Gies & Bolton 1986). The residuals have revealed weak emission components in the Balmer lines and in some He II lines. Unfortunately, the potential for error in the methods used to obtain the 'pure emission' components is too great (particularly if the observed absorption line depths vary with orbital phase) and the data quality too poor to attempt to investigate the emission profiles for the subtle features seen in Fig. 3.4. Likewise, while the shapes of the Balmer lines shown in Fig. 3.6 show some variability which is probably due to contamination by wind emission, I do not feel it is worthwhile attempting to subtract absorption components – the two reasonably strong emission lines are investigated further in the next section.

Radial velocity curves

Using the IRAF package FXCOR the spectra were cross-correlated with observations of the radial velocity template 19 Cep which is of similar spectral type to the companion

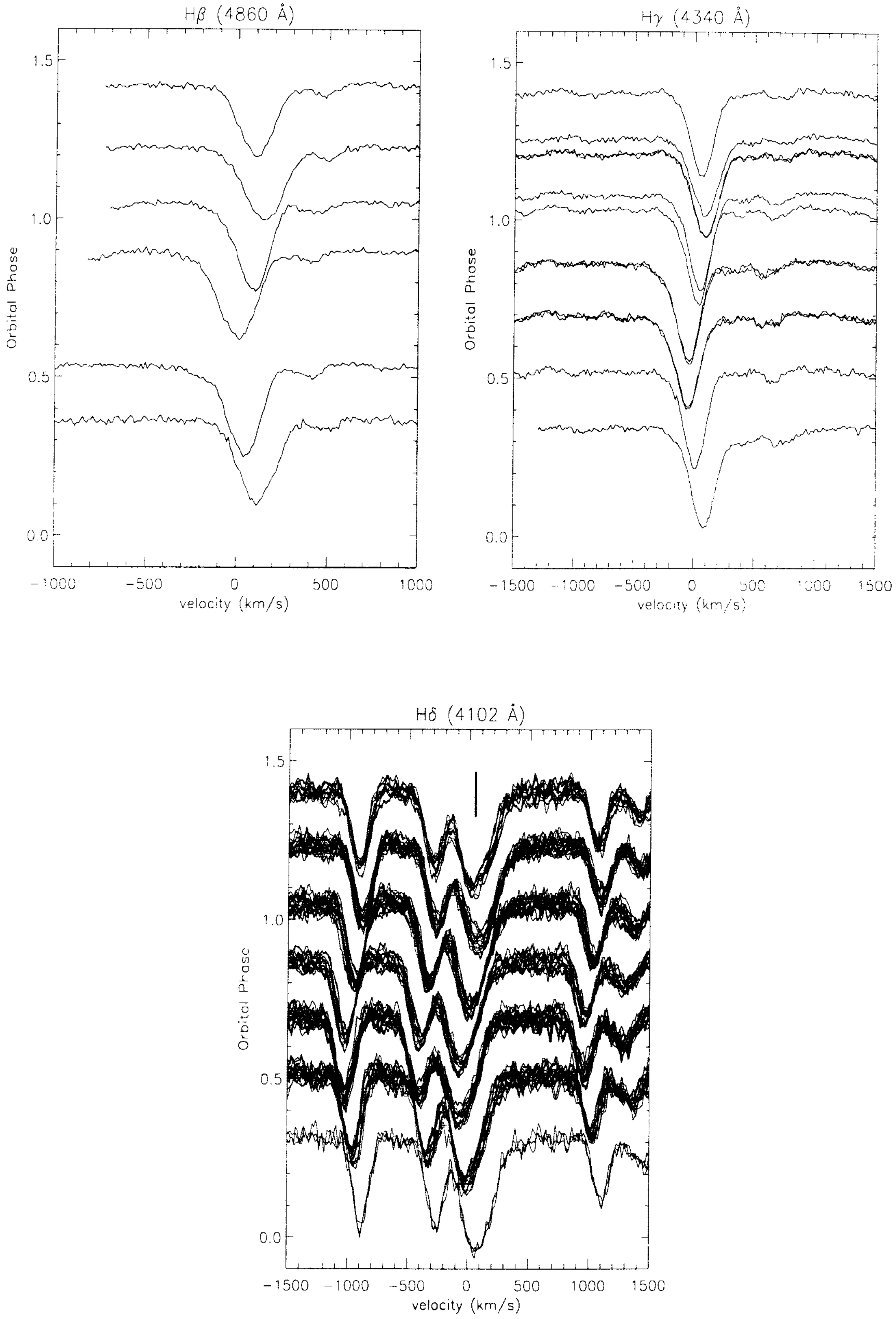

Figure 3.6: Hydrogen absorption line profiles. It can be seen that the only variability of these lines is due to the orbital motion of the star and that there is no additional wind component.

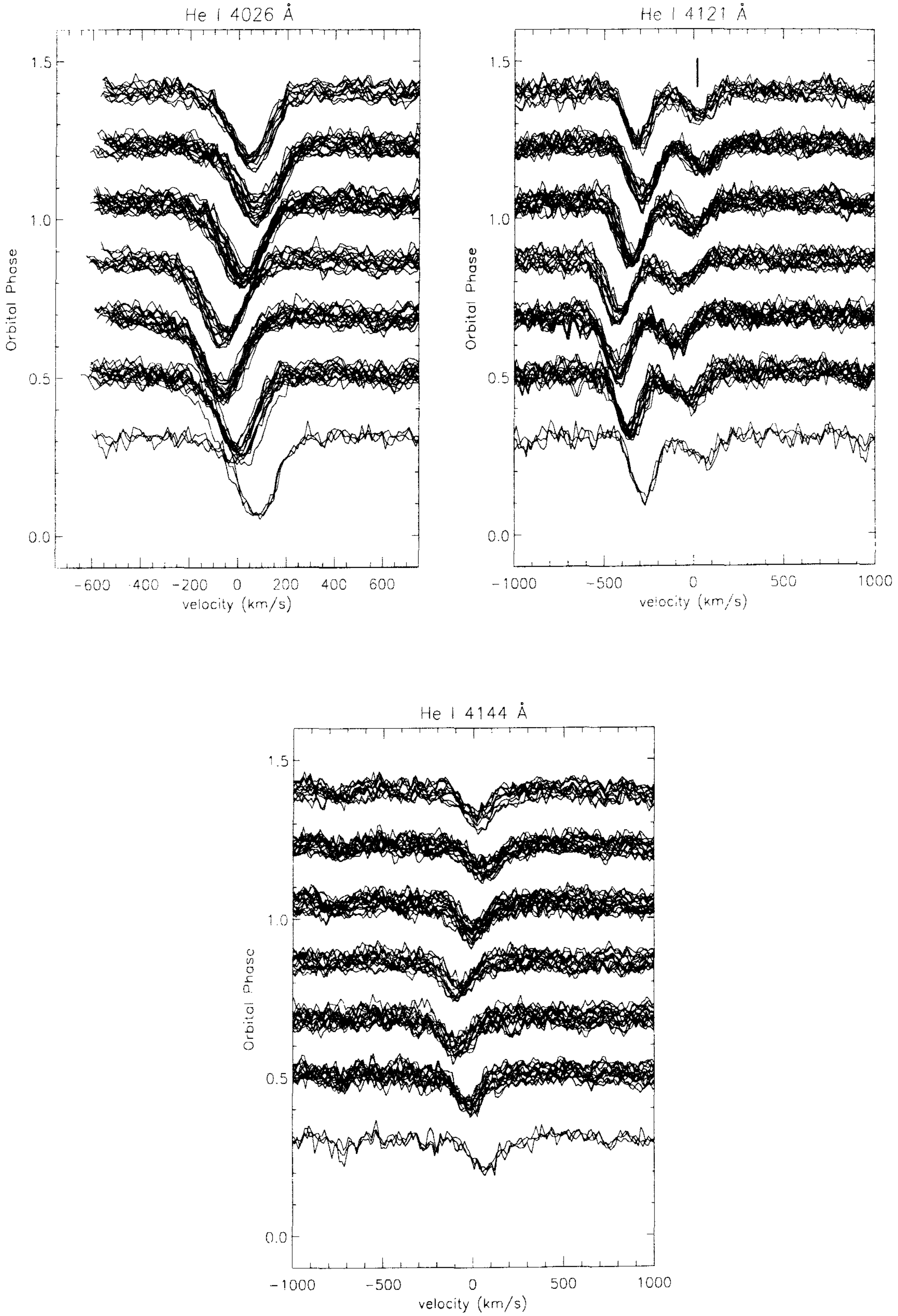

Figure 3.7: Helium absorption line profiles. It can be seen that the only variability of these lines is due to the orbital motion of the star and that there is no additional wind component.

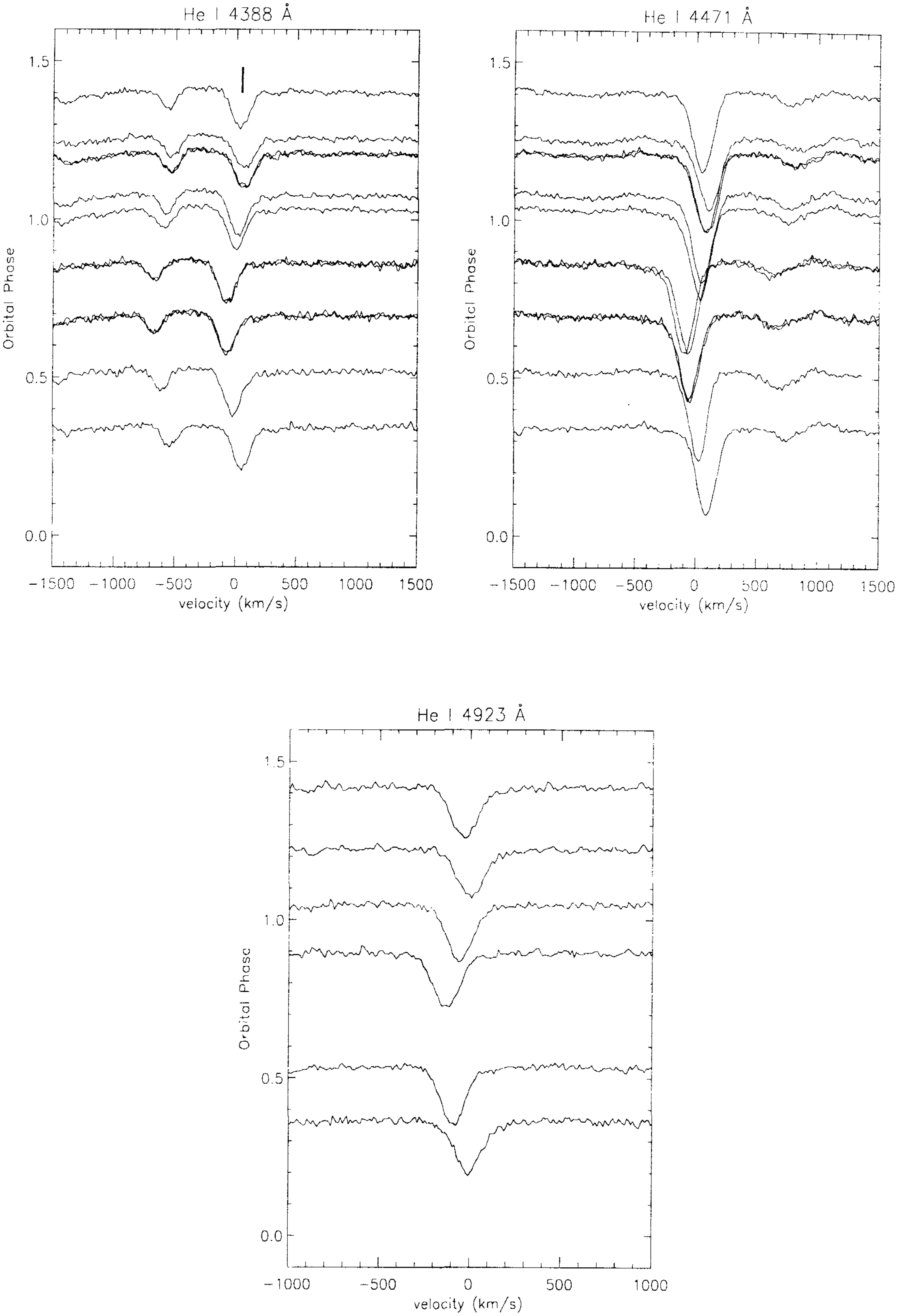

Figure 3.8: Helium absorption line profiles. It can be seen that the only variability of these lines is due to the orbital motion of the star and that there is no additional wind component.

of Cyg X-1. While in theory the cross-correlation technique involves shifting the target spectra until the features match up with those in the template spectrum, in practice the filtered Fast Fourier Transforms of the target and template are simply multiplied together – this is the equivalent of shifting. The FFT requires that the spectra are *log-linearised* – i.e. instead of having bins of equal wavelength the bins have equal velocity (or equal $\log\lambda$). As wavelength information is lost it is also important that all spectra cover the same wavelength range – for this reason there are fewer radial velocity curves plotted in Figs. 3.9 and 3.10 than spectral lines in Figs. 3.6, 3.7 and 3.8.

The difference in velocity between absorption lines of the template and those of Cyg X-1 could then be measured. The IDL routine CURVEFIT, which calculates a non-linear least squares fit, was used to fit a sine wave of the form

$$V = \gamma + K\sin(2\pi(\phi_{orb} - \Delta\phi_{orb})) \tag{3.1}$$

to the radial velocity data. Here V is the radial velocity, γ the systemic velocity, K is the velocity semi-amplitude, ϕ_{orb} is the orbital phase and $\Delta\phi_{orb}$ the orbital phase shift. Points with $V \geq 1000$ km/s or associated error ≥ 100 km/s were rejected from the fit, although this was not the case for any of the data points here. The fit was then computed again, this time rejecting any points more than 4σ from the fit - again none was rejected here. Gaussian weights were applied (i.e. the points were weighted by the inverse square of their associated error). Radial velocity curves for the hydrogen and helium lines are shown in Figs. 3.9 and 3.10 respectively. The error bars shown on the plots correspond to $\chi^2_{reduced} = 1$ and reflect uncertainties in the cross-correlation procedure - such as noise in the spectrum and differences between the line shapes of Cyg X-1 and 19 Cep which cause the cross correlation function to deviate from Gaussian behaviour.

Clearly the radial velocity curves fit the sinusoid very well. There is no evidence for any deviation around phase 0.5 or 0.6 which we would expect if an additional blue-shifted wind component were present. I note that there is some discrepancy between the value of K for the system (Table 3.1.1) and the values for some of the individual lines – this is probably due to contamination by wind emission and/or line-formation at different levels of the atmosphere but is still within the scatter seen in Fig. 3.2. As this is merely a simple radial velocity study to determine whether or not there is any evidence for a photo-ionisation wake it was not necessary to deblend any of the lines prior to cross correlation – this may also contribute to some of the variability in K and γ.

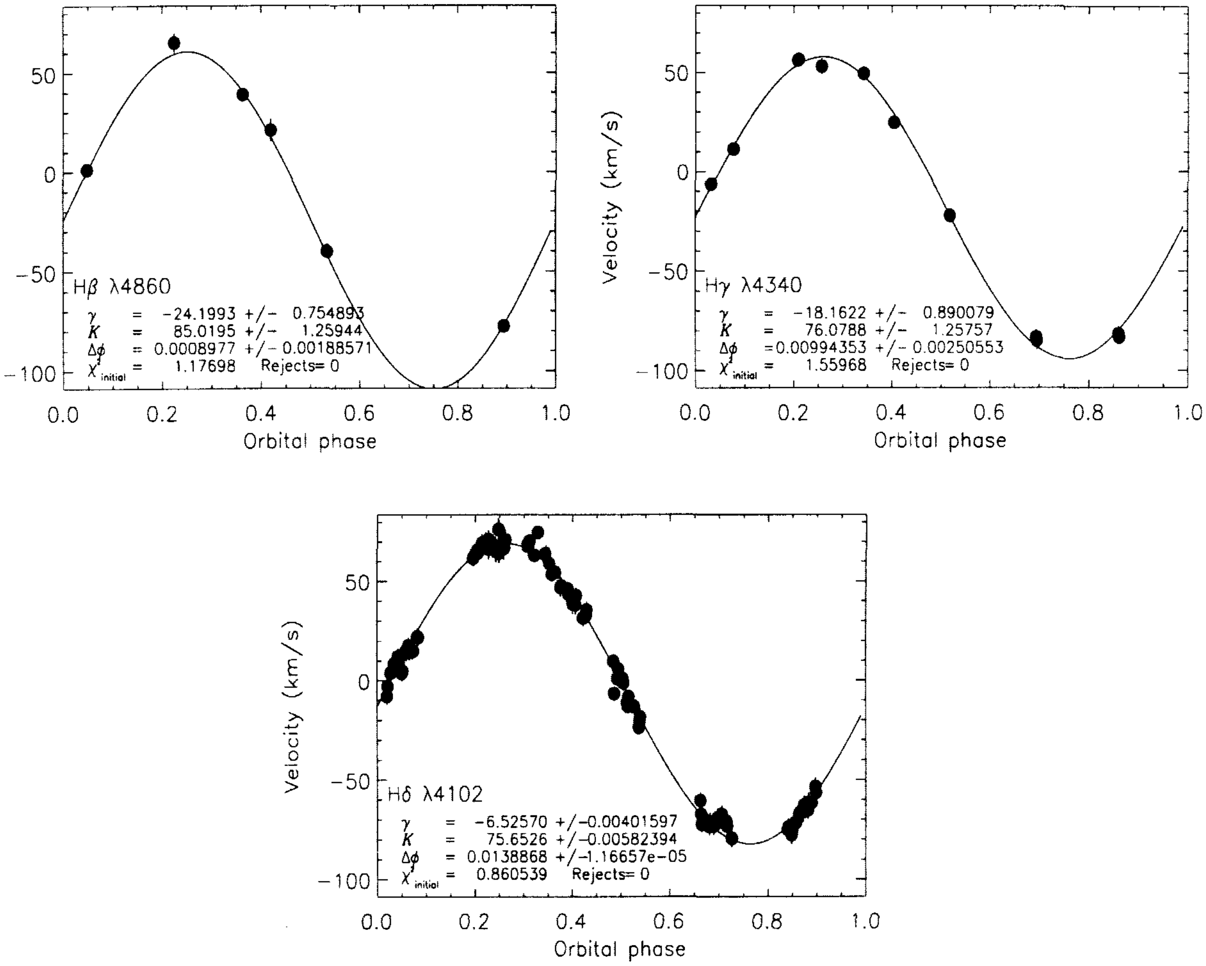

Figure 3.9: Radial velocity curves for the hydrogen absorption lines showing a good fit to a sinusoid. Error bars correspond to $\chi^2_{reduced} = 1$. Note that Hδ is blended with N III λ4097 which may contribute to K and γ.

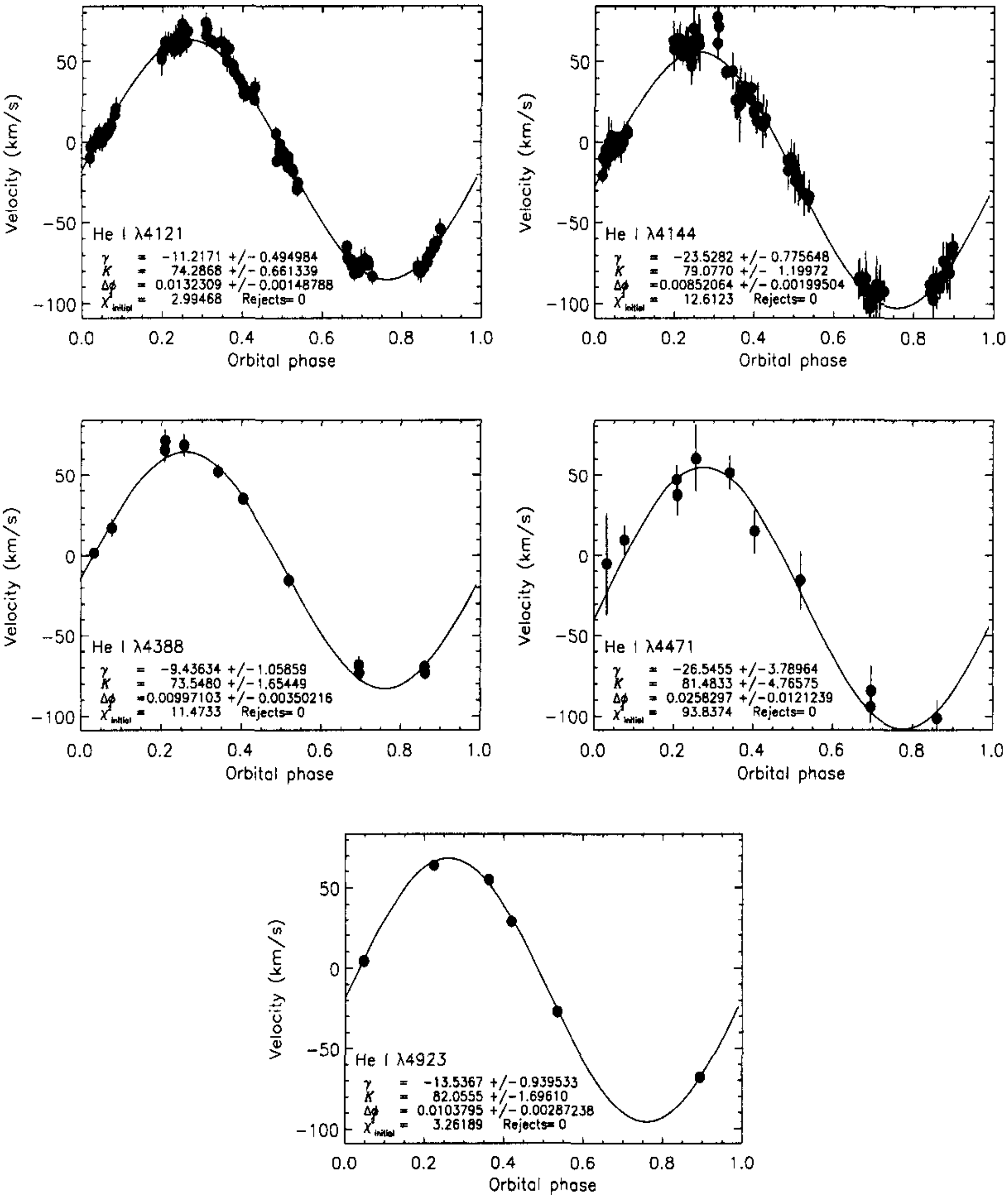

Figure 3.10: Radial velocity curves for the helium absorption lines showing a good fit to a sinusoid. Error bars correspond to $\chi^2_{reduced} = 1$. Note that He I,λ4121 is blended with Si IV λ4116 which may contribute to K and γ. There is also a number of very small O II lines close to He I λ4471

3.2.3 Results - emission lines

For completeness the two prominent emission lines, Hα and He II λ4686 are now considered. The line profiles are shown in Fig. 3.11. Both lines show that *more than one component* is present – Hα is thought to be the superposition of a wind P Cygni profile and an additional emission component; He II λ4686 is a superposition of photospheric absorption and an emission component. Both additional emission components are thought to be produced in the accretion stream in the region of the L1 point on account of their radial velocity curves (e.g. Aab et al. 1983, Sowers et al. 1998). While these plots contain no particularly interesting new results, they do have more complete phase coverage and a better signal-to-noise ratio than any published text on Cyg X-1. To achieve full phase coverage previous authors have resorted to using spectra from more than one orbit. As noted by Walker, Yang & Glaspey (1978) and as investigated in the next chapter, this should not be tried as there is significant orbit-to-orbit variability.

Figs. 3.12 and 3.13 show trailed spectrograms of the two emission lines, which have been created using the velocity and phase binning routines in MOLLY and plotting routines in IDL (shading in red indicates emission; yellow indicates absorption). This is the first such plot created for the He II line and while Sowers et al. (1999) published a Hα trailed spectrogram, their data were from various different orbits and of significantly worse signal-to-noise ratio. Unfortunately the phase coverage for the Hα spectra shown here is far from complete but an absorption component can be seen blueward of the (stationary) emission component, as can the appearance of an additional emission component at phase 0.3–0.5, blue-shifted to a velocity of ~ -400 km/s. The He II has better coverage and the absorption component can be seen to shift around the emission component. Comparison of the two trailed spectrograms would suggest that the additional emission of both lines is blue-shifted during phases 0–0.5 and then red-shifted for the second half of the orbit – when, in the case of Hα, it combines with the P Cygni emission

In order to study these emission lines previously, authors have attempted to subtract the absorption spectrum of a standard star of similar spectral type (e.g. Gies & Bolton 1986, Ninkov, Walker & Yang 1987a). As well as being a somewhat dubious method (for reasons given in Gies & Bolton 1986 and Chapter 2) this method is particularly unsuitable for Hα with its P Cygni profile rather than a simple photospheric absorption line.

It is interesting to note that Hutchings, Crampton & Bolton (1979) recovered the 'pure' Hα emission using this method and discovered what appeared to be a variable blue-

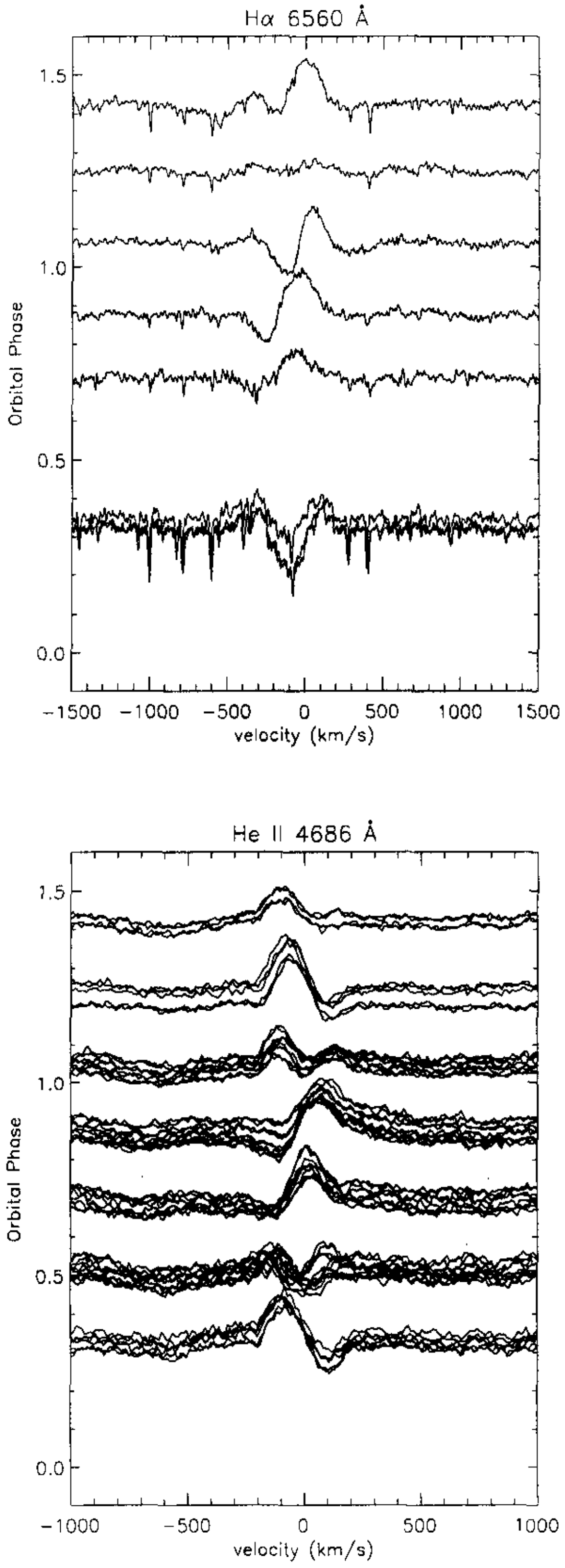

Figure 3.11: Profiles of the peculiar Hα and He II λ4686 emission lines. In both cases it can be seen that more than one component is present – it is thought that an emission component formed in/near the accretion stream is superimposed on the P Cygni (Hα) and absorption (He II) components.

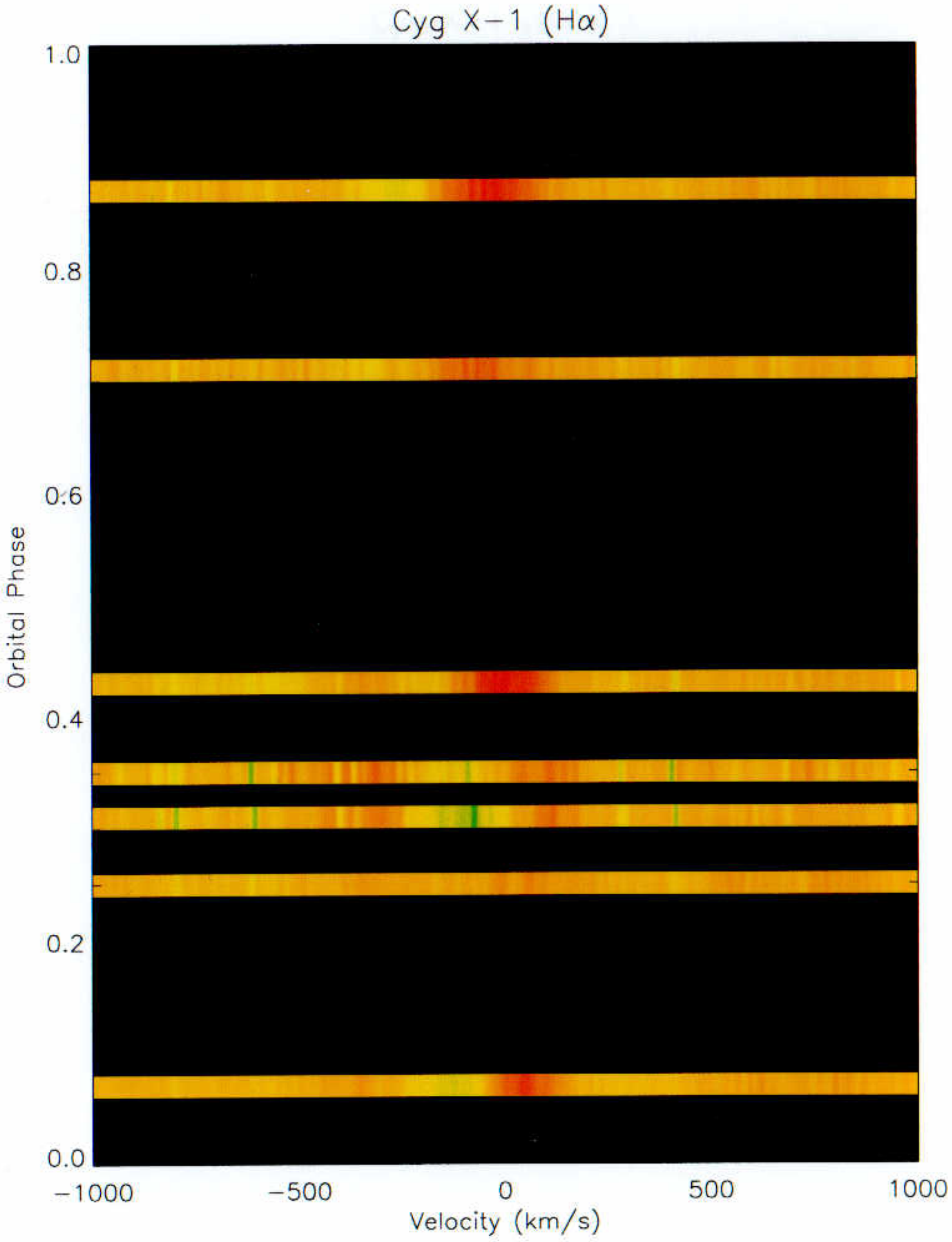

Figure 3.12: Trailed spectrogram of the peculiar Hα emission line. The additional blue-shifted emission (plotted in red) component can be seen at orbital phases 0.3–0.5 but merges with the P Cygni profile after this.

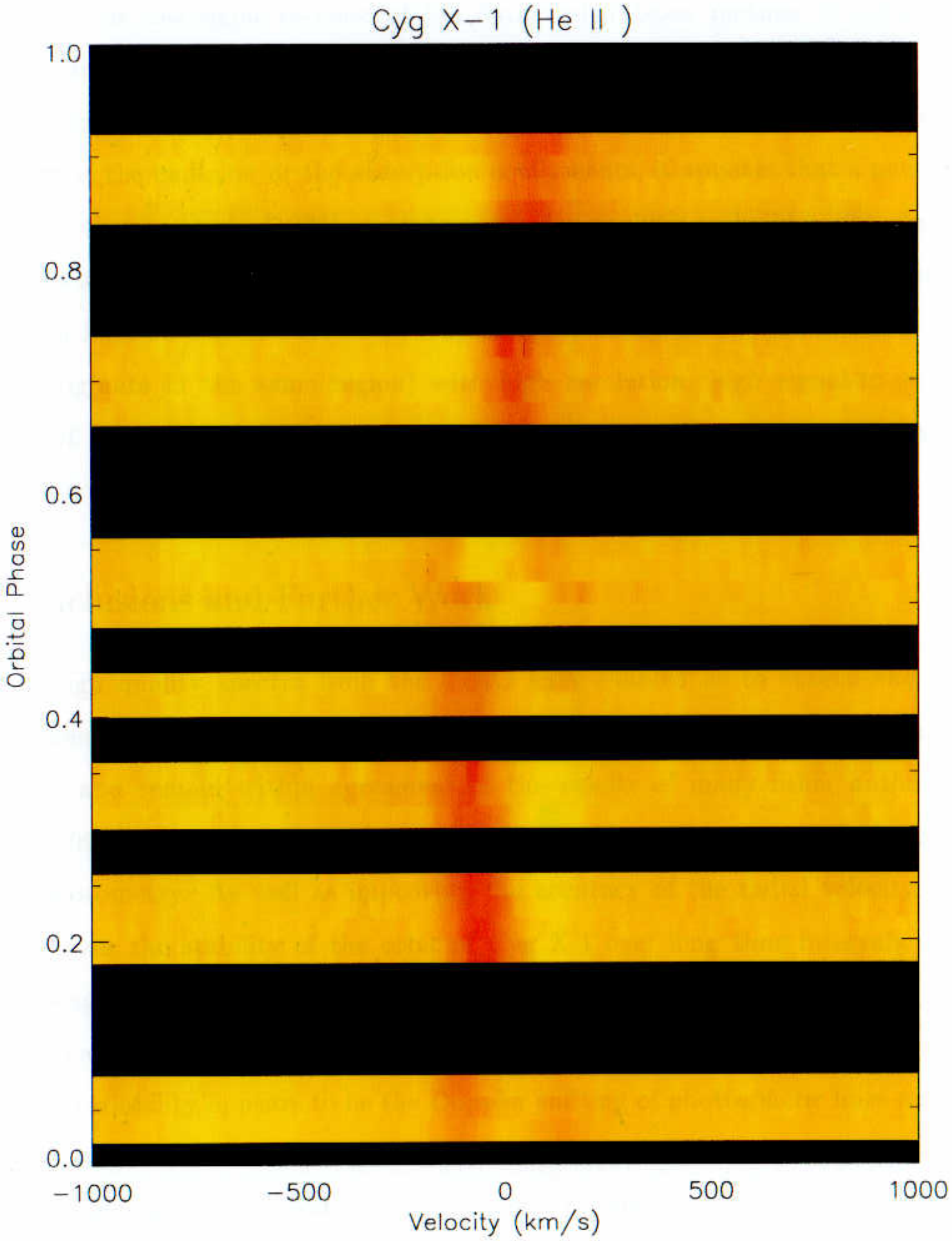

Figure 3.13: Trailed spectrogram of the peculiar He II λ4686 emission line. The additional emission (plotted in red) component can be seen throughout the orbit, moving almost in antiphase (~ 120° e.g. Hutchings et al. 1973) with the photospheric absorption (plotted in yellow).

shifted absorption component in the residual profiles and therefore possible evidence for a photo-ionisation wake. However, the absorption trough appeared at phase 0.2, reached a maximum depth at phase 0.5 and was only just present at phase 0.7. If these results were due to a photo-ionisation wake then the geometry of the model would need to be re-assessed. The low signal-to-noise of the data and dubious method of obtaining the emission profiles probably renders this unnecessary.

To investigate all the emission lines *accurately* (including all the Balmer lines etc) of Cyg X-1, be it the emission or the absorption components, it appears that a new method is necessary. Sowers et al. (1998) use a tomographic analysis to build a two component profile of Hα and are relatively successful. However, to improve on what they have done, all the emission lines should be studied (ideally simultaneously as the emission components probably originate in the same region) with high resolution, high signal-to-noise data spanning *all* phases of *a single* orbit. Without this then the orbit-to-orbit variations considered in the next chapter will cause confusion.

3.3 Conclusions and Further Work

Our new, high quality spectra from the CrAO have enabled us to extend the baseline for the ephemeris by over 400 days. Consequently we have refined the orbital period of Cyg X-1 and remain within agreement of the results of many other authors. Our value of 5.599829 days for the orbital period also provides an accurate fit to 27 years' worth of photometry. As well as improving the accuracy of the radial velocity curve it also emphasizes the stability of the orbit of Cyg X-1 over long time intervals. Further multiwavelength analysis will follow in the next chapter.

Despite looking at a number of absorption lines in the INT spectra of Cyg X-1, the only orbital variability appears to be the Doppler shifting of photospheric lines as the star approaches and recedes. There is no evidence for an additional blue-shifted absorption component due to a photo-ionisation wake, either in the spectra themselves or in the radial velocity curves. I note that previous authors have found hidden emission components in various lines (particularly the Balmer lines), diminishing at orbital phase 0.5 – this would be expected in accordance with the Hatchett-McCray (1977) effect. However, the low resolution of the data and the many errors involved in attempting to subtract the absorption spectrum make it unwise to investigate this hidden emission here.

It seems unlikely that a black hole system, such as Cyg X-1, which is a bright X-ray source should not be observed to heat and hence attenuate the wind sufficiently to produce an optically thick photo-ionisation wake as in the case of Vela X-1. In fact it is more likely that with an X-ray luminosity of $\geq 10^{37}$ ergs/s (e.g. Smith, Margon & Conti 1973) the X-ray heating is sufficient to *completely* ionise the wind in the region of the black hole. Consequently the wind is slowed in all but the shadow of the X-ray source and so shocks at the interface between the fast 'shadow' wind and the region of high ionisation are not probed in these data (Kaper 2000, private communication). This scenario may not be compatible with the focussed stellar wind model of Friend & Castor (1982), Gies & Bolton (1986a) – however the focussed stellar wind model does not sufficiently deal with X-ray ionisation. Clearly both models should be developed simultaneously in order to explain the results seen here and in the next chapter. It would be an interesting exercise to determine the wind velocity of Cyg X-1 at different orbital phases to see to what extent the wind is fully ionised.

An alternative suggestion is simply that the inclination angle of Cyg X-1 is too small for the photo-ionisation wake to obscure our line of sight. This could be much more easily tested by making phase-resolved spectroscopic observations of neutron star systems of similar X-ray luminosities and various inclination angles to determine how far out of the orbital plane the photo-ionisation wake can be detected.

It is also interesting to note that whereas the predicted X-ray luminosity of the majority of OB HMXBs is less than that observed this is not the case for Cyg X-1. With the X-ray luminosity inversely proportional to the fourth power of the wind velocity (assuming the X-ray luminosity is due to accretion from the wind only) this suggests that in most cases (but apparently not in Cyg X-1) the wind is slowed in the region of high ionisation trailing the compact object, i.e. the Strömgren zone (Kaper 1998). However, the X-ray hardness ratio of Cyg X-1 is seen to peak at high orbital phases and this could be due to the absorption of soft X-rays by the photo-ionisation wake in the line of sight – although other mechanisms have been suggested, e.g. absorption by the wind and/or accretion stream (e.g. Bałucińska–Church et al. 2000). Something different takes place in the Cyg X-1 system as the X-ray luminosity suggests that the wind is completely ionised in the region of the black hole – the focussing of the wind into quasi-Roche lobe overflow may be responsible here. As there is certainly evidence for an accretion disc and Comptonising corona the wind accretion relationship above is probably not relevant here.

The focussed nature of the stellar wind of Cyg X-1 complicates matters as the P Cygni profile of the Hα emission is superimposed by an additional emission component thought to originate in the region of the L1 point. Likewise the He II λ4686 is also thought to be a superposition of a photospheric absorption line and emission from the region of the L1 point. To study either of the components of each line it is important not to introduce errors through subtraction of a standard star spectrum. The tomographic method used by Sowers et al. (1998) has proved successful and would be a recommended way forwards. Full phase coverage of a single orbit is required for this so that orbit-to-orbit variations can be eliminated and it would be advisable for the Hα and He II λ4686 lines to be studied together, both having additional emission components originating in a similar region.

In collaboration with A.E. Tarasov, D.R. Gies and K. Ayani, Hα spectra have been obtained by telescopes at the Crimean Astrophysical Observatory, the McDonald Observatory and the Bisei Astronomical Observatory during the same week. By observing 'simultaneously' with three telscopes at such evenly spaced time zones, we should have almost complete phase coverage of a single orbit (although the Bisei data may be of insufficient resolution to be used directly) and consequently high quality tomograms should be achievable. This is work in progress.

Chapter 4

PERIODIC AND FLARING VARIABILITY OF CYGNUS X-1

In collaboration with R.P. Fender, V. Larionov, V.M. Lyuty, A.E. Tarasov, G.G. Pooley, W.S. Paciesas & P. Roche[1]

Following the revision of the orbital ephemeris of Cyg X-1 in the previous chapter, we now turn to a study of variability at other wavelengths.

The orbital period has been well-defined in the optical (e.g. Voloshina, Lyuty & Tarasov 1997) and infrared photometry (Leahy & Ananth 1992, Nadzhip et al. 1996) for over a decade. A 5.6 day modulation has also been discovered in X-ray data collected by *Ariel V*/ASM (Holt et al. 1976), *RXTE*/ASM (Zhang, Robinson & Cui 1996) and *CGRO*/BATSE (e.g. Paciesas et al. 1997). Finally, Pooley, Fender & Brocksopp (1999) have recently reported that the orbital period is present in the radio emission. Here, for the first time, the orbital period is studied in all wavebands simultaneously. The chapter ends with a more detailed look at the orbital modulation at radio wavelengths – we find that it can be reasonably well described by a simple model of free-free absorption by varying optical depths of the stellar wind as the radio source moves around the supergiant.

A second 'modulation' of ~ 150 days has been detected (Pooley, Fender & Brocksopp 1999) and this is probably related to the 294 day period found in X-ray data by Priedhorsky, Terrell & Holt (1983) and in optical data by Kemp et al. (1983, 1987). We find

---

[1] Published in MNRAS, 309, 1063 (1999). Additional spectroscopy and study of the radio orbital modulation included here.

that the shorter period is present in all our datasets and suggest that it is caused by precession of the accretion disc.

A number of (anti-)correlated events between the radio and X-ray emission have been reported and these have generally taken place at the time of a transition from one X-ray state to another. Here we look at the small scale flaring behaviour of Cyg X-1 and find further evidence for correlated behaviour between the radio and soft X-ray lightcurves.

The presence of modulations at all wavelengths and correlated behaviour between the X-ray and radio strongly suggest that there is a connection between the accretion disc and the radio-emitting jet that is not probed sufficiently in current X-ray models. In this chapter we lay the groundwork for more detailed future modelling of the jet/disc system.

4.1 Observations

Data were collected between 1996 April and 1998 September, a summary of which can be found in Table 4.1.

To ease comparison between datasets the optical and infrared magnitudes have been converted into mJy using the O'Dell conversion factors (O'Dell et al. 1978).

Table 4.1: Summary of observations

Band	Source	Observation Period
Hard X-rays (20–100 keV)	*CGRO*	April 1996–Sept 1998
Soft X-rays (2–10 keV)	*RXTE*	April 1996–Sept 1998
UBV	SAI	June 1996–Sept 1998
Spectroscopy	CrAO	June 1996–Sept 1998
JHK	SPG+CrAO	June 1997–Sept 1998
Radio	RT	Oct 1996–Sept 1998*

CrAO – Crimean Astrophysical Observatory

SAI – Sternberg Astronomical Institute

SPG – St. Petersburg University

RT – Ryle Telescope, Cambridge, UK

* There is also one point from April 1996

X-ray

Our hard X-ray data came from the BATSE instrument on the Compton Gamma Ray Observatory (*CGRO*) and were processed using the standard BATSE earth occultation software. Further details can be found in Paciesas et al. (1997). Soft X-ray data have been obtained from the Rossi X-ray Timing Explorer (*RXTE*); we use the ASM public archive data from the web (http://xte.mit.edu). A detailed description of the ASM, including calibration and reduction is published in Levine et al. (1996).

Optical

The photometric UBV data were obtained by the pulse-counting photometer of the Crimean Laboratory (Nauchny, Crimea) of Sternberg Astronomical Institute; the 60 cm telescope was used. All observations were made with reference to the local standard BD +35°3816, $V = 9.976$, $B - V = 0.590$, $U - B = 0.064$ (Lyuty 1972).

Our spectra were taken at the Crimean Astrophysical Observatory using the coudé spectrograph of the 2.6 metre telescope. The detector was a CDS9000 (1024×256 pixels) CCD array. All observations were made in the second order of a diffraction grating with reciprocal dispersion of 3Å/mm and resolution of 25000. The typical exposure time for each spectrum totalled 40 minutes for Hα and 1.5 hours for He II λ4686 resulting in a S/N of ~100. The spectra were reduced using standard flat field normalisation and sky subtraction techniques. Wavelength calibration was achieved using ThAr comparison spectra. Note that the earlier of these He II are the same spectra that were used previously (Chapter 2).The water lines were removed from the Hα spectra and equivalent widths calculated.

Infrared

The infrared data were collected using an InSb photometer of St. Petersburg University which is attached to the 0.7m telescope of the Crimean Observatory. The detector operates at the temperature of liquid nitrogen. η Cygni was used as the standard star and the measurements have an accuracy of 0.03 magnitudes. This accuracy may appear unlikely on seeing the amount of scatter present in the infrared lightcurve compared with the optical. However the variability is thought to increase at the longer wavelengths and so is probably intrinsic – this has been confirmed with more accurate observations of Cyg X-1 at Campo Imperatore (V. Larionov, private communication). Further analysis is in progress.

Radio

15 GHz radio monitoring took place at the Ryle Telescope of the Mullard Radio Astronomy Observatory, Cambridge. The radio data are presented here as 10 minute integrations with a typical rms uncertainty of 1 mJy; the phase calibrator used was B2005+403. Further details may be found in Pooley & Fender (1997).

We have also made use of radio data from the Green Bank Interferometer (details of which may be found in Waltman et al. 1994) which monitors this and many other sources at 2.25 and 8.3 GHz.

4.2 Results

Long term lightcurves for BATSE, ASM, *UBVK* band photometry and the radio are shown in Fig. 8.1.

Perhaps the most notable feature is the very distinct anticorrelation between the two X-ray bands during the period MJD 50200–50330. As mentioned previously, this is typical of the transition to the high/soft state and back to the hard again. Unfortunately we only have one radio point during this period – on MJD 50226 the flux reached 18 mJy. However, this was during the transition and VLA monitoring towards the end of the high/soft state period showed that, as found during previous state changes, the radio flux had dropped to ~5 mJy (Zhang et al. 1997). Some authors (Belloni et al. 1996, Esin et al. 1998) have concluded that Cyg X-1 did not fully reach the soft/high state on this occasion in which case we may expect the radio source to not have disappeared as before (but see also Gierliński et al. 1999). However, it should be noted that the radio source of GX339−4 diminishes during its X-ray intermediate/high state (Fender et al. 1999) and, given the many similarities between these two systems in terms of their X-ray and radio properties, we may expect Cyg X-1 to behave likewise.

It is also immediately apparent that there is a long term modulation in the radio, referred to as the '150 day' period in Pooley, Fender & Brocksopp (1999); it has now been monitored for five cycles. This is studied in more detail in Section 4.2.2.

There are many flares in the X-ray and radio light curves, the majority of which seem to correlate between the different wavelength regimes. This is perhaps to be expected as the emission is all thought to be associated with the black hole and accretion disc. The majority of the X-ray flares appear to be of comparable amplitudes but there are two in the ASM data which increase above this level. The flares at MJD ~50650 and ~ 51010

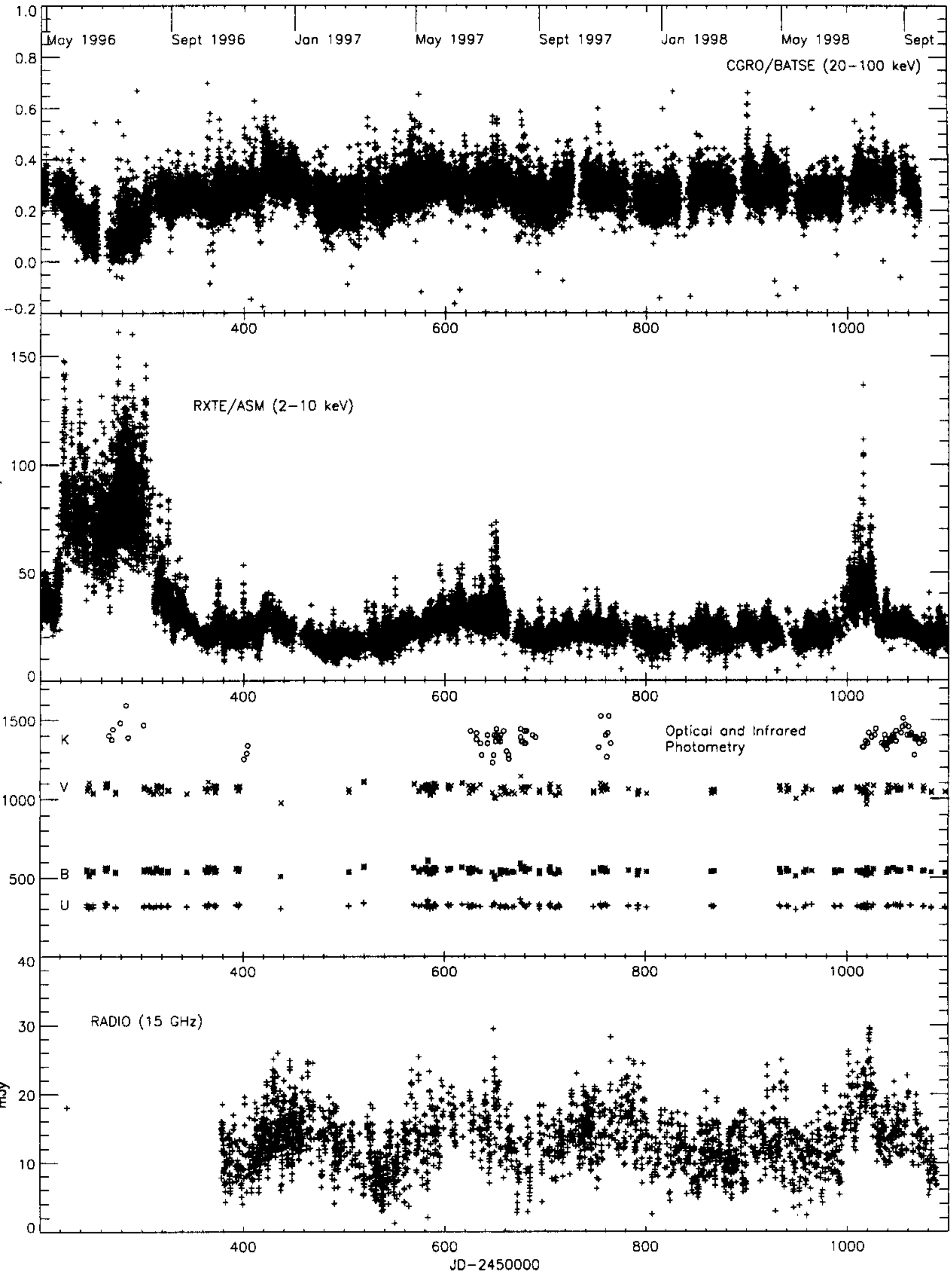

Figure 4.1: BATSE, ASM, optical, infrared and radio lightcurves for the full 2.5 years or our observations (MJD 50200–51100).

are studied in further detail in Section 4.2.3.

In contrast to this, the optical photometry shows a very flat lightcurve with few deviations, other than orbital modulation. There are a few flares but whilst the behaviour of one optical band is generally correlated with the others, there appears to be no correlation with the other wavelength regimes. In particular, there is one flare of note that occurred at MJD 50583 in the U and B bands and is distinctly not correlated with any soft X-ray behaviour. This is addressed in more detail in Bochkarev & Lyuty (1998). Therefore it is perhaps surprising that the equivalent width of the Hα emission line was apparently anti-correlated with the soft X-rays during the soft X-ray state, being significantly below its usual value – indeed, the emission component of the line essentially disappeared, with a value of ~0.25 Å compared with an average value of −0.7 Å during the low/hard state. We suggest that this was due either to additional ionisation in the stellar wind at this time, or dilution by a stronger free-free component. We do not include the equivalent width data in Fig. 8.1 as it does not cover the full period. Instead, we address it in further detail in Section 4.2.1 and 4.2.2.

Unfortunately our infrared data are more scattered and it is difficult to see if there are any flares. It appears that there are none and that generally it follows the same flat shape of the optical. However, there are a number of possible deviations from this. It appears that the flux is slightly increased during the X-ray high/soft state and then falls to below the mean shortly after the transition to the low/hard state. This is the case in all four bands, although we show only the K band here. We note that there is a single point in the U, B and V bands soon after this that is also well below the mean flux level. There may also be a peak in the infrared at MJD 51055, approximately forty days after the X-ray flare.

4.2.1 The Orbital Period

We use the ephemeris of Brocksopp et al. (1999) with P_{orb}=5.599829±0.000016 days. The STARLINK package PERIOD was used to fold all data on the orbital period with superior conjunction of the black hole corresponding to the zero point (JD 2441874.707).

We were surprised to see that the optical photometry did not fold onto this period satisfactorily, in contradiction to Brocksopp et al. (1999) when a much longer dataset was used. We therefore separated the data according to the X-ray state and, for the hard state, removed flares and scatter above $\sim 3\sigma$ from all datasets. The resulting mean lightcurves

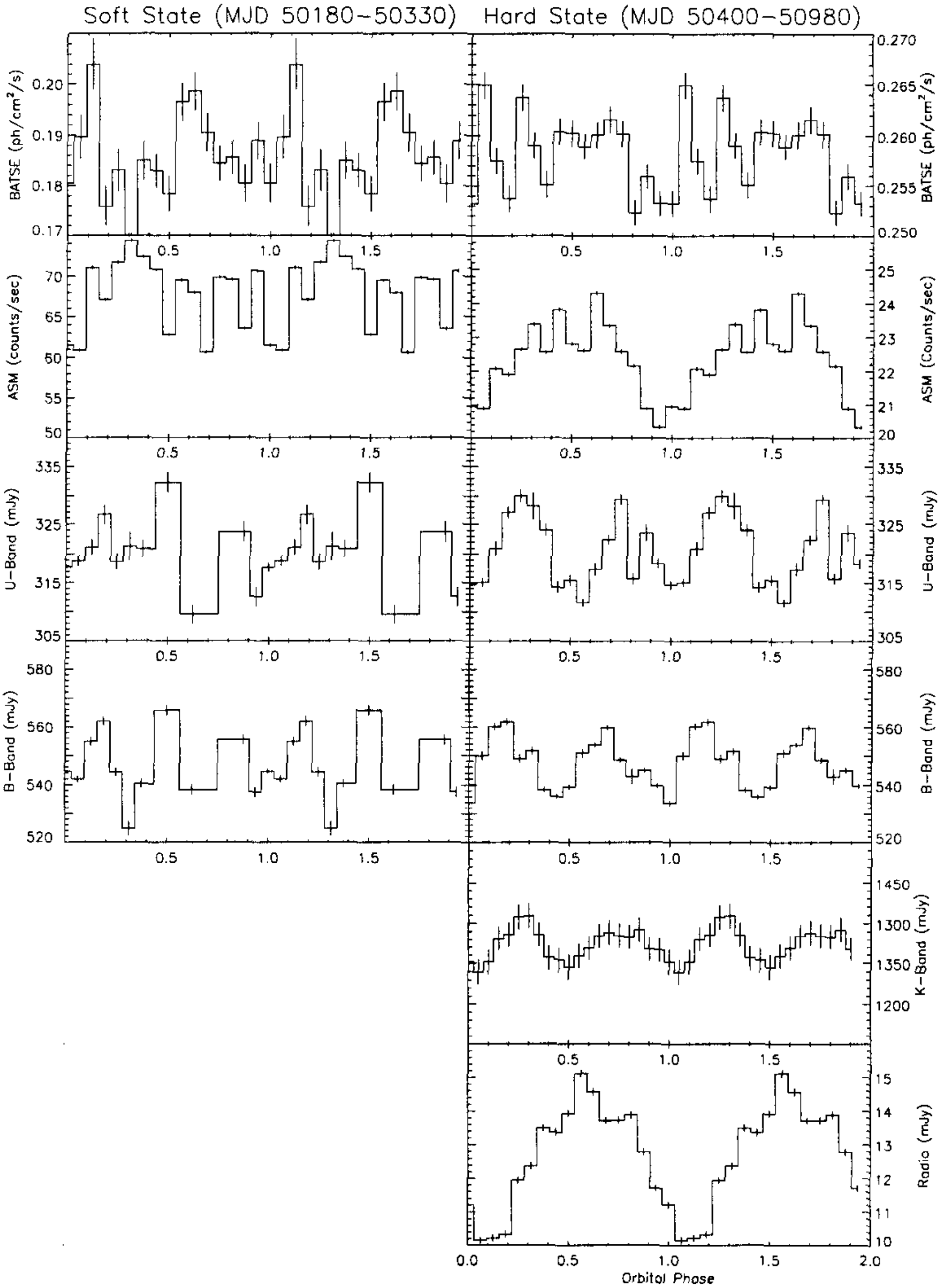

Figure 4.2: Lightcurves folded onto the 5.6 day orbital period. Plots on the left correspond to the soft X-ray outburst of May–August 1996. Plots on the right correspond to the return to the low/hard state; flares have been removed prior to folding. BATSE is at the top, then ASM, *U*, *B*, *K* and radio. (We only have sufficient *K* band and radio monitoring during the hard state)

are shown in Fig. 4.2.

The low/hard state

We now find that, during the low/hard state, the orbital modulation is much more apparent in the optical (as found by Voloshina, Lyuty & Tarasov 1997) and the soft X-ray (this was also found by Cui, Chen & Zhang 1998). Contrary to this, when the flares/scatter (above $\sim 3\sigma$) have been removed, the BATSE data no longer appears to modulate on the orbital period, despite clearly showing modulated behaviour in Paciesas et al. (1997). This suggests that either the flares occur periodically or some component modulates during the flaring periods. The radio modulation does not change significantly when the flares are removed.

The optical and infrared show the double-peaked ellipsoidal modulation that we would expect from a star with a tidally distorted companion. As we have insufficient infrared data from the time of the 1996 high/soft state we cannot say whether or not the orbital modulation is disrupted. The amplitude of the infrared modulation is comparable with that of Nadzhip et al. (1996) ($\sim 4\%$), not with that of Leahy & Ananth (1992) ($\sim 7\%$).

Pooley, Fender & Brocksopp (1999) discovered that the 15 GHz radio phase is offset from the ASM data by about 0.67 days. This delay was also apparent at other radio frequencies and increased with wavelength. We find that extending the dataset does not dispute this result and also notice that there is a phase difference between the minima of *all* our datasets (R.H.S. of Fig. 4.2) – the optical reaches its minimum at phase zero (by definition) with the X-rays slightly beforehand and the infrared and radio at increasing longer delays. It is not clear exactly where these lags originate but this is probably an optical depth effect – I note that the frequency-dependence is diminished on extending the radio lightcurves further and so it is possible that this effect is not real (see Section 4.4). It is interesting that there is a similar phase delay between the hard and soft X-rays in Cyg X-3 (Matz 1997).

We also fold all of our equivalent width data for Hα and He II λ4686 (Fig. 4.3); errors on each point are $\sim 10\%$. Fitting a double peaked sine wave to the two datasets yields a reduced $\chi^2 \sim 0.07$ for Hα and 0.01 for He II; this suggests that while the apparent structure seen in at least the latter may be real, more accurate error estimation would be appropriate.

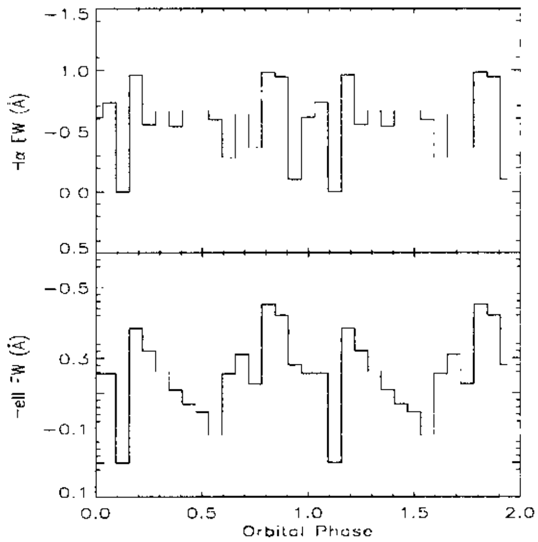

Figure 4.3: All Equivalent width data of Hα and He II folded on the orbital period. Errors ~ 10%.

4.2.2 The Long Term Period

A Lomb–Scargle period search suggests that there is also a period of 142.0 ± 7.1 days present in the 15 GHz radio data (the '150 day period' of Pooley, Fender & Brocksopp 1999) – power spectra have also been computed for the other datasets, including 2.25 and 8.3 GHz radio data from the Green Bank Interferometer, and are shown in Fig. 4.4. The maximum peak in each is indicated (> 95% confidence) and it is clear that this same long period is highly significant at all three radio frequencies and also in the X-rays (note that the X-ray datasets required some averaging in order for PERIOD to read the files – this may have resulted in some artefacts). The orbital period is the dominant peak in the optical dataset.

Folding the data on this 142 day period confirms that it is present at each wavelength (Fig. 4.5) although it is not really a sinusoidal modulation (e.g. fitting a sine wave to the 15 GHz plot yields a reduced χ^2 of 3.7 to > 95% confidence). Comparing the three radio plots shows that this time the amplitude of modulation and the time of phase zero do not show the strong wavelength-dependence exhibited by the orbital modulation. T_0 corresponds to JD2450395.19±3. This period can also be detected in the X-rays and optical; the B band is included in Fig. 4.5 and, while it does not initially appear to show such definite structure, it is only an excess at phase 0.0 that makes this modulation dubious and we find that this excess is due to the flare at ~ MJD50670. Perhaps surprisingly, we find no

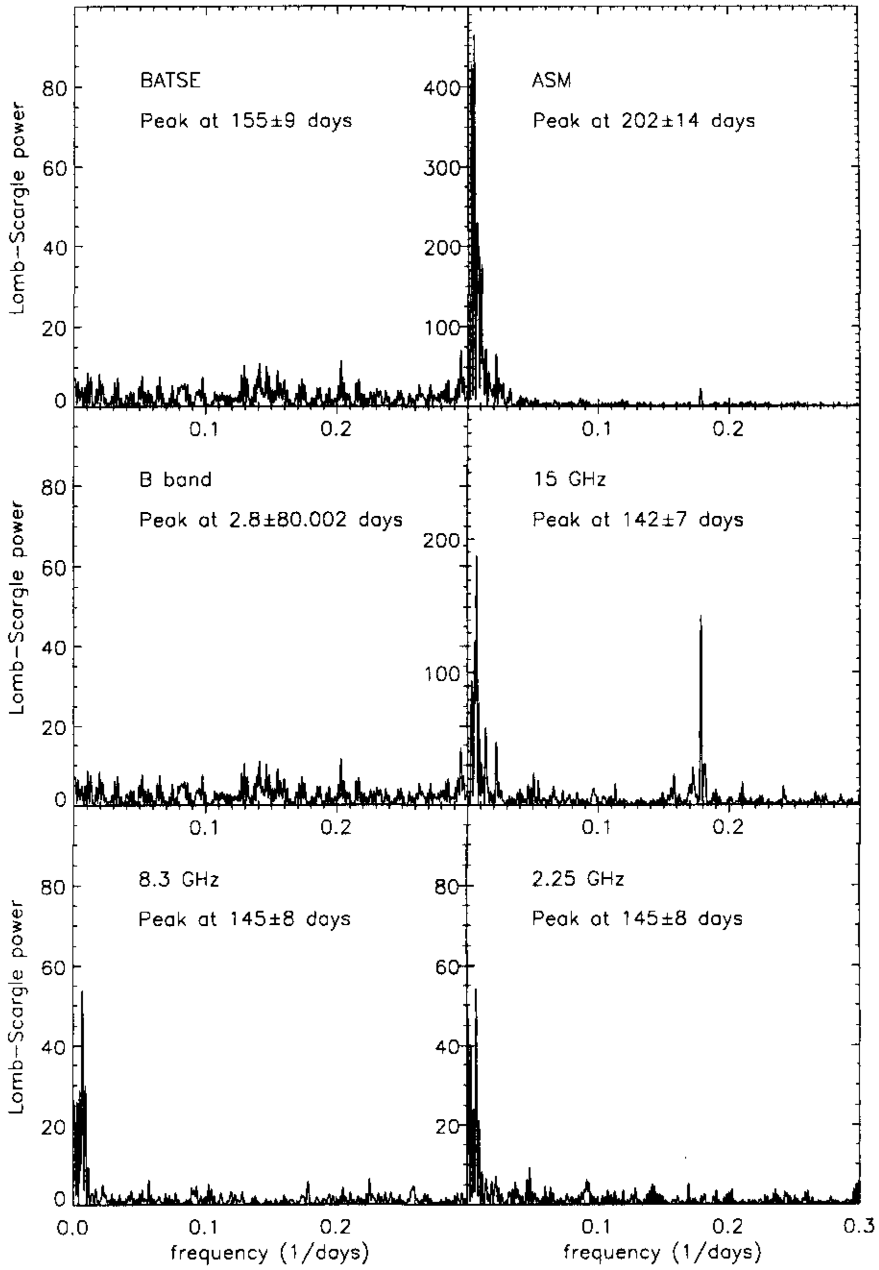

Figure 4.4: X-ray, *B* band photometry and radio (including GBI at 2.25 and 8.3 GHz) Lomb-Scargle power spectra (low/hard state only). 95% confidence maximum peaks are indicated. Note that the long modulation is the dominant peak in the radio data, the orbital period is dominant in the optical.

evidence for the 294 day period found by Priedhorsky, Terrell & Holt (1983) and Kemp et al. (1983, 1987).

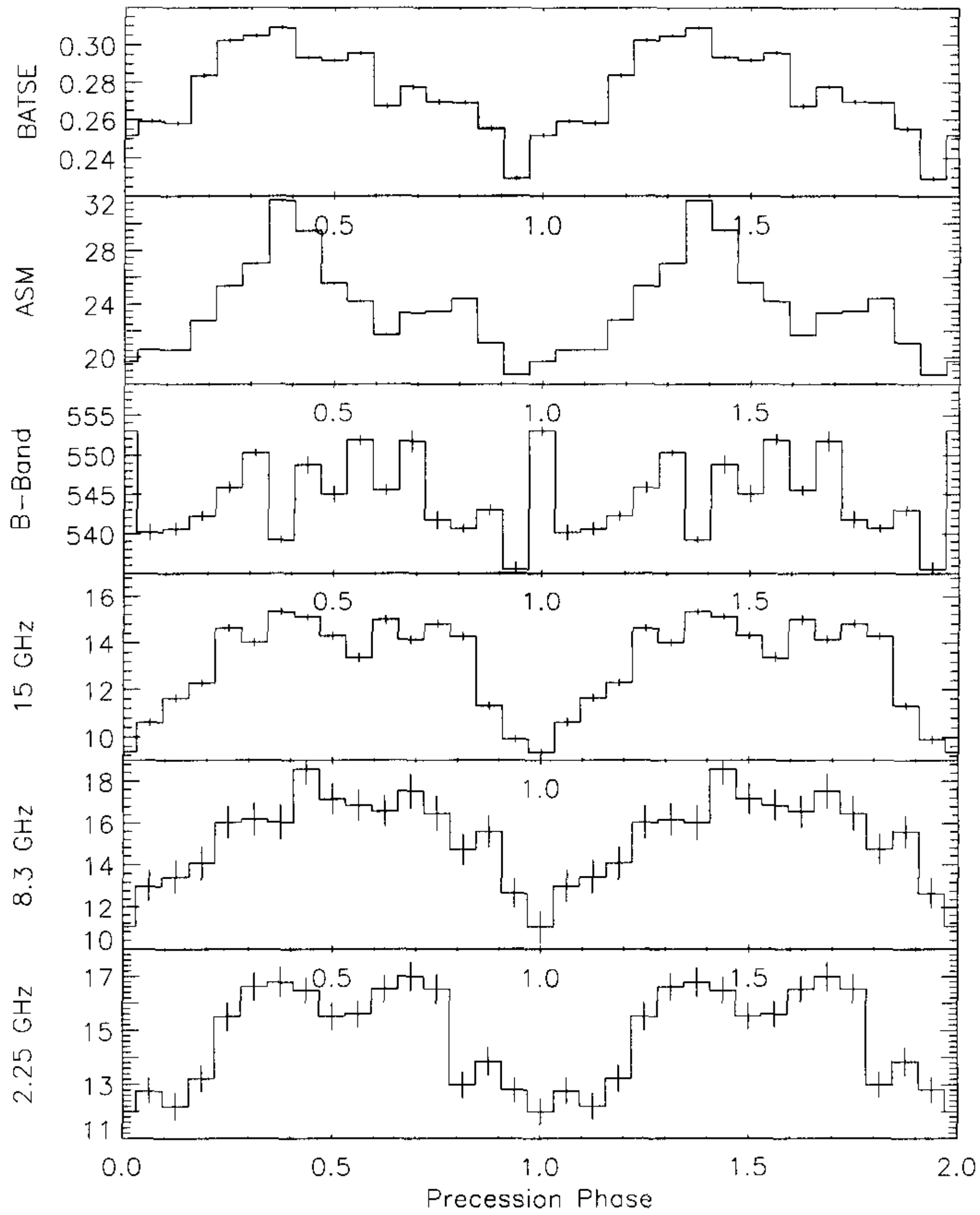

Figure 4.5: X-ray, B band photometry and radio (including GBI at 2.25 and 8.3 GHz) data folded on the 142 day period (low/hard state only). All units are mJy except for BATSE (photon/cm^2/s) and ASM (counts/s)

(N.B. Fig. 4.5 includes data from the hard X-ray state only. We also note that the X-ray flux in Fig. 4.5 appears different from that of Fig. 4.2 (R.H.S.). This is because flares have *not* been removed before folding the data on the 142 day period.)

Bruevich et al. (1978) calculate the disc contribution of the optical luminosity to be $\sim 2\%$ which is equivalent to the apparent modulation of the B Band in Fig. 4.5. We can therefore assume that the 142 day period in the optical is related to the accretion disc, rather than the supergiant.

If we are to assume that the modulation is due to the precession of the accretion disc (as found in other X-ray binaries) then there is no reason to expect the period to remain constant over a decade. This is particularly true for a system accreting via a wind, which has a more variable accretion rate than for Roche lobe overflow. To investigate this further, we have looked at the public access BATSE data from before the 1996 high/state transition. While before this time there was some modulation at 142 days, it was considerably less than since the state change. Incidentally, the 294 day modulation was slightly stronger before the transition but is not present in the last 2.5 years' worth of data. We therefore assume that it is indeed possible for the precession period to change.

However, Larwood (1998) shows that the ratios of the orbital and precessional periods for other X-ray binaries with precessing discs are approximately equal; 294 days is too large for Cyg X-1 to show a similar ratio, whereas 142 days is much more suitable. We use the calculations of Larwood (1998) to calculate the angle, δ between the inclined disc and the orbital plane.

$$\frac{P}{P_p} = \frac{3}{7}\beta^{3/2}\frac{qR^{3/2}\cos\delta}{(1+q)^{1/2}} \tag{4.1}$$

where P is the orbital period, P_p is the precessional period, q is the mass ratio, R is the ratio between the Roche radius and the accretion disc radius and β=β_P=Paczyński's radius (Larwood 1998, Paczyński 1977). R and β_P are given by:

$$R(q) = \frac{0.49}{0.6 + q^{3/2}\ln(1+q^{-1/3})} \tag{4.2}$$

$$\beta_P(q) = \frac{1.4}{1+[\ln(1.8q)]^{0.24}} \tag{4.3}$$

This gives an angle δ=37° between the disc and the orbital plane.

For an accretion disc of area A inclined at angle i, the orbital inclination, the projected area observed is $A\cos i$. When the disc is tilted towards us through angle δ the projected area is increased to $A\cos(i-\delta)$ and the soft X-ray emission will be a maximum. Likewise the soft X-ray emission will be a minimum for a projected area of $A\cos(i+\delta)$.

From Fig. 4.5 the ratio of soft X-ray maximum to minimum emission is ~ 1.62. We use this to deduce that Larwood's model fits our data if we assume $i = 20°$. This is rather low (e.g. Bruevich et. al. (1978) suggest $i = 40 - 60°$, Kemp et al. (1979) $i = 60 - 70°$) and has *enormous* implications for the masses of the two components; it appears that some refinement to the model is necessary.

The radiative warping model of Wijers & Pringle (1998) predicts a long period of 180 days for Cyg X-1. Again, our value of 142 is closer than 294 but it still suggests that some aspect of the model does not fit. This model invokes more parameters which are not well-known, such as viscosity and mass accretion rate rather than just the mass ratio, and so it is not surprising that the predicted and actual values do not agree.

Spectrospcopy

It is perhaps surprising that no evidence for any long period in the spectroscopy has been reported. If we assume that the accretion disc is precessing then we may expect some obscuration of the accretion stream (and hence the emission lines) by the disc. Even if the precession model is incorrect and some variable mass transfer is more appropriate then variability of the emission lines would be expected. We therefore look more closely at the emission line spectra for the presence of a 142 day modulation.

In order to do this the dataset has been extended so as to include additional spectra from 1998 and 1999. Unfortunately we have insufficient He II λ4686 spectra to fully sample the 142 days and so only Hα is considered here, both in terms of equivalent widths and trailed spectrograms. It should be noted that all spectra have been taken by the same telescope and instruments and all equivalent width points have been measured by A.E. Tarasov, thus providing a homogeneous dataset (although admittedly it would have been beneficial to compare results with observations of a standard star to confirm this).

We consider first the complete equivalent width dataset which spans three years. Various methods of period searching were used, including the Lomb–Scargle and CLEAN algorithms and an epoch-folding routine. No conclusive periods were detected.

The equivalent width data were folded on the 142 day period and are shown in the top

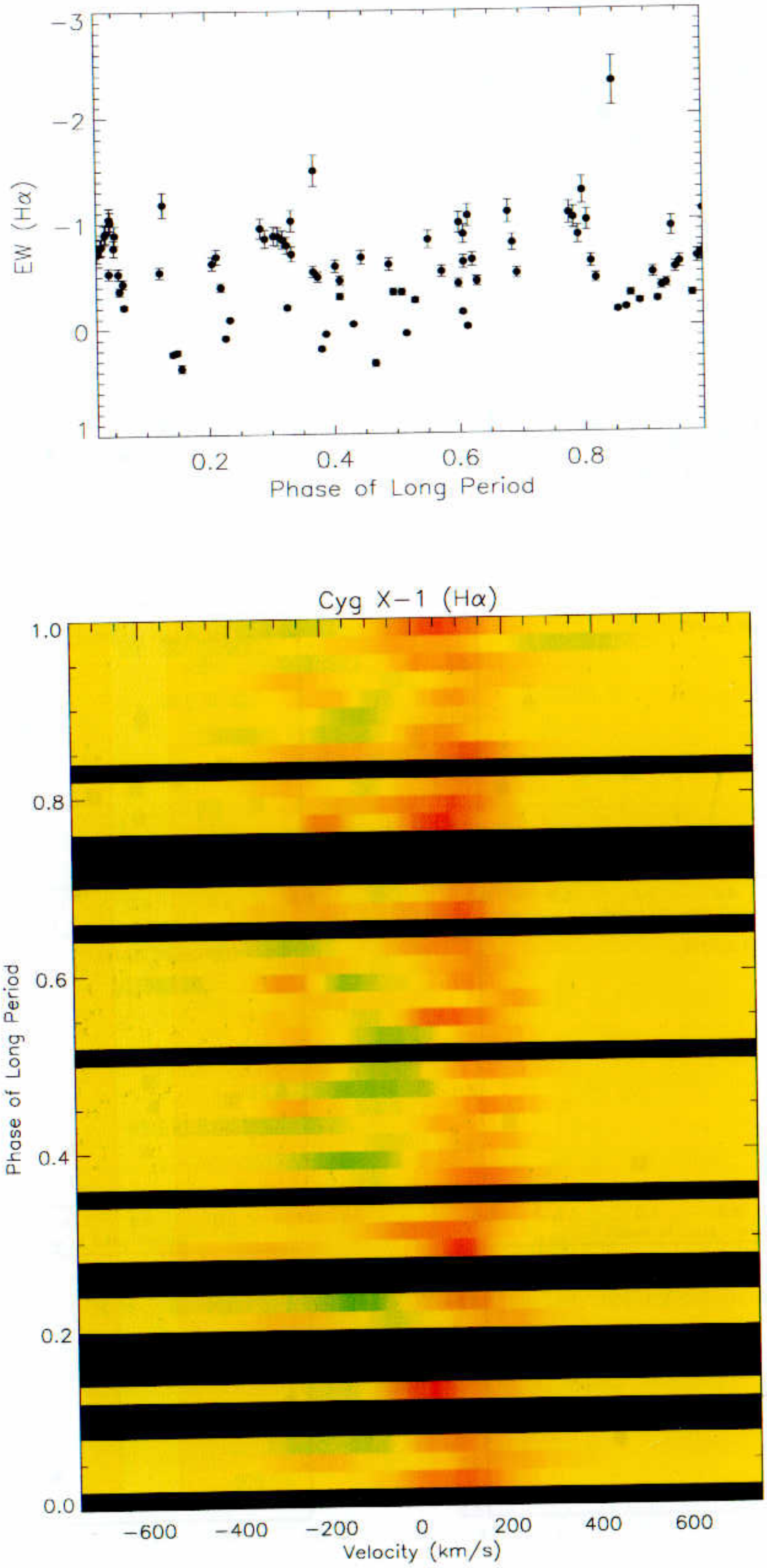

Figure 4.6: Top: Hα equivalent width data folded on the 142 day period and showing no more variability than we might expect from a non-uniform stellar wind. Bottom: Hα trailed spectrogram with spectra positioned at corresponding phases of the long period and showing possible variations in both velocity and intensity around phases 0.4–0.7.

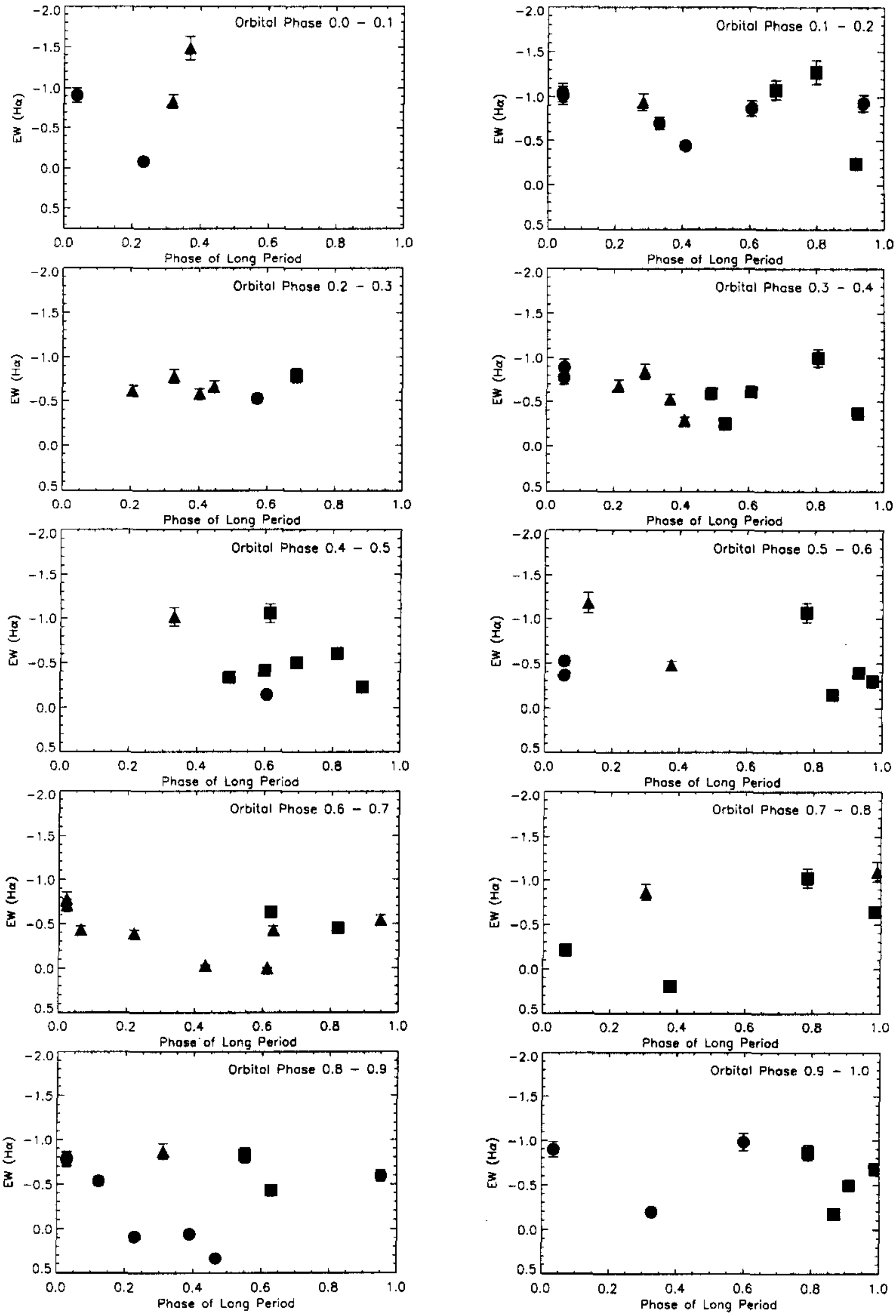

Figure 4.7: Hα equivalent width data split into orbital phase bins and folded on the 142 day period. Most plots appear to be scattered, bearing no relationship to the long period – however, it may be worth considering orbital phases 0.1–0.4 more carefully.

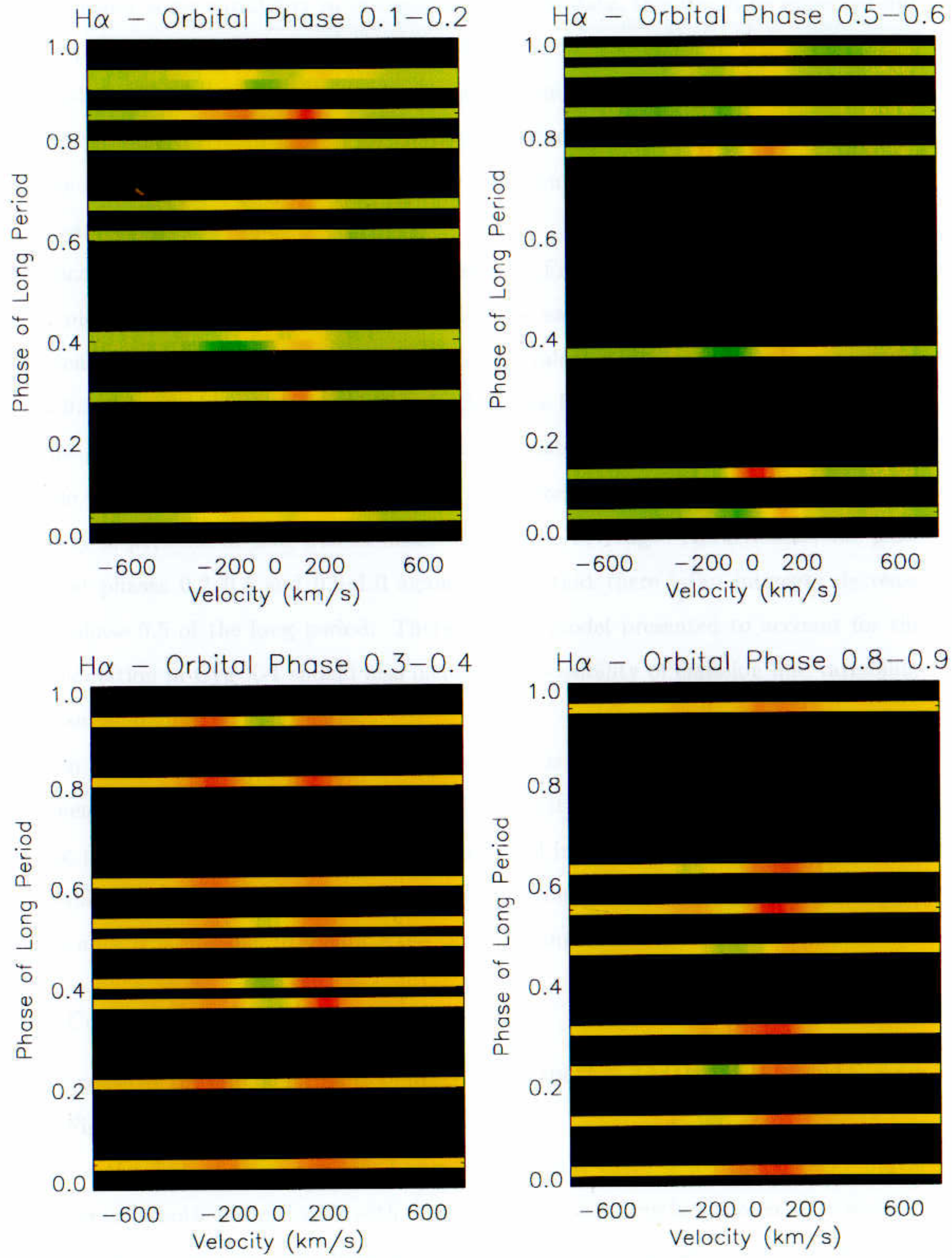

Figure 4.8: Hα trailed spectrograms for specific orbital phases. Spectra are positioned at the corresponding phases of the long period as for Fig. 4.6. Note the very variable behaviour just after the two conjunctions (top two plots) whereas at all intervening phases the profiles are stationary with perhaps a decrease in intensity around phase 0.5 (bottom

part of Fig. 4.6; the spectra are plotted as a trailed spectrogram in the bottom part. While there is clearly some variability in the equivalent width data, this would be expected due to a component of the emission line being produced by the non-uniform stellar wind; there is no evidence for a periodic nature. On the other hand, the trailed spectrogram hints at possible 'periodic' variability, with an increase in velocity and decrease in intensity seen at phase 0.5; alternatively these may just be selection effects determined by the orbital phases sampled at this time.

To account for the orbital variability present in Fig. 4.6, we split the data into ten orbital phase bins and repeat the last two plots for each bin. Again, there seems to be no evidence for any periodic variability in the equivalent width data – although orbital phases 0.1–0.4 may be worth considering further (see Fig. 4.7). Likewise it now appears that the profiles and intensities of the lines are variable across the 142 day period just *after* the two conjunctions (see Fig. 4.8). Unfortunately it is not clear whether the long variability is periodic or not, due to insufficient phase coverage. Nevertheless, the plots at orbital phases 0.2–0.5 and 0.6–1.0 again suggest that there is an intensity decrease around phase 0.5 of the long period. Therefore any model presented to account for the long modulation in Cyg X-1 should also include the possibility of emission line variability at the corresponding orbital phases.

Given the irregular structure of a stellar wind it is likely that variations in the wind components of the emission lines are distorted and so it would be of more benefit to study the long period in the 'pure emission'. As mentioned in the previous chapter, it may not be possible to study the pure emission components (i.e. the part arising in the accretion stream) until it is possible to separate the various components of the lines.

4.2.3 Correlated Flares

We now consider the two larger flares of MJD 50630–50670 and MJD 50980–51080 in more detail (Fig. 4.9).

During the first of these periods it can be seen that there is a pair of X-ray flares, simultaneous in both energy bands with the radio 'flare' occurring in between. (On removal of the orbital period this radio flare is more pronounced). The second flaring period is very different as this time there does not seem to be any obvious correlation between ASM and BATSE. It is clear from Fig. 8.1 that the hard X-ray lightcurve changes very little compared with the ASM and radio, despite some violent activity in the accretion disc. We

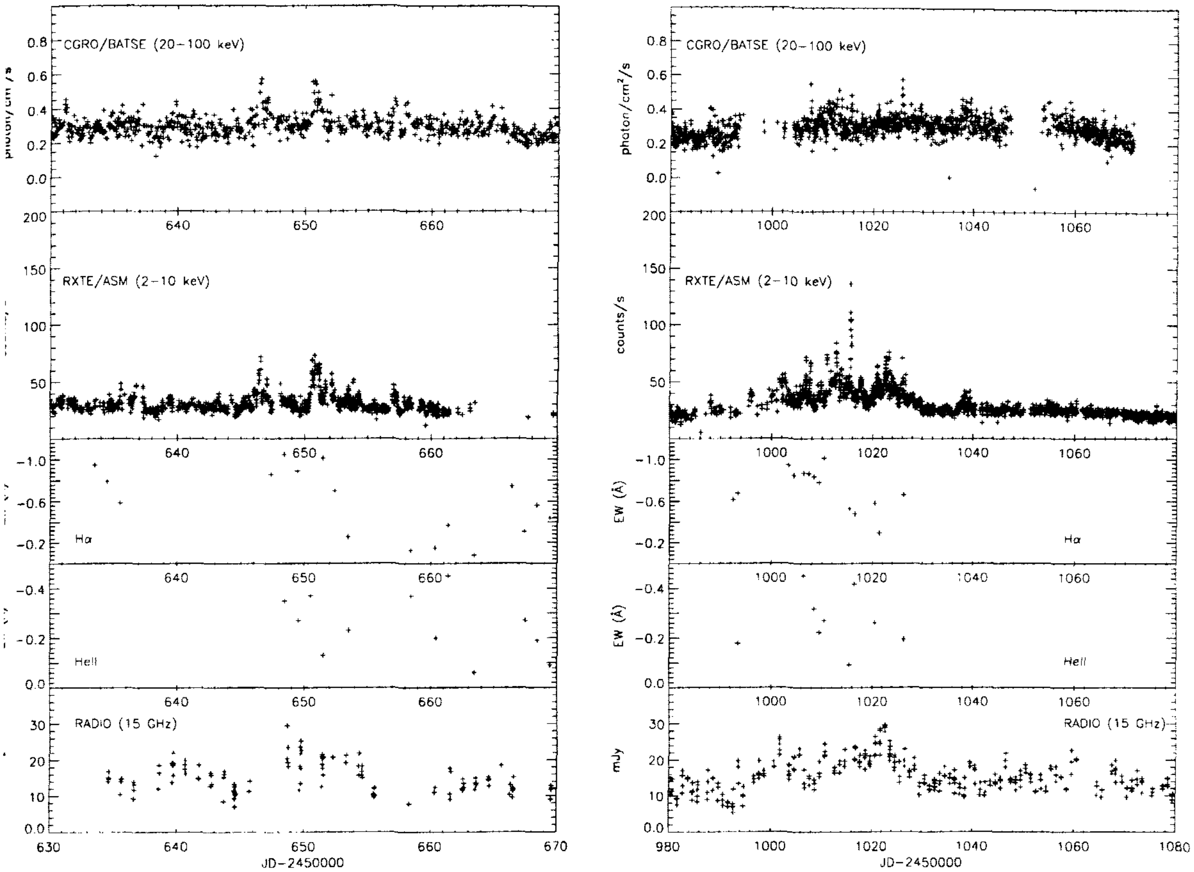

Figure 4.9: X-ray and radio lightcurves and equivalent widths during flare periods MJD 50630–50670 and 50980–51080

also note that the radio is much more active than previously - rather than just a small flux increase it appears to roughly follow the shape of the ASM lightcurve.

Given the strong anti-correlation between ASM and BATSE during a state change and the strong correlation during the first flare, it is possible that in this second flare we are seeing some sort of hybrid between the two. This may have been observed before - Cui, Chen & Zhang (1998) comment on a flare just prior to the state change during which the ASM spectral behaviour was similar to that of the high/soft state, but clearly not a state change. Maybe this flare is also a precursor to a state change, or possibly a 'failed' state change accompanied by a radio flare which may be a typical early signature of a transition to the high/soft state (Zhang et al. 1997).

The equivalent widths do not really show any behaviour related to the accretion disc activity. Both flare periods show a decay in equivalent width for Hα but as single system

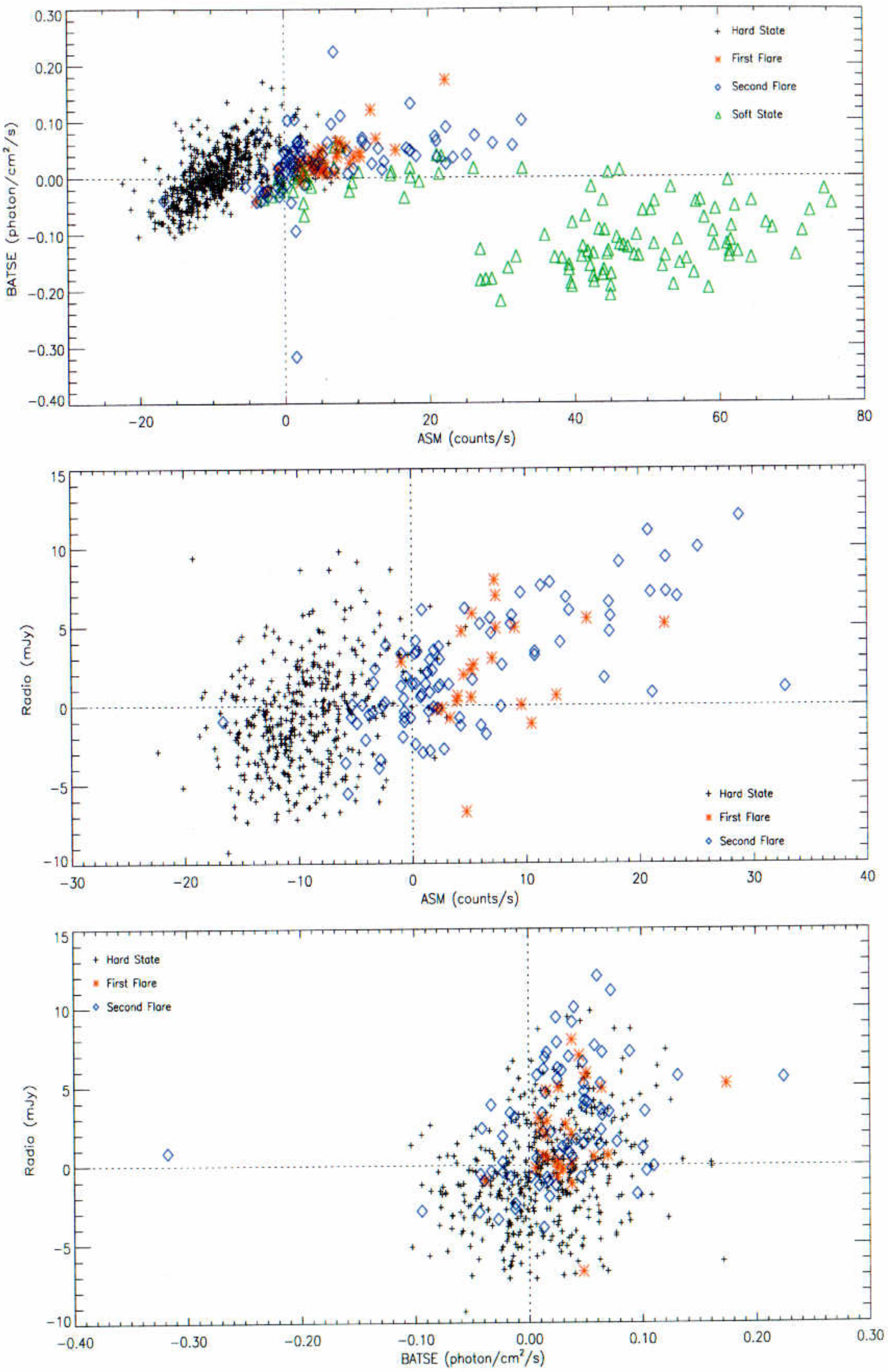

Figure 4.10: X-ray and radio flux-flux plots.

Table 4.2: Spearman rank correlation coefficients (r) of plots in Fig. 4.10. Numbers in brackets following the value of r indicate the number of data points in the sample – thus it can be shown by Student's t test that all correlations in the table have a 99% confidence limit.

	Hard State	Flare 1	Flare 2	Soft State
ASM/BATSE	0.59 (550)	0.83 (36)	0.39 (80)	−0.54 (115)
ASM/Radio	0.30 (402)	0.30 (23)	0.70 (88)	–
BATSE/Radio	0.25 (400)	0.27 (27)	0.31 (77)	–

supergiants also show a similar equivalent width variability it is presumably independent of the X-ray behaviour.

We then generate flux-flux plots for the X-rays and radio. (It is clear from Fig. 8.1 that to plot radio or X-rays against the optical/infrared photometry would yield nothing; this is also the case for the X-ray/equivalent widths). However, flux-flux plots for the optical only show very strong correlations confirming that all bands share a common emission region). To do this we have removed the mean orbital light curves (un-normalized), firstly because we know each data set shows orbital modulation and it is other correlations that we wish to find and secondly because the radio is offset from the X-rays by 0.12 in orbital phase. We note that by removing the mean lightcurve some of the residuals become negative – this is because we have not removed flaring periods prior to subtracting the mean lightcurves. The fluxes were then binned on 1 day and the fluxes of corresponding bins plotted.

Fig. 4.10 shows the three flux-flux plots. Stars and hollow shapes correspond to the different flare/transition periods and the intervening low/hard state in between is shown by crosses.

It is immediately clear that there are a number of correlations. We have already mentioned the anti-correlation between ASM and BATSE when Cyg X-1 is in the high/soft state; this can be seen in the top plot of Fig. 4.10. There is a large amount of scatter due to the variable flaring in the soft X-rays. During the quiescent low/hard state there is a reasonable correlation between the two X-ray bands, although the radio only seems loosely correlated with the X-rays; the possible offset between the radio and X-ray long term period seen in Fig. 4.5 may be adding to the scatter. There is a strong correlation between the two X-ray datasets during the first flare, but again, only scatter in the radio/X-ray plots. Finally, a strong correlation between the radio and soft X-rays can be seen during the second flare.

Spearman rank correlation coefficients (r) have been calculated for each of the sub-plots of Fig. 4.10 and are shown in Table 4.2. r is defined as the ratio of the covariance of the two datasets to the product of their standard deviations and takes values in the range -1.0 – $+1.0$. Most convincing correlations are obtained for hard and soft X-rays during the first flare, high/soft state and quiescent low/hard state and for the soft X-rays and radio during the second flare. We note that a considerably higher value of r can be obtained if we assume that the radio lags the X-rays by 2.5 days, during the first flare only – a value obtained by trial and error. If we are to assume that this lag is real then it would imply that the 15 GHz radio emission becomes optically thin a maximum distance 6.5×10^{13} metres from the X-ray source. However as the only lag apparent in our data is 0.67 days between the radio and X-ray orbital modulation, 2.5 days seems unlikely to be real. r is not improved if we assume this shorter lag, although as the orbital period has been removed prior to creating the flux-flux plots this may be expected.

4.3 Discussion

In summary, we find that the orbital period and also a longer period modulation, probably due to precession of an accretion disc, are present at all wavelengths. We also find that there is correlated behaviour between the radio and X-rays although the nature of this correlation varies from flare to flare. This implies that the X-rays and radio are coupled as expected for a disc/jet system. The optical and infrared do not show any behaviour related to the X-rays or radio and appear to share a separate emitting region.

It is necessary to draw together all of the results obtained for Cyg X-1 and create a consistent model that includes all available data – not just, for example, the X-rays as in the case of some previous works. This model needs to address:

- The orbital modulation across the spectrum during the low/hard state
- The long period (precessional) modulation across the spectrum during the low/hard state
- The lack of optical and soft X-ray orbital modulation during the high/soft state
- Decrease of radio emission during high/soft state
- Existence of correlated flaring behaviour between radio and X-rays

Table 4.3: Summary of the orbital and precessional modulations across the spectrum and their physical interpretations. For BATSE we use the dataset prior to removal of $> 3\sigma$ points.

	% Orbital modulation (Standard error $\times 10$)	Physical interpretation
BATSE 20–100 keV	1.9 (1.0)	Stellar wind absorption
XTE 2–10 keV	9.0 (0.3)	Stellar wind absorption
U (0.36μm)	2.9 (1.4)	Ellipsoidal modulation
B (0.43μm)	2.6 (0.7)	Ellipsoidal modulation
V (0.55μm)	2.4 (0.7)	Ellipsoidal modulation
J (1.25μm)	4.2 (0.3)	Ellipsoidal modulation
H (1.65μm)	5.2 (0.4)	Ellipsoidal modulation
K (2.20μm)	2.5 (0.2)	Ellipsoidal modulation
RT (15 GHz)	19.4 (1.2)	Stellar wind absorption
GBI (8.3 GHz)	17.6 (0.1)	Stellar wind absorption
GBI (2.3 GHz)	6.8 (13.4)	Stellar wind absorption

	% Precessional modulation (Standard error $\times 10^3$)	Physical interpretation
BATSE 20–100 keV	18.0 (0.1)	Precession of disc/jet
XTE 2–10 keV	25.8 (0.2)	Precession of disc
U (0.36μm)	2.6 (15.1)	Precession of disc ?
B (0.43μm)	1.5 (2.6)	
V (0.55μm)	2.1 (7.0)	
J (1.25μm)	?	
H (1.65μm)	?	
K (2.20μm)	?	
RT (15 GHz)	23.9 (8.3)	Beaming/projection of jet
GBI (8.3 GHz)	25.7 (41.0)	Beaming/projection of jet
GBI (2.3 GHz)	17.2 (40.0)	Beaming/projection of jet

- The occasional lack of correlation between hard and soft X-rays
- The general lack of non-modulated variability in the optical and infrared lightcurves, other than occasional flares which appear unrelated to X-ray behaviour

The details of the periodic behaviour of Cyg X-1 are summarised in Table 4.3. The percentage modulations are calculated using the formula

$$\frac{(max - min)}{(max + min)} \times 100$$

The orbital modulation of the optical and infrared is due to the ellipsoidal shape of the supergiant, both due to distortion of the star itself and due to the shape of the focussed stellar wind. In the case of the radio and X-rays, the frequency-dependent phase lags and degree of modulation suggests line-of-sight absorption by the wind to be responsible. Stellar wind absorption could not account for the long-period variability, particularly as the degree of modulation does not vary with frequency, and so precession and/or radiative warping of the accretion disc seems the most likely cause. This is supported by our calculations in Section 4.2.2.

To account for both periods we adopt the conical jet model of Hjellming & Johnston (1988) for the radio emission (detailed radio modelling will be presented in a later paper). The production of continuous synchrotron emission requires a continuous flow of relativistic electrons and magnetic field from the accretion disc. We therefore find it extremely unlikely that this could occur throughout the proposed corona that is currently the only accepted model for the X-rays. A collimated jet is much more feasible and we see no reason why the hard X-rays are not emitted from the base of this jet, produced when seed photons from the accretion disc are up-scattered as previously suggested. The jet model is also supported by VLBA images at 8 and 15 GHz (Fig. 2.7, Stirling et al. (1998, 2000 in prep.).

The apparent precession of the X-rays questions previous models of Cyg X-1. While an optically thick corona could precess with the accretion disc providing it had some non-uniform geometry, it is generally accepted that the corona is optically thin (e.g. Cui et al. 1997). In this case the corona would not precess with the disc unless it was a very thin layer *just* above and below the disc, and therefore the BATSE modulation should be comparable with that of ASM. This is not so and it can be seen in Table 4.3 that the BATSE modulation is considerably less than that of ASM; in fact it is more comparable with that of the radio. This suggests that the jet may be responsible for the production

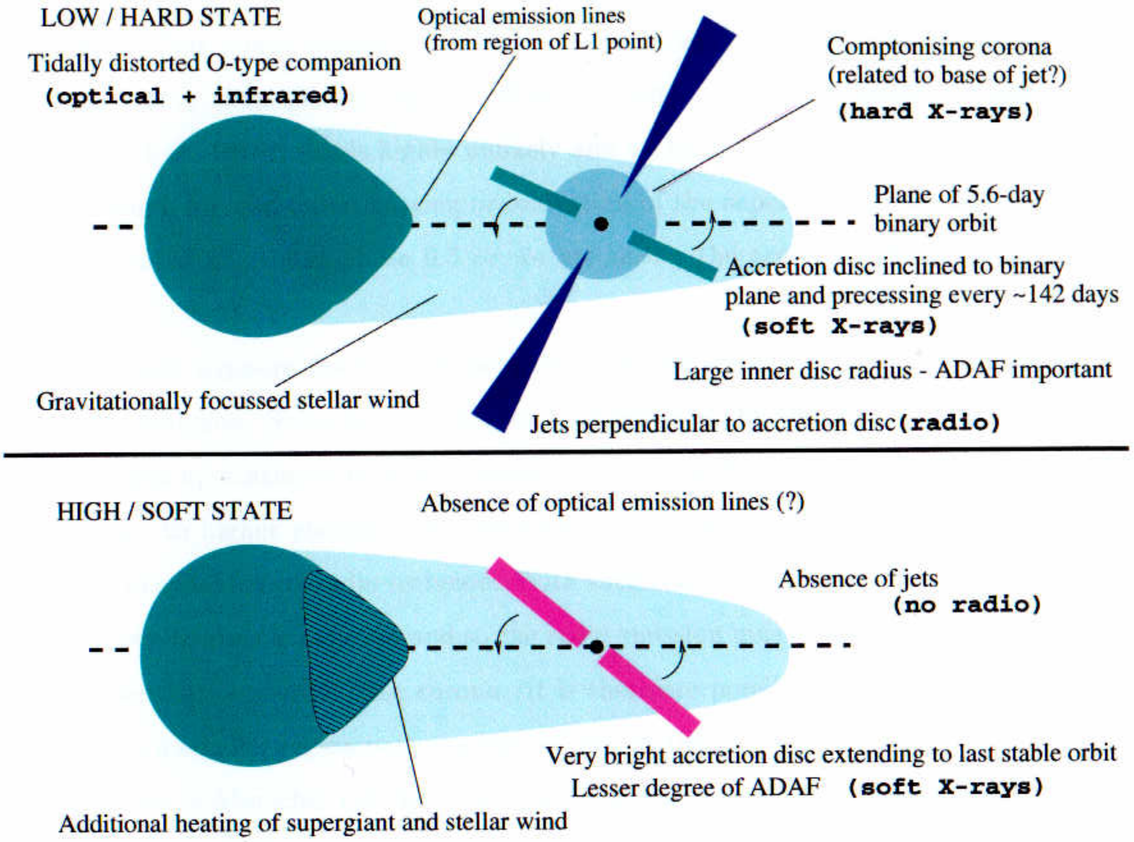

Figure 4.11: Schematic showing the emission regions of Cyg X-1 during the hard and soft X-ray states.

of the hard X-rays. Likewise if, as predicted, the low/hard state is explained by an optically thin advection dominated accretion flow (ADAF) then neither should the soft X-rays display the precession modulation. Therefore, *either* the soft X-ray flux during the low/hard state does not entirely come from an optically thin ADAF *or* we must assume a radiatively-driven warp model. Radiation warping could cause the disc to become flared and so partial eclipses would produce the modulation. However, we feel that the Wijers & Pringle (1998) model is not able to fit our data quantitatively and some further refinements are necessary.

The increased mass flow during the high/soft state results in soft X-ray flaring of a magnitude much greater than the amplitude due to the orbital variability which is why this modulation appears to disappear. The lack of orbital modulation in the optical at this time is not so easily explained. Voloshina, Lyuty & Tarasov (1997) discovered that the orbital modulation does not 'disappear' but becomes single peaked with a maximum occurring at the same phase as the X-rays, rather than the standard double peaked ellipsoidal variability. This might suggest that, during this period, the luminosity of the accretion disc was higher than the supergiant. However, with a disc contribution of only $\sim 2\%$ (Bruevich et al. 1978), this is highly unlikely and we think that either the accretion disc is bright enough for additional heating or ionization of the supergiant to become significant and observable at orbital phase 0.5 or we are seeing the accretion stream from the L1 point.

Our results support the theories in which free-free emission in the disc produces the soft X-ray emission. Some of these X-rays (and perhaps also lower energy photons in the disc) are then up-scattered by a hot corona either side of the disc, via the inverse Compton mechanism, to higher energies. Acceleration of disc electrons along magnetic field lines gives rise to synchrotron radio emission. With such constant radio flux levels, a continuous injection of electrons is required and so the radio emission must be coming from collimated jets, rather than a more diffuse corona. It is therefore possible that the hard X-ray flux comes from a smaller region near the base of the jet than thought previously. We also use the equations of Marscher (1983) to calculate that the contribution to the hard X-ray flux of synchrotron self-Compton scattering by the jet is probably negligible ($<< 1\%$).

The different types of correlated and anti-correlated behaviour can be explained in terms of different events taking place within the system. It appears that small flares occurring in the X-rays and radio are a result of slightly increased mass flow. Transitions to the high/soft state also involve increased mass flow but, in addition, the inner disc radius decreases considerably and a lesser degree of advection takes place. Where there appears to be no correlation or anti-correlation between the hard and soft X-rays it is possible that we have a 'failed' state change; indeed, we find spectral softening in both ASM and BATSE data at the time of this second flare. Although the radio states are generally thought to be anti-correlated with the soft X-rays, it seems that the *transitions* from one state to another are accompanied by radio flares which may explain the relatively strong radio flux at this time.

The apparent lack of correlation between the photometry and the X-rays during the low/hard state is not surprising as the supergiant is so bright that any additional luminosity due to irradiation is negligible. Indeed, we show in Brocksopp et al. (1999) and Lyuty et al. (2000 in prep.) that the small deviations from orbital modulation are a result of the wind, although we have shown in Section 4.2.2 that there is also a small contribution from the accretion disc.

In drawing everything together we find that previous models need slight alterations to explain all of our results. Fig. 4.11 shows a schematic of Cyg X-1 which tries to include all information obtained about the system.

During the low/hard state optical and infrared emission is dominated by that of the stellar wind of the supergiant. In particular, the two emission lines Hα and He II λ4686 are produced in the accretion stream, near the L1 point. At this time, the soft X-ray emitting accretion disc has a large inner radius and advection dominated flow. It is inclined to the orbital plane of the system and precesses with a period of ~142 days by means of a radiation-driven mechanism. Small radio jets are emitted from the centre of the disc and precess with it. Hard X-rays are emitted as the result of upscattering of the soft X-ray photons to higher energies by a small corona at the base of the jet.

When Cyg X-1 enters the less common soft X-ray state the accretion disc extends much further towards the black hole and the ADAF is restricted to the corona (Esin et al. 1998). Increased activity in the disc causes additional heating and ionization of the stellar wind, resulting in a loss of the Hα emission line. The jets and corona disappear, presumably disrupted by either the inner edge of the accretion disc or the heated stellar wind and the material advected into the black hole.

4.4 The Radio Orbital Modulation

Detecting the orbital period of black hole X-ray binaries in optical and infrared photometry is a standard procedure and double-peaked orbital lightcurves, due to the gravitational pull on the star by the black hole, are expected – minima occur in the lightcurves at the two conjunctions. However, it is not so common to detect the orbital period in X-ray or radio data – in the previous section (and Brocksopp et al. 1999) we postulate that these modulations could be the result of phase dependent absorption by the stellar wind. Since the publication of Brocksopp et al. 1999, Wen et al. 1999 have studied the orbital modulation of the *RXTE* soft X-ray data and their model of wind absorption is relatively successful (see Fig. 4.12). The X-ray orbital lightcurves have also been studied by Balucińska-Church et al. (2000) who found that the duration and phase of the minima are also variable and likely to be due to 'clumpiness' in the stellar wind.

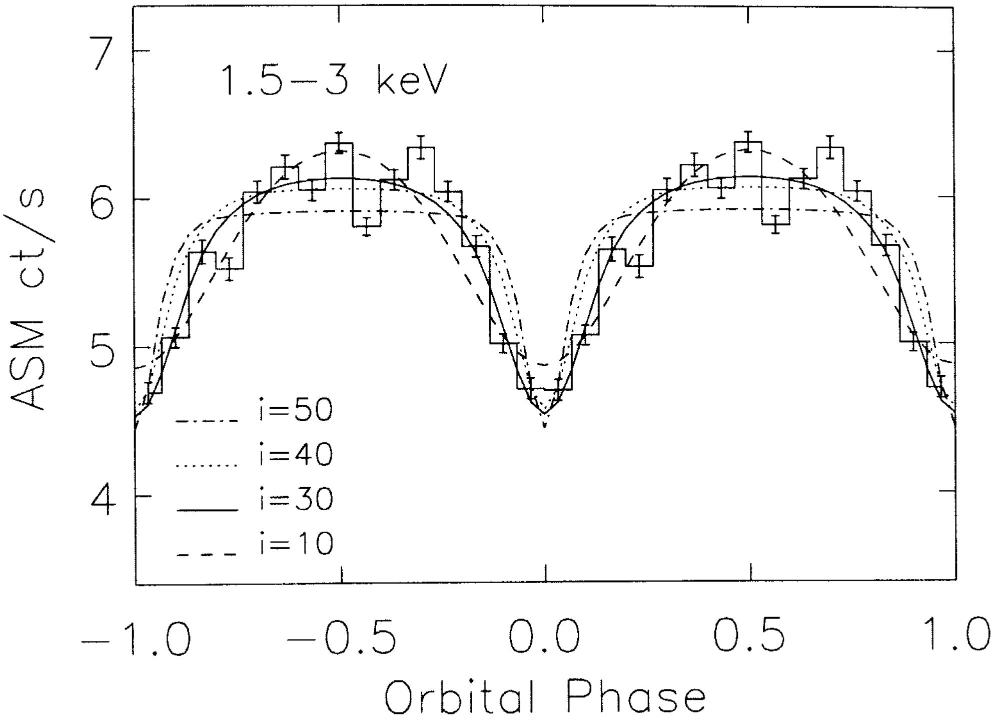

Figure 4.12: Soft X-ray lightcurve folded on the orbital period and overplotted with model curves for various inclination angles (from Wen et al. 2000).

I consider now the radio lightcurve and the possibility that it too undergoes phase dependent absorption. For the initial construction of the model I use 15 GHz data from the Ryle Telescope, Cambridge – most of which was used in the previous section, although the lightcurve has been extended – and data at 8.3 and 2.25 GHz from the Greenbank Interferometer. However, it is hoped that the model will eventually be able to cope with any frequency emitted in the jets. Flares have been removed from the lightcurves. All parameter symbols and their values are summarised in Table 4.4.

4.4.1 The Model

In Pooley, Fender & Brocksopp (1998) it was discovered that the radio emission of Cyg X-1 was modulated on the orbital period with an amplitude that, perhaps surprisingly, increased with the frequency of the emission; not what we would expect for a typical free-free absorption law. This indicates, firstly that the density of the wind cannot be treated as constant along the line of sight – indeed, there is *no* stellar wind model which considers

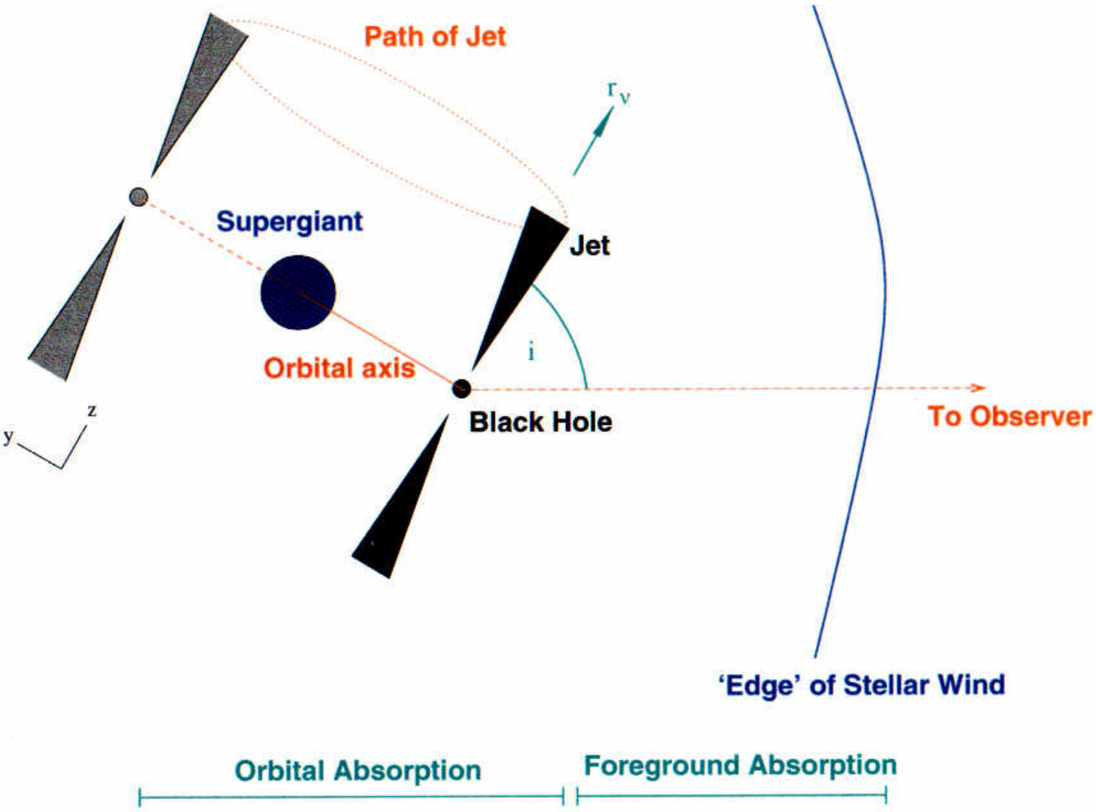

Figure 4.13: Schematic showing the Cyg X-1 system as considered in this simple model for the radio modulation.

the wind density to be constant – and secondly that the optical depth along the jet is not constant.

The work of Leitherer, Chapman & Koribalski (1995, and references within) was used to determine the (frequency dependent) radius from the supergiant at which the stellar wind becomes optically thin to free-free absorption of radio emission:

$$W_\nu = 4.0 \times 10^{17} T^{-1/2} (\gamma g_\nu)^{1/3} \left(\frac{\dot{M} z}{\mu v_\infty \nu} \right)^{2/3} \text{ cm} \tag{4.4}$$

The resultant values of W_ν are listed in Table 4.4.

It can be seen in Table 4.4 that the stellar wind remains optically thick a significant distance outside the binary orbit at all three frequencies considered here. It is therefore important to consider two different absorption components – the first as the jet moves around the binary orbit (which provides the modulation), and a second caused by absorption in the foreground between the orbit and the wind radius (which lowers the flux by a

Table 4.4: Parameters used in construction of a simple model to explain the orbital modulation in the radio emission of Cyg X-1. Where three values are given they correspond to frequencies 2.25, 8.3 and 15 GHz respectively. References: 1. Gies & Bolton (1986), 2. Gies & Bolton (1986a), 3. Friend & Castor (1982), 4. Leitherer, Chapman & Koribalski (1995)

Parameter	**Symbol**	**Value**
Observed flux	S_ν	see text
Intrinsic flux	S_0	see text
Frequency	ν	2.25, 8.3, 15 GHz
Distance to system	D	2.5 kpc
[1]Orbital inclination	i	30°
[1]Orbital separation†	d	3.3×10^{12} cm
[2]Radius of star	r^*	1.387×10^{12} cm
[2]Initial wind density	ρ_o	3.72×10^{-14} g/cm^3
[2]Power index	α	1.05
[3]Temperature of star/wind	T	30 000 K
[3]Mass transfer rate	$\dot{M}$	2.0×10^{-6} M$_\odot$/yr
[2]Wind velocity	v_∞	1580 km/s
[4]Wind radius (Eq. 4.4)	W_ν	20, 8.2, 5.4 $\times 10^{13}$ cm
Distance from centre of star	R	$0 - W_\nu$
Wind density	ρ_ϕ,ρ_f	see text
Distance from BH to site of radio emission	r_ν	20, 8.2, 2.8 $\times 10^{13}$ cm
Optical depth	τ_ϕ,τ_f	see text
Absorption coefficient	κ_ϕ,κ_f	see text
Absorption correction	A_ν	see text
[4]Gaunt factor*	g_ν	6.4, 5.7, 5.4
Mass of proton/electron	m_i,m_e	1.67×10^{-24} g, 9.11×10^{-28} g
Ionic charge	z	1
Gaunt factor	$\bar{g}_{ff}$	(assume) ~ 1
No. electrons/ion	γ	1
Mean molecular weight	μ	1

†$d = d_1 \sin i(1+q)/q$, $q = 0.487$

*$g_\nu = 9.77(1 + 0.13 \log(T^{3/2}/z\nu))$

constant amount).

We assume that the radio emission is absorbed by the wind via the free-free mechanism:

$$\kappa = 0.018T^{-3/2}z^2 n_e n_i \nu^{-2}\bar{g}_{ff} = 3.46 \times 10^{-19}\nu^{-2}\frac{\rho^2}{(m_e + m_i)^2} \tag{4.5}$$

Then the observed flux is:

$$S_\nu = S_0 e^{-(\tau_\phi + \tau_f)} = S_0 e^{-\int(\kappa_\phi + \kappa_f)dr} \tag{4.6}$$

The absorption components κ_ϕ and κ_f are determined below:

The orbital absorption

The focussed stellar wind model of Gies & Bolton (1986a) and Friend & Castor (1982) is used. We take Equation 2 of Gies & Bolton (1986a) for the wind density:

$$\rho_\phi = \left(\frac{r^*}{R}\right)^2\left(\frac{\rho_0}{(1 - r^*/R)^\alpha}\right) \tag{4.7}$$

This is substituted into the equation for κ above:

$$\Longrightarrow \kappa_\phi = \frac{6.4 \times 10^{60}R^{-4}\nu^{-2}}{(1 - 1.387 \times 10^{12}R^{-1})^{2.1}} \tag{4.8}$$

The foreground absorption

Once outside the orbit the equation of Gies & Bolton (1986a) is no longer valid however it is sufficient just to consider the stellar wind as a spherical shell expanding at the value of v_∞.

$$\rho_f = \frac{-3\dot{M}}{8\pi v_\infty}(R^{-2} - W_\nu^{-2}) \tag{4.9}$$

Again, this is substituted into the equation for κ above:

$$\Longrightarrow \kappa_f = 2.83 \times 10^{19}\nu^{-2}(R^{-2} - W_\nu^{-2})^2 \tag{4.10}$$

The radio emission is produced at discrete positions along the jet where the distance from the black hole to the emission site is r_ν – observational studies of systems such as GRS 1915+105 (e.g. Mirabel & Rodriguez 1999, see Fig. 1.11) have indicated that the jet becomes optically thin to high frequencies first and therefore a $r_\nu \propto \nu^{-p}$ (p is a positive constant) relationship is appropriate. Indeed, theoretical work by Blandford &

Königl (1979) (see Chapter 1) has predicted that a continuous jet, as seen here, will have $r_\nu \propto \nu^{-1}$ and a flat spectrum (as observed – Fender et al. 2000).

Combining (i) the work of Blandford & Königl (1979), (ii) the 8 and 15 GHz VLBA images of Cyg X-1 (Stirling et al. 2000 in prep., see Chapter 2) and (iii) the observation that the 2.25 GHz is barely modulated and so probably at a comparable radius from the jet as the wind radius, reasonable values of r_ν were estimated for each frequency and can be seen in Table 4.4.

With knowledge of the absorption at each point in the stellar wind and the position of the radio emission site it was possible to integrate along the line of sight from the observer to the jet. This was repeated for 360 positions on the circle traced by the jet in the frame of the binary system. It was assumed that the angle between the line of sight and the circle traced by the jet remained constant and was equivalent to the inclination angle of the binary system. It is also assumed that all radio emission comes from a single jet – Doppler boosting of the approaching jet and Doppler de-boosting of the receding jet lead to significant differences between the observed flux of each and so this is indeed a reasonable assumption.

4.4.2 Results and Discussion

The model, as it stands, does not represent the observation sufficiently well. To create the plots shown in Fig. 4.14 the above expression for κ_ϕ has been multiplied by a factor A_ν, where $A_{15} = 1/8$, $A_{8.3} = 1/2$, $A_{2.25} = 1$. The factors by which the orbital absorption needs to be reduced in order for the model to fit the observations are very significant. Unfortunately, it is most probable that our lack of understanding of the structure of the stellar wind is the primary cause of error in the model. In the region of the black hole the wind is heated to an extreme at which it is totally ionised and, as mentioned in the previous chapter, the region of high ionisation is unable to support the acceleration of the wind. The wind is therefore slowed and becomes optically thin. In the Cyg X-1 system it is unknown to what radius from the black hole the high ionisation region reaches. If it intercepts our line of sight to the radio emission then there will be a region of optically thin wind not accounted for in the model. On the other hand, if there is no point along the line of sight for which the wind is fully ionised then, again, we will have over-estimated the absorption as the wind is assumed to be fully ionised in the above equations for κ. These effects of ionisation are *not* taken into account in the Friend & Castor (1982) model

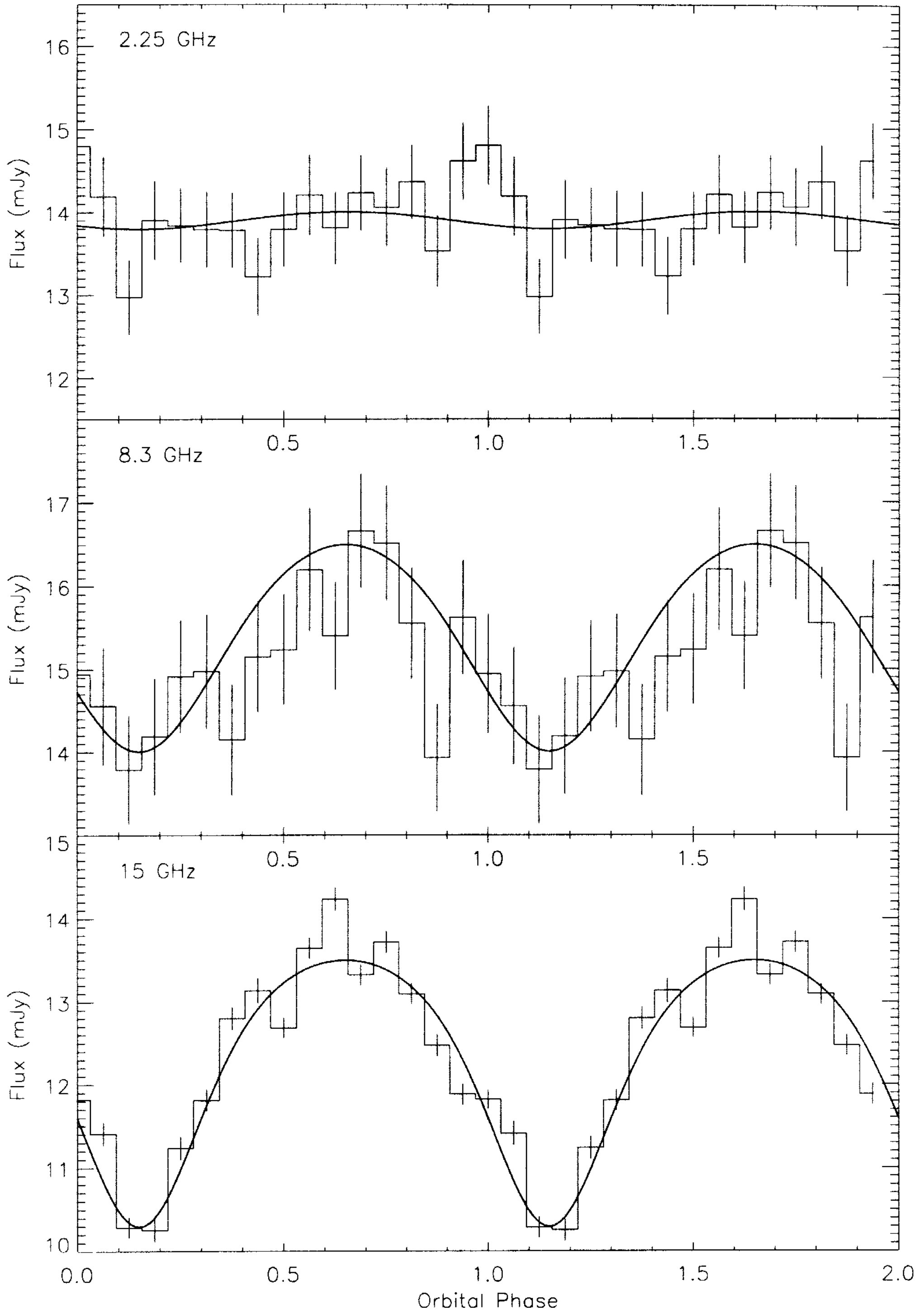

Figure 4.14: The radio data at 2.25, 8.3 and 15 GHz folded on the orbital period. Theroretical curves are also plotted showing that the model fits the data well, once modified in ways mentioned in Section 4.4.2.

for the focussed stellar wind of Cyg X-1. Likewise inhomogeneities in the wind are not included – a constant velocity has been assumed for the wind although it is expected that a line-driven wind is 'clumpy' with different lines accelerating by different amounts.

At all three frequencies the foreground absorption (κ_f) is calculated to be zero – this is indeed possible as the density of the wind beyond the binary orbit is very small (Gies & Bolton 1986a). It appears even more likely as recombination of the ionised wind at large distances from the supergiant has not been taken into account – therefore we might have expected to *over*-estimate κ_f. However *if* the flat spectrum is an intrinsic property of the jet then this should not be the case – i.e. S_0 should be the same for each frequency. Instead the model requires $S_{0,15\mathrm{GHz}} = 13.5$ mJy, $S_{0,8.3\mathrm{GHz}} = 16.5$ mJy, $S_{0,2.25\mathrm{GHz}} = 14$ mJy suggesting that the flux has been subject to frequency dependent foreground absorption. Further investigations should include the possibility of an *observed* flat spectrum that is *not intrinsic* to the system. It should also be noted that, as a result of the low flux of Cyg X-1 in the hard state, the errors of the GBI data are generally of the order 20–40 %. It may be that 3 mJy is an insufficient difference to discount a flat spectrum.

An additional property that is not represented by the model is the phase offset seen in all radio lightcurves – the theoretical curves have been shifted in phase by 0.15 in order to match the obsrvations. While Pooley, Fender & Brocksopp (1999) and Brocksopp et al. (1999) find a frequency dependence to this offset it is not confirmed in the extended datasets used here. However, the offset is still very much present in the mean lightcurves. A possible cause of this could be some sort of drag effect – as the black hole passes through the stellar wind the jets may be 'swept back' and trail behind slightly. Frequencies emitted towards the far end of the jet (i.e. lower frequencies) would then be delayed by a greater amount than frequencies emitted nearer the black hole.

This phase offset can be simply modelled – assuming that the phase delay is dominated by self-absorption of the jet, the jet will lag the black hole by a distance $\frac{r_\nu}{v_{jet}} \times v_{orb}$, where v_{jet} and v_{orb} are the jet and orbital velocities respectively. This corresponds to a phase lag of $\frac{r_\nu}{v_{jet} \times P_{orb}}$ where P_{orb} is the orbital period. By assuming $r_\nu \sim 8.2 \times 10^{13}$ cm then a phase lag of 0.15 could be produced by a jet travelling at $v_{jet} \sim 0.01$c – while this is mildly relativistic, it is probably an underestimate.

As mentioned a number of times previously, the presence of the orbital period in the radio emission is unexpected – indeed the only other systems for which this has been the case are LSI +61°303 and Cir X-1. In both cases the period is much longer than that of Cyg X-1 (26.5 and 16.6 days respectively) and the nature of the radio emission is also very different. Rather than the smooth sinusoid of Cyg X-1, these two sources show periodic radio outbursts thought to be produced at periastron of an eccentric orbit (Taylor & Gregory 1982; Haynes, Lerche & Murdin 1980). Therefore even if the companion stars emit strong stellar winds (as certainly is the case for LSI +61°303), it is unlikely that the wind absorption model can be applied here – it would predict a *minimum* at periastron as this is the point at which the wind is most dense. However, it is interesting to note that the only previous attempt to model the radio modulation of Cyg X-1 is Han (1993). She also invokes an elliptical orbit with an inclined jet – this can be discounted given the lack of evidence for anything other than a circular orbit in optical spectroscopy presented in the literature (see e.g. Chapter 2 and references within).

One important application and test of this absorption model will be the lightcurve prediction of jet emission at other frequencies, in particular the mm and infrared emission close to the black hole. Cyg X-1 has been detected at mm wavelengths but there is insufficient data available to detect any orbital modulation. A comparison of the model and lightcurves at higher frequencies would also be useful in probing the regions of higher ionisation around the black hole.

Chapter 5

INTRODUCTION TO LMC X-3

5.1 Historical Background

Most high X-ray luminosity sources ($> 10^{38}$ ergs/s) in the Galaxy are located in heavily obscured regions, in the disc or towards the Galactic centre. The low obscuration of the Large Magellanic Cloud ($A_V < 1$ mag.; Feast, Thackeray & Wesselink 1960) made it an attractive target for the study of bright X-ray sources.

The three brightest X-ray sources in the LMC were discovered by the *Uhuru* satellite and designated LMC X-1, LMC X-2 and LMC X-3 (Leong et al. 1971). Follow up observations by *Copernicus* and *OSO-7* confirmed (and improved the accuracy of) the positions; variability of the observed flux was also noticed (Rapley & Tuohy 1974, Markert & Clark 1975). Long term X-ray lightcurves were obtained by the *Ariel V* satellite with LMC X-3 being the brightest and most variable of the five sources detected – despite changing by a factor of ~ 10 in intensity, no regular periodicities were found in the 1.5–15 day range (parts of the lightcurve were contaminated with data from other sources which may contribute to this; Griffiths & Seward 1977).

U, *B* and *V* photometry of the three bright LMC X-ray sources was attempted by Warren & Penfold (1975) in order to find an optical counterpart for each one. A faint OB star was found in the LMC X-3 X-ray error box with a B band magnitude of ~ 17 and this seemed a likely candidate – the counterparts to LMC X-1 and LMC X-2 were less conclusive. Spectroscopy of this star by Cowley, Crampton & Hutchings (1978) revealed a blue OB star with strong H absorption lines, weak He I lines, weak Hβ P Cygni emission and no evidence for either absorption or emission at He II λ4686.

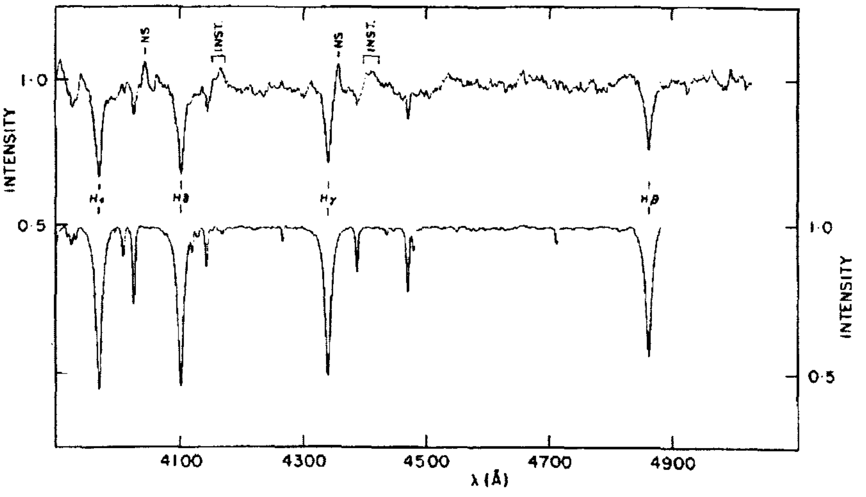

Figure 5.1: The optical spectrum of LMC X-3 (top) compared with the spectrum of a 'normal' B3 star (bottom) in which the absorption lines are much stronger ('NS' and 'INST' refer to night sky and instrumental effects respectively, Cowley et al. 1983).

Johnston et al. (1978) made observations with the, then relatively new, *HEAO* 1 X-ray satellite resulting in vastly improved (by a factor of 8) positions for LMC X-1, LMC X-2 and LMC X-3. The *HEAO* 1 position for LMC X-3 was consistent with the proposed B star optical counterpart, although a second optical star (F type) was found in the error box. Optical spectroscopy revealed a large radial velocity for the B star, confirming that it was indeed a member of the LMC. Further *HEAO* 1 observations confirmed the variable nature of the X-ray source and revealed a series of non-periodic fluctuations on a timescale of hours at its maximum brightness (Johnston, Bradt & Doxsey 1979).

It was not until 1983 that LMC X-3 joined Cyg X-1 as the second known black hole candidate. Cowley et al. (1983) determined an orbital period of 1.7049 days from radial velocity measurements of H and He I absorption lines. They calculated the orbital parameters and, since the orbit of a short period interacting binary should quickly circularise, they considered the eccentricity to be zero. The lack of X-ray eclipses placed an upper limit of 70° on the inclination angle; the rotational velocity of the optical star, assuming synchronous rotation with the orbit, implied a lower limit of 50°. The magnitude and temperature of the optical star suggested a mass range of 4–8 $M_\odot$ – consequently the mass function required the mass of the compact object to be 7–14 $M_\odot$, well above the maximum mass for a neutron star. In this case, however, the mass of the black hole was probably larger than the optical star and also perhaps larger than the black hole in the

Cyg X-1 system.

Cowley et al. (1983) further classified the spectrum of the optical counterpart as that of a B3 V star, although the absorption lines were half as strong as those in a typical B3 star – perhaps due to an additional continuum component associated with the X-ray source (e.g. an accretion disc). Weak Hβ P Cygni profiles were also seen, but not in all observations.

The first theoretical model for LMC X-3 was presented by Paczyński (1983) in order to improve on and simplify the calculations of Cowley et al. (1983). The model took into account the lack of X-ray eclipses and required the optical star to not be larger than its Roche lobe, plus knowledge of the stellar radius. Using the observed binary parameters of Cowley et al. (1983) and a radius of 6 $R_\odot$, a lower limit of 10 $M_\odot$ was obtained. Mazeh et al. (1986) used the subsequent observations of Van der Klis, Tjemkes & Van Paradijs (1983) to show that as there is apparently a contribution to the optical flux from an accretion disc, the radius of the star could be considerably less than that assumed by Paczyński (1983). Using a variety of smaller stellar radii, Mazeh et al. (1986) calculated lower limits to the mass of the black hole (2.2–4.3$M_\odot$) – although they were probably greater than the mass of a neutron star it was decided that the possibility of a 'heavy neutron star' could not be ruled out. Bochkarev et al. (1988) later developed the orbital lightcurve models to allow for the fact that the X-ray emission must be anisotropic – previous models had assumed a spherical X-ray source, i.e. a neutron star. They modelled the optical lightcurve, including an anisotropic X-ray emission source (i.e. a limb-darkened accretion disc) in order to reconfirm the black hole nature of the system and also determined the (unlikely) parameters required for the compact object to be a neutron star. They further suggested observations in the ultra-violet regime, which would reveal fluorescent resonance lines of heavy elements and therefore confirm the presence of a thick disc and its interception of the X-ray emission – this would explain the lack of strong heating of the star.

Attempts to detect a radio counterpart have been made. In a radio survey of supersoft, persistent and transient sources in the Magellanic Clouds, Fender, Southwell & Tzioumis (1998) find that there is no radio source coincident with LMC X-3 above 0.12 mJy. With the whole survey taking place within a twelve hour run and considering that a radio source such as Cyg X-1 placed at the distance of the LMC would have a flux density of $\sim$ 0.05 mJy, this is hardly surprising. The radio counterpart is addressed further in Chapter 7.

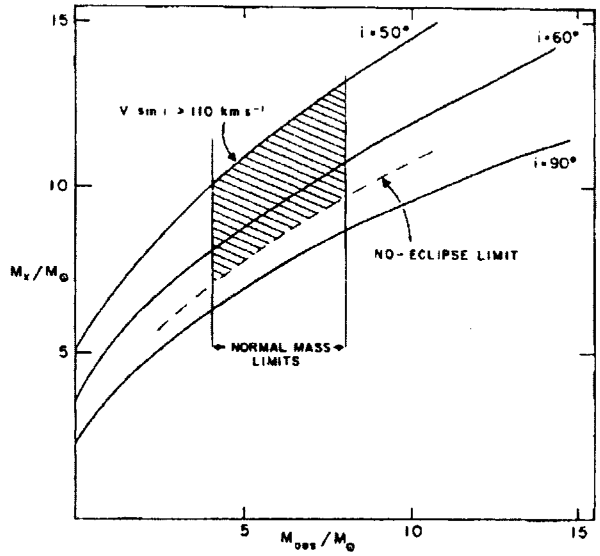

Figure 5.2: The range of permitted masses for the two components of the LMC X-3 binary system (Cowley et al. 1983).

5.2 X-ray Properties

It was surprising that despite being the only two black hole candidates known at the time, LMC X-3 and Cyg X-1 did not seem to show similar X-ray properties (Weisskopf et al. 1983). LMC X-3 displayed a thermal spectrum, *much* softer than the power law spectrum of Cyg X-1, and showed more similarities with most *other* bright X-ray sources. Additionally LMC X-3 did not appear to vary rapidly according to a shot-noise model, as was the case for Cyg X-1 – this was unfortunate as it was thought that aperiodic rapid variability was a signature of accretion onto a black hole and could hence be used in classification. Furthermore, there was no evidence for the orbital period in the X-ray data – whether this was on account of a low inclination angle, lack of partial occultation by a disc or accretion stream, lack of stellar wind to provide orbital absorption effects, the continual soft state nature of the system or a combination was not clear.

The problem was resolved by White & Marshall (1984) who noticed that while LMC X-3 had an unusually soft spectrum compared with X-ray binaries in the low/hard state (e.g. Cyg X-1, GX 339−4), it *was* comparable with the soft state spectra of the same objects – indeed GX 339−4 in the soft state is even softer (Fig. 5.3). They further noted that the rapid variability of Cyg X-1 was *absent* when it was in the soft state. Although the model of accretion onto a black hole via a cool disc (Shakura & Sunyaev 1973) had been modified so as to include a corona (Shapiro, Lightman & Eardley 1976) in order for

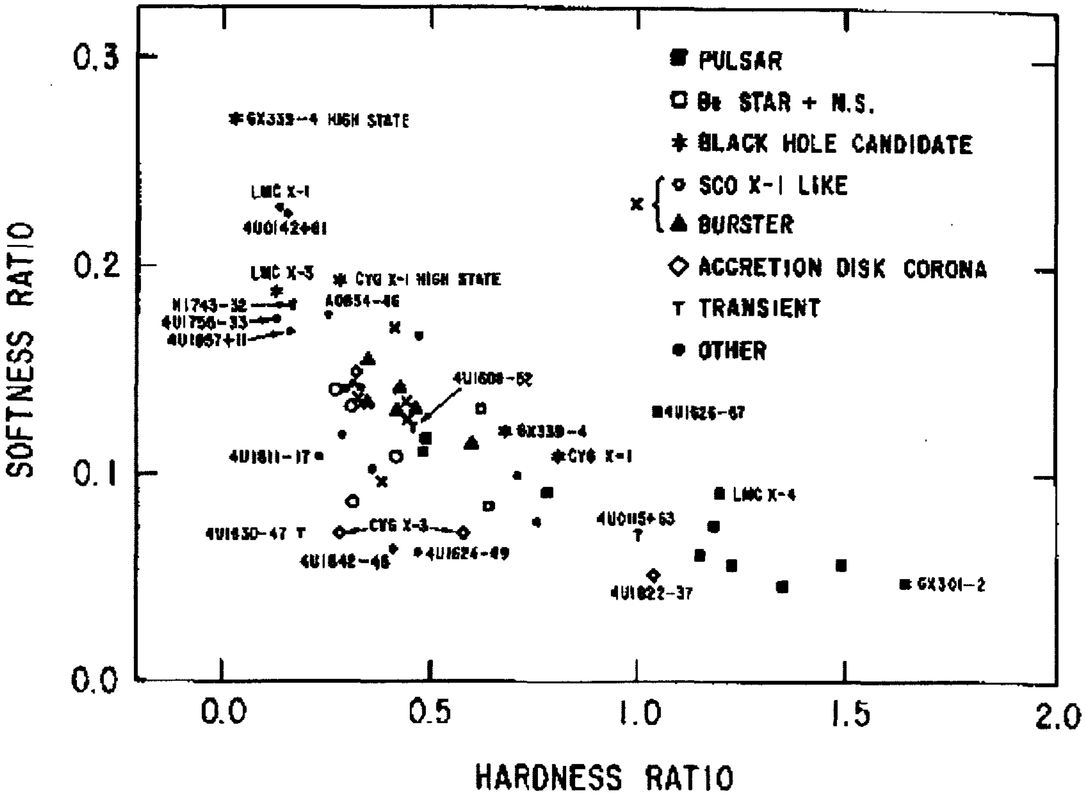

Figure 5.3: X-ray colour-colour diagram showing 55 sources associated with accretion processes. A class of ultra-soft sources, including LMC X-3, seemed to be emerging (White & Marshall 1984).

it to fit the hard state spectrum of Cyg X-1, it was interesting to see that the original model was indeed appropriate for LMC X-3. It therefore seemed as though an accretion disc was present in the system.

LMC X-3 was later observed with *EXOSAT* and the spectrum studied in more detail (Treves et al. 1988) – simple models of thermal bremsstrahlung, a power law or a blackbody did not fit the data sufficiently. A combination of blackbody and thermal bremsstrahlung gave a reasonable χ^2 but unlikely parameters for the corona; a Comptonisation model (after Sunyaev & Titarchuk 1980) also gave a reasonable χ^2 but required a very low temperature and high optical depth, severely constraining the temperature at which the plasma becomes transparent and the possible thickness of the disc. Treves et al. (1990) later used a disc blackbody spectrum (after e.g. Mitsuda et al. 1984, Makishima et al. 1986 – see Chapter 1) for the soft component and an additional power law to explain the spectrum at higher energies – as a single (as opposed to a combination of two different components), more complex model with fewer free parameters, this disc blackbody model was physically more reliable and fit the data equally well.

The nature of the variability of LMC X-3 was finally determined by Cowley et al. (1991), who found a $\sim$ 198 (or perhaps $\sim$ 99) day period in *Ginga* and *HEAO* 1 X-ray data. They also confirmed previous claims that the X-ray hardness and intensity were correlated below 13 keV, although there was no apparent relationship for higher energies.

Cowley et al. (1991) suggested that this long period could be explained in terms of disc precession, changes in the mass transfer rate or a combination of the two. Ebisawa et al. (1993) investigated this further using the same *Ginga* dataset and a 'general relativistic accretion disc' model. They confirmed the work of Treves et al. (1990) in that the spectrum consists of a soft thermal disc component, which hardens as the intensity increases, plus a hard power law from the corona, which is independent of any intensity increase and hence $\dot{M}$. They found that the soft component variability is well-fit by an optically thick accretion disc model with a constant inner disc radius and variable mass transfer rate. The $\sim$ 20 day delay between the X-rays and optical (see below) could then be explained in terms of the disc crossing time.

One peculiar aspect of LMC X-3 (and also LMC X-1) was that it had always been observed in the soft state (as defined by Van der Klis 1995). A three year *RXTE* monitoring campaign by Wilms et al. (2000) finally yielded evidence for hard states, which took place during (some of ?) the minima of the long cycle. Wilms et al. (2000) also noted that the 198 day 'period' was not at all stable during the observations, varying in the range 200–300 days. They fitted the X-ray spectrum with the standard multi-temperature disc blackbody (after e.g. Mitsuda et al. 1984, Makishima et al. 1986 – see Chapter 1) plus a power law at higher energies and compare the fit parameters with the lightcurve. The disc temperature and the photon index showed a clear correlation with the source intensity (Fig. 5.4); furthermore, the spectrum of one of the observations showed no evidence for a disc component and the spectrum of the subsequent observation showed that a transition back to the soft state was taking place (see Fig. 7.6). This was confirmed by Boyd & Smale (2000) who also used a statistical approach to show that there is no long-term periodicity in the *RXTE*/ASM lightcurves but that the times between the minima are related by rational fractions.

As no spectral evolution with source intensity is expected during a precession cycle, these results suggest that the state changes, and hence the long modulations, are caused by a variable mass transfer rate – as seen in Cyg X-1 and other X-ray binary systems in which state changes are observed to take place. While this was first suggested by Ebisawa

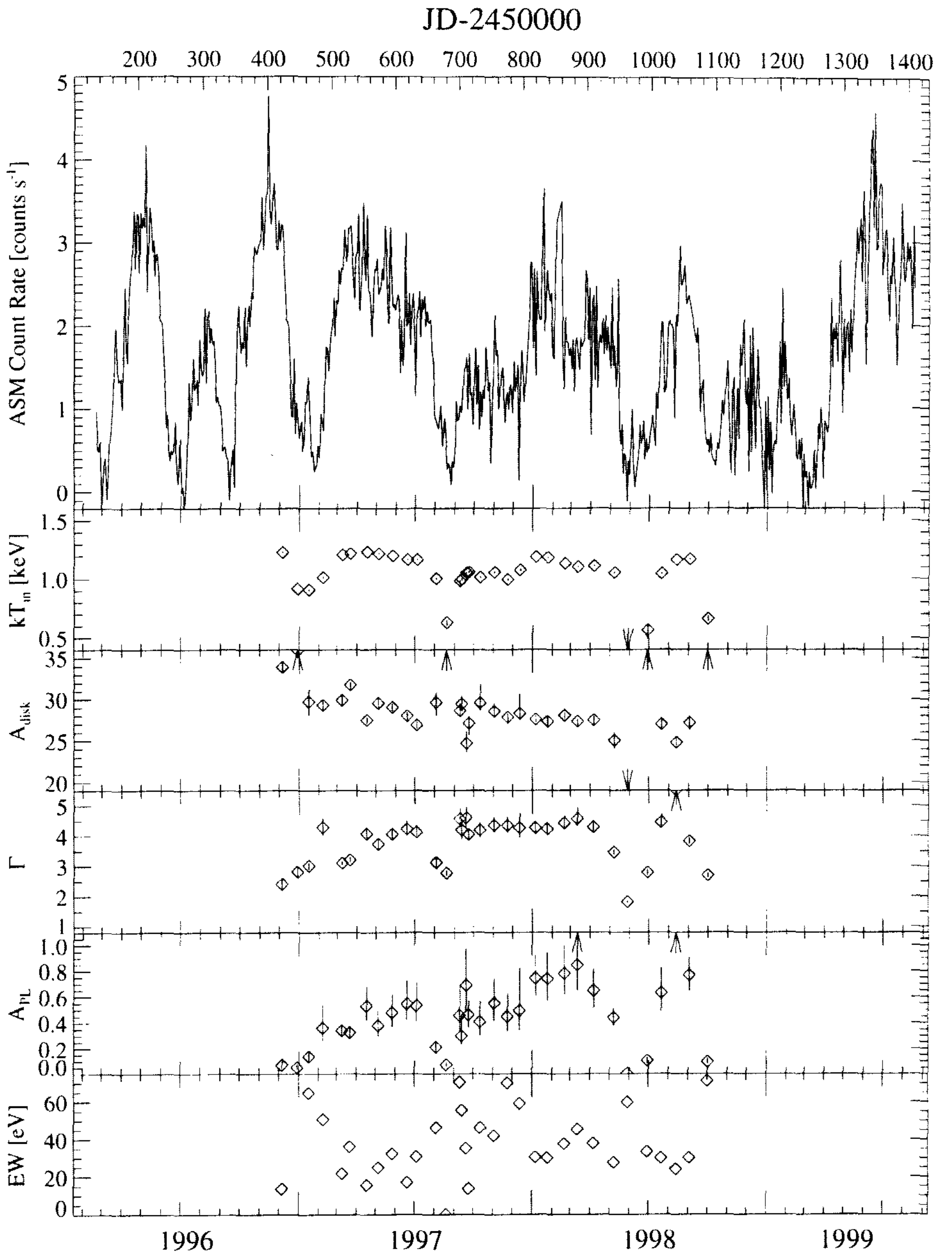

Figure 5.4: The *RXTE* lightcurve of LMC X-3 – correlations between the X-ray flux and the spectral fit parameters can be clearly seen, indicating that the spectrum hardens during the minima (Wilms et al. 2000)

et al. (1993), there seems to be a general assumption within the community that LMC X-3 is a precessing disc source – these results confirm that it probably is not the case. The nature of the modulation of LMC X-3 is investigated further in Chapter 6; a model invoking a wind-driven limit cycle as the cause of the variable mass transfer rate (Shields et al. 1986) is also discussed (at the suggestion of Wilms et al. 2000).

The most recent transition to the hard state was observed again by *RXTE* and the hard spectrum showing no evidence for a disc component was confirmed (Boyd et al. 2000). This was the first time that the full set of hard state properties had been observed in LMC X-3 or in any non-Galactic source – timing analysis revealed a characteristic power spectrum complete with QPO at 0.46 Hz.

5.3 Ultra-violet, Optical and Infrared Properties

Following the discovery of the 1.7 day orbital period in the radial velocity measurements, U, B and V photometry of LMC X-3 was obtained by Van der Klis, Tjemkes & Van Paradijs (1983). Their mean lightcurves showed a minimum at phase 0.5 and, with the addition of the 1974 data from Cowley et al. (1983) a minimum at phase 0.0 was also revealed. Ellipsoidal variations were present, as in the case of Cyg X-1. The scatter about a sine wave was large and it was found that each group of data had a significantly different (≤ 0.5 mags.) mean magnitude. They therefore subtracted the mean magnitude from each dataset to confirm the orbital period in the photometry, although the new measurements were shifted 0.1 in phase with respect to the previous ones. The authors suggested that this apparent long term variation could be the result of intrinsic changes in the star, similar to those observed in Be stars, or the precession of an accretion disc.

Khruzina & Cherepashchuk (1984) modelled the photometric lightcurves in terms of ellipsoidality, X-ray heating and eclipsing of the star by the accretion disc (and vice versa). They considered both isotropic and anisotropic X-ray sources and found that, regardless of model used, the mass of the compact object did indeed point to a black hole nature.

Further V band (and some B band) observations were made to a much greater accuracy with a CCD camera (Van der Klis et al. 1985); although they were unable to achieve full phase coverage, the resultant orbital lightcurve contained significantly less scatter than previously. They obtained a more accurate ephemeris, although it depended on the lightcurve being symmetric – only the case on very short timescales, given the dramatic chnages in magnitude caused by the long term variability. As it was apparent that the minimum at phase 0.0 (i.e. superior conjunction of the X-ray source) was *deeper* than that at phase 0.5, there seemed to be some other component contributing to the orbital lightcurve. Comparisons with theoretical ellipsoidal lightcurves suggested that either mutual partial star/disc eclipses or X-ray heating of small parts of the stellar surface could explain this phenomenon.

Additional V band photometry was obtained by Van Paradijs et al. (1987), along with simultaneous *EXOSAT* X-ray observations. They attempted to create two independent curves – orbital and long variability – the second of which showed a correlation with the X-ray flux. This suggested that X-ray heating of the disc (the star is shielded from the X-ray source by the thick disc) was responsible for the long variability and further analysis of the disc (following Paczyński 1983 and Mazeh et al. 1986) suggested that the thick disc was rather cool ($T < 15000$ K) and radiated via the reprocessing of X-rays.

A more detailed model for the orbital modulation of LMC X-3 was developed by Kuiper, Van Paradijs & Van der Klis (1988) to explain (i) the distortion of the companion star and its inhomogeneous surface brightness distribution, (ii) X-ray heating of the star and (iii) the presence of an accretion disc – which contributes an additional source of light, partially (completely?) shields the star and partially eclipses/is eclipsed by the star. This model included the effects of a thick disc, differing from the model of Khruzina & Cherepashchuk (1984), and had been successful in explaining the lightcurves of SMC X-1 and Cen X-3. While their extreme lower limit to the mass of the compact object was still greater than the maximum mass of a neutron star, they acknowledged that the model is dependent on the long optical variability and the distance to the LMC (e.g. using distances of 40, 50 and 60 kpc yields $M_s \sim 0.5$–1.5, 1.0–3.0 and 1.5–4.8 $M_\odot$ respectively).

With the apparent presence of an accretion disc in the LMC X-3 system, Treves et al. (1988a) made quasi-simultaneous ultra-violet, optical and infrared observations – LMC X-3 was a unique black hole candidate in that it was possible to study the disc in all three wavelengths, independently of the star (the star in Cyg X-1 dominates the disc and the disc of A0620–00 is too faint in the ultra-violet). They estimated the ultra-violet contribution of the B star from previous observations during a flux minimum of the long 'period' and fit a reddened Kurucz (1979) model for a B3 V star (with $T \sim 19000$ K). On subtraction of the model from their more recent (bright state) observations a reddened blackbody disc spectrum could be fit to the residuals.

Cowley et al. (1991) further investigated the long variability in B, V and R photometry and found that the optical lightcurves preceded that of the X-ray by $\sim$ 20 days. There appeared to be no colour variations over the orbit but, on removal of the ellipsoidal variations from the optical data, it appeared that the system reddened as the V band

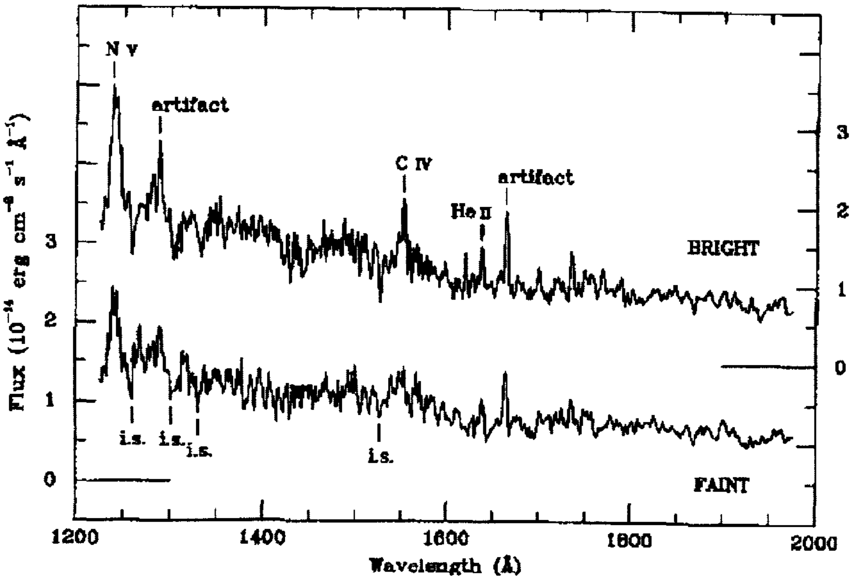

Figure 5.5: *IUE* spectra of LMC X-3 during bright and faint epochs of the lightcurve – each spectrum is the composite of ten original spectra. The difference in strength of the emission lines between the bright and faint epochs can be seen clearly. The three emission lines associated with the accretion disc, *IUE* artefacts and interstellar lines are marked (Cowley et al. 1994).

intensity increased (e.g. $V \sim 17.6, V - B \sim -0.25$; $V \sim 16.7, V - B \sim 0$). This implied that the disc (cooler and redder than the star) makes a significant contribution to intensity and colour at maximum light. They then removed an assumed colour and magnitude for the B star and found a correlation between the disc colour and intensity – i.e. the disc becomes bluer as it brightens, as one would expect.

Additional ultra-violet data were obtained from *HST* and *IUE* and showed that the 198 day 'period' did not continue as expected, the source dropping into a low optical/ultraviolet state – in fact, a 99 day period with some peaks missing seemed a better description of the lightcurve (Cowley et al. 1994). The *HST* spectrum showed high excitation emission features, which would usually be expected in a much hotter star, (C IV, N V, He II) suggesting the presence of a hot envelope or disc. Fitting the continuum with model atmospheres also required either a hotter star or an additional (disc) component. A comparison of *IUE* spectra from bright and faint parts of the lightcurve showed that the emission lines weakened when the source became fainter and vice versa – once again, this was consistent with a precessing accretion disc (although it was not inconsistent with changes in mass transfer rate either; see Fig. 5.5).

Chapter 6

PERIODIC VARIABILITY OF LMC X-3 ?

In collaboration with P.J. Groot & J. Wilms

The recent results that LMC X-3 shows evidence of transitions to the hard state during the minima of its long 'period' justify its inclusion in this thesis. Data have been obtained in the V and B bands for six years, initially with a view to model the lightcurves in terms of a precessing accretion disc. Following Wilms et al. (2000), the optical lightcurves are now investigated for signatures of a variable mass transfer rate instead.

6.1 Observations

Data were obtained by various observers (I was not one of them) at the 0.91m Dutch Telescope of the European Southern Observatory in Chile; it was equipped with a 512×512 TEK CCD and standard Johnson V and B filters. The observations were made between 1993 and 1999 in a total of sixteen different observing runs as part of the University of Amsterdam's monitoring program for X-ray binaries. Each observing run lasted 1–4 weeks, typically 2–12 observations of LMC X-3 would be made in a night and significantly more of the points were made in the V band. Typical exposure times were five (V band) and seven (B band) minutes. Varying numbers of bias frames were taken, typically about ten at the beginning and ends of the night, and a total of 5–10 sky and dome flats each night. No dark frames were used.

All data were reduced as a single dataset (by hand – not automatically) using IRAF. Bias and flat field frames were checked individually and faulty ones discarded. The bias frames for each night were combined with IMCOMBINE, which calculated the median value of all the frames for each position on the chip. An empirical rejection method (sigclip) was used in which the median was computed ignoring the lowest and highest values, the value of σ about this median was determined and then any points more than 2σ from this point were rejected. This was repeated for as long as there were points more than 2σ from the median. The combined bias was subtracted from each flat field and image frame using IMARITH. COLBIAS was then used to fit the median of the overscan region with a first order Chebyshev polynomial, to reject points 2σ from the fit and to subtract the fit from the flat field and image frames. The flat field frames were combined in a similar way to the biases (IMCOMBINE) and were normalised to unity with NORMALIZE; finally the images were divided by the combined and normalised flat field using IMARITH.

IRAF was again used in order to obtain the photometry. Fifteen stars were selected on each frame, including LMC X-3. The mean FWHM was determined for each frame using IMEXAMINE and this was then used to determine the radius of the aperture and the sky annulus – the aperture was set to 1.5 times the FWHM, the inner radius of the surrounding annulus of sky was 4 times the FWHM and the width of the sky annulus was 5 times the FWHM.

Instrumental magnitudes for the fifteen stars were obtained by assuming that the point spread function of each was a Gaussian, determining the number of counts within an aperture centred on the peak of the Gaussian and subtracting the number of counts in the sky annulus (APPHOT); the instrumental magnitude is defined as $-2.5\,\lg\,(\mathrm{gain} \times \mathrm{counts})$. The resultant magnitudes were then studied for stability over the six year monitoring campaign. Only two stars (see Van der Klis et al. 1985 for details of these two stars and a finding chart) appeared to remain stable and thus be suitable for differential photometry.

The two reference stars were calibrated with the IRAF tasks within PHOTCAL, using photometric standard stars in the fields of PG 0231+051 and Mark A (Landolt 1992). In order to check the calibration, zeropoints of the calibrator observations were determined according to Equation 6.1 and hence the reference star magnitudes could be determined by assuming that the zeropoints remained constant.

$$\mathrm{Z.P.} = V_{\mathrm{real}} - \Bigg(V_{\mathrm{inst.}} - \Bigg(-2.5\,\lg\,(\mathrm{exp.\,time})\Bigg) - (\mathrm{airmass} \times \mathrm{extinction\,coeff.})\Bigg) \qquad (6.1)$$

Extinction coefficients for the Dutch Telescope are 0.11 (V) and 0.23 (B) and airmasses were calculated using SETAIRMASS – I note that it would have been beneficial to monitor the stability of these values over the period of the observations. However, since it is the

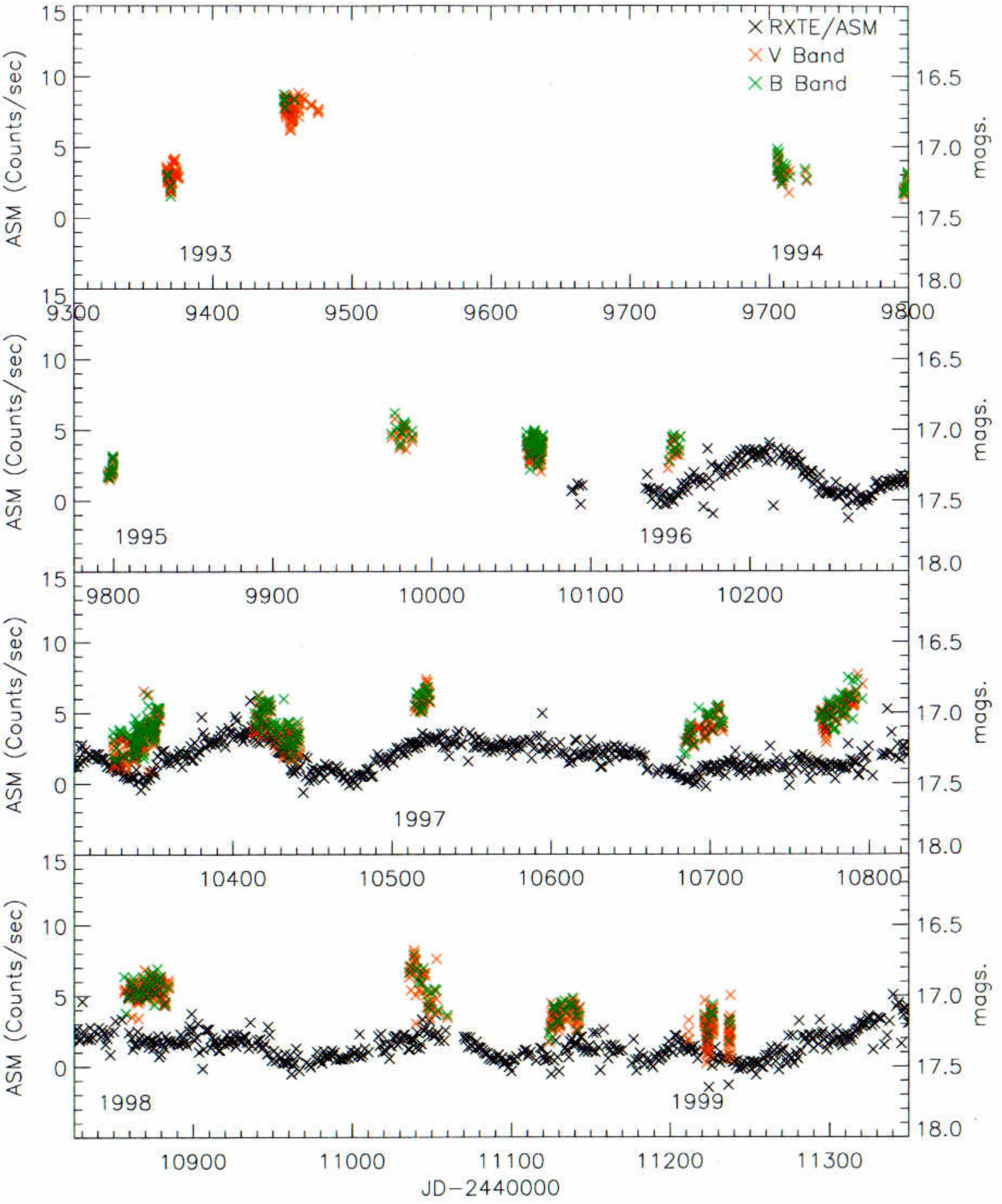

Figure 6.1: V and B band photometry of LMC X-3 spanning 1993–1999. All available simultaneous X-ray data from the *RXTE*/ASM are also plotted (daily averaged points).

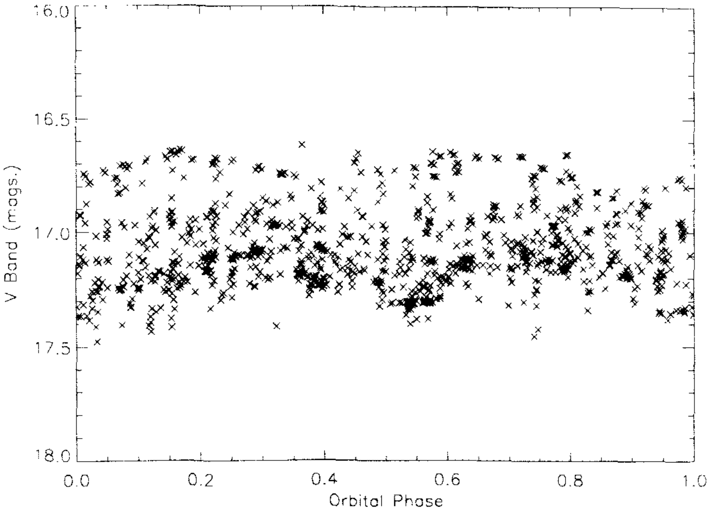

Figure 6.2: *V* band photometry of LMC X-3 spanning 1993–1999 folded on the orbital period – a surprisingly scattered plot for what was thought to be a well-defined ephemeris.

relative variability of the differential photometry that is of interest here, the absolute magnitudes are not so important.

Thus LMC X-3 could be calibrated against the results of the reference stars. As there was relatively little data for the standards, given the length of the monitoring campaign, the calibration of LMC X-3 depended heavily on the stability of the two reference stars used for the differential photometry over the time of the observations.

The calibrated dataset is plotted along with all available simultaneous *RXTE*/ASM data (daily averaged points) in Fig. 6.1. It is apparent that some parts of the optical lightcurve correlate well with the X-ray although this is not always the case – e.g. there is clearly very different behaviour taking place towards the end of 1996 and the end of 1997. These correlations are investigated further in Section 6.2.

6.2 Results – The Long Modulation

The Orbital Lightcurves

The complete dataset was initially folded on the 1.7 day orbital period, which has been well established in radial velocity measurements and also in the optical photometry of various authors (see Chapter 5 for references). It was therefore quite surprising to find that the resultant plot was little more than scatter (Fig. 6.2). Clearly the large variability of the lightcurve is sufficient to ensure no smooth mean orbital lightcurve may be obtained from datasets spanning such a long period of time.

While it was perhaps tempting to follow the line of research of previous authors – to split the data into sub-datasets, subtract the mean magnitude and then recombine into a smooth orbital curve – as the ultimate aim of the project was to investigate the long modulation, this loss of information did not seem a productive way forward. It should also be noted that in the case of the precessing disc system LMC X-4, Heemskerk et al. (1989) find that on removal of the orbital period an orbital residual is left – this is caused by the different heating effects caused at different angles of the precessing accretion disc. Reversing this effect shows that removing the long modulation will not result in a pure ellipsoidal curve and so I do not attempt it here.

The effect that the long modulation has on the orbital lightcurve can be seen in Fig. 6.3. The dataset has been divided according to observing session, each session typically spans 1–4 weeks. The various sub-datasets have been folded on the 1.7 day orbital period. In a number of the plots it can be seen that the two maxima/minima are not equal in magnitude – while previous authors have assumed that they are observing e.g. an accretion stream, it is clear from these plots that whether or not the lightcurve is ascending or descending according to the 'long period' is more likely to be responsible. While occasional sub-datasets show a smooth orbital lightcurve, it is more common for them to be scattered or to show a number of superimposed double-peaked curves. The latter half of 1996 shows clearly that within just 2–4 weeks the data from the different orbits becomes incomparable without some method of 'removing' the long modulation. Fitting the mean orbital curves with splines and comparing them shows that phase shifts of up to 0.15 take place between the different observing sessions.

Period Searching

The study of the long modulation is therefore of great importance if the orbital lightcurves are ever to be understood properly; however, this is somewhat difficult on account of the lack of periodicity to the variability. Power spectra were computed for the photometry using the discrete Fourier transform routine in the STARLINK package PERIOD. The data were then split into ten orbital phase bins and the power spectra computed. In all cases there were no peaks in the power spectra that did not also appear in the window function of the Fourier transform. The Lomb-Scargle algorithm (PERIOD) was used for comparison

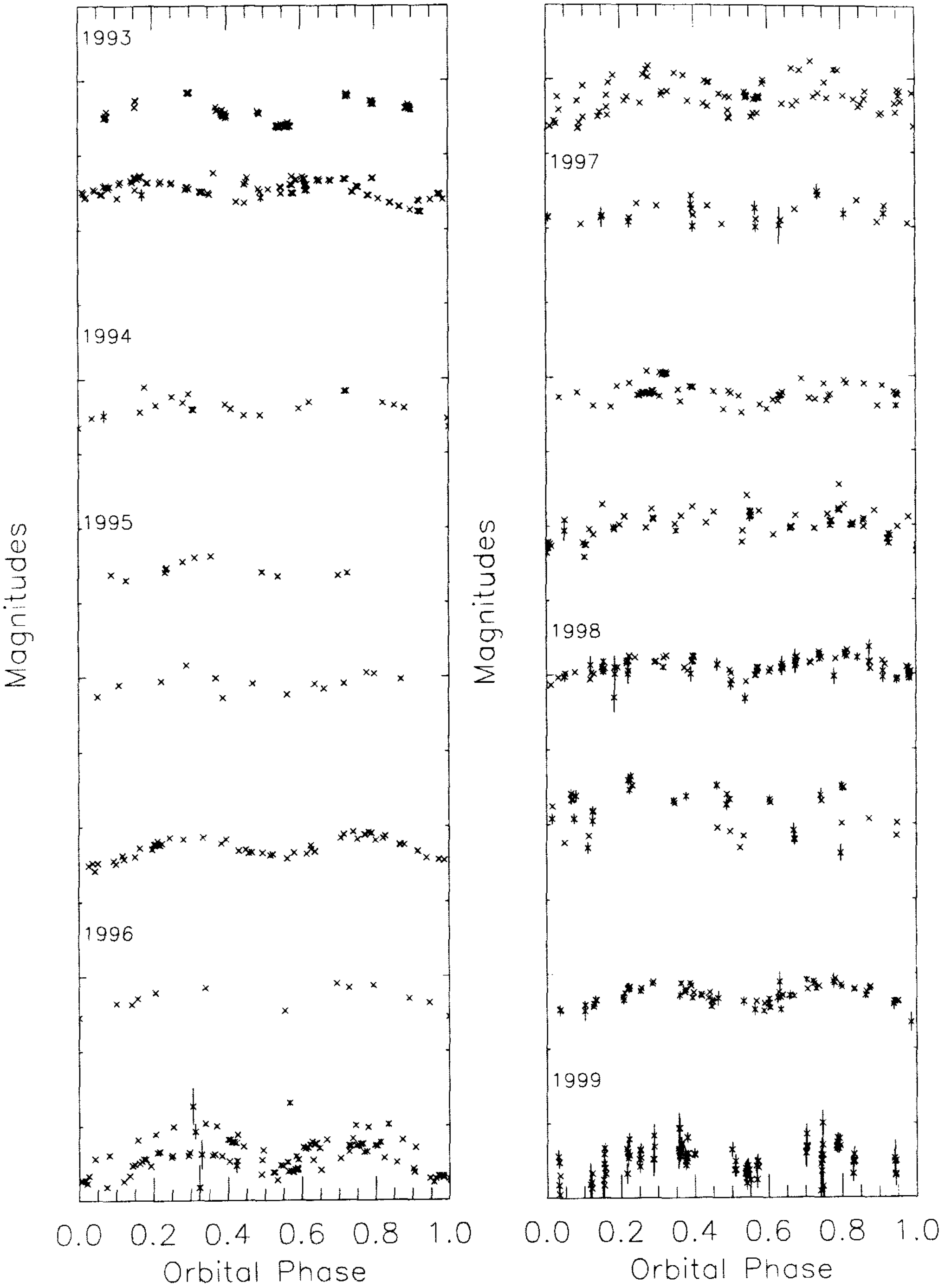

Figure 6.3: Mean orbital lightcurves in the V band for the sixteen different observing sessions, each lasting 1–4 weeks. The tick marks on the magnitude axis are 0.5 magnitudes apart and the successive observing sessions have been shifted by 1 magnitude for clarity. Large amounts of variability can be seen from one session to the next and frequently within the few-week observing session (e.g. 1996).

and similarly yielded no convincing modulation.

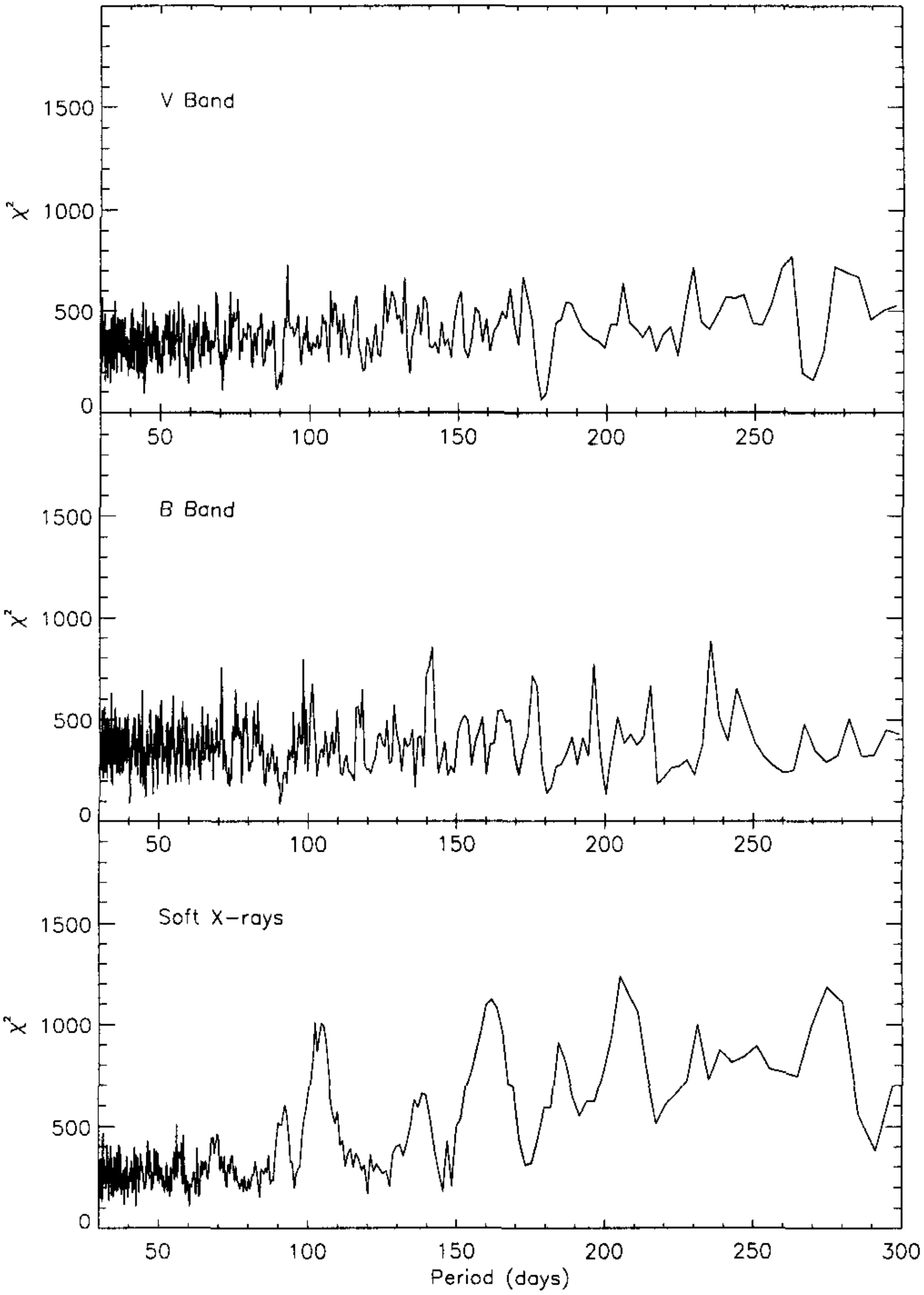

Figure 6.4: Results of epoch-folding the optical photometry and also the *RXTE*/ASM data on periods in the 30–300 day range. No discrete peaks are apparent, although all three show maxima in the 200–300 day range.

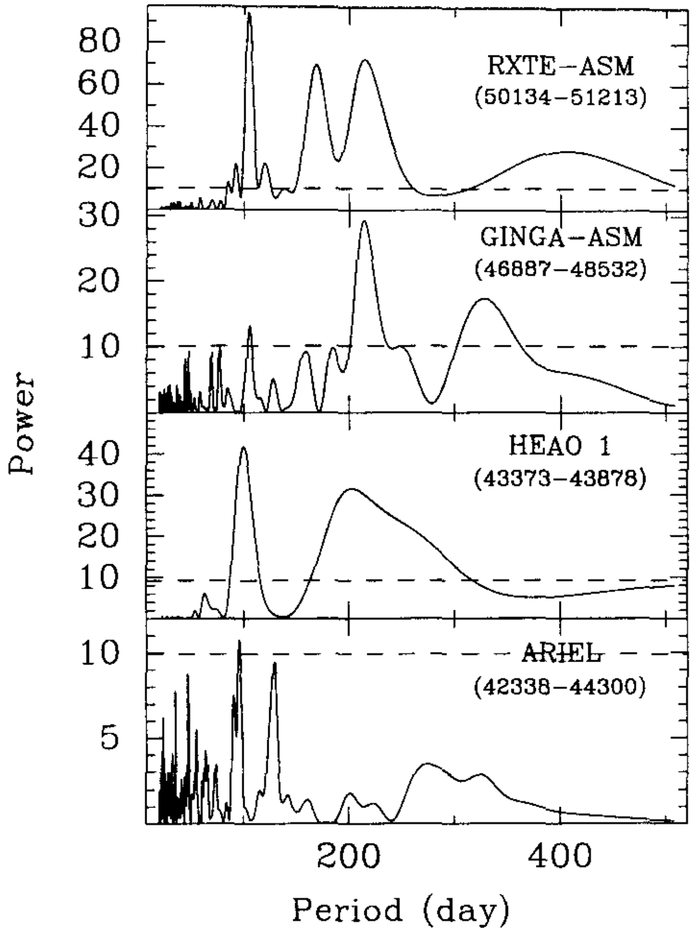

Figure 6.5: Lomb-Scargle periodgrams generated from the *RXTE*, *Ginga*, *HEAO* 1 and *Ariel* V lightcurves. The dashed horizontal lines indicate the 99% confidence limits. Numbers in parentheses refer to JD−2400000 (Paul, Kitamoto & Makino 2000).

One reason for the lack of results in the power spectra could be the very intermittent sampling of the optical lightcurves (see Fig. 6.1). The alternative method of 'epoch-folding' was therefore used – a technique which has been developed specifically for poorly sampled datasets. In this method the lightcurve is folded on a range of different periods and the mean curves fit with straight lines (i.e. along the phase axis) if a period is present then there should be a clear peak in a plot of χ^2 vs. period. Unfortunately the results of this were equally inconclusive – the data were treated as a whole and also as three sub-datasets, approximately 700 days in length although the sampling for each varied, and periods in the ranges 30–300, 30–150 and 150–300 days were tested. The process was repeated with *RXTE* data spanning approximately the last two thirds of the optical coverage.

Fig. 6.4 shows the results of epoch-folding the optical photometry on periods in the 30–

300 range for the complete dataset. For comparison the same procedure was applied to the *RXTE*/ASM data, using all available data. Note that the optical observations preceded those of the *RXTE* by ~ 850 days, although very few optical points were obtained during this time: the X-ray lightcurve was extended to JD 2451521. There are no peaks relating to a well-defined period in any of the three datasets, although peaks at 205, 275, 160 and 105 days in the X-ray plot reach more than 3σ above the noise level; it is also worth noting that the maximum χ^2 for each dataset falls in the 200–300 day period range. The sampling of the optical datasets is probably still a major factor in this; it is also worth emphasising that the orbital modulation has not been removed from the optical datasets and is not present in the X-rays.

The 198 day period found by Cowley et al. (1991) has already been found to vary slightly – indeed Cowley et al. (1994) later suggested that it was actually half this value. More recently Wilms et al. (2000) found a broad peak in their dynamical power spectrum suggesting that the period was variable in the 200–300 day range. The different values of periods suggested in the literature have been investigated by Paul, Kitamoto & Makino (2000) who obtained and compared long term lightcurves from the *HEAO 1*, *Vela 5B*, *Ariel V*, *Ginga* and *RXTE* satellites. While they confirmed the 198 day period, they found that it was only present in the *HEAO 1* dataset. Peaks in their Lomb-Scargle periodograms appeared at 105, 214 and 328 days in the *Ginga* data and 104, 169 and 216 days in the *RXTE* data (in loose agreement with the results of epoch-folding above – note that a shorter dataset was used by Paul, Kitamoto & Makino 2000). They also noted that the broad peak at 200 days in the *HEAO 1* power spectrum was resolved into two narrower peaks in the *RXTE* power spectrum and that therefore the peaks at 100 and 200 days are not related (see Fig. 6.5). They further noticed that splitting the *RXTE* dataset into two halves yields different peaks in the power spectra for each. Wilms et al. (2000) reached similar conclusions from plotting a dynamical periodogram with the *RXTE* data.

Following the 'periods' reported by Wilms et al. (2000) and Paul, Kitamoto & Makino (2000) the optical lightcurves were folded on a selection of values and the resultant plots shown in Figs. 6.6 and 6.7. In the top two plots of each column the optical data have been folded on values suggested by Wilms et al. (2000); the bottom part of the figure shows the optical data folded on periods reported by Paul, Kitamoto & Makino (2000). Dotted lines across the plots show the mean magnitude in each filter. The same value of JD_0 has been used for all plots (JD 2445626) – this is somewhat arbitrary but is the closest time of

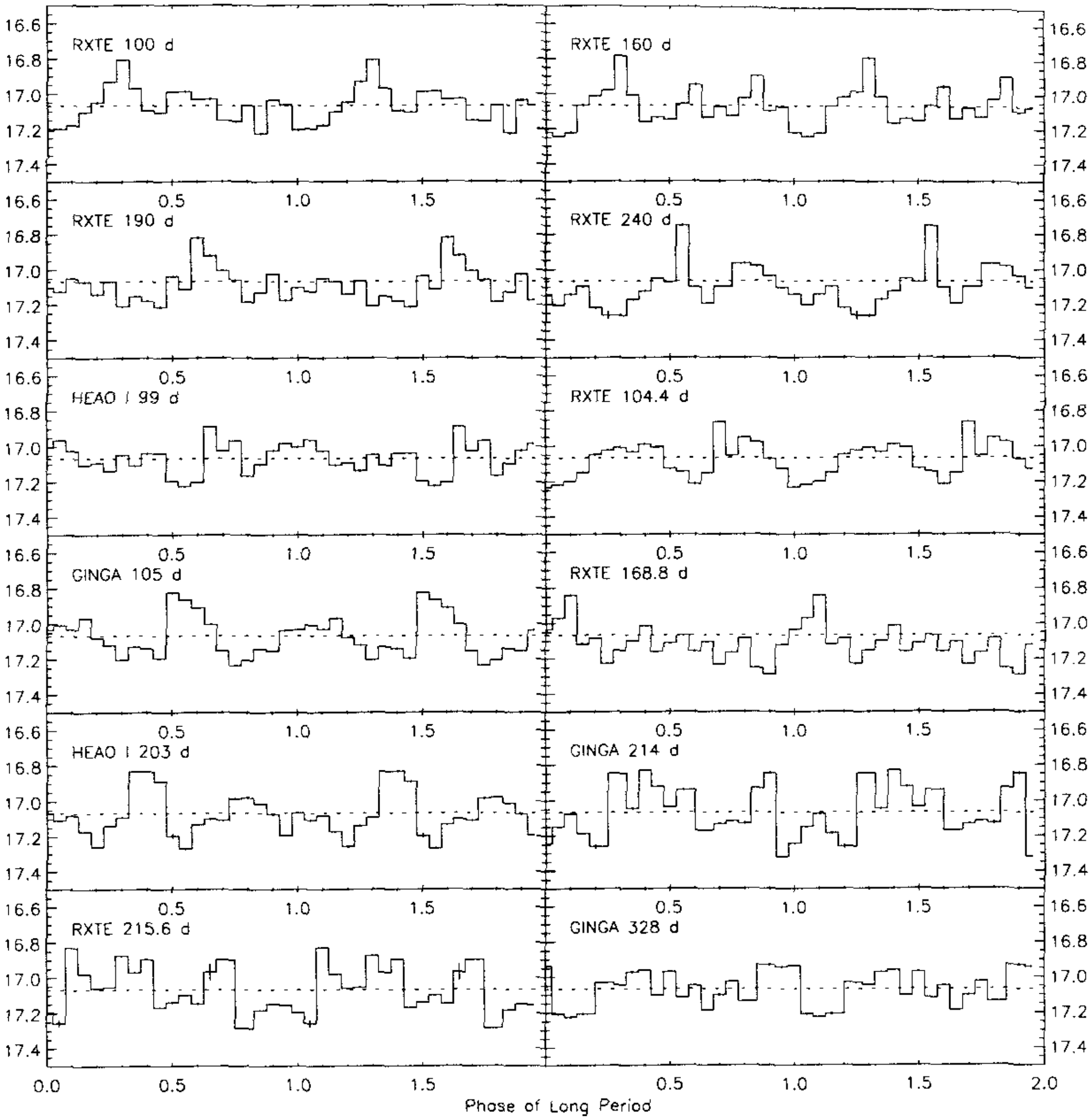

Figure 6.6: The V band photometric data folded on various 'long periods' which have been reported in the literature. The top four plots are based on values quoted by Wilms et al. (2000); the bottom eight plots are based on values quoted by Paul, Kitamoto & Makino (2000).

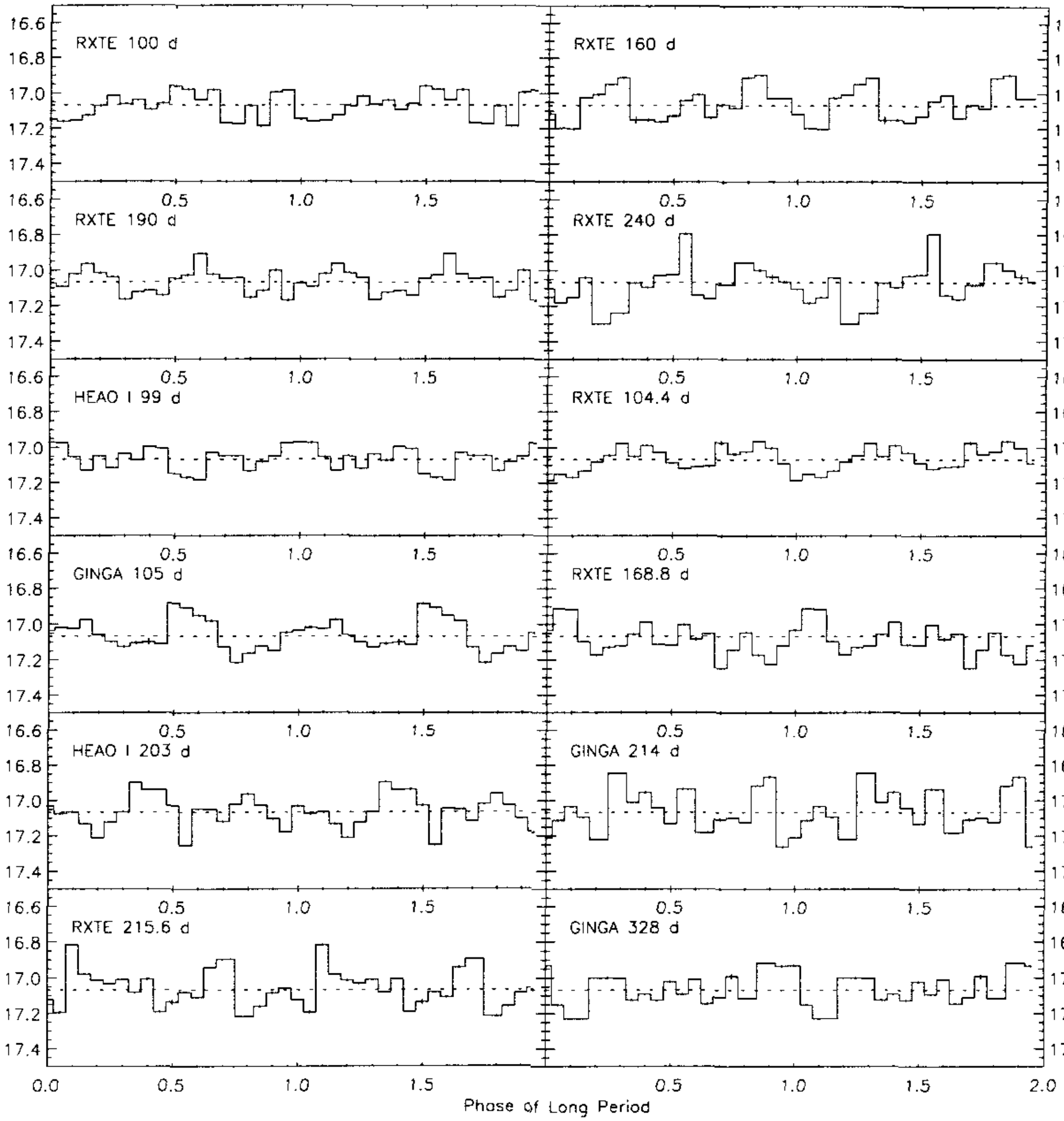

Figure 6.7: The B band photometric data folded on various 'long periods' which have been reported in the literature. The top four plots are based on values quoted by Wilms et al. (2000); the bottom eight plots are based on values quoted by Paul, Kitamoto & Makino (2000).

minimum light (assuming a long period of $\sim$ 100 days) to the orbital ephemeris of Cowley et al. (1983).

After such unsuccessful period searching it is rewarding to see at least some evidence of the reported X-ray periods in the optical data with amplitudes significantly greater than 3σ. The V band plots suggest that periods of 104, 203 and 240 may well be present in the data. The B band does not really confirm this but with considerably less data points in the lightcurve this is hardly surprising. However, fitting a sine wave to the plots and measuring χ^2 shows that none of these 'periods' can be believed to 99% confidence (using PERIOD). This could perhaps be expected given the variability seen in the long period by Paul, Kitamoto & Makino (2000) – the data sampling does not allow us to break it down into shorter lightcurves as these authors did with the X-ray data.

Unfortunately the sampling seems to be complicating the results again, particularly as the B and V plots are not always consistent with each other. Again, there has been no provision made for the presence of the orbital period in the data and there is insufficient coverage for plots to be made for the individual orbital phase bins. This line of research could be vastly improved by obtaining regularly sampled long term lightcurves in two or more optical filters – it would be an ideal project for a southern hemisphere robotic telescope.

Comparison with the X-ray Lightcurve

As it is suspected that the optical and X-ray lightcurves are correlated it is perhaps surprising that the possible periodicities found in the X-ray lightcurves are not particularly apparent in the optical photometry. Likewise it is surprising that the optical/X-ray flux-flux plots do not show any convincing correlation (e.g. Spearman rank correlation coefficient $\sim$ 0.5 for the end of 1996 the section of the lightcurve that (by eye) appears most correlated). While the variability of the long period and the presence of the orbital period in the optical data seem to be the main causes, it seems as though the sampling of the optical data may still be contributing to this and so cross-correlation of the X-ray and optical lightcurves was attempted in order to confirm this correlation.

The discrete cross-correlation function was obtained for each X-ray/optical pair and the resultant plots shown in Fig. 6.8 – the optical magnitudes were converted into fluxes (mJy) (using the Johnson conversions) in order to do this. A clear peak can be seen in the centre of the plots, suggesting that the X-ray and optical lightcurves are indeed

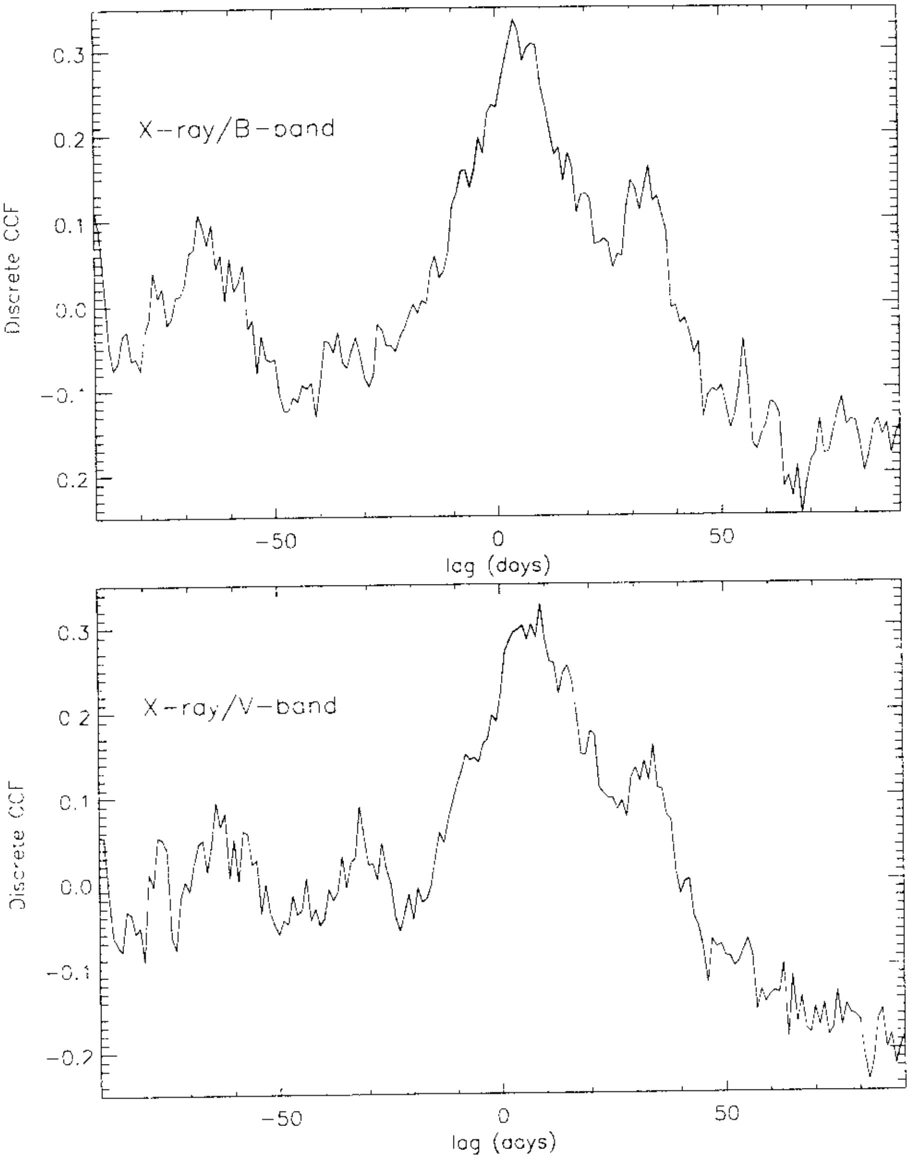

Figure 6.8: The X-ray lightcurve cross-correlated with the B (top) and V band (bottom) lightcurves. A positive correlation and 5–10 day X-ray lag can be seen.

correlated. Furthermore, the X-ray lightcurve appears to lag the optical by ~ 5–10 days – this is approximately half of the lag found by Ebisawa et al. (1993), possibly suggesting variability in disc size or viscosity if the lag is related to the disc crossing time for the mass flow (see below). Unfortunately the time resolution of the data is insufficient to determine any lag between the V and B band lightcurves. This lag would suggest that reprocessing of X-rays into optical emission or irradiation of the B star is *not* dominating the optical emission in LMC X-3; the correlation between the X-ray and optical would suggest that ellipsoidal modulation of the star is not dominating the optical emission either.

The Optical Colours

Despite a limited amount of B band data the photometry was daily averaged and $B-V$ colours determined. Following Cowley et al. (1991) the $B-V$ data was plotted against the V band. Cowley et al. (1991) found correlated behaviour, in that the system became redder when the intensity increased, suggesting that the intensity increase was due to the brightening of a cool component, probably an accretion disc – however, this correlation does not appear to be present in our data, which obviously covers a much longer timescale (Fig. 6.9). This is a somewhat strange result and it is unlikely that the intensity increases are wavelength independent. As investigated further below, it is more likely that the poor B band coverage and hence the daily averaging is a major contributor to this lack of correlation.

To investigate this apparent lack of correlation further, the $B-V$ colour data were

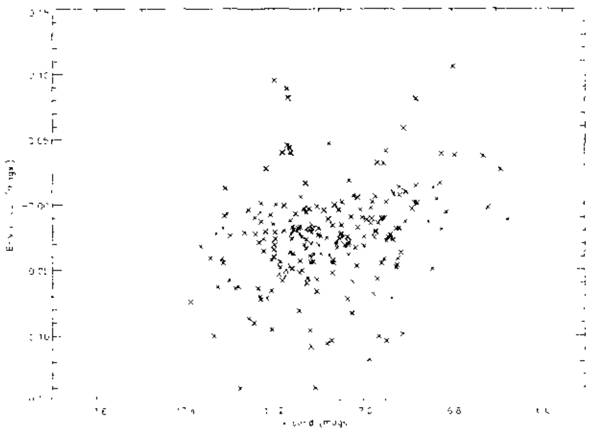

Figure 6.9: The $B-V$ colours plotted against the V band intensity. It appears that the correlation observed by Cowley et al. (1991) does not appear in our data.

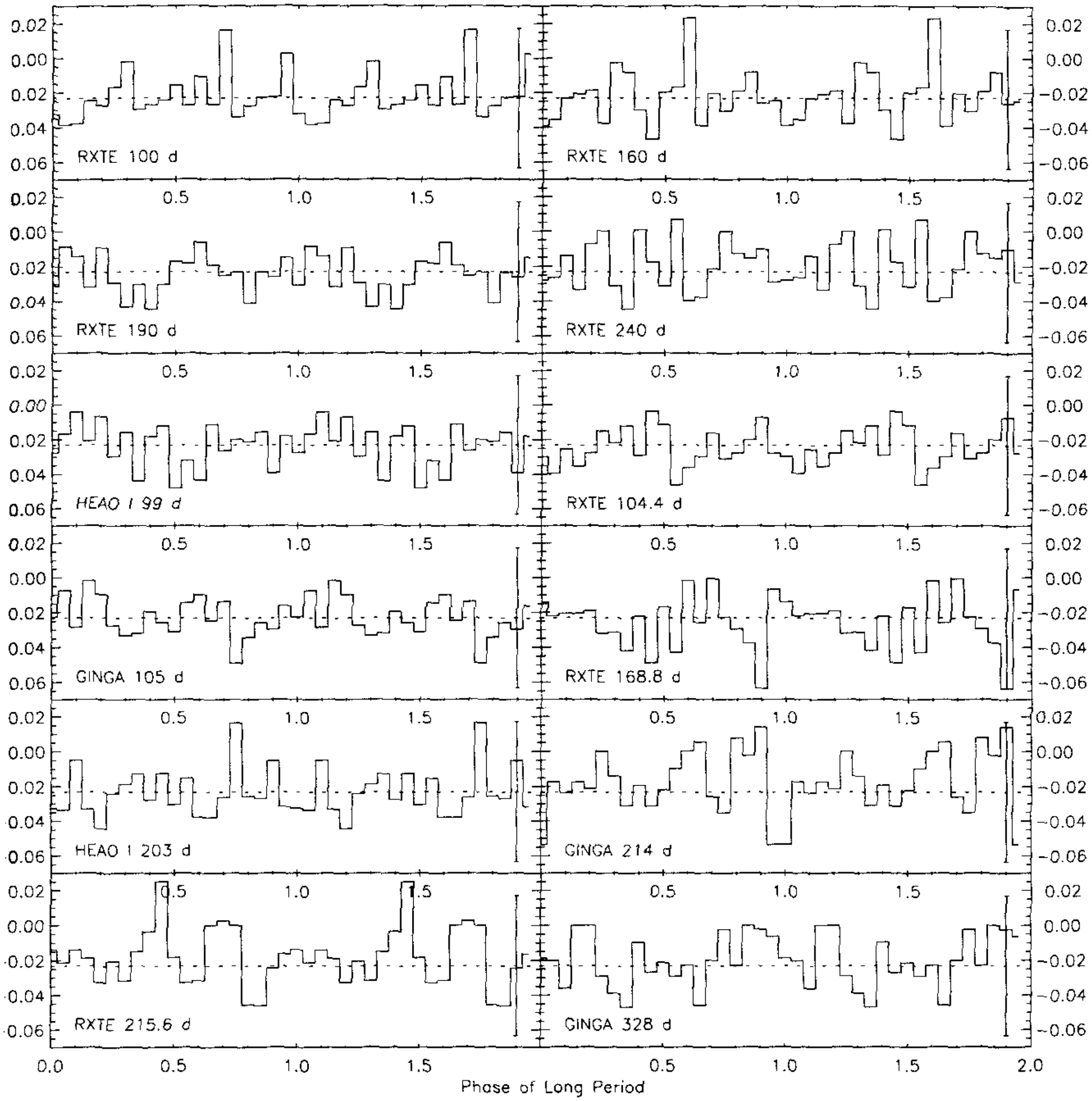

Figure 6.10: The $B-V$ colours folded on various 'long periods' which have been reported in the literature: a 1σ error bar is shown in each plot. The top four plots are based on values quoted by Wilms et al. (2000); the bottom eight plots are based on values quoted by Paul, Kitamoto & Makino (2000). Note that vertical scales are not the same as for Figs. 6.6 and 6.7

folded on the various long periods reported in the literature as for Figs. 6.6 and 6.7 – the resultant plots are found in Fig. 6.10. Despite the smaller range on the magnitude axes (compared with Figs. 6.6 and 6.7), there is no evidence for a long modulation at any of the suggested period values. Again, the implictions of this result are discussed below.

6.3 Discussion

While the variation of a long modulation is not accounted for in traditional models of disc precession (e.g. Larwood 1998), more recent models including tilted/twisted discs due to coronal winds (e.g. Schandl & Meyer 1994) and/or radiatively warped discs (e.g. Wijers & Pringle 1999) can allow for these variations. Therefore, the fact that changes in the long period are observed in LMC X-3 (and Cyg X-1? – see Chapter 4) does not rule out the possibility that the 'modulation' is caused by a precessing disc. However, in a precessing system there should be a varying amount of obscuration by the disc and a hardening of the spectrum should be seen at low intensities (Paul, Kitamoto & Makino 2000). They found that there is only a very weak positive correlation between the intensity and the 3–5 keV/1.5–5 keV hardness ratio which is not sufficient to be suggestive of precession. Neither are the spectral changes suggestive of a warped disc. They concluded that given the multiple peaks present in the power spectrum (i.e. a fairly stable peak at $\sim$ 100 days and a highly variable one at $\geq$ 130 days) it is possible that a combination of precession and mass transfer rate variability may be present – pure mass transfer rate variability seems unlikely follwing the work of Kuulkers et al. (1996) and Hasinger & Van der Klis (1989).

The correlation between the X-ray and optical lightcurves again does not necessarily distinguish between precession and varying mass transfer rate; but as the X-ray source changes spectral state (Wilms et al. 2000) a varying mass transfer rate seems likely for both X-ray and optical emissison, given the correlation. Furthermore, the five day X-ray lag does indeed rule out any suggestion of the optical emission being the result of reprocessing of X-rays. Were reprocessing responsible for the optical emission then we would expect to see optical delays of a few seconds instead (although obviously not in this dataset given the insufficient time resolution). The five day lag is most likely to represent the disc crossing time for increased mass flow passing through the disc as the system changes from the hard state to the soft and vice versa. One would normally expect the cooler, redder emission to come from the outer parts of the disc, with the hotter ultra-violet and X-ray emission found at smaller radii and so any new material entering the accretion flow would emit first in the V band and (apparently) ~ 5 days later reach the inner, X-ray emitting regions.

The lack of correlation between the V band and the $B-V$ colours may appear to contradict this suggestion. However if the disc is imagined to consist of a series of concentric rings emitting at X-ray, ultra-violet, U, B, V and infrared wavelengths with progressively increasing disc radius, then a 5 day optical to X-ray delay would probably be consistent with a ≤ 1 day V to B band delay. Consequently the daily averaging due to poor B band coverage has hidden the delay information and hence the correlation.

Furthermore if the modulation were caused by a radiatively warped disc, as thought to be the case for e.g. Her X-1, then we might expect to see the same modulation in the optical colours. The daily averaged data would no longer be a problem as the presence of a modulation in the colours due to radiative warping would not be dependent on a short annulus crossing time - instead, additional radiation from warped parts of the accretion disc would contribute to the optical colours and 'periodic' variability of a much greater scale than shown in Fig. 6.10 would be observed.

Alternatively, a flat, precessing disc would not be expected to show any periodic colour variability as the relative amounts of V and B emission would not change as different projected areas of the disc are observed. However, precession models require a rigid, tilted disc to tidally precess around the compact object and it is extremely unlikely that this would be possible; neither do the models explain what may tilt the disc in the first place. It is probable that disc precession is purely an idealised simplification of a warped, precessing disc and so it is unlikely that a flat precessing disc is present in LMC X-3. The $B-V$ colour observations are summarised in Fig. 6.11.

In summary, the presence of a variable 'long period', the hard state behaviour during the dips of the modulation (as found by Wilms et al. 2000), the delayed correlation between the X-ray and the optical lightcurves and the lack of variability of the $B-V$ colours are all suggestive that the long modulation of LMC X-3 is indeed due to a variable mass transfer rate.

Such a modulation caused by a variable mass transfer rate could indeed take place, if a model of an accretion disc wind instability limit cycle is considered. Shields et al. (1986 and references within) showed that X-rays emitted in the inner part of the accretion disc of X-ray binaries (and also quasars, AGN, CVs) will subject the outer parts of the disc to Compton heating, sufficient to drive a corona and possibly a wind from the disc. It was

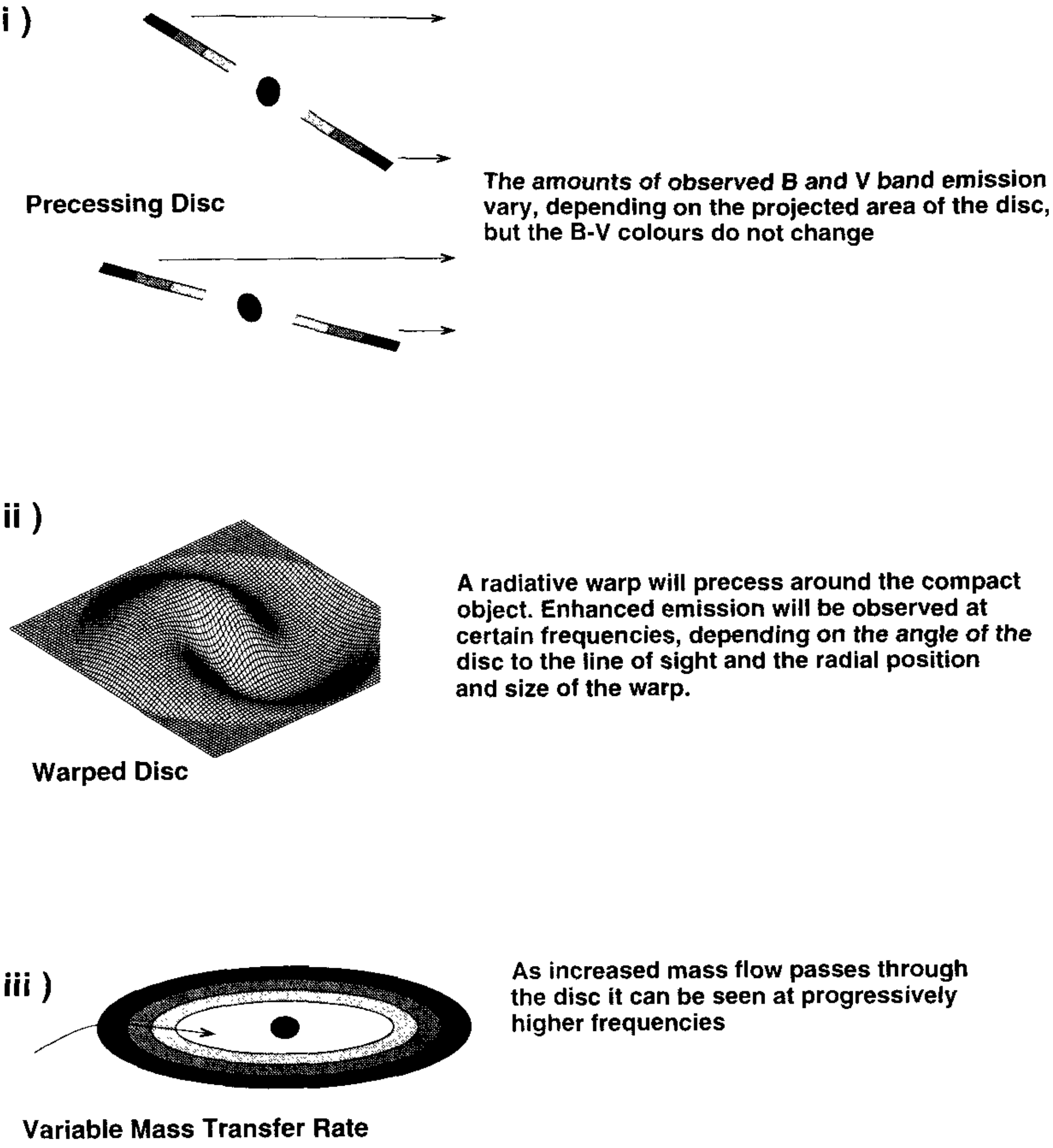

The amounts of observed B and V band emission vary, depending on the projected area of the disc, but the B-V colours do not change

A radiative warp will precess around the compact object. Enhanced emission will be observed at certain frequencies, depending on the angle of the disc to the line of sight and the radial position and size of the warp.

As increased mass flow passes through the disc it can be seen at progressively higher frequencies

Figure 6.11: A schematic suggesting the possible behaviour of the photometric colours in three different systems with i) a flat, precessing disc, ii) a radiatively warped disc (figure from Maloney & Begelman 1997) and iii) a variable mass transfer rate

thought that such a wind could occur at a disc radius one tenth that at which the escape velocity equals the isothermal sound speed of the Compton-heated coronal gas. The model was extended to include attenuation and scattering of X-rays from the central source and the effects of inverse Compton cooling due to radiation emitted locally by the disc, thus enabling observational consequences of the phenomenon to be predicted and tested.

If the mass loss rate of the wind is small compared with the mass accretion rate then the wind-driving disc can remain in a steady state. However, if the disc luminosity and hence the mass loss rate of the wind exceed a critical value, then the mass of the disc and (following some delay) the mass accretion rate will decrease, reducing the luminosity of the X-ray source to a point at which it is insufficient to drive the Compton-heated wind. Thus a limit cycle is maintained. As the mass flow deficit passes radially through the disc on a viscous timescale it can be observed first in the optically emitting region of the disc and later in the inner X-ray emitting parts, producing the X-ray lag observed in LMC X-3. With the limit cycle requiring $\geq 90\%$ of the mass flow to be expelled from the system, the large amplitude oscillations of LMC X-3 can also be explained.

A way in which these results could be tested would be to obtain simultaneous high time resolution ($\sim$ hours) X-ray, ultra-violet, optical and infrared data over the course of a cycle of variability – this would enable much more accurate timing analysis than possible with the dataset presented here. Further confirmation of the hard states in the dip of the modulation could be obtained from the discovery of a radio jet, as seen in other X-ray binaries during the hard state – this is investigated further in the next chapter. The long modulation of Cyg X-1 should also be re-examined in the context of the Compton-heated coronal wind model as a number of authors have thought it an unlikely pure-precession candidate (e.g. Ogilvie & Dubus, 2000).

Chapter 7

THE RADIO COUNTERPART OF LMC X-3

In collaboration with R.P. Fender & J. Wilms

While there are many similarities between Cyg X-1 and LMC X-3, in the sense that they are both found in the same two X-ray states and show periodicities on similar timescales, they differ greatly in that LMC X-3 has not been observed to have a radio counterpart. There are a number of possible reasons for this - either there is no radio counterpart and the systems are less similar than they seem, or the observations have not been sufficiently sensitive due to the large distance to the LMC. LMC X-1 cannot be detected in the radio either, but this is partly attributed to its location in a radio-emitting nebula (e.g Fender, Southwell & Tzioumis 1998, and references within).

Fender & Hendry (2000) showed that for all known radio-emitting black hole X-ray binaries in the low/hard state and Z-sources on the horizontal branch, their radio flux density is inversely proportional to the square of their distance (Fig. 7.1). Thus all black hole X-ray binaries and Z-sources appear to have similar intrinsic radio luminosities and it is their distance from us that determines their observed flux densities.

Consequently it would appear that the lack of radio emission observed from LMC X-3 may be due purely to its distance from us - previous observations have lasted less than an hour in total integration time and this is not sufficient. A longer observation was obtained at the Australia Telescope Compact Array in 1998, details of which can be found below.

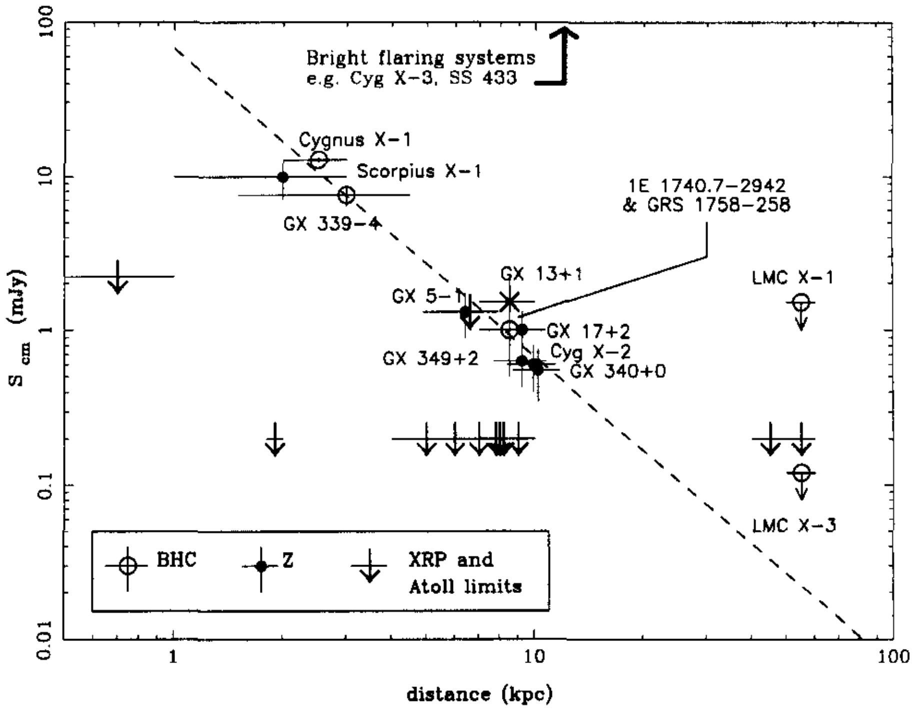

Figure 7.1: A plot of the mean radio emission against distance estimate for the persistent black hole and Z-source X-ray binaries. All sources appear to obey a $S_{cm} \propto d^{-2}$ law. Upper limits to the radio emission from atoll sources and X-ray pulsar systems are also included (Fender & Hendry 2000). The previous best upper limit to the flux density of LMC X-3 is shown in the bottom right-hand corner.

7.1 Observations

Radio observations were made at the ATCA on 5 April 1998. All six telescopes were used in the 750A configuration, which is characterised by baselines in the range 77–3750 metres. The two detectors on each antenna were set to adjacent frequencies within the 6cm band (C band; 4800, 4928 MHz) – a technique which enables a $\sqrt{2}$ improvement in signal-to-noise. The compact radio galaxy PKS 1934−638 was used as a flux (primary) calibrator and observed at the beginning of the run; a second flux calibrator (PKS 0823−500) was also observed at the end as a back-up. The phase reference source (secondary) was PKS 0539−530 and observed for $\sim$ 3 minutes every $\sim$ 15 minutes.

The data recorded by a radio telescope is a collection of 'visibilities' – amplitude and phase information of the signals reaching each baseline over time, and this is obtained in the (ground-based) *uv* plane of the telescope. The *uv* data is edited and calibrated before being Fourier transformed back into the plane of the sky (the image plane), in order to obtain a realistic image of the source.

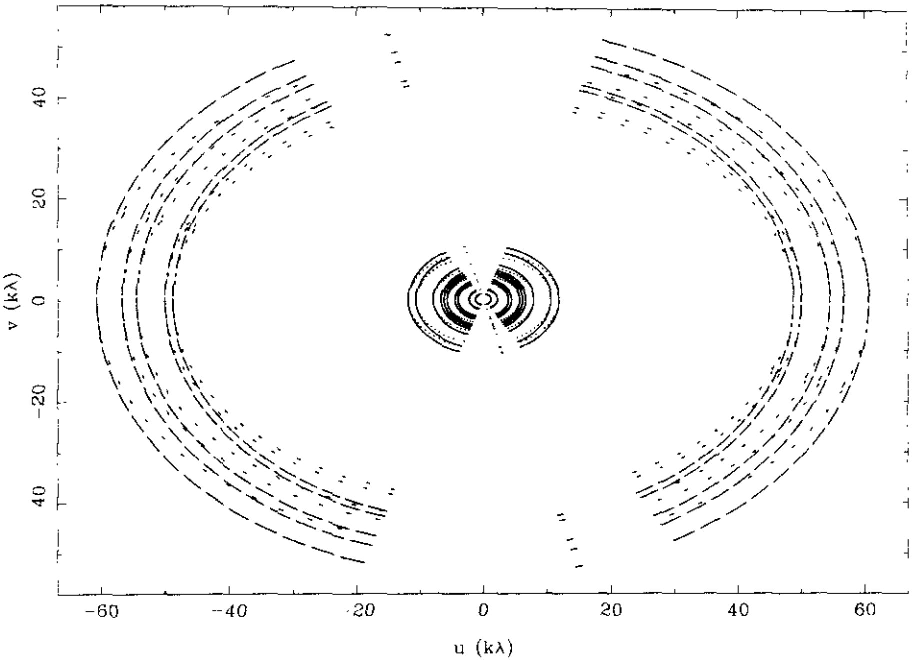

Figure 7.2: Plot showing the fairly good *uv* coverage of the LMC X-3 observations at 4.8–4.9 GHz in 1998.

The LMC X-3 observations were reduced using the MIRIAD software, which was written specifically for the ATCA although it can also be used for data from other telescopes (Sault, Teuben, Wright 1995). Standard flagging, calibration and imaging techniques were applied, further details of which can be found below.

Flagging

Radio datasets require editing or 'flagging' of discrepant points caused by e.g. terrestrial interference, antenna tracking inaccuracies, poor weather, malfunctioning receivers, data recording errors etc. The first stage is simply to determine which antennas stopped working at any time during the observations and to flag the corresponding points.

The visibilities were then examined more closely. TVFLAG was used to view the amplitudes of the signal for each baseline at each of the thirteen different frequency channels for each band. The mean amplitudes were subtracted from the data and any discrepant points in the residuals removed. The scaling of the display was then changed so that further points could be flagged - the process was repeated until there were no further problems.

A second flagging technique was then used – BLFLAG plots the amplitudes against time, averaging over all channels, and individual points can be deleted from any baselines if necessary. The target source was not flagged until after calibration.

Calibration

The target source visibility data needs to be calibrated in terms of flux, phase and polarisation. MIRIAD models the response of an antenna to radiation by:

$$g(t)g_p(\nu)\exp(i2\pi\tau(t)(\nu-\nu_0)) \tag{7.1}$$

where $g(t)$ is the time- (but not frequency-) dependent antenna gain, $g_p(\nu)$ is the bandpass function which varies with frequency and τ is the delay between arrival times at different antennas and calculated with respect to a fixed reference frequency. Leakages from one polarisation to another are also taken into account. These (complex valued) parameters are dependent on atmospheric and instrumental conditions at the time of observing.

MFCAL was used to determine the bandpass function of the (unpolarised) primary calibrator; GPCAL was then used to determine the antenna gains. The two steps were repeated for the secondary and then the flux scale, obtained from calibration of the primary, was applied to the secondary using GPBOOT. The final stage was to copy the calibration tables from the secondary calibrator source to LMC X-3 (GPCOPY) which enabled flux (primary) and phase, gain and polarisation (secondary) solutions to be applied.

Imaging

The calibrated *uv* data could then be Fourier transformed back into the image plane using INVERT (image size=1500 pixels, cell size=1.5"/pixel). Multi-frequency synthesis was used so that all frequencies within the two adjacent bands could be imaged simultaneously without averaging. As this was a detection experiment maximum signal-to-noise was considerably more important than resolution and so natural weighting was used visibilities at the centre of the *uv* plane, where there is denser *uv* coverage and hence greater sensitivity, are given a higher weight (see Fig. 7.2).

The resultant 'dirty map' does not give direct information about the source because it is only the Fourier transform of the *incomplete uv* plane (Fig. 7.3). To reconstruct an image of the actual source it is necessary to deconvolve the dirty map (i.e. the Fourier transform of the sampled distribution) with the 'dirty beam' (the Fourier transform of the sampling function) – the deconvolution attempts to account for those parts of the *uv* plane that were unsampled. The CLEAN algorithm is used for this task and the MIRIAD

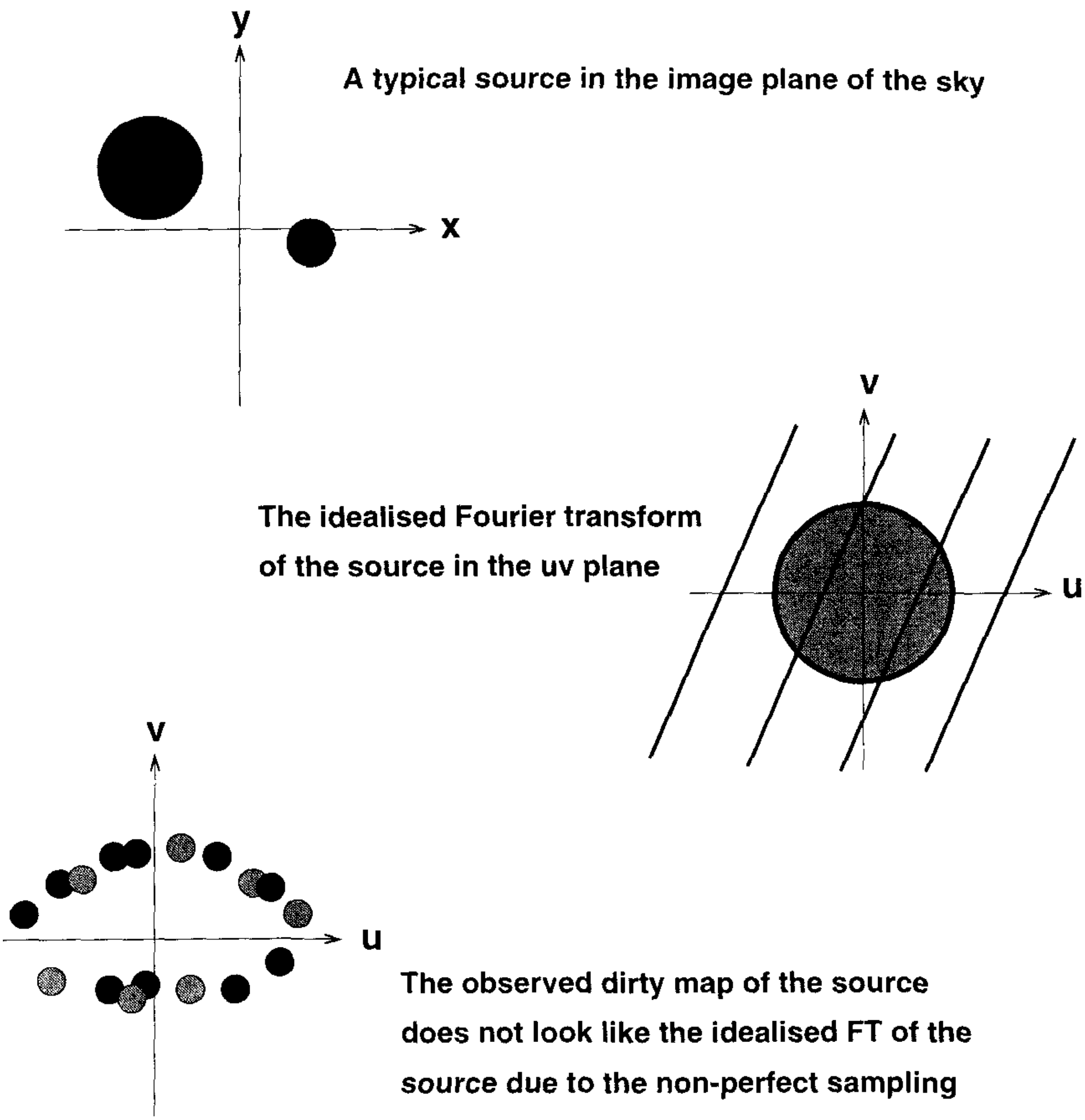

A typical source in the image plane of the sky

The idealised Fourier transform of the source in the uv plane

The observed dirty map of the source does not look like the idealised FT of the source due to the non-perfect sampling

Deconvolution with the sampling function is therefore required in order to reconstruct an image of the source

Figure 7.3: Schematic showing the reason why the dirty map needs CLEAN*ing* before a true image of a source can be obtained (adapted from lecture at MERLIN *summer* school (2000)). The synthesised image of a source (dirty map) is formed by the Fourier transform of the observed *uv* data. As the result of incomplete sampling of the *uv* plane, the dirty map is not a good replica of the source and requires deconvolution with the dirty beam (the FT of the sampling function).

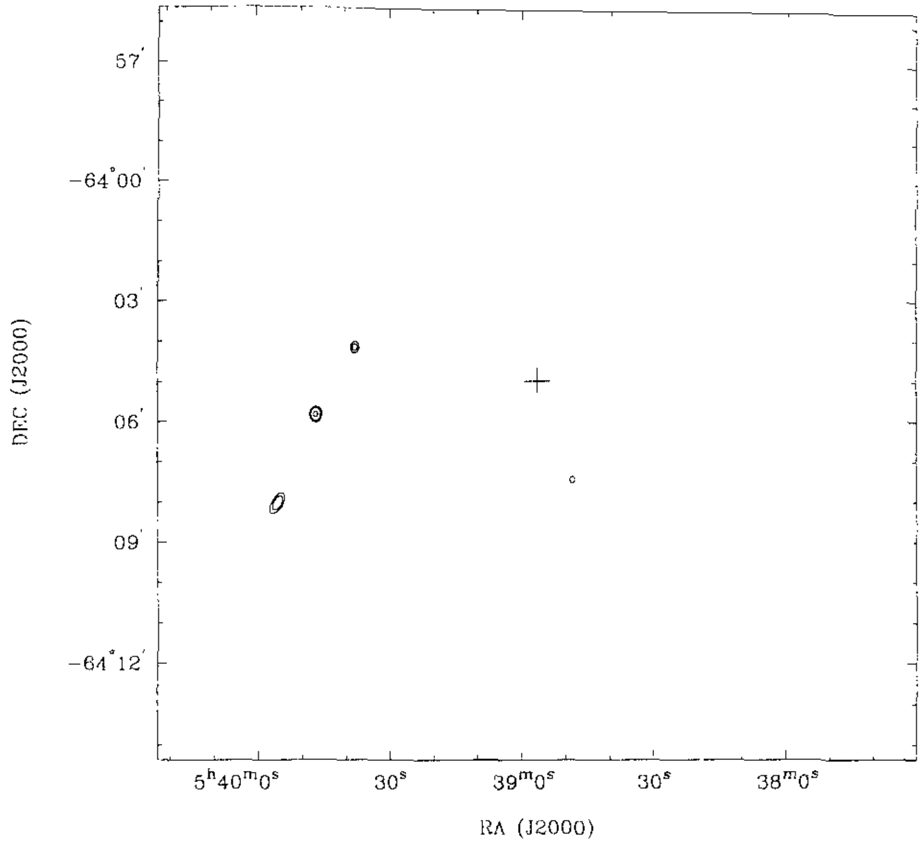

Figure 7.4: The resultant 'map' of LMC X-3 after the 1998 observations – the position of LMC X-3 is marked with a cross. The r.m.s. noise was 0.003 mJy and contour levels are set at -1, 0.5, 1, 3, 6, 12 mJy.

routine CLEAN automatically implements one of three algorithms, depending on the size of the source – in the case of LMC X-3 the Clark (1980) algorithm was the most appropriate. Gradually a model of the image plane is built up from the brightest point spread functions found in the dirty map. Iterations should continue until all real signals in the dirty map have been accounted for, but so that no noise or side-lobe signals are included.

Finally RESTOR was used to convolve the idealised model of the image plane, created by CLEAN, with the Gaussian CLEAN beam so that a more realistic map of the image plane could be obtained (Fig. 7.4).

7.2 Discussion and Implications

It is clear from Fig. 7.4 that the observing run failed to detect a radio source in LMC X-3 – a small compact point source at the centre of the map (i.e. at the cross) would have been

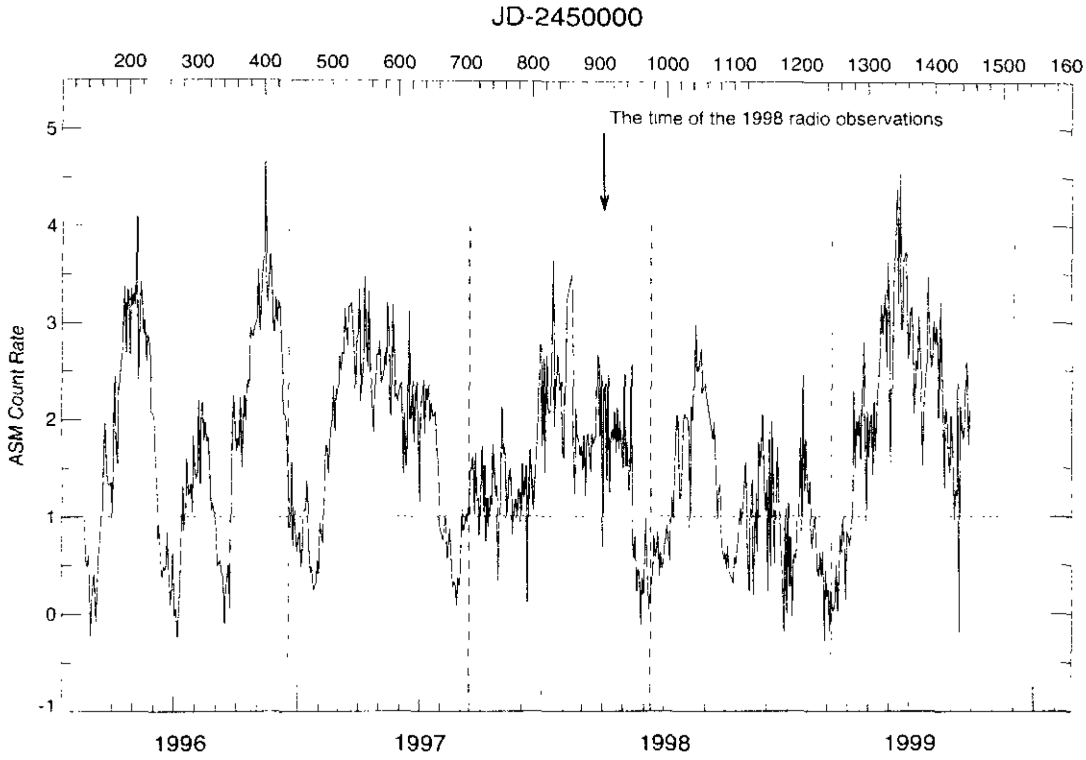

Figure 7.5: The *RXTE* soft X-ray lightcurve of LMC X-3 from the time of the monitoring campaign of Wilms et al. (2000). The hard states (< 1 cps) can be seen to be roughly periodic. The time of the 1998 radio observations is marked clearly the source is not in the hard state at this time and so a radio detection should not be expected.

present had a detection been achieved. The 3σ upper limit to the source as determined by these observations is 0.10 mJy.

There are two reasons why these observations were unsuccessful. As seen in previous chapters, other X-ray binaries such as Cyg X-1 and GX 339−4 do not emit a radio jet during the soft X-ray state. When these observations of LMC X-3 were obtained the source was indeed in the soft state (see Fig. 7.5). Therefore a radio counterpart should *not have been expected* (or hoped for!).

Furthermore, the observations were obtained during a total integration time of 8.5 hours – a much deeper observation than anything previously. Assuming a distance of 44.5 kpc to the LMC (e.g. Udalski et al. 1998) and the d^{-2} luminosity law of Fender & Hendry (2000), an observed flux density of 0.05 mJy can be expected from LMC X-3. The sensitivity of the ATCA can be calculated as:

$$\Delta S_{\rm rms} \sim \frac{0.0195\, S_{\rm sys}}{\sqrt{tB}} \;\; {\rm mJy} \qquad (7.2)$$

where $\Delta S_{\rm rms}$ is the rms flux sensitivity, $S_{\rm sys}$ is the system sensitivity (= 420 Jy at 6 cm - the ATCA is marginally more sensitive at 13 cm than 6 cm but, as the former is highly susceptible to interference, the latter is more appropriate for a detection experiment), t is the integration time (mins.) and B is the bandwidth (=128 mHz). Therefore to obtain a $> 3\sigma$ detection of a 0.05 mJy source, a total integration time of 48 hours is required - considerably longer than LMC X-3 has ever been observed for.

The signal-to-noise can be further improved by a factor of $\sqrt{2}$ by setting the two receivers of each antenna to adjacent frequencies within the same waveband - **therefore a 48 hour observation of LMC X-3 during a hard state period should definitely result in the detection of a radio counterpart, unless LMC X-3 is considerably different from all other X-ray binaries.**

The *RXTE* lightcurve (Fig. 7.5) shows that the hard states can be predicted reasonably well - they occur approximately every 270 ± 15 days and last for 1-1.5 months. Although not every dip in the long modulation actually reaches the hard state, the X-ray spectra clearly show when it does - i.e. in Fig. 7.6 observation 28 shows a pure hard state, observation 29 shows the subsequent transition and the other two observations show the more common soft state.

Unfortunately, our attempts to secure 48 hours of ATCA observing time have been unsuccessful in that it is seen as too much time to give to a project in which 'the scientific return would be small'.

However, the detection of a radio counterpart to LMC X-3 is *extremely* important to our understanding of X-ray binaries. It would confirm that while the various systems appear to have different types of behaviour, it is actually the same physical processes occurring in each one. Of the five X-ray states apparent in X-ray binaries, it is the soft state that is the least understood. This is partially due to well-studied systems, such as Cyg X-1, making the transition so rarely - Cyg X-1 radio monitoring programs have so far been unable to record a full transition to the soft state and back to the hard (although this has been achieved for GX 339−4; see Fig. 1.6) - and so we are still unsure of the characteristics of the soft state and the initial signatures of a state change. All transitions from the hard state in LMC X-3 look similar at X-ray wavelengths and occur frequently and quasi-periodically; therefore predicting the time of the state transition and observing the formation of the jet will be possible. This is not the case for systems such as Cyg X-1 or the soft X-ray transients, which cannot be anticipated. Hence LMC X-3 is a vital

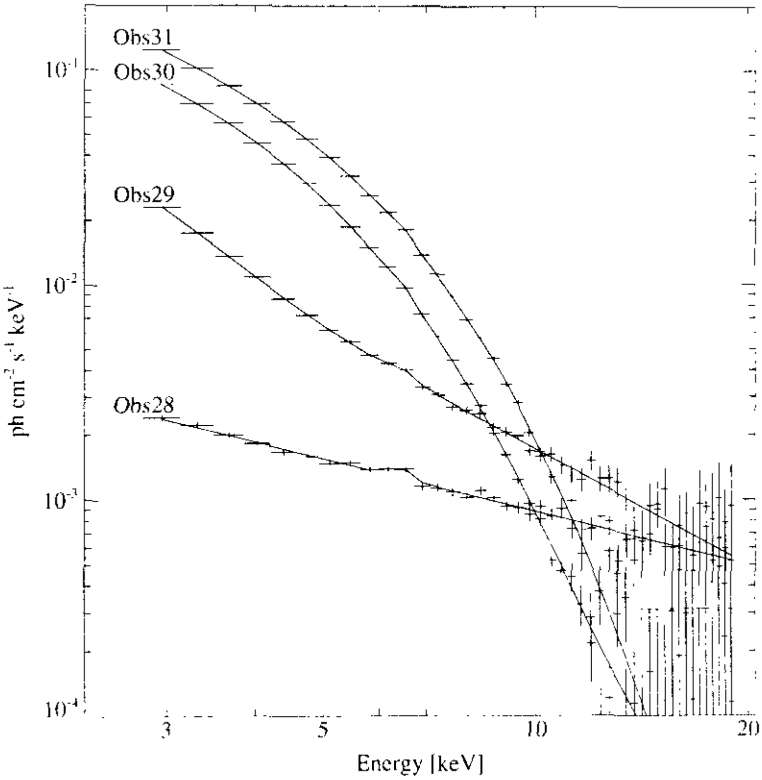

Figure 7.6: The *RXTE* X-ray energy spectra of LMC X-3 (Wilms et al. 2000). Obs28 shows a pure hard state spectrum with no evidence for an accretion disc spectrum. The disc contribution increases through the transition (Obs29) and dominates the spectrum on returning to the soft state (Obs30, 31).

system to study.

More generally, if a radio counterpart to LMC X-3 could be found, it would be the first time that radio emission has been detected from any of the LMC X-ray binaries or from *any* extragalactic X-ray binary (LMC X-1 is not a good alternative to study due to its apparent lack of hard state behaviour and also to its position within a radio nebula). This would add support to the 'short' distance to the LMC (44.5 kpc, e.g. Udalski et al. 1998) and also to the theory that the intrinsic radio luminosity of all persistent X-ray binaries is similar. It would be an important result as it would enable the radio-emitting X-ray binaries to be used as 'standard candles' for future observations with the Square Kilometre Array.

It would seem that either a change of heart or a dramatic increase in sensitivity of a southern hemisphere radio telescope is required before these predictions can be confirmed.

Chapter 8

THE 1997 OUTBURST OF THE X-RAY TRANSIENT GS 1354–64

In collaboration with P.G. Jonker, R.P. Fender, P.J. Groot, M. van der Klis & S.J. Tingay[1]

Soft X-ray transients are a class of low mass X-ray binaries in which instabilities in the accretion disc cause a sudden increase in mass accretion rate onto the compact object, resulting in an outburst (see e.g. Charles 1998 and references within). While reminiscent of the dwarf *novae* class of cataclysmic variables (Van Paradijs 1996) these outbursts occur with intervals typically 10–20 years and usually decline over several months (Tanaka & Lewin 1995; Van Paradijs & McClintock 1995), sometimes displaying 'mini outbursts' as they do so (e.g. GRO J0422+32 began to rise again $\sim$125 days after the onset of the initial outburst, peaking $\sim$15 days later. See Tanaka & Shibazaki 1996 and references within). In between outbursts the X-ray transients lie in a quiescent state and this gives us an excellent opportunity to study the companion star.

Although these objects are frequently referred to as *soft* X-ray transients on account of their ultrasoft X-ray spectra during the outbursts, an increasing number of their outbursts do *not* show the soft component (e.g. GRO J1719–24, Van der Hooft et al. 1996). Instead the power law component dominates the energy spectrum, reminiscent of the low/hard X-ray state of the persistent source Cyg X-1. However, as the term 'hard X-ray transient' has previously been used to describe the Be star+neutron star binaries (which typically

---

[1] Accepted for publication in MNRAS

show hard X-ray spectra) we do not use this term here.

A large number of the X-ray transients have been classified as black hole candidate (BHC) X-ray binaries – where possible, the preferred method is to determine the mass function (e.g. Charles 1998 and references within) but in a large number of cases a black hole nature has been suggested on account of the X-ray properties. Following the *unification* scheme for the X-ray power density spectra of neutron stars and BHCs proposed by Van der Klis (1994; 1995), the power spectra of BHCs can be sorted according to the mass accretion rate: this is thought to increase from the low state, through the intermediate state and the high state, up to the very high state (but see also Homan et al. 2000). During the low state strong band-limited noise is present. In this scheme low frequency ($\lesssim 1$ Hz) quasi-periodic oscillations (QPOs) seen in the low state are seen as an aspect of the low state noise. Recently, Psaltis, Belloni, & Van der Klis (1999) reported correlations between the frequencies of QPOs and broad band power spectral features of neutron star and black hole X-ray binaries. Transitions between X-ray states have been observed during the rise and subsequently during the decay of an outburst for a number of sources (e.g. GS 1124–68 (Ebisawa et al. 1994), GRO J1655–40 (Méndez et al. 1998)).

Ground-based follow up observations of X-ray transients have shown that outbursts also occur at optical and radio frequencies. A0620–00, GRO J1655–40, GS 2023+338 (V404 Cyg) and GS 1124–684 are examples of X-ray transients detected in all three wavelength regimes (Tanaka & Lewin 1995, and references within); in particular, the X-ray, optical and radio behaviour for GS 2023+338 were correlated during the 1989 outburst (Han & Hjellming, 1992) and it is interesting to note that during this outburst (as in the case of GS 1354–64) the source remained in the low/hard state (e.g. Tanaka & Lewin 1995).

The optical emission is thought to be the result of reprocessing of X-rays in the disc – the disc absorbs X-rays and re-emits them at lower energies, delaying the optical by a few seconds as reported by Hynes (1998) in the case of GRO J1655–40. The radio appears to be the result of beamed synchrotron emission taking place in relativistic ejections of material from the centre of the disc: this may be in response to material being transported through the disc by the instability and so we might expect some correlation between the radio and the X-ray/optical behaviour. However, a comparison between the radio lightcurves of A0620–00, GS 1124–68 and GS 2000+25 suggests that their profiles depend on inclination angle, the number of ejections, the time between them and their strength and speed (Kuulkers et al. 1999). Therefore, as the radio emission may be anisotropic in the observer's frame, unlike (presumably) X-ray and optical, we might instead expect that it is *not* observed to be so closely correlated with these two components as they are with each other.

GS 1354–64

On 1987 February 13, the ASM on board the *Ginga* satellite (Swinbanks 1987) discovered GS 1354–64, observing it until 1987 August (Makino et al. 1987). The X-ray data were well fit by a soft disc blackbody component, with inner disc temperature of ~0.7 keV, and a hard power law with photon index 2.1 (Kitamoto et al. 1990). These X-ray properties are common for X-ray transients during outburst (Tanaka and Lewin 1995) and hint at a black hole nature for the compact object. It was also observed in the optical during the outburst, yielding magnitudes of $V \sim 16.9$, $B \sim 18$ (Kitamoto et al. 1990). GS 1354–64 had not previously been observed in the radio.

The position of this source on the sky is consistent with the position of two other transient sources; Cen X-2 (Francey et al. 1971) and MX 1353–64 (Markert et al. 1979). Cen X-2 was the first 'soft X-ray transient' discovered and one of the brightest (Tanaka & Lewin 1995). The outbursts of MX 1353–64 (1972) and GS 1354–64 (1987 and 1997) reached much lower intensities and showed different X-ray spectral properties – if Cen X-2 and MX 1353–64 were the same source as GS 1354–64 then it must show at least four different states (Kitamoto et al. 1990). This is not unfeasible – e.g. GX 339–4 has been observed in four states, Cyg X-1 in three (see Fender 2000, and references within) – and the field is not so crowded that it is likely that a number of different X-ray transients are so close together; it is therefore probable that these sources are indeed one and the same, in which case we note that the 1997 outburst was significantly sub-Eddington. The error circles for the positions of each 'source' can be found in Kitamoto et al. (1990). We investigate the nature of the various states further in Section 4.

GS 1354–64 was observed in outburst again in 1997 November. Preliminary results from the ASM on board the Rossi X-ray Timing Explorer (*RXTE*) showed a rise from 16 to 50 mCrab in the first half of November (Remillard, Marshall & Takeshima 1997); the BATSE instrument on the Compton Gamma Ray Observatory (*CGRO*) detected hard X-rays up to 200 keV which rose from 60 to 160 mCrab (Harmon & Robinson 1997). The optical and infrared counterparts were also detected with magnitudes of $R \sim 16.9$, $B \sim 18.1$ (Nov. 22; Castro-Tirado, Ilovaisky & Peterson 1997) and $J \sim 15.35$, $K \sim 13.95$

(Nov. 20; Soria, Bessell & Wood 1997). Optical spectroscopy during the decay revealed strong emission lines corresponding to Hα, Hβ and He II λ4686 plus weaker He I λ4471 and Hγ emission (Buxton et al. 1998). The Hα emission profile varied from single- to double-peaked over three nights of observations during the decay from outburst, indicating the presence of an accretion disc. The radio counterpart was detected at 2.5, 4.8 and 8.6 GHz with a flux of 1–3 mJy (Nov. 24/25; Fender et al. 1997). No indication of the orbital period was detected at any wavelength.

A recent paper by Revnivtsev et al. (2000) gives an analysis of *RXTE*/ASM, HEXTE and PCA data during the outburst. Their work indicates that the X-ray energy spectrum is dominated by a power law, typical of X-ray binaries in the low/hard state. However, the fit is improved by the addition of a 6.4 keV iron line and a reflection component suggestive of the presence of an accretion disc; low energy disc photons are upscattered by a Comptonising corona to higher energies, resulting in the X-ray emission. Here we present *B*, *V* and *R* photometry and radio data from the outburst, combining it with further *RXTE*/PCA analysis and public ASM and *CGRO*/BATSE data.

8.1 Observations

We have obtained public *RXTE*/ASM, *RXTE*/PCA and *CGRO*/BATSE data for the 1997 outburst of GS 1354–64. Lightcurves for this and for our optical and radio data are shown in Fig. 8.1.

8.1.1 X-ray

The *RXTE* satellite observed GS 1354–64 ten times with the onboard proportional counter array (PCA; Jahoda et al. 1996). We present only the analysis of the first nine of these since the count rates were too low and the observing time too short during the last observation to constrain our fit parameters. During the outburst a total of nearly 60 ksec of good data was obtained. A log of the observations we present here (following background corrections) can be found in Table 8.1. During ~4% of the time only 4 of the 5 PCA detectors were active – when this was the case the data were averaged. The count rates quoted are approximate because they depend on the background model and can vary over an observation.

All the data were obtained in each of three modes. The Standard 1 mode has a time resolution of 1/8 s in one energy channel (2–60 keV). The Standard 2 mode has a time

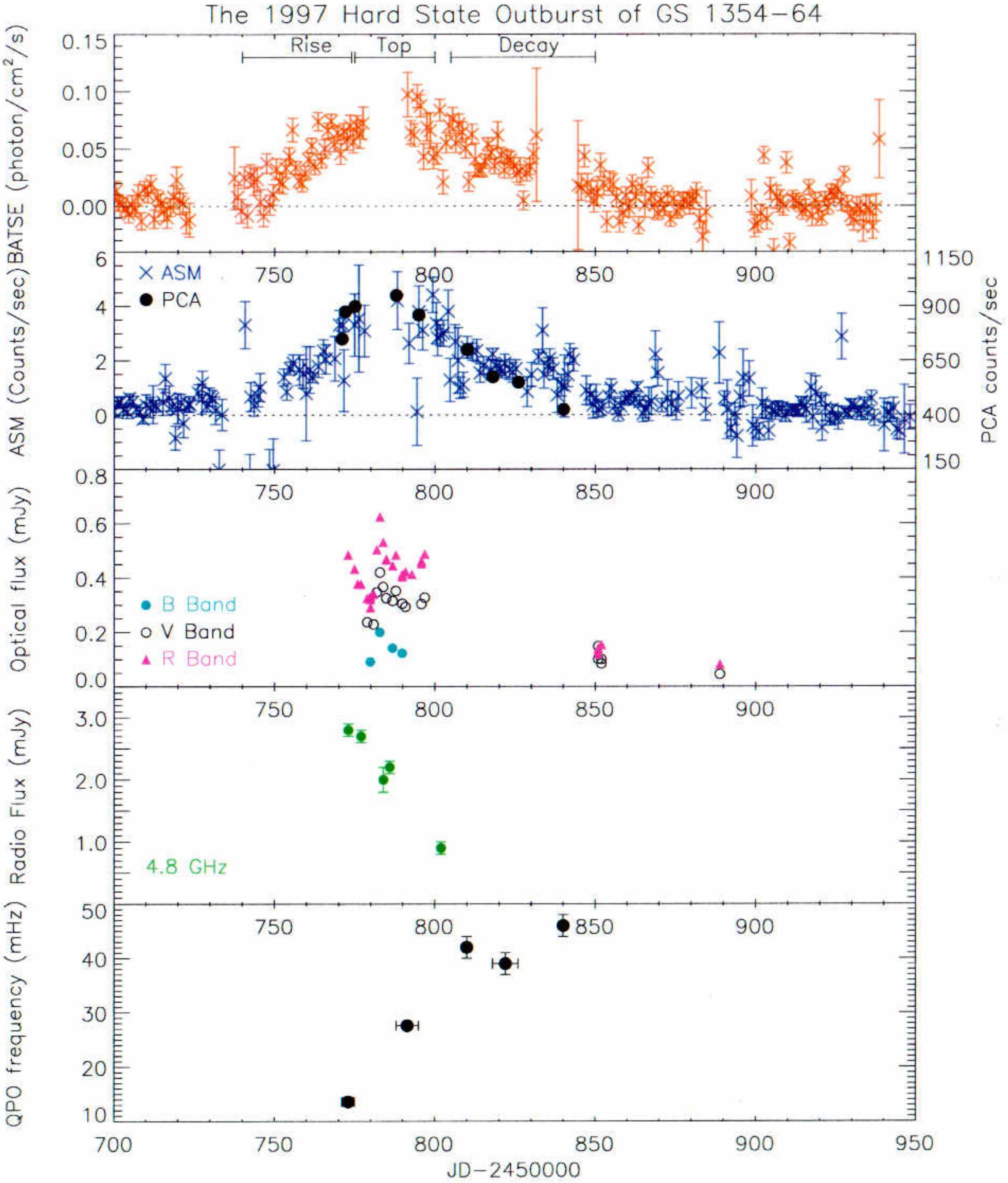

Figure 8.1: BATSE, ASM, PCA, optical and radio (4.8 GHz) lightcurves of the 1997 outburst for the period 8 October 1997 – 16 May 1998. Radio lightcurves at other frequencies are shown later in this paper. Error-bars on the optical points are smaller than the symbols.

resolution of 16 s and the effective 2–60 keV PCA energy range is covered by 129 energy channels. In addition, high time resolution data (with a time resolution of 125 μs or better) were obtained for all observations in at least 64 energy channels covering the effective 2–60 keV PCA energy range.

Additional soft (2–12 keV) X-ray data has been obtained from the ASM on board *RXTE*; we use the public archive data from the web (http://xte.mit.edu). A detailed description of the ASM, including calibration and reduction is published in Levine et al. (1996). Our hard (20–100 keV) X-ray data came from the BATSE instrument on the Compton Gamma Ray Observatory (*CGRO*) and was processed using the standard BATSE earth occultation software. Again, we have used the public archive data from the web. A detailed overview of the BATSE instrument can be found in Fishman et al. (1989).

8.1.2 Optical

The optical counterpart to GS 1354–64 was observed on 18 nights during 1997 November/December and 2 nights the following February. Further observations taken a year later revealed no source suggesting that the source in quiescence has $V \geq 22$ (≤ 0.005 mJy). The 0.91m Dutch telescope at the European Southern Observatory in Chile was used, equipped with a 512×512 TEK CCD and standard Johnson B and V, and Cousins R

Table 8.1: Log of the *RXTE*/PCA observations. The penultimate column indicates the category of the observation (see text).

Number	Observation ID	Date &	Total on source observing time (ksec.)	Category	Mean count rate (cts/s)
1	20431-01-01-00	1997-11-18	3.2	rise	~750
2	20431-01-02-00	1997-11-19	6.0	rise	~875
3	20431-01-03-00	1997-11-22	8.4	rise	~900
4	20431-01-04-00	1997-12-05	7.6	top	~950
5	20431-01-05-00	1997-12-12	6.4	top	~860
6	30401-01-01-00	1997-12-27	7.0	decay1	~700
7	30401-01-02-00	1998-01-04	7.7	decay2	~575
8	30401-01-03-00	1998-01-12	6.1	decay2	~550
9	30401-01-04-00	1998-01-26	7.4	decay3	~425

filters. Typical exposure times were 20 minutes in B and 5 minutes in V and R (although there were also some 10 minute observations in all three bands).

The data were processed using routine bias subtraction and flat field division in IRAF. Aperture photometry was applied, both to GS 1354−64 and to eight field stars; the coordinates of these stars are shown in Table 8.2. The photometry was then calibrated (also with IRAF) using photometric standard stars in the fields of PG 0231+051 and Mark A (Landolt 1992). Magnitudes are given in Table 8.3. The magnitudes were converted into mJy to ease comparison with the radio fluxes; Johnson conversions were used for the B and V bands, Cousins for the R band.

8.1.3 Radio

Radio observations were made at the Australia Telescope Compact Array at 1.384, 2.496, 4.800 and 8.640 GHz at eight epochs during the period JD 2450773 - JD 2450802 (1997 November 20, 24, 25 and December 1, 2, 3, 4, 19). The array was in configuration 6C, which included the 6 km antenna, giving a nominal angular resolution of $\sim$ 1 arcsec at 8.640 GHz. Standard flagging, calibration and imaging techniques were used within MIRIAD; the flux calibrator was PKS 1934−638 and the phase calibrator was PMN J1417−5950. The integration times for the first epoch totalled 2.5 hours at each frequency; typical integration times for following epochs were <1 hour, yielding reasonable S/N but unfortunately poor

Table 8.2: Identifiers, coordinates (J2000 equinox) and magnitudes of the eight reference stars used in the photometry. The 'BJF' part of the identifier refers to Brocksopp, Jonker, Fender et al. 2000 (this work)

Identifier, RA, Dec.	V (mags)	$B-V$ (mags)	$V-R$ (mags)
BJF J135807.07−644309.9	16.269 (0.005)	0.987 (0.016)	0.632 (0.006)
BJF J135807.94−644309.3	16.028 (0.004)	1.111 (0.013)	0.646 (0.005)
BJF J135815.53−644305.1	15.446 (0.002)	1.905 (0.014)	1.088 (0.002)
BJF J135814.93−644337.6	15.797 (0.003)	1.570 (0.015)	0.895 (0.003)
BJF J135813.21−644348.4	15.506 (0.002)	1.914 (0.015)	1.084 (0.002)
BJF J135809.39−644439.1	15.463 (0.003)	0.889 (0.006)	0.557 (0.003)
BJF J135807.71−644513.1	15.036 (0.002)	0.937 (0.005)	0.559 (0.002)
BJF J135811.18−644516.0	15.026 (0.002)	0.811 (0.005)	0.485 (0.002)

Table 8.3: Calibrated magnitudes for our optical photometry. Errors are given in parentheses.

JD−2450000	B	V	R
772.87	–		16.89 (0.01)
774.86	–		17.02 (0.02)
775.86	–		17.16 (0.01)
776.86	–	–	17.17 (0.02)
778.86	–	18.02 (0.07)	17.32 (0.02)
779.84	–	–	17.34 (0.03)
779.85	–		17.30 (0.01)
779.86	19.18 (0.07)	–	17.45 (0.06)
780.85	–	18.06 (0.02)	17.28 (0.01)
781.85	–	17.64 (0.03)	16.85 (0.01)
782.84	18.32 (0.02)	17.40 (0.03)	16.62 (0.01)
783.84	–	17.55 (0.01)	16.79 (0.01)
784.85	–	17.68 (0.01)	16.93 (0.01)
784.86	–	–	16.93 (0.01)
786.86	18.70 (0.03)	17.71 (0.07)	16.99 (0.02)
787.85	–	17.59 (0.01)	16.89 (0.01)
789.85	–	–	17.07 (0.02)
789.85	18.85 (0.14)	17.75 (0.02)	17.09 (0.01)
790.84	–	17.79 (0.01)	17.04 (0.01)
792.85	–	–	17.07 (0.05)
795.84	–	17.75 (0.02)	16.95 (0.03)
795.84	–	–	16.97 (0.01)
796.84	–	17.67 (0.02)	16.89 (0.01)
850.88	–	–	18.41 (0.22)
850.88		18.95 (0.40)	18.28 (0.10)
850.88	–	–	18.29 (0.06)
850.88		18.53 (0.31)	18.24 (0.14)
851.89	–	18.95 (0.02)	18.14 (0.01)
888.88	–	19.82 (0.14)	18.83 (0.06)

uv coverage (the *uv* plane is the projection of the antenna baselines onto the plane of the sky). As a result, for most epochs the synthesised beam from the observations was extremely elongated. Furthermore the sparse *uv* coverage meant that the flux densities measured were a function of the cell size used in making the maps, as a result of different gridding in the FFTs. Both effects resulted in difficulty in measuring reliably the flux densities at the epochs with the shortest observations. In order to improve the situation, we combined data from two adjacent days (for Nov 24/25, Dec 01/02 and Dec 03/04), which significantly improved the *uv* coverage in all three cases. In addition, as well as performing point-source fits to the final (naturally weighted) images, we also performed point-source fits in the *uv* plane, thereby avoiding gridding errors. On Dec 3/4 data were collected in two adjacent bands, centred on 2.240 and 2.496 GHz respectively, and

Table 8.4: ATCA observing log, and results of image-plane (naturally weighted) and *uv*-plane point-source fits to the data.

Date (JD−2450000)	Frequency (GHz)	Total Time (hrs)	Image plane fit (mJy)	*uv* plane fit (mJy)	Linear Pol. (3σ)	Circular Pol. (3σ)
773	1.384	2.5	2.6 ± 0.2	3.6 ± 0.1	<8%	<7%
	2.496		2.8 ± 0.1	2.9 ± 0.1	<9%	<8%
	4.800		2.8 ± 0.1	2.9 ± 0.1	<6%	<6%
	8.640		1.6 ± 0.1	1.9 ± 0.1	<15%	<16%
777-778	1.384	0.7	2.5 ± 0.5	2.3 ± 0.3		
	2.496		2.5 ± 0.1	3.7 ± 0.2		
	4.800		2.7 ± 0.1	3.7 ± 0.3		
	8.640		2.5 ± 0.1	2.2 ± 0.2		
784-785	2.368	0.58	3.5 ± 0.1	3.7 ± 0.3		
	4.800		2.0 ± 0.2	2.7 ± 0.2		
	8.640		1.5 ± 0.1	2.2 ± 0.3		
786-787	4.800	1.25	2.2 ± 0.1	3.1 ± 0.2		
	8.640		1.8 ± 0.2	3.9 ± 0.5		
802	4.800	0.75	0.9 ± 0.1	1.7 ± 0.1		
	8.640		1.1 ± 0.1	1.8 ± 0.4		

combined to improve the S/N by $\sqrt{2}$ at an effective frequency of 2.368 GHz.

In Table 8.4 we present the ATCA observing log and results of our image-plane and *uv*-plane fits to a point source. It is clear that both the image-plane and *uv*-plane results follow a similar trend, steadily declining by a factor ~ 2 in the month between Nov 20 and Dec 19. It is also clear that the spectrum is generally flat, especially at lower ($\leq$ 4.800 GHz) frequencies. Between 4.800 - 8.640 GHz the spectrum appears to be initially optically thin, but gradually flattens until becoming inverted by the last detection on Dec 19. We note that the *uv*-plane fits invert one epoch earlier than those of the image plane.

8.2 Results and Analysis

8.2.1 X-ray*

* *Note that the X-ray data reduction and construction of power spectra was the work of* P.G. Jonker

The X-ray lightcurves in Fig. 8.1 have a triangular shape, as defined by Chen, Shrader & Livio (1997) with a possible secondary outburst during the decay at ~ JD 2450835. It is clear from Fig. 8.1 that the soft and hard X-rays are well correlated – we obtain a value of 0.6 for the Spearman rank correlation coefficient between the daily averaged *RXTE*/ASM and *CGRO*/BATSE lightcurves, despite the poor S/N. We also note that the energy spectra of both X-ray bands are dominated by a power law component (Harmon & Robinson 1997, Revnivtsev et al. 2000) which indicates a common origin, i.e. a Comptonising corona which upscatters low energy (optical and UV) disc photons to higher energies (e.g. Van Paradijs 1998). This is significantly different from the 1987 outburst, when the X-rays showed a soft disc blackbody spectrum (Kitamoto et al. 1990). *In the 1997 outburst the presence of an accretion disc can be inferred only indirectly with the inclusion of a reflection component in the soft X-ray spectrum (Revnivtsev et al. 2000).*

Other than the average flux levels shown in Fig. 8.1 for each of the *RXTE*/PCA observations there was no variability to be seen directly. Instead, for all PCA observations we calculated power spectra with a Nyquist frequency of 512 Hz using data segments of 512 s length each in one combined broad energy band ranging from 2–60 keV. To characterise the power spectra (1/512–512 Hz) we used a fit function consisting of a broken power law, plus a Lorentzian with its frequency fixed at 0 Hz to describe the low frequency noise component. We also included a second Lorentzian to describe the QPO on top of the noise

Table 8.5: Properties of the two Lorentzians and the broken power law component. The frequency of the noise component was fixed at 0 Hz.

Category	Rise	Top	Decay1	Decay2	Decay3
rms QPO (%)	10 ± 2	10 ± 1	10 ± 2	10 ± 2	9 ± 2
FWHM QPO (mHz)	4.4 ± 1.5	7 ± 1	11^{+11}_{-6}	19 ± 7	11^{+10}_{-4}
ν_{QPO} (mHz)	13.6 ± 0.8	27.6 ± 0.6	42 ± 2	39 ± 2	46 ± 2
rms noise (%)	23.1 ± 0.2	22.1 ± 0.2	21.8 ± 0.5	24.1 ± 0.3	25.7 ± 0.5
FWHM noise (Hz)	3.84 ± 0.06	4.87 ± 0.07	5.1 ± 0.1	4.8 ± 0.1	4.6 ± 0.2
rms break (%)	33.4 ± 0.6	27.7 ± 0.4	27.3 ± 0.7	26.3 ± 0.4	26.8 ± 0.8
ν_{break} (mHz)	56 ± 5	60 ± 4	91 ± 7	96 ± 4	110 ± 10
α $(\nu < \nu_{break})$	0.59 ± 0.07	0.100 ± 0.001	0.12 ± 0.05	$(-3 \pm 5) \times 10^{-2}$	0.22 ± 0.07
α $(\nu > \nu_{break})$	1.46 ± 0.01	1.53 ± 0.03	1.55 ± 0.05	1.82 ± 0.05	1.9 ± 0.1

component. The noise Lorentzian became negative when it was treated as a free parameter. Errors on the fit parameters were determined using $\Delta\chi^2$=1.0 (1σ single parameter). Power arising in the power spectrum due to Poisson noise has been subtracted – this also takes deadtime into account. The fit to the normalised (Belloni & Hasinger 1990) power spectrum of observations 4 and 5 combined is shown in Fig. 8.2.

We divided the outburst into three parts on the basis of the X-ray lightcurve: the rise, the top, and the decay (see Table 8.1, Fig. 8.1). The decay observations were further subdivided into three parts in order to follow the changes in the fit parameters during the decay of the outburst.

The properties of our fit parameters are given in Table 8.5. We detect a QPO at low frequencies; its frequency increased from 13.6 ± 0.8 mHz at the rise to 46 ± 2 mHz at the end of the decay. The FWHM also increased over this *range from* 4.4 ± 1.5 *mHz to* 11^{+10}_{-4} mHz. The break frequency increased gradually from 56 ± 5 mHz during the rise to 110 ± 10 *mHz during the last part of the decay.* The power law index at frequencies below the break frequency changed from 0.59 ± 0.07 during the rise to 0.100 ± 0.001 at the top, during the decay it varied between 0.22 ± 0.07 and $(-3 \pm 5) \times 10^{-2}$. At frequencies above the break frequency the power law became gradually steeper with indices of 1.46 ± 0.01 during the rise to 1.9 ± 0.1 during the last part of the decay.

The increasing of the frequency at which the QPO and break occur suggest that the inner radius of the disc is decreasing as the outburst takes place (Revnivtsev et al. 2000).

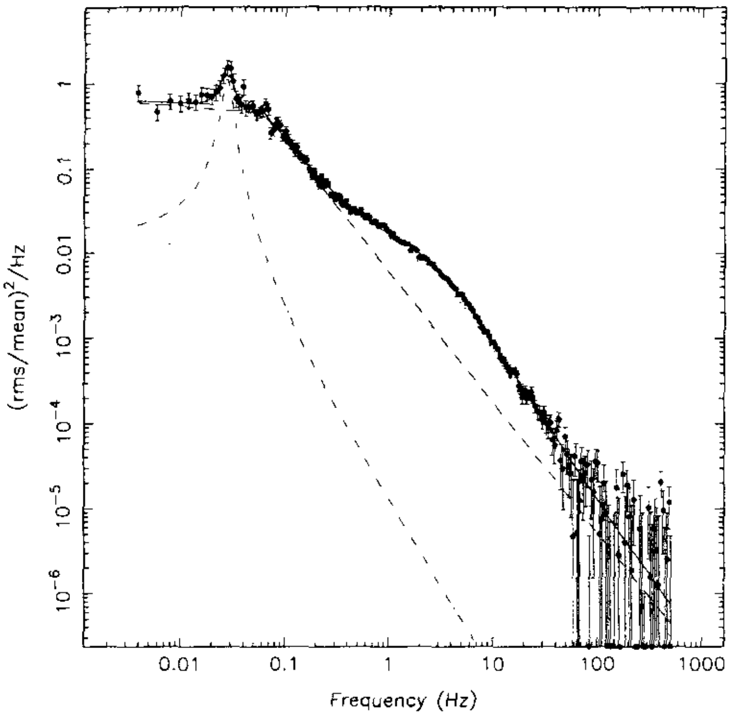

Figure 8.2: Normalized (Belloni & Hasinger 1990) power spectrum of observations 4 and 5 combined. The power arising in the power spectrum due to Poisson noise has been subtracted. The solid line represents the best fit to the data.This best fit function is built up by three components. The dashed line represents the contribution of the broken power law component, the dotted line represents the contribution of the Lorentzian component with its frequency fixed at 0 Hz, and the dashed-dotted line represents the contribution of the Lorentzian used to represent the QPO.

A general softening of the spectrum, consistent with this geometry, was also observed and was seen previously in GS 1354−64 by Kitamoto et al. (1990). A similar increase in frequency of low-frequency QPOs was discovered during an outburst of the X-ray transient GRO J1719−24 by Van der Hooft et al. (1996). If the increasing frequencies of the QPOs really do relate to the inner disc then it is interesting to note that the inner disc radius does not appear to increase again during the decay from outburst.

From the high fractional rms amplitude of the low frequency noise throughout the outburst, the hard spectrum (Revnivtsev et al. 2000) and the relatively low intensity increase (compared with the outbursts of Cen X-2 (Francey et al. 1971) and MX 1353−64 (Markert et al. 1979) – we investigate this further in Section 8.3) we conclude that the source was in the low/hard state during the entire outburst (see for reference Van der Klis 1995). This is unusual as the majority of X-ray transients enter the high/soft state during outbursts; known exceptions include GRO J0422+32 (e.g. Sunyaev et al. 1993), GRO J1719−24 (e.g. Van der Hooft et al. 1996) and GS 2023+338, although in the latter case it is possible that the system was in a soft but absorbed state at its peak, then returning to the low/hard state (Życki, Done & Smith 1999).

While the increase in QPO frequency and in break frequency during the decay of the outburst is *not* a common feature of BHCs whilst in the low/hard state, it appears that it *is* a typical feature during the *outbursts* of X-ray transients (see Section 4). Observations of the persistent BHC's during *transitions* from the low/hard to the high/soft state would be useful to determine whether or not the QPO frequency increases at these times – *RXTE* observations of the 1996 Cyg X-1 transition to the soft (intermediate?) state suggest that although a mHz QPO was present and the frequency certainly varied, it was not simply a frequency increase during the transition (Cui et al. 1997).

8.2.2 Optical

Our optical observations show that the X-ray increase was accompanied by an optical outburst reaching $B \sim 18.3$, $V \sim 17.3$ and $R \sim 16.6$ at maximum. As is typical for X-ray transients (e.g. Van Paradijs & McClintock (1995) and references within), the subsequent decline was considerably longer than that of the X-rays, taking at least 120 days. Further observations a year later revealed no source, suggesting that there had been a brightening of ≥ 5 mags. above the quiescent level.

The photometry suggests that the optical and X-ray events were not as well correlated as would be expected in a 'normal' soft X-ray transient event, in which the dominant source of optical emission would be reprocessing of X-rays. Indeed, whereas the X-rays produce a gradual rise and decay the optical photometry appears to peak at least three times. The three apparent peaks are labelled on Fig. 8.3.

The first 'peak' occurs prior to our observations, but can be inferred from the R-band decline at the beginning of the dataset. The X-rays have begun to rise by this point but there is still a $\geq$10 day delay after our initial R band observations before the X-ray peak is reached. This optical peak is unlikely to be the result of reprocessing of soft disc X-rays on account of the low X-ray flux and the lack of evidence for a disc component in the X-ray energy spectrum. (It is not impossible, despite the lack of correlation e.g. GRO

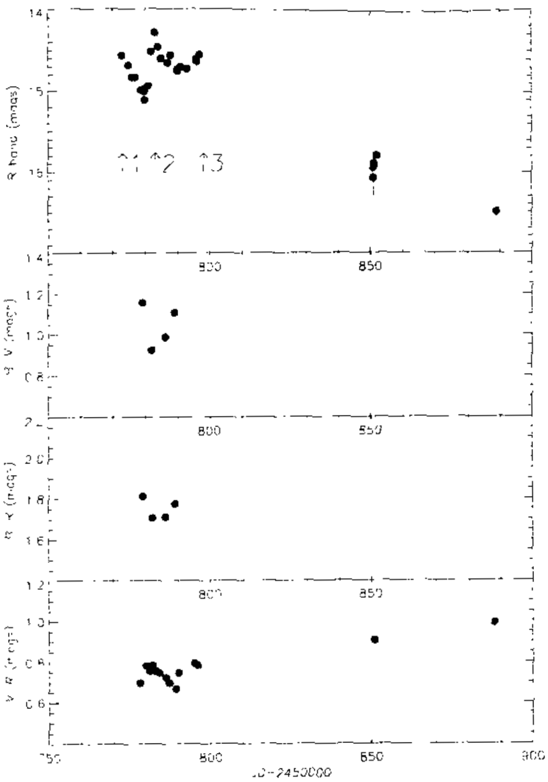

Figure 8.3: Dereddened R-band photometry and $B-V$, $B-R$ and $V-R$ colour evolution (corrected for interstellar extinction using $E(B-V) \sim 1$ (Kitamoto et al. 1990) and the A_λ/A_V relations of Cardelli, Clayton & Mathis (1989)). Error bars are plotted but are smaller than the symbols in the colour plots. Arrows on the R-band plot indicate the three apparent peaks in the photometry.

J1655−40 shows an anti-correlated X-ray/optical outburst but echo mapping shows that reprocessing of X-rays is still the dominant contributor to the optical flux during hard X-ray flaring (Hynes et al. 1998).)

A similar phenomenon is seen in dwarf novae - as the disc instability moves inwards from the outer parts of the disc, the outburst is seen first in the optical and then in the ultraviolet. While it should be feasible that this phenomenon occurs also in X-ray transient events, it has rarely been observed (e.g GRO J1655−40, Orosz 1997). If this is the case for this outburst of GS 1354−64 then our data suggests that the instability takes $\geq$10 days to cross the disc and peak in the X-rays. This is not impossible - Orosz (1997) calculates an optical lead of 6 days - but would place fairly large lower limits on the size of the orbit and/or donor star. The outburst of GRO J1655−40 was different from that of GS 1354−64 in that it reached the high/soft state (possibly the very high state (Méndez et al. 1998)), it was considerably more luminous at all wavelengths and the profiles of its rise to maximum in the BATSE and ASM data for GRO J1655−40 were considerably longer. In particular, the hard X-ray rise occurred ∼ 30 days after the soft X-rays – a phenomenon not seen in the case of GS 1354−64, where the ASM and BATSE data appear well correlated on account of both X-ray bands being dominated by the (same?) power law component. GRO J1655−40 may therefore not be a suitable system with which to compare GS 1354−64.

The second peak (and only peak for which both the rise and decay were observed) took place during the 'top' period of the X-ray lightcurve (∼JD2450784) and was observed in all three optical bands. Without full X-ray coverage and better S/N in the X-ray bands it is not possible to say whether there is any evidence for correlated X-ray/optical behaviour. There is the hint of a small decline in the X-rays coincidentally with the decay of this second optical peak but the S/N does not allow us to be conclusive. If the optical and X-ray were correlated then we would assume that the second optical peak was produced by the reprocessing of X-rays; a non-correlation would suggest that a second instability had passed through the optical-emitting regions of the disc.

The V and R bands also suggest the presence of a third rise in the lightcurve, ∼15 days after the time of the first maximum; it may also be hinted at in the X-rays, although a more significant secondary X-ray outburst takes place during the decay around JD 2450835. These small secondary maxima during the decay of an outburst are seen commonly in X-ray transients (e.g. GRO J0422+32, Callanan et al. 1995) and are due to additional, smaller instabilities.

Using the reddening correction determined by Kitamoto et al. (1990), $E(B-V) \sim 1$, and the A_λ/A_V relations of Cardelli, Clayton & Mathis (1989) we have corrected our photometry for interstellar extinction ($A_B \sim 4.1$, $A_V \sim 3.1$, $A_R \sim 2.3$). In Fig. 8.3 we plot dereddened R-band magnitudes and colour evolution over time.

We have no colour information for peak 1 but the $B-V$, $B-R$ and $V-R$ colours for peak 2 all hint at being anti-correlated with the photometric lightcurve, although there may be a delay of ∼ 0.5 days in the case of the latter. (Alternatively it is possible that the $V-R$ colours are actually anti-correlated with the other colours, in which case there must be an additional contribution to $V-R$ from some other component, perhaps the jet.) The colours also suggest that the source became bluer during the rise to peak 2: this could be explained by a disc instability moving inwards as the temperature and density of the disc will be increasing inwards. On the decay from peak 2 the colours redden, consistent with the disc cooling. We notice that the $B-V$ and (to a lesser extent) the $B-R$ colours vary more significantly than $V-R$; this suggests that, while the whole disc is brightening, the hot inner regions do so in particular and this causes a greater brightening in the B band than the other two. This would be expected and shows that at shorter wavelengths the disc spectrum dominates the optical emission. Clearly improved coverage of future outbursts would be extremely beneficial in order to confirm these possibilities.

Although we have only one pair of B band/ASM points (and these are separated by 1.5 days), we also calculate the ratio of X-ray to optical luminosity, $\xi = B_0 + 2.5 \log F_x(\mu\mathrm{Jy})$, where B_0 is the extinction corrected B magnitude and F_x is the X-ray flux (Van Paradijs & McClintock 1995). Assuming $E(B-V) \sim 1$, an interstellar extinction (A_B) of 4.1 mags, and 1 crab $\sim$ 75 counts/sec ($RXTE$/ASM) $\sim$ 1060 μJy we obtain a value of $\xi = 19$. This is slightly lower than that of other X-ray transients, indicating that the source might be under-luminous in the X-rays typically, $\xi = 22$ (± 1). We note that during the 1987 outburst the ratio was calculated to be ~ 16. This is surprisingly low and was thought likely to be due to errors in the reddening corrections and/or non-simultaneity of the observations (Van Paradijs & McClintock 1995). During the 1997 outburst it appears that the optical emission was dominated by viscous heating from the disc with minimal reprocessing. Other potential sources for the optical excess are synchrotron emission from the jet and/or a possible contribution due to irradiation of the companion star, although this may be insignificant given the low magnitude of the source in quiescence.

It has been suggested that the dwarf novae obey a relationship (Warner 1995)

$$M_v(\mathrm{max}) = 5.74 - 0.259 P_{orb}(h) \tag{8.1}$$

where M_v(max) is the maximum absolute visual magnitude attained during the outburst by the (non-irradiated) disc. Assuming an orbital period of 15 hours (P. Charles, private communication) then this suggests that the maximum apparent magnitude for the disc of GS 1354−64 is $V \sim 20$. Since the outburst reaches a brigher maximimum than this it appears that irradiation of the companion star is a significant effect.

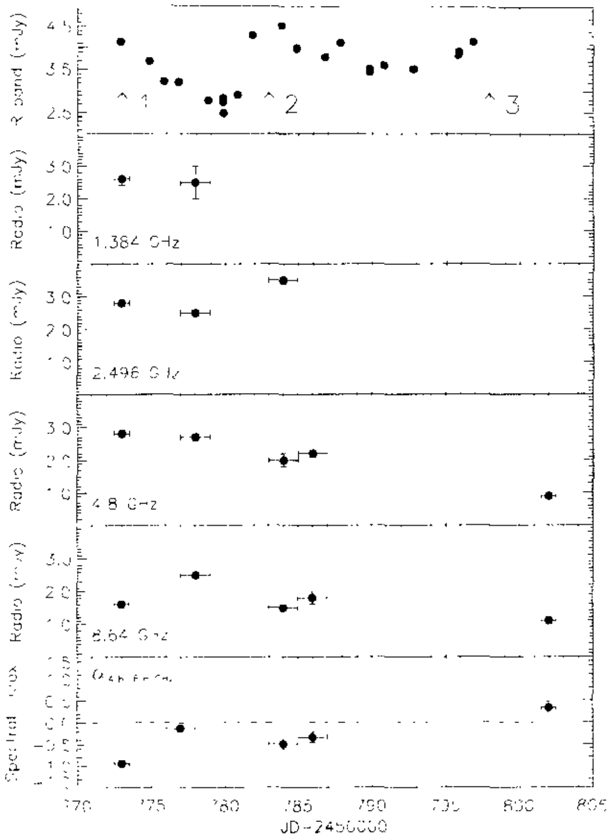

Figure 8.4: The R-band photometry and radio lightcurves at 1.4, 2.5, 4.8 and 8.6 GHz on an expanded scale. Evolution of the spectral index (α) at 4.8 and 8.6 GHz is shown in the bottom panel. Arrows on the R-band plot indicate the three apparent peaks in the optical photometry.

8.2.3 Radio

We have observed the radio counterpart to GS 1354−644 for the first time. Detected at 1.384, 2.496, 4.8 and 8.64 GHz it is a weak source of 1–3 mJy and our radio maps show no evidence for extension – combining data from the first two epochs suggests that the upper limits to the source extension are 11.2, 6.9 and 4.9 $\times 10^3$ AU at 2.5, 4.8 and 8.6 GHz respectively, assuming a distance of $\sim$ 10 kpc (Kitamoto et al. 1990). This is not really surprising given such a low flux and the rather short exposure times of our observations. We have also determined the radio position of GS 1354−644 by assuming a point source and fitting a Gaussian – by assuming an error of 200 mas on the position of the phase calibrator we calculate the position of GS 1354−644 to be R.A.: 13:58:09.7, dec:

−64:44:05.8 (±200 mas) at 4.8 GHz – the positional error is dominated by the uncertainty in the absolute coordinates of the phase calibrator.

Lightcurves at all four observing frequencies are shown in Fig. 8.4. Surprisingly, the radio frequencies are not well correlated with each other – although they all seem to follow similar trends, in that some rise has taken place prior to our observations and a second rise may have occured just after the second optical peak. Exact time differences cannot be measured as each radio point contains data spanning up to two days. (Note that it is possible that this apparent lack of correlation between the radio frequencies may be an artefact of the poor *uv* coverage). The lack of correlation with the X-rays and optical photometry is perhaps surprising and possibly due either to our lack of data coverage or to reasons given by Kuulkers et al. (1999). Each maximum is probably associated with an ejection event as seen in e.g. A0620−00 (Kuulkers et al. 1999).

While we would expect a certain frequency dependency in the relative delays and luminosities for these ejection events, the lack of obvious correlation is surprising. Correlated radio/optical behaviour has been observed previously (e.g. GS 2023+338, Han & Hjellming 1992) and it is possible that had we better radio coverage and/or S/N then the same might be true here for all radio frequencies.

Fig. 8.4 also shows the evolution of the spectral index ($S_\nu \propto \nu^\alpha$ where α is the spectral index, ν is the frequency and S_ν is the flux density at ν in mJy) over the period of our observations. The spectral indices are also tabulated in Table 8.6 and were determined by fitting the above power law to the data at 4.8 and 8.6 GHz – the other frequencies were not used to calculate the spectral index as they were not measured at every epoch. Clearly α is generally negative particularly at the first epoch, corresponding to optically thin synchrotron emission. The spectrum becomes inverted at the final epoch which is probably consistent with a partially self-absorbed continuous jet as seen in Cyg X-1 and GX 339−4 (e.g. Fender 2000 and references within). Alternatively the spectrum inversion could be indicative of a plasmon ejection emitting optically thick synchrotron emission which will evolve to optically thin at successively lower frequencies as the plasmon expands (see e.g. Kuulkers et al. 1999 for further evidence of this phenomenon) – however this is more typically seen in *soft* X-ray transient outbursts. We note that using the *uv* plane fluxes from Table 8.4 results in the spectrum inverting one epoch earlier.

By combining data from adjacent epochs, we have improved the S/N sufficiently to measure upper limits to the linear and circular polarisation. These limits are determined

Table 8.6: The spectral index calculated for each epoch of our radio observations. Only the 4.8 and 8.6 GHz data have been used so as to be consistent at every epoch.

JD−2450000	α	error
773	−0.95	0.07
777/8	−0.13	0.05
784/5	−0.49	0.12
786/7	−0.34	0.12
802	0.13	0.14

from fits to the image plane with percentages calculated as a fraction of the (image plane) total flux density; they can be found in Table 8.4. It is interesting to note that linear polarisation of the soft X-ray transient 4U 1630−47 (Flux density ~ 0.5–3 mJy) was detected at 27% i.e. a level that we would have picked up had it been the case for GS 1354−64. However, observations of GS 2023+338 (Han & Hjellming 1992) and GX 339−4 (Corbel et al. 2000) in the *hard* state yielded linear polarisations of 1-4% and this may turn out to be a value common to the hard state sources (which are probably partially self-absorbed).

While our optical investigation has suggested that the optical emission is the result of one or more heating waves travelling inwards through the disc, it is also interesting to note that the optical fluxes are comparable with those of the radio, suggesting that the flat spectrum associated with the central radio source might extend to higher frequencies. A flat synchrotron spectrum beyond the radio regime has been seen in a number of X-ray binaries in the low/hard X-ray state e.g. Cyg X-1 to the mm wavelengths and GRS 1915+105 to the infrared (Fender et al. 2000). It is therefore feasible that there may be a contribution to the optical emission from the jet.

To investigate this further we plot the extinction corrected spectrum for our optical data, plus the published infrared (J and K band) points of Soria, Bessell & Wood (1997) and the radio fluxes quoted in Table 8.1 which are from the same epoch as the IR (Fig. 8.5). We have also extended the spectrum down to 843 MHz with the inclusion of a data point from the Molonglo Observatory Synthesis Telescope (MOST) (Hunstead & Campbell-Wilson, private communication). This plot indicates that while the B and V band data are too bright to be associated with the radio, the R band and the infrared points seem to lie approximately in a straight line - the best fit spectral index to the radio, infrared

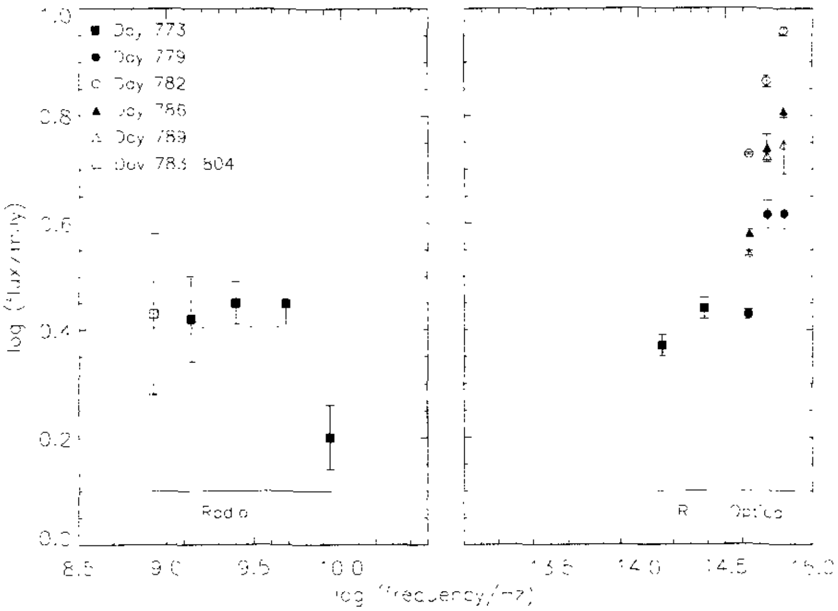

Figure 8.5: Spectrum ranging from radio through to optical. We include the infrared (J and K band) points of Soria, Bessell & Wood (1997) and the MOST data of Hunstead & Campbell-Wilson (private communication). Optical and infrared data have been corrected for interstellar extinction using a reddening estimate of $E(B-V) = 1$ (Kitamoto et al. 1990) and values of A_λ/A_V from Cardelli, Clayton & Mathis (1989). The dotted line is the best fit straight line through the radio, infrared and R-band ($\alpha \sim 0.004$)

and R band points is 0.004 ± 0.01, which is consistent with flat synchrotron emission up to the near infrared. In contrast to this, the optical data alone yields a spectral index of 1.12–1.68, depending on the epoch, and the B and V data alone yields $\alpha \sim$0.02–0.97. With a theoretical thermal disc spectrum (with no irradiation) of $S_\nu \propto \nu^{1/3}$ (e.g. Frank, King, Raine, 1992 and references within) it is probable that there may be some additional optical component causing the steeper optical spectrum at some epochs. However, we note that without full coverage of the spectrum through the sub-mm and infrared regimes we cannot be certain the spectrum really is flat from radio to near-infrared.

We note that the 8.64 GHz point is somewhat discrepant. While it is possible that there is some systematic error due to the poor *uv* coverage, we point out that it may take some time after the ejection for the spectrum to invert, i.e. become dominated by a steady self-absorbed flow. For example the radio spectrum of V404 Cyg did not invert until $\sim$ 25 days after the initial (hard state) outburst (Fender 2000a, Han & Hjellming 1992).

Table 8.7: Comparison between outbursts of Cen X-2, MX 1353−64 and GS 1354−64, which may all be the same source. X-ray peaks are quoted for the 1-10 keV range. See Tanaka & Lewin (1995) and references within. Note that WX Cen is an unrelated bright variable star, but was originally found in the large error box of Cen X-2.

Source	Date	Duration (months)	Soft X-ray Peak (mCrab)	X-ray State	Optical Peak (mags)
Cen X-2	1966–1967	~ 8	~ 8000	(Very?) high/soft	$V > 13.5$ (WX Cen)?
MX 1353−64	1972	~ 11	75	low/hard	–
GS 1354−64	1987	~ 6	≥ 300	high/soft	$V \geq 16.9$ (BW Cir)
GS 1354−64	1997	~ 5	50	low/hard	$V \geq 17.3$ (BW Cir)

8.3 Comparison with other outbursts

8.3.1 *Previous (possible) outbursts of GS 1354−64*

We summarise the four possible outbursts of GS 1354−64 in Table 8.7. It is clear that the characteristics (i.e. the spectrum and luminosity) of each outburst are very different

Kitamoto (1990) concluded that for GS 1354−64 to have produced all three outbursts known by that date, then the source must show four distinct X-ray states, i.e. very high, high/soft, low/hard and faint/off states. Although less bright, the 1997 outburst appears to show a similar state to that of the 1972 event reported by Markert et al. (1977). However, as Kitamoto et al. (1990) demonstrate, the error boxes of the various satellites which may have detected GS 1354−64 cover a large area on the sky: if the system were to enter another 'Cen X-2 type' outburst then it would confirm that the source can indeed display such a wide range of X-ray spectral behaviour it may then be possible to confirm whether or not the three sources are one and the same. Given the the lack of crowding in the field of GS 1354−64 it is probably more likely that the four sources are one and the same, as opposed to a number of different X-ray transients so close together.

8.3.2 Other X-ray transients reaching only the hard state

An increasing number of supposed 'soft' X-ray transients have been shown to remain in the low/hard X-ray state, the X-ray spectra showing little contribution from a soft disc component. A list of hard state X-ray transients can be found in Table 8.8. In comparing

Table 8.8: Comparison between the five BHC X-ray transients which have remained in the low/hard state throughout an outburst.

Source	Date	X-ray Spectrum	mHz QPO During Outburst?
GS 1354−64	1997	low/hard	ν increases
GS 2023+338	1989	[1]low/hard (mostly?)	?
GRO J0422+32	1992	[5]low/hard	[6]mHz QPO present
GRO J1719−24	1993	[9]low/hard	[9]ν increases
XTE J1118+480	2000	[11]low/hard	[12,13]ν increases

Source	Radio Spectrum	Optical Peak Preceding X-ray Peak?	Optical/X-ray Luminosity Ratio
GS 1354−64	flat → inverted	Yes	optically bright
GS 2023+338	[2]flat → inverted	[3]Yes	[4]optically bright
GRO J0422+32	[7]flat → inverted	[8]Possibly	? (no soft X-ray obs.)
GRO J1719−24	[10]flat	?	? (no soft X-ray obs.)
XTE J1118+480	[14]inverted	?	[15]optically bright

1. Tanaka & Lewin (1995)	2. Han & Hjellming (1992)	3. Chen, Shrader, Livio (1997)
4. Van Paradijs & McClintock (1995)	5. Van der Hooft et al. (1999)	6. Kouveliotou et al. (1992)
7. Shrader et al. (1994)	8. Callanan et al. 1995)	9. Van der Hooft et al. (1996)
10. Hjellming et al. (1993)	11. Hynes et al. (2000)	12. Yamaoka et al. (2000)
13. Wood et al. (2000)	14. Dhawan et al. (2000)	15. Garcia et al. (2000)

these five objects a number of trends can be seen, some of which may turn out to be indicative of low/hard state outbursts of the X-ray transients.

We find that an increase in QPO frequency, a flat (or inverted) synchrotron radio spectrum and an over-bright optical counterpart may be properties common to the low/hard state X-ray transients – although not exclusively so, as an increase in QPO frequency appears to be a common feature of the soft X-ray transients also (e.g. GS 1124−68, Van der Klis 1995) – however it should be noted that the QPOs detected in the soft state tend to occur at higher frequencies. It is rare for the onset of a soft X-ray transient event to be observed in the optical but at least two of these low/hard state events have been observed to peak in the optical before the X-ray, suggesting that something other than reprocessing of X-rays dominates the optical emission. While these trends are clearly tentative we note that none of these systems provides an exception to the 'rule' either they follow the trends or there have been insufficient observations to determine either way.

There is a sixth source, Aql X-1, which also shows some (but not all) of these trends it has been omitted from Table 8.8 as it is a neutron star X-ray transient, its X-ray spectral properties classifying it as an atoll source (Cui et al. 1998, Reig et al. 2000). However, Aql X-1 has also been observed to peak in the optical before the soft X-rays (Shahbaz et al. 1998) and also demonstrates an increase in QPO frequency throughout the outburst (Cui et al. 1998). It should, however, be pointed out that the QPOs seen in Aql X-1 are found at kHz frequencies rather than the mHz QPOs found in the tabulated sources. Consequently it may be incorrect to compare them, but see also Psaltis, Belloni, Van der Klis (1999). Unlike the BHC systems there is no optical excess. Although there was a weak radio counterpart to the outburst (Hjellming et al. 1990) there was no spectral information Aql X-1 is currently one of only a small number of atoll sources for which radio counterparts have been detected.

It is also worth comparing these five sources with the low/hard states of persistent black hole X-ray binaries. While mHz QPOs have been reported in these systems (e.g. Vikhlinin et al. 1994 and references within), an increase in QPO frequency is not a typical feature of the low/hard state for these systems and so it may seem surprising that we see it here. However, although the transients remain in the low/hard state the change in QPO suggests that the inner disc radius is decreasing – it therefore appears that the transition to the soft state is initiated but not completed. Therefore this increase in QPO frequency should probably be considered a feature of the *transition*, rather than of the state itself –

this would be consistent with the inner radius of the disc changing during the transition but remaining constant once a stable X-ray state is reached. This theory could be easily tested for the persistent sources during a transition, although *RXTE* observations of the 1996 transition of Cyg X-1 suggest that it may not be just a simple increase in frequency with flux (Cui et al. 1997) – further investigation of this would be useful. The radio behaviour of the persistent sources is very similar to that of these five transients – for example, Cyg X-1 (Brocksopp et al. 1999) and GX 339−4 (Corbel et al. 2000) both emit flat spectrum jets whilst in the low/hard state. This jet is quenched on reaching the soft state – this is probably also the case for soft X-ray transients, although the material ejected during the state transition will continue to produce bright radio emission, despite being physically decoupled from the accretion process (e.g. A0620−00, Kuulkers et al. 1999).

8.4 Discussion

Our multiwavelength dataset has enabled us to make a number of suggestions as to what took place during the outburst of GS 1354−64 in 1997 November. The optical and radio lightcurves suggest that there were two maxima during the outburst, the first prior to our observations and the second at ~JD2450784, depending on wavelength. There is also the hint of a third optical rise just following the X-ray peak (JD2450796) – by this time it is possible that the disc is sufficiently bright in X-rays for the third optical brightening to be the result of X-ray reprocessing in the disc (although this is not confirmed by the hard X-ray energy spectrum). For future outbursts, simultaneous X-ray and high time resolution optical observations would be extremely beneficial; discovery of the 13 mHz QPO (mentioned in Section 3.1) in the optical would help to determine the efficiency of the reprocessing of soft X-rays.

It is clear that the optical lightcurve reached a local maximum *before* the X-rays peaked. While common in dwarf novae outbursts, a preceding optical peak is not generally seen in X-ray transient events – quite possibly only due to the fact that it is the X-ray satellites which tend to discover them. If this is the case then it is unlikely that reprocessing of X-rays was the dominant source of optical emission. (However, it is possible if there is some non-straightforward disc geometry e.g. GRO J1655−40 (Hynes et al. 1998)). Our comparison of 'soft' X-ray transients which remain in the low/hard X-ray state for the duration of the outburst shows that GS 2023+338 and possibly GRO J0422+32 were also observed to peak in the optical before the X-ray. While this may be coincidence in timing of the observations, we consider the possibility that in these hard state transients the X-ray emission is at a sufficiently low level for the inwards travelling instability to dominate the optical emission; in outbursts with a soft X-ray component reprocessing of X-rays would dominate instead. This is confirmed by the surprisingly high optical/X-ray luminosity ratios that these low/hard state sources have – in a 'normal' soft event the relative X-ray luminosity would be much higher, than in the hard state sources.

If the peak of the X-ray lightcurve corresponds to the time at which the instability reaches the hot inner regions of the disc then a disc-crossing time of ∼10 days is inferred. For this to be true then the disc and therefore the orbit must be large. The fact that no orbital period has been determined for this source could also suggest that the orbit may be large (this may also contribute to the possible over-bright optical emission mentioned in Section 8.2.2) although it is more likely that there is insufficient optical data for any periodicities to be determined. If, indeed the orbit *is* large then BW Cir must be an evolved star filling its Roche Lobe, suggesting a similar type of system to GRO J1655−40.

This inferred disc-crossing time is very long and it is unlikely that the disc of a system with such a low soft X-ray luminosity and hard X-ray spectrum would extend to a small inner radius. It is also unlikely that the instability could trigger a radio ejection before reaching the innermost regions of the disc and causing the X-ray peak. The increase in QPO frequency suggests that the increase in soft X-ray luminosity is the result of the inner disc radius decreasing; the surface area of the disc and the temperature of the inner regions are therefore increasing. This would be consistent with other X-ray binaries the low/hard state is characterised by a large inner disc radius and this decreases on transition to the high/soft state (e.g. Esin et al., 1998).

Therefore it appears that the instability moves inwards, emitting in the optical regime. As the transported mass fills the 'hole' at the centre of the disc on a viscous timescale, the soft X-ray emission from the corona increases. This scenario is comparable with that suggested by Shahbaz et al. (1998) to explain the optical/X-ray delay of the 1997 outburst of the neutron star X-ray transient Aql X-1.

If we assume that a radio event is triggered when the instability reaches the inner edge of the disc then this considerably reduces the required disc crossing time (i.e. the disc crossing time becomes the delay between the optical and radio peaks (∼ 1–2 days) rather than the delay between the optical and X-ray) and seems more likely. From observations of other sources in the hard state it is probable that this radio event is the ejection of weak, continuous jets. We would expect the emission from the jets to be characterised initially by partially self-absorbed synchrotron radiation, becoming optically thin over time to successively lower frequencies – however without resolving the jets we would not necessarily expect to observe this. It is also possible that individual plasmon ejections take place, although these are more commonly seen in the soft X-ray transient outbursts.

Alternatively (or additionally?), we also note that the optical and radio data have comparable fluxes. It is therefore possible that an ejection event took place, emitting synchrotron radiation at optical and increasingly longer wavelengths as the ejected material became optically thin at increasing distances from the central source. The flat spectrum (Fig. 8.5), *apparently extending* from radio wavelengths to the R band, would certainly support this scenario. If, as our value of ξ suggests, the optical component is over-bright *then synchrotron should not* be discounted as a possible contributor to the optical emission in addition to the thermal disc spectrum.

It is important to consider the implications of a jet (or *mass ejection*) that *emits flat* spectrum synchrotron radiation over such a wide range of frequencies. While there are a number of models that work reasonably well for the 'flat spectrum' AGN, *none of these* is consistent with the *much flatter* radio – (sub-)mm spectra of e.g. Cyg X-1, GRS 1915+105 and Cyg X-3 (Fender et al. 2000 and references within). The most convincing explanation for the flat spectrum is synchrotron radiation from a partially self-absorbed jet. With the power of the jet directly proportional to the bandwidth, detection of a high frequency cut-off to the flat spectrum would be very useful in determining the power of the jet – this has not been found in any of the flat spectrum X-ray binaries.

In summary, our limited observations suggest that the 1997 outburst of GS 1354−644 was the result of an instability crossing the disc on a slow viscous timescale, emitting at optical wavelengths. As the instability reached the (large) inner radius of the disc it triggered a mass ejection which emitted synchrotron radiation at radio wavelengths and possibly through to the near infrared (and optical?) regime. The X-ray source remained in the low state throughout, gradually becoming brighter as the instabilities carried more matter into the hot inner regions and subsequently decreasing the inner disc radius. These results clearly reflect the importance of simultaneous optical, infrared and radio studies of future X-ray transient events.

Chapter 9

CONCLUSIONS

The conclusions reached, following the multiwavelength investigation of variability in black hole X-ray binaries, have already been outlined in the relevent chapters. They are summarised again below by considering, firstly, the three sources individually and, secondly, the low/hard state sources as a single class of objects.

Cygnus X-1

Optical spectroscopy of Cyg X-1 has enabled revision of the orbital ephemeris and, subsequently, a detailed multiwavelength study of the orbital modulation. This has been extended for the radio regime and a simple model of stellar wind absorption presented to explain the radio modulation. The possible 'precession' period has also been found at all wavelengths and further work is required to investigate this phenomenon – whether or not the observations really are consistent with precession, the mechanisms involved and a search for some signature of these mechanisms in the optical spectroscopy. Cyg X-1 has recently demonstrated correlated behaviour between the soft X-rays and radio and this, combined with the correlated long period behaviour in the two wavelength regimes, should contribute to our understanding of the disc:jet connection in X-ray binaries.

LMC X-3

The long term behaviour of LMC X-3 has been studied in the optical photometry, in conjunction with the recent discovery of low/hard X-ray spectral states. No stable periods have been found and this is consistent with analysis of the X-ray lightcurves. The correlation between the X-ray and optical data and also the X-ray delay would suggest that increased mass flow through the disc is observed as it passes through the cold outer regions into the hot inner regions. This could be confirmed by acquiring optical data with better time resolution and the inclusion of ultraviolet observations. The radio counterpart to LMC X-3 has not been detected in the observations presented here but comparison with Cyg X-1 suggests that this is not surprising and that detection is hampered by the large amounts of observing time required.

GS 1354−64

Multiwavelength study of GS 1354−64 has shown that it belongs to an increasing number of X-ray transients observed to remain the low/hard state throughout the outburst. Despite limited data, evidence has been found for a flat spectrum radio jet as well as the direct observation of the instability crossing the accretion disc. The frequency variability of the mHz QPO needs careful interpretation but also appears to be an important feature of hard state systems.

It is clear from the previous chapters that Cyg X-1, LMC X-3 and GS 1354−64 are appropriate sources for a study of black hole X-ray binaries in the low/hard state. Cyg X-1 and LMC X-3 have been considered black hole candidates for nearly three and two decades respectively, as the result of mass estimates; GS 1354−64 is an extremely likely source on account of its X-ray spectral and timing properties and its absence of bursts or pulses.

While the three systems behave very differently they do indeed show hard state behaviour:

- most of the time, in the case of Cyg X-1
- occasionally, quasi-periodically, in the case of LMC X-3
- during some, but not all, outbursts, in the case of GS 1354−64

This work has enabled potential properties of the hard state to be established and/or reinforced - as well as the characteristic hard X-ray energy spectrum and power spectrum which define the low/hard state, sources in this state also display evidence for a flat spectrum radio jet (often extending to much higher frequencies) and a low-frequency QPO of variable frequency (apprently depending on spectral hardness and certainly not correlated with X-ray flux). Transient sources which only reach the low/hard state during their outbursts also appear to have suprisingly high optical:X-ray luminosity ratios, suggesting that the optical emission is not dominated by X-ray reprocessing but instead the instability causing the outburst can actually be observed directly as it crosses the accretion disc.

Studying these sources has revealed what a useful phenomenon this state is – it is during the hard state that jets can be observed and also when it is most straightforward to investigate periodic behaviour (the long term and orbital periods of Cyg X-1 cannot be studied during the soft state as seen in Chapter 1). In the *soft* X-ray transients there is no chance of observing the instability because the optical emission is dominated by reprocessing of X-rays from the luminous accretion disc. While the hard state of LMC X-3 is yet to be exploited to the same extent, its discovery has already shown that LMC X-3 is not such a 'different' type of X-ray binary – it follows the same spectral state behaviour but conveniently changes state more frequently than any other source.

Investigations of the long periods of Cyg X-1 and LMC X-3 have shown clearly that invoking accretion disc precession is often a convenient 'band-wagon to jump on' – while in the case of Cyg X-1 it appears successful in explaining the multiwavelength observations (more recent VLBA images of the jet indicate the presence of a 'kink', reminiscent of the processing jets of SS 433 – R. Spencer, private communication), the state changing behaviour of LMC X-3 suggests otherwise. It is possible that further spectral investigation of Cyg X-1 may reveal a similar variability of accretion flow instead of classical precession.

Regardless of the mechanism by which the long period of Cyg X-1 is produced, the fact that this and also the orbital period are observed at all wavelengths is extremely significant in the study of the disc:jet connection: likewise the X-ray:radio correlated behaviour seen in Cyg X-1 and the peculiar relationships between the lightcurves at different frequencies in GS 1354–64. These multiwavelength observations are crucial if we are ever to determine the nature of the coupling between the disc and the jet.

A number of future projects arise directly from this work and include:

- Disc:jet connection – multiwavelength observations of correlated outbursts, state changes and accretion rate variability, precession etc.
- Further investigation into the nature of long periods of Cyg X-1 and other sources
- Detect radio emission in LMC X-3 and image radio jets in other hard state sources – are they really as ubiquitous as we think?
- Observe the instabilities moving through the accretion disc of transient sources. This will result in greater understanding of outburst mechanisms and jet ejection

REFERENCES

Aab O.E., 1983a, Izv. S.A.O. 17, 6

Aab O.É., 1983, SvAL., 9, 315

Aab O.É., Bychkova L.V., Kopylov I.M., Kumaïgorodskaya R.N., 1983, SvA, 27, 603

Aab O.É., Bychkova L.V., Kopylov I.M., Kumaïgorodskaya R.N., 1984, SvA, 27, 603

Aab O.É., Bychkova L.V., Kopylov I.M., Kumaïgorodskaya R.N., Chentsov E.L., 1981, SvAL, 7, 230

Abell G.O., Margon B., 1979, Nature, 279, 701

Abramowicz M., Czerny B., Lasota J.P., Szuszkiewicz E., 1988, ApJ, 332, 646

Abt H.A., Hitzen P., Levi S.G., 1977, ApJ 213, 815

Avni Y., Bahcall J.N., 1975, ApJ, 197, 675

Balog N.I., Goncharskij A.V., Cherepashchuk A.M., 1981, SvA 25, 67

·Bałucińska-Church M., Church M.J., Charles P.A., Nagase F., LaSala J., Barnard R., 2000, MNRAS, 311, 861

Beall J.H., Knight F.K., Smith H.A., Wood K.S., Lebofsky M., Rieke G., 1984, ApJ, 284, 745

Belloni T., Hasinger G., 1990, A&A, 230, 103

Belloni T., Mendez M., van der Klis M., Hasinger G., Lewin W.H.G., van Paradijs J., 1996, ApJ, 472, 107

Blandford R.D., Königl A., 1979, ApJ, 232, 34

Blandford R.D., Payne D.G., 1982, MNRAS, 199, 883

Bochkarev N.G., Lyuty V.M., 1998, AstL, 24, 277

Bochkarev N.G., Sunyaev R.A., Khruzina T.S., Cherepashchuk A.M., Shakura N.I., 1988, SvA, 32, 405

Bolton C.T., 1972, Nature, 235, 271

Bolton C.T., 1975, ApJ, 200, 269

Bowyer S., Byram E.T., Chubb T.A., Friedmann H., 1965, Science, 147, 394

Boyd P.T., Smale A.P., Homan J., Jonker P.G., Van der Klis M., Kuulkers E., 2000, ApJL in press

Braes L.L.E, Miley G.K., 1971, Nature, 232, 246

Braes L.L.E, Miley G.K., 1976, Nature, 264, 731

Brocksopp C., Fender R.P., Larionov V., Lyuty V.M., Tarasov A.E., Pooley G.G., Paciesas W.S., Roche P., 1999, MNRAS, 309, 1063

Brocksopp C., Tarasov A.E., Lyuty V.M., Roche P., 1999, A&A, 343, 861

Brucato R.J., Kristian J., 1973, ApJ 179, L79

Brucato R.J., Zappala R.R., 1974, ApJ 189, L71

Bruevich V.V., Kilyachkov N.N., Sunyaev R.A., Shevchenko V.S., 1978, *Pis'ma Astron. Zh.*, 1, 544

Buxton M., Vennes S., Ferrario L., Wickramasinghe D.T., 1998, IAUC 6815

Callanan et al., 1995, ApJ, 441, 786

Canalizo G., Koenigsberger G., Peña D., Ruiz E., 1995, Rev. Mex. 31, 63

Cardelli J.A., Clayton G.C., Mathis J.S., 1989, ApJ, 345, 245

Castor J.I., Abbott D.C., Klein R.I., 1975, ApJ, 195, 157

Castro-Tirado A.J., Ilovaisky S., Pederson H., 1997, IAUC 6775

Chakrabarti S., Titarchuk L, 1995, ApJ, 455, 623

Charles P.A., 1998, 'Theory of Black Hole Accretion Disks', Eds. Abramowicz M., Bjornsson G. & Pringle J., CUP

Chen W., Shrader C.R., Livio M., 1997, ApJ, 491, 312

Chen X., Abramowicz M., Lasota J.P., Narayan R., Yi I., 1995, ApJ, 443, L61

Clark B.G., 1980, A&A, 89, 377

Corbel S., Fender R.P., Tzioumis A.K., Nowak M., McIntyre V., Durouchoux P., Sood R., 2000, A&A, 359, 251

Cowley A.P. et al., 1991, ApJ, 381, 526

Cowley A.P., Crampton D., Hutchings J.B., 1979, AJ, 83, 1619

Cowley A.P., Crampton D., Hutchings J.B., Remillard R., Penfold J.E., 1983, ApJ, 272, 118

Cowley A.P., Schmidtke P.C., Hutchings J.B., Crampton D., 1991, ApJ, 429, 826

Crary D.J. et al., 1996, A&AS, 120, 153

Cui W., Chen W., Zhang S.N., 1998, ASP Conference Series, 138, 75

Cui W., Ebisawa K., Dotani T., Kubota A., 1998, 493, L75

Cui W., Zhang S.N., Chen W., Morgan E.H, 1999, ApJ, 512, L43

Cui W., Zhang S.N., Focke W., Swank J., 1997, ApJ, 484, 383

Davis R., Hartmann L., 1983, ApJ, 270, 671

Dhawan V., Pooley G.G., Ogley R.N., Mirabel I.F., 2000, IAUC 7395

Done C., Mulchaey J.S., Mushotzky R.F., Arnaud K.A., 1992, ApJ, 395, 275

Dove J.B., Wilms J., Begelman M.C., 1997, ApJ, 487, 747

Ebisawa K., Makino F., Mitsuda K., Belloni T., Cowley A.P., Schmidtke P.C., Treves A., 1993, ApJ, 403, 684

Ebisawa K., et al., 1994, PASJ, 46, 375

Esin A.A., Narayan R., Cui W., Grove J.E., Zhang S.N., 1998, ApJ, 505, 854

Eyles C.J., Skinner G.K., Willmore A.P., Rosenberg F.D., 1975, MNRAS, 173, 63p

Falcke H., Biermann P.L., 1996, A&A, 308, 321

Feast M.W., Thackeray A.D., Wesselink A.J., 1960, MNRAS, 121, 337

Fender R.P., 2000, MNRAS submitted

Fender R.P., 2000a, To be published in Proc. ESO workshop 'Black Holes in binaries and galactic nuclei', Eds Kaper L., Van den Heuvel E.P.J. and Woudt P.A., Springer-Verlag

Fender R.P., Garrington S.T., McKay D.J., Muxlow T.W.B., Pooley G.G., Spencer R.E., Stirling A.M., Waltman E.B., 1999, MNRAS, 304, 865

Fender R.P., Hendry M.A., 2000, MNRAS, 317, 1

Fender R.P., Pooley G.G., Durouchoux P., Tilanus R.P.J., Brocksopp C., 2000, MNRAS, 312, 853

Fender R.P., Rayner D., Norris R., Sault R.J., Pooley G.G., 2000a, ApJ, 530, L29

Fender R.P., Southwell K., Tzioumis A.K., 1998, MNRAS, 298, 692

Fender R.P., Tingay S.J., Higdon J., Wark R., Wieringa M., 1997, IAUC 6779

Fender et al., 1999, ApJ, 519, L165

Fishman G.J. et al., 1989, Proc. GRO Science Workshop, NASA, Ed. Johnson W.N.

Francey R.J. 1971, nature Phys. Sci. 229, 228

Frank J., King A., Raine D., 1992, 'Accretion Power in Astrophysics', CUP

Fransson C., Fabian A.C., 1980, A&A, 87, 102

Friend D.B., Castor J.I., 1982, ApJ, 261, 293

Garcia M., Brown W., Pahre M., McClintock J., Callanan P., Garnavich P., 2000, IAUC 7392

Gerend D., Boynton P.E., 1976, ApJ, 209, 562

Gierliński M., Zdziarski A.A., Poutanen J., Coppi P.S., Ebisawa K., Johnson W.N., 1999, MNRAS, 309, 496

Gies D.R., Bolton C.T., 1982, ApJ, 260, 240

Gies D.R., Bolton C.T., 1984, ApJ, 276, L17

Gies D.R., Bolton C.T., 1986, ApJ, 304, 371

Gies D.R., Bolton C.T., 1986a, ApJ, 304, 389

Gilfanov M., Churazov E., Revnivtsev M., 1999, A&A, 352, 182

Griffiths R.E., Seward F.D., 1977, MNRAS, 180, 75p

Hadrava P., 1998, ftp: sunstel.asu.cas.cz, pub/fotel/fotel3.tex

Han X., 1993, PhD. thesis, New Mexico Institute of Mining and Technology

Han X., Hjellming R.M., 1992, ApJ, 400, 304

Harmon B.A., Robinson C.R., 1997, IAUC 6774

Hasinger G., Van der Klis M., 1989, A&A, 225, 79

Hatchett S., McCray R., 1977, 211, 552

Haynes R.F., Lerche I., Murdin P., 1980, A&A, 87, 299

Heemskerk M.H.M., Van Paradijs J., 1989, A&A, 223, 154

Herrero A, Kudritzki R.P., Gabler R., Vilchez J.M., Gabler A., 1995, A&A, 297, 556

Hjellming R.M. et al., 1999, ApJ, 514, 383

Hjellming R.M., 1973, ApJ, 182, L29

Hjellming R.M., Gibson D.M., Owen F.N., 1975, Nature, 256, 111

Hjellming R.M., Han X., Roussel-Dupre, 1990, IAUC 5112

Hjellming R.M., Johnston K.J., 1988, ApJ, 328, 600

Hjellming R.M., Rupen M.P., Shrader C.R., Campbell-Wilson D., Hunstead R.W., McKay D.J., 1993, ApJ, 470, L105

Holt S.S., Boldt E.A., 1975, Nature, 256, 108

Holt S.S., Kaluzienski L.J., Boldt E.A, Serlemitsos P.J., 1976, Nature, 261, 213

Homan J., Wijnands R., Van der Klis M., Belloni T., Van Paradijs J., Klein-Woldt M., Fender R.P., Méndez M., 2000, ApJ submitted

Horne K., 1986, PASP, 98, 609

Hutchings J.B., Crampton D., Bolton C.T., 1979, PASP, 91, 796

Hutchings J.B., Crampton D., Glaspey J., Walker G.A.H., 1973, ApJ, 182, 549

Hynes R.I., 1998, *New Astronomy Reviews*, 42, 605

Hynes R.I., Mauche C.W., Haswell C.A., Shrader C.R., Cui W., Chaty S., 2000, ApJL submitted

Hynes R.I., O'Brien K.O., Horne K., Chen W., Haswell C.A., 1998, MNRAS, 299, L37

Jahoda K., Swank J.H., Giles A.B., Stark M.J., Strohmayer T., Zhang W., Morgan E.H. 1996, SPIE, 2808, 59

Johnston M.D., Bradt H.V., Doxsey R.E., 1979, ApJ, 233, 514

Johnston M.D., Bradt H.V., Doxsey R.E., Gursky H., Schwartz D.A., Schwarz J., Van Paradijs J., 1978, ApJ, 225, L59

Jonker P.G., Van der Klis M., Wijnands R., Homan J., Van Paradijs J., Méndez M., Ford E.C., Kuulkers E.,& Lamb F.K. 2000, ApJ, in pressKaper L., 1998, ASP Conference Series, 131, 427

Kaper L., Hammerschlag-Hensberge G., Zuiderwijk E.J., 1994, A&A, 289, 846

Kemp J.C. et al., 1979, ApJ, 228, L23

Kemp J.C. et al., 1983, ApJ, 271, L65

Kemp J.C., Herman L.C., Barbour M.S., 1978,AJ 83, 962

Kemp J.C., Karitskaya E.A., Kumsiashvili M.I., Lyuty V.M., Khruzina T.S., Cherepashchuk A.M., 1987, SvA, 31, 170

Kennett M., Melrose D., 1998, PASA, 15, 211

Khaliullin Kh.F., 1975, SvAL, 1, 59

Khaliullin Kh.F., Khaliullina A.I., 1981, SvA 25, 593

Khruzina T.S., Cherepashchuk A.M., 1984, SvA, 28, 173

Kitamoto S., Tsunemi H., Pedersen H., Ilovaisky S.A., Van der Klis M., 1990, ApJ, 361, 590

Koide S., Shibata K., Kudoh T., 1998, ApJ, 495, L63

Kopylov I.M., Sokolov V.V., 1984, SvAL, 10, 315

Kouveliotou et al., 1992, IAUC 5592

Kuiper L., Van Paradijs J., Van der Klis M., 1988, A&A, 203, 79

Kurucz R.L., 1979, ApJS, 40, 1

Kuulkers E., Fender R.P., Spencer R.E., Davis R.J., Morison I, 1999, MNRAS, 306, 919

Kuulkers E., Van der Klis M., Vaughan B.A., 1996, A&A, 1996, 311, 197

Lamers H.J.G.L.M., Cassinelli J.P., 1999, 'Introduction to Stellar Winds', C.U.P.

LaSala J., Charles P.A., Smith R.A.D., Balucińska-Church M., Church M.J., 1998, MNRAS 301, 285

Landolt A.U., 1992, ApJ, 140, 340

Larwood J., MNRAS, 1998, 299, L32

Leahy D.A., Ananth A.G., 1992, MNRAS, 256, 39p

Leibowitz E.M., 1984, MNRAS, 210, 279

Leitherer C., Chapman J.M., Koribalski B., 1995, ApJ, 450, 289

Leong C., Kellogg E., Gursky H., Tananbaum H., Giacconi R., 1971, ApJ, 170, L67

Lester D.F., Nolt I.G., Stearns S.A., Straton P., Radostitz J.V., 1976, ApJ, 205, 855

Levine A.M., Bradt H., Cui Wei., Jernigan J.G., Morgan E.H., Remillard R., Shirey R.E., Smith D.A., 1996, ApJ., 469, L33

Lloyd C., Walker E.N., 1989, Proc. 23rd ESLAB Symp.'Two Topics in X-ray Astronomy', vol.1,'X-ray Binaries', Bologna, Italy, 13-20 Sept.1989, Paris, Noordwijk, p.511.

Lochner J.C., Swank J.H., Szymkowiak A.E., 1991, ApJ, 376, 295

Lyuty V.M., 1972, Peremennye zvezdy 18, 417

Lyuty V.M., 1985, SvA, 29, 429

Lyuty V.M., Sunyaev R.A., Cherepashchuk A.M., 1973, SvA, 18, 684

Lyuty V.M., Sunyaev R.A., Cherepashchuk A.M., 1974, SvA, 17, 1

Méndez M., Belloni T., Van der Klis M., 1998, ApJ, 499, 187

MacGregor K.B., Vitello P.A.J., 1982, ApJ, 259, 267

Makino F. et al., 1987, IAUC 4342

Makishima K., Maejima Y., Mitsuda K., Bradt H.V., Remillard R.A., Tuohy, I.R., Hoshi, R., Nakagawa M., 1986, ApJ, 308, 635

Maloney P.R., Begelman M.C., 1997, ApJ, 491, 43

Markert T.H., Clark G.W., 1975, ApJ, 196, L55

Markert T.H., et al. 1979, Ap. J. Suppl., 39, 573

Marscher A.P., 1983, ApJ, 264, 296

Martí J., Rodríguez L.F., Mirabel I.F., Parades J.M., 1996, A&A, 306, 449

Mason K.O., Hawkins F.J., Sanford P.W., Murdin P., Savage A., 1974, ApJ 192, L65

Matz S.M., 1997, Proc 4th Compton Symposium, p808

Mazeh T., Van Paradijs J., Van den Heuvel E.P.J., Savonije G.J., 1986, A&A, 157, 113

McCollough M.L. et al., 1999, ApJ., 517, 951

Mihalas D., 1978, 'Stellar Atmospheres', (2nd Ed.: San Francisco: Freeman)

Mirabel I.F., Rodríguez L.F., 1999, ARA&A, 37, 409

Mitsuda et al., 1984, PASJ, 36, 741

Miyamoto S., Kitamoto S., 1989, Nature, 342, 773

Molteni D., Sponholtz H., Chakrabarti S.K., 1996, ApJ, 457, 805

Nadzhip A.E., Khruzina T.S., Cherepashchuk A.M., Shenavrin V.I., 1996, Astron. Rep. 40, 338

Narayan R., Garcia M.R., McClintock J.E., 1997, ApJ, 478, L79

Narayan R., Mahadevan R., Quataert E., 1998, 'Theory of Black Hole Accretion Disks', Eds. Abramowicz M., Bjornsson G. & Pringle J., CUP

Narayan R., Yi I., 1994, ApJ, 428, L13

Natali G., Fabrianesi R., Messi R., 1978, A&A, 62 L1

Ninkov Z., Walker G.A.H., Yang S., 1987, ApJ 321, 425

Ninkov Z., Walker G.A.H., Yang S., 1987a, ApJ 321, 438

Nowak M.A., Wilms J., Vaughan B.A., Dove J.B., Begelman M.C., 1999, ApJ, 515, 726

O'Dell S.J., Puschell J.J., Stein W.A., Owen F., Porcas R.W., Mufson S., Moffett T.J., Ulrich M.H., 1978, ApJ, 224 22

Ogawura Y., Mitsuda K., Masai K., Vallerga J.V., Cominsky L.R., Grunsfeld J.M., Kruper J.S., G.R. Ricker, 1982, Nature, 295, 675

Ogilvie G.I., Dubus I., 2000, MNRAS accepted

Oppenheimer J.R., Volkov G.M., 1939, Phys. Rev., 55, 374

Orosz J., 1997, ApJ, 477, 876

Paciesas W.S., Robinson C.R., McCollough M.L., Zhang S.N., Harmon B.A., Wilson C.A., 1997, IAUS, 188, 225

Paczyński B., 1977, ApJ, 216, 822

Paczyński B., 1983, ApJ, 273, L81

Papaloizou J.C.B., Terquem C., 1995, MNRAS, 274, 987

Paul B., Kitamoto S., Makino F., 2000, ApJ, 528, 410

Pooley G.G., Fender R.P., 1997, MNRAS, 292, 925

Pooley G.G., Fender R.P., Brocksopp C., 1999, MNRAS 302, L1

Pottschmidt K., König M., Wilms J., Staubert R., 1998, A&A, 334, 201

Pottschmidt K., Wilms J., Nowak M.A., Heindl W.A., Smith D.M., Staubert R., 2000, A&A, 357, L17

Pottschmidt K., Wilms J., Staubert R., Nowak M.A., Dove J.B., Heindl W.A., Smith D.M., 1999, 5th Compton Symposium, in press

Priedhorsky W.C., Terrell J., Holt S.S., 1983, ApJ 270, 233

Pringle J.E., 1996, MNRAS, 281, 357

Psaltis D., Belloni T., Van der Klis M. 1999, ApJ, 520, 262

Rapley C.G., Tuohy I.R., 1974, ApJ, 191, L113

Reig P., Méndez M., Van der Klis M., Ford E.C., 2000, ApJ, 530, 916

Remillard R., Marshall H., Takeshima T., 1997, IAUC 6772

Revnivtsev M.G., Trudolyubov S.P., Borozdin K.N., 2000, MNRAS, 312, 151

Sault R.J., Teuben P.J., Wright M.C.H., 1995, Astronomical Data Analysis Software and Systems IV, ASP Conference Series, 77, 433

Schandl S., Meyer F., 1994, A&A, 289, 149

Seyfert C.K., Popper D.M., 1941, ApJ 93, 461

Shafter A.W., *Harms R.J., Margon B.*, Katz J.I., 1980, ApJ, 240, 612

Shahbaz T., Bandyopadhyay R.M, Charles P.A., Wagner R.M., Muhli P., Hakala P., Casarés J.,Greenhill, J., 1998, MNRAS, 300, 382

Shakura N.I., Sunyaev R.A., 1973, A&A, 24, 337

Shapiro S.L., Lightman A.P., Eardley D.M., 1976, ApJ, 204, 187

Shields G.A., McKee C.F., Lin D.N.C., Begelman M.C., 1986, ApJ, 306, 90

Shrader C.R., Wagner R.M., Hjellming R.M., Han X.H., Starrfield S.G., 1994, ApJ, 434, 698

Smith H.E., Margon B., Conti P.S., 1973, ApJ 179, L125

Soria R., Bessell M.S., Wood P., 1997, IAUC 6732

Sowers J.W., Gies D.R., Bagnuolo W.G. (Jr), Shafter A.W., Wiemker R., Wiggs M.S., 1998, ApJ, 506, 424

Stirling A.S., Spencer R.E., Garret M., 1998, New Astronomy Reviews, 42, 657

Sunyaev R.A., Titarchuk L.G., 1980, A&A, 86, 121

Sunyaev et al, 1993, A&A, 280, L1

Swinbanks D., 1987, Nature, 326, 322Tanaka Y, Lewin W.H.G., 1995, 'X-Ray Binaries' Chap 3, Eds. Lewin W.H.G., Van Paradijs J., Van den Heuvel E.

Tanaka Y., Lewin W.H.G., 1995, 'X-ray *Binaries*' *Chap*. 3, Eds. Lewin W.H.G., Van Paradijs J., Van den Heuvel E.

Tanaka Y, Shibazaki N., 1996, ARAA, 34, 607

Tananbaum H., Gursky H., Kellogg E., Giaconni R., Jones C., 1972a, ApJ, 177, L5

Tananbaum H., Gursky H., Kellogg E., Levinson R., Schreier E., Giaconni R., 1972, ApJ, 174, L143

Tavani M., Fruchten A., Zhang S.N., Harmon B.A., Hjellming R.M., Rupen M.P., Bailyn C., Livio M., 1996, Ap

J, 467, L81

Taylor A.R., Gregory P.C., 1982, ApJ, 255, 210

Terrell N.J., 1972, ApJ, 174, L35

Titarchuk L., 1994., ApJ., 434, 570

Treves A. et al. 1990, ApJ, 364, 266

Treves A. et al., 1980, ApJ, 242, 1114

Treves A., Belloni T., Bouchet P., Chiapetti L., Falomo R., Maraschi L., Tanzi E.G., 1988a, ApJ, 335, 142

Treves A., Belloni T., Chiapetti L., Maraschi L., Stella L., Tanzi E.G., Van der Klis M., 1988, ApJ, 325, 119

Udalski A., Pietrzynski G., Wozniak P., Szymanski M., Kubiak M., Zebrun K., 1998, ApJ, 509, L25

Van Paradijs J. et al., 1987, A&A, 184, 201

Van Paradijs J., 1996, ApJ, 464, L138

Van Paradijs J., 1998, 'The Many Faces of Neutron Stars', page 279, Eds. Buccheri R., Van Paradijs J., Alpar M.A.

Van Paradijs J., McClintock J.E., 1995, 'X-Ray Binaries' Chap 2, Eds. Lewin W.H.G., Van Paradijs J., Van den Heuvel E.

Van der Hooft F., et al. 1996, ApJ, 458, L75

Van der Hooft F., et al. 1999, ApJ, 513, 477

Van der Klis M., 1994, A&A, 283, 469

Van der Klis M., 1995, 'X-Ray Binaries' Chap 6, Eds. Lewin W.H.G., Van Paradijs J., Van den Heuvel E.

Van der Klis M., Clausen J.V., Jensen K., Tjemkes S., Van Paradijs J., 1985, A&A, 151, 322

Van der Klis M., Tjemkes S., Van Paradijs J., 1983, A&A, 126, 265

Van der Laan H., 1966, Nature, 211, 1131

Vikhlinin A. et al., 1994, ApJ, 424, 395

Voloshina I.B., Lyuty V.M., 1995, Astron Nachr., 316, 85

Voloshina I.B., Lyuty V.M., Tarasov A.E., 1997, SvAL, 23, 3

Wade C.M., Hjellming R.M., 1972, Nature, 235, 272

Walker E.N., 1972, MNRAS, 160, 9p

Walker E.N., Brownlie G.D., Mason K.O., Sanford P.W., Quintanilla A.R., 1976, Nature, 263, 393

Walker E.N., Quintanilla A.R., 1974, MNRAS, 169, 247

Walker E.N., Quintanilla A.R., 1978, MNRAS, 182, 315

Walker G.A.H., Yang S., Glaspey J.W., 1978, ApJ 226, 976

Waltman E.B., Fiedler R.L., Johnston K.J., Ghigo F.D., 1994, AJ, 108, 179

Wardle J.F.C., Homan D.C., Ojha R., Roberts D.H., 1998, Nature, 395, 457

Warner B., 1995, 'Cataclysmic Variable Stars', page 146, Cambridge Astrophysics Series

Warren P.R., Penfold J.E., 1975, MNRAS, 172, 41p

Webster B.L., Murdin P., 1972, Nature, 235, 37

Weisskopf M.C., Kahn S.M., Darbro W.A., Elsner R.F., Grindlay J.E., Naranan S., Sutherland P.G., Williams A.C., 1983, ApJ, 274, L65

Wen L., Remillard R.A., Bradt H., 2000, ApJ, 532, 1119

White N.E., Marshall F.E., 1984, ApJ, 281, 354

Wijers R.A., Pringle J.E., 1999, MNRAS, 308, 207

Wijnands R., & Van der Klis M, 1999, ApJ, 514, 939

Wijnands, 2000, 33rd COSPAR Scientific Assembly, astro-ph/0008096

Wilms J., Nowak M.A., Dove J.B., Fender R.P., di Matteao T., 1999, ApJ, 522, 460

Wilms J., Nowak M.A., Pottschmidt K., Heindl W.A., Dove J.B., Begelman M.C., MNRAS in press, astro-ph/0005489

Wilson R.E., Fox R.K., 1981, AJ 86, 1259

Wood K.S. et al., 2000, ApJL submitted

Yamaoka K., Ueda Y., Dotani T., Durouchoux P., Rodriguez J., 2000., IAUC 7427

Zhang S.N., Cui W., Harmon B.A., Paciesas W.S., Remillard R.E., van Paradijs J., 1997a, ApJ, 477, L95

Zhang S.N., Mirabel I.F., Harmon B.A., Kroeger R.A., Rodríguez L.F., Hjellming R.M., Rupen M.P., 1997, 4th Compton Symposium, 410, 141

Zhang S.N., Robinson C.R., Cui W., 1996, IAUC 6510

Życki P.T., Done C., Smith D.A., 1999, MNRAS, 309, 561